The Production of Meson Resonances in K^{-}-p interactions at 10 GeV/C

by

David Peter Dallman

A Thesis presented for the degree of

Doctor of Philosophy

of the University of London

Department of Physics
Imperial College
London, S.W.7.

May, 1970.

ABSTRACT

This thesis is a study of some of the strong interactions which occur in the collisions of 10 Gev/c kaons with stationary protons in a liquid hydrogen bubble chamber.

Chapters 1-6 deal with the collection and analysis of the data and are of fairly general relevance to the experiment as a whole. In chapter 7 the existence of four enhancements in mass spectra involving a kaon and one or more pions is demonstrated and chapter 8 is concerned with a determination of the quantum numbers of these peaks.

In the following four chapters (9-12) the production mechanisms for the six quasi two-body reactions in which the enhancements are observed are fully discussed. The last chapter summarises briefly the main conclusions of the work and what the future prospects may be.

CONTENTS

PREFACE

The author joined the High Energy Nuclear Physics group at Imperial College in October 1964. The first 6 months were spent attending the prescribed postgraduate lecture courses and assisting in the 3.5 Gev/c and 6 Gev/c K^-p experiments then in progress in the group.

The first exposures for the 10 Gev/c K^-p experiment were made in February 1965 and ~~In~~ in April 1965 the author joined this experiment. From then onwards the author and his colleagues were responsible for the analysis of the part of the film allocated to the Imperial College group.

CHAPTER 1

INTRODUCTION

The last ten years has seen the discovery of a wealth of structure in the interactions of hadrons, the particles which interact via the strong nuclear force. Before 1960 a few resonances had been found in pion-nucleon scattering; for example, the excited state we now call $N^*(1236)$ had been reported by Fermi and his co-workers (1) as far back as 1952. This is to be compared with the most recent compilation of particle data (2) which contains more than 80 well-established resonances, as well as many more less certain ones.

We now regard these resonant states and the previously known "elementary particles" (those which live long enough to be directly observed) on an equal footing; the latter are the ground states of the hadronic mass spectrum and cannot therefore decay by a strong interaction.

Because of the complexity of this spectrum it seem unreasonable to expect that these resonances are all "elementary" particles. There have been several speculations regarding the possible existence of some more fundamental entities out of which the known hadrons could be constructed. The best known of these is the quark hypothesis which was first suggested by Gell-Mann (3) following the success of the group SU(3) in the classification of particle states. After several years of negative searches there have, in the last year, been two positive claims for the observation of quarks (4), although there has been some controversy (5) regarding possible alternative explanations of at least one of these experiments.

A possible alternative to a sub-particle approach is the theoretical proposal, originally put forward by Chew (6) in which the hadrons are considered to form a mutually self-consistent set of particles interacting among themselves. This is the so-called strong interaction bootstrap idea.

Present developments in hadron physics, both theoretical and experimental, can be broadly divided into two types:

i) <u>Classification of particle states</u>

Experimentally this means determining all of the quantum numbers of the resonant states: mass (M), width (Γ), spin-parity (J^P), baryon number (B), hypercharge (Y), isotopic spin (I), and others where relevant.

Theoretically, one approach is to study SU(3) and higher symmetries with the aim of explaining the observed properties of the states by assigning them to multiplets which are representations of the groups.

ii) <u>Dynamics of the strong interaction</u>

For this there is no satisfactory theory at present. Field theory, with its requirement of a separate field for each particle seems to be a long way from the truth and the perturbation approach which has been so successful in quantum electrodynamics is not applicable to hadrons because of their very strong coupling.

The theoretical approach has therefore tended to be a phenomenological one, that is to say, one writes down possible forms for the scattering amplitude, often suggested by a model of some kind, which (hopefully) satisfy basic accepted maxims like unitarity and analyticity, and then compares the predictions of these amplitudes with the experimental data.

Experimentally, the only way at present of studying hadron interactions is to scatter a beam of accelerated particles on a stationary target, although it should soon be possible to study the collisions between two beams of protons. The theoretical models are tested best by having accurate data at as many incident energies as possible. Thus the general trend is towards the acquisition of more and more data and its rapid analysis, and towards higher and higher energies, thus requiring larger and larger accelerators.

The experiment described in this thesis is one of a series in which the Imperial College high energy group has participated during the last six or seven years, involving the interactions of negative kaons and protons. A liquid hydrogen bubble chamber is used both as the target and as the detector of the particles produced in the interactions. The bubble chamber, which developed from the cloud chamber used in cosmic ray studies, after an initial idea of Glaser (7), has been one of the most useful devices for studying high energy particles.

Units

As is now customary in high-energy physics, physical quantities are expressed in units such that $\hbar = c = 1$. Energies will usually be quoted in GeV (sometimes MeV); the corresponding unit for momenta is written GeV/c to avoid confusion.

$$1\text{GeV} = 10^9\text{ev} = 1\cdot6022.10^{-3}\text{ erg}$$

The present experiment is a collaborative effort among the high energy groups in Aachen, East Berlin, CERN, Imperial College and Vienna (8) (referred to as the ABCLV collaboration). It uses a K^- beam of momentum 10·12 GeV/c which, at the time the experiment was started, was the highest momentum ever achieved with separated K^- particles. Of the results so far published (9-22), those of particular interest, which do not form part of the work in this thesis, should perhaps be mentioned briefly.

Seven examples of the production of the strangeness -3 hyperon Ω^- have been found (18), which make a significant contribution to the world total of about 30. A determination of the spin of this particle may soon be possible; confirmation of the value 3/2 expected from SU(3) symmetry would be a useful result; any other value would be very interesting indeed.

Two new strangeness -2 Ξ^* resonances have been reported (17) and the Ξ(2030) state previously seen by the Brookhaven-Syracuse collaboration at lower energy (23) has been confirmed. These resonances can only be studied easily in K^- interactions; if one expects as much structure as has been found in the S = -1 and S = 0 baryon spectra (and there is no reason to expect otherwise), there is still a lot to discover about Ξ systems.

Finally, an attempt has been made (22) to begin a systematic experimental study of the multi-particle final states which account for such a large proportion of the interactions at high energies. However an extension of the technique described in ref. 22 to 5 or more particles in the final state would seem to be too complex to be of much practical use, since it would require one to consider distributions on surfaces in multi-dimensional hyperspaces.

CHAPTER 2

DATA COLLECTION

2.1 Details of runs

The first exposures in the experiment were made early in 1965 at the CERN proton synchrotron (24), using the separated beam known as O2 in conjunction with the 1·5 metre British National Hydrogen Bubble Chamber (BNHBC).

Subsequent exposures have used the U3 beam (later modified to U4) together with the CERN 2 metre hydrogen bubble chamber.

Table 2·1 shows, for each run, the number of photographs, their distribution among the five laboratories and the average number of kaons per picture.

Where it is necessary to distinguish between the different runs, the experiment numbers allocated to them in CERN will be used (see Table 2·1). Thus the exposures in the British chamber constitute experiment 75, while the runs in the 2 metre chamber are experiments 10, 12, and 13 respectively. The results presented in this thesis are (mainly) from experiments 75 and 10 only.

TABLE 2.1

FILM DISTRIBUTION

Experiment number	75	10	12	13	ALL
Bubble chamber	BNHBC		CERN HBC		-
Date of exposure	MAR 65	AUG 66	FEB 68	APR 69	-
Average K^- per frame	5	10	10	8	-
Film allocation (in 1000's of frames)					
Aachen	37	19	22	24	102
Berlin	25	4	13	21	63
Cern	80	23	165	75	343
London	26	6	27	57	116
Vienna	32	18	13	21	84
TOTAL	200	70*	240	198**	708

* not including 60,000 frames which had a too-high pion contamination and have not been analysed.

** 15,000 frames still in reserve.

2.2 Beams

Secondary charged particle beams at high energy accelerators are normally produced by allowing some of the protons circulating in the main accelerator ring to hit a metal target. From the large numbers of different types of particle produced, those of the type and momentum required are selected by suitable combinations of electric and magnetic fields.

Pure beams of charged kaons are among the hardest to produce, for the following reasons:

i) the ratio of negative kaons to negative pions produced from the target with momenta around 10 GeV/C is only of the order 0·1.

ii) the mean lifetime of K^- (about 12·35 nsec.) is less than that of π^- (26·03 nsec.) so that the K/π ratio decreases with increasing distance from the target. At a distance of L metres downbeam this ratio will have fallen to a fraction f of its initial value where

$$f \doteq \exp(-L/140) \qquad (2.1)$$

The lengths of beam used in this experiment are in the range 160–180 metres; this gives a value for f at the bubble chamber (assuming for the moment that there is no mass separation in the beam) of about 0·30.

iii) The number of kaons reaching the bubble chamber should be as high as possible to make the most efficient use of the exposure. The optimum number is about 10; if there are a lot more than this, interpretation of the photographs may become difficult. If one requires the pion contamination to be less than 5% this means that no more than 1 pion in 700 can be allowed to reach the chamber.

2.2.1 The 02 and U3 beams

Both these beams (25, 26) can be divided into three stages. In the first stage the particles are collected from the target and the first momentum analysis is carried out; the next stage involves a separation according to the particle mass and finally, in the last stage, the momentum is redefined and the particles are spread out in the vertical plane before entering the bubble chamber.

The technique of radio-frequency (RF) separation used in this experiment requires a very short burst of particles since the RF cavities are under power for only a few microseconds at a time.* To achieve this the technique of fast-ejection is used in which a fast kicker magnet, energised by a condenser discharge, deflects the protons circulating in the main accelerator ring onto the target. In this way all 20 bunches of protons (if necessary) can be removed in about 2 μsec.

Figure 2·1 shows the components used in the two beams, which are similar in most respects; table 2·2 lists some of their parameters.

* The bubble chamber also needs a relatively short burst of particles but this is of the order of milliseconds, so it is the RF requirement which is the determining factor.

FIG. 2.1 LAYOUT OF O2 AND U2 BEAMS

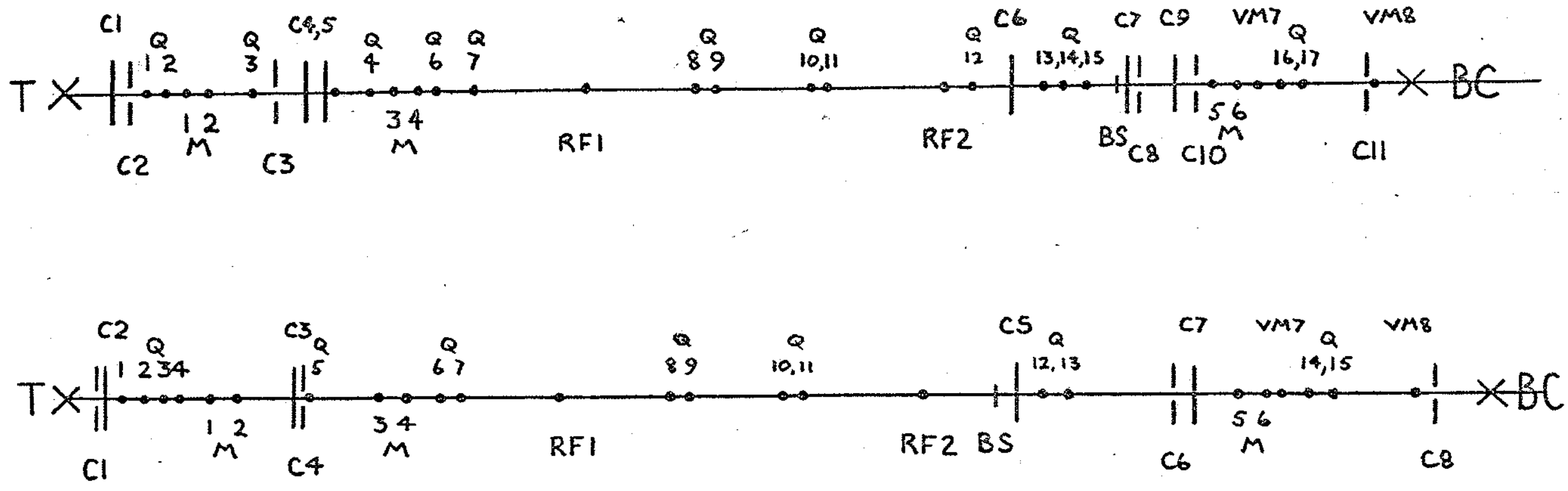

MAGNETS

M	Horiz. bending
VM	Vert. bending
Q	Quadrupole

T	Target
RF	RF cavity
BS	Beam stopper
BC	Bubble chamber

COLLIMATORS

Horizontal

Vertical

TABLE 2.2

BEAM PARAMETERS

		O2 (exp.75)	U3 (exp.10)
Primary beam momentum (Gev/c)		21.5	20.6
Target		Internal	External
Material		copper	copper
Height (mm)		7	2
Width (mm)		2	1
Length (mm)		100	150
Production angle at target (mrad)		40	0
Max. collimation angles: vertical		-	$\pm$ 7.5
(mrad) horizontal		-	$\pm$ 5
Solid angle acceptance (μsr)		-	150
Phase space acceptance (Gev/c.μsr)		6	-
Relative momentum bite (%)		4	0.25
Length of beam (m.)		180	165.5
Cavity separation (m.)		50	50
RF frequency (MH_z)		2855	2855
Beam composition (%)	K	64.7 $\pm$ 3.0	45.0
	μ	23 $\pm$ 2	50.0
	π	10 $\pm$ 1	< 5
	$\bar{p}$	2.3 $\pm$ 0.5	< 1
K/all hadrons		84 $\pm$ 4	> 90

Where not explicitly stated the following description refers to the U3 beam.

i) Particle collection and first momentum analysis

The use of an external target in U3 enables the particles to be collected at 0°, thus taking advantage of the strong forward peaking of the secondary particles. The collimators C1, C2 define the angular acceptances in the horizontal and vertical directions respectively. The lens system Q1-Q4 has two roles; horizontally it focuses the beam at the momentum slit C4; vertically, it gives a magnification sufficient to produce an opening angle of $\pm$ 1 mrad in the centre of the first RF cavity.

The bending magnets M1, M2 provide a momentum dispersion in the horizontal plane which is analysed at the momentum slit C4. The quadrupole Q5 and the bending magnets M3, M4 cancel the momentum dispersion of the transmitted beam and make it parallel in the vertical (mass separation) plane.

ii) RF separation

This technique was developed as an improvement over electrostatic separation following the original idea of Panofsky (27). The first operation of the two-cavity system in the O2 beam is described in reference 28. Each RF cavity exerts a sinusoidally time-varying deflecting force on the particles in the vertical plane. The relative phase of RF1, RF2 can be adjusted to any desired value and is then kept constant by means of a servo-system. Particles of the same momentum but with different masses will take different times to travel from RF1 to RF2, a distance of about 50 metres. The difference in times for kaons and pions at 10 GeV/C is about 0.2 nsec and this is of the same order as the period of the RF fields. The separation is achieved in the ideal situation by giving the unwanted particles (pions in this case) equal and opposite deflections in the two cavities and letting them hit the brass beam stopper which is centred on the beam axis. The wanted particles (kaons) have an overall deflection which enables them to miss the beam stopper and continue down the beam line.

Quantitatively, the difference in RF phase between the times of arrival in the second cavity of a pion and a kaon which were together in the first cavity is, in the relativistic limit, given by:

$$\delta = \left(\frac{wL}{2p^2c^2}\right)\left(m^2(\pi) - m^2(K)\right) \tag{2.2}$$

where w is the RF angular frequency, L is the cavity separation and p is the momentum.

The lens system Q8-Q11 between the cavities has a magnification of -1 so that if the relative phase is chosen to give zero net deflection for pions, the net deflections for kaons will be:

$$\begin{aligned} A(t) &= -A_o \sin wt + A_o \sin(wt + \delta) \\ &= 2A_o \sin\left(\tfrac{1}{2}\delta\right) \cos\left(wt + \tfrac{1}{2}\delta\right) \end{aligned} \tag{2.3}$$

The phase wt at which the particles enter RF1 is approximately random, since the period of the RF (about 0·3 nsec) is much smaller than the duration of the particle burst (a few μsec).

This simple discussion has neglected the following factors:

a) The cavities have a finite length over which the deflections are produced. For the present size of cavity (2 or 3 metres) this correction is small.

b) Because of the acceptance requirements of the cavity system, the beam has an angular opening of $\pm$ 1 mrad in the vertical plane. This means that the beam stopper has to subtend an angle of $\pm$ 1 mrad in order to stop all the pions.

From equation (2·3) it can be seen that the number of kaons which pass the beam stopper is greatest when

$$\delta = (2n - 1)\pi \quad , \quad n = 1, 2, 3, \ldots\ldots\ldots \qquad (2.4)$$

However, because of the cosine factor in (2·3) there will always be some kaons which hit the beam stopper.

The RF system is designed to satisfy (2·4) with n = 1; from (2·2) this fixes the ratio of w/p^2. One also wishes to eliminate antiprotons from the beam; this can be done provided

$$\frac{wL}{2p^2c^2}\left(m^2(\bar{p}) - m^2(\pi)\right) = 2m\pi \,, \; m = 0, 1, 2, 3, \ldots \qquad (2.5)$$

Equations (2·4) and (2·5) are in fact satisfied at the same RF frequency for momenta of 10·32 GeV/C, 10·12 GeV/C respectively. The latter is the momentum at which the experiment is performed; it is not quite the optimal value for kaon transmission but both types of unwanted particle should be efficiently removed.

iii) Final momentum analysis

This is necessary to reduce the background of muons which have appeared after the first momentum slit, mainly from the decays of pions.

Being leptons, they would not cause interactions in the bubble chamber, but if there are too many of them, the picture quality will be reduced.

The collimator C5 immediately behind the beam stopper (BS) redefines the vertical acceptance which partially reduces the muon background. The quadrupole doublet Q12, Q13 produces horizontal and vertical foci in collimators C6, C7; the doublet Q14, Q15 images C6 into the centre of C8 which is the second momentum slit; dispersion at this slit is provided by the bending magnets M5, M6. The doublet Q14, Q15 also shapes the beam in the vertical plane for entry into the chamber; the vertical magnets VM7, VM8 are used to obtain the correct entry angle and level at the chamber.

2.2.2 Tuning

Initial values for the currents in the bending magnets and quadrupoles are calculated for the required momentum by the program TRAMP. These currents are varied by small amounts around the starting values and the beam profile is studied using scintillation counters which are positioned at various places along the beam, e.g. attached to the collimator jaws. Eventually, optimum values for the currents are obtained and the beam is then "tuned" for that particular momentum. The RF pulse is adjusted to coincide with the arrival of the particle burst and the parameters of the RF system are then optimised using two counters, one just behind the beam stopper, the other just before the bubble chamber.

2.2.3 Monitoring during a run

Throughout a run the quality of the beam which enters the chamber has to be checked at regular intervals.

The most serious consideration is possible contamination from unwanted particles, especially hadrons. An estimate of this can be obtained by inspecting the film for interactions of certain types. Using results from other experiments (and from previous runs of the same experiment, if any) one can calculate the proportions of K^- and π^- interactions at 10 GeV/C which give rise to a visible decay of a neutral strange particle (V^o). These numbers depend on the size of the chamber; for the 2 metre HBC they are 22%, 7% respectively, for the volume of the chamber which we scan for interactions. The observed percentage from a sample of film should lie between these values and from it the K/π ratio can be calculated. The possibility of anti-proton contamination has been ignored here as it is usually a less serious problem than that of pion contamination.

Further, a knowledge of the total cross-sections for K^- and π^-, combined with the total number of interactions of any sort observed in the sample enables the average number of hadrons entering the chamber to be calculated. Comparing this with the average number of tracks observed gives by subtraction the number of muon tracks.

One view of each roll of film exposed in the run is developed as soon as possible and scanned for interactions with and without a visible V^0 decay. Also on every tenth frame the number of beam tracks is counted. This gives a reasonably accurate determination of the contamination but unfortunately it takes about 4-5 hours for the film to be developed and scanned, by which time 2 or 3 more rolls have been taken.

To enable serious contamination to be quickly detected so that the beam can be modified as soon as possible, a test strip of about 10-15 frames is cut from the end of each roll and developed separately in the experimental area. In this way one can get a background estimate within about 1 hour after the completion of a film.

For still more rapid feedback to the beam control it is possible to take polaroid photographs (development time about 10 seconds) and to inspect the chamber visually through a porthole.

Every 6–8 hours about 200 frames are taken with the RF switched off; if the beam stopper is functioning correctly the only particles reaching the chamber are then muons so that no interactions should be seen.

Estimates of the background from unwanted particles for experiments 75 and 10 are given in table 2·2.

A typical run of say 200,000 photographs takes about two weeks to complete.

2.3 Bubble Chambers

The bubble chamber detects high energy charged particles in the following way; if a particle passes through the chamber liquid (hydrogen in this experiment) when the latter is in a superheated state the ionisation produced provides a situation in which small bubbles can form along its path. The mechanism for bubble formation is not entirely understood at present but it is generally accepted that local heating in regions of about 10^{-6}cm radius is responsible (29). This heat arises when delta rays - electrons knocked from their orbits by the Coulomb field of the passing particle - of about 1 kev lose their energy.

When the bubbles have grown to a suitable size (typically 150μ) and before they have drifted too far away from their initial positions (no more than about 10μ), the chamber is illuminated and photographed. Three or four cameras are used so that the different views they see of the line of bubbles contain enough information for the path of the particle in space to be calculated.

A magnetic field is applied throughout the chamber; the trajectory of a particle is then a helix with axis along the field direction. The curvature of the helix is related to the momentum of the particle.

The working temperature of a liquid hydrogen bubble chamber is about 27°K and the hydrogen is brought into a superheated state by a rapid reduction in pressure. After 10-20 msec pressure conditions are uniform throughout the chamber and this is arranged to coincide with the entry of the burst of particles. When the bubbles have reached the required size (this takes a few msec) and have been photographed, the pressure is immediately reapplied to prevent spontaneous boiling throughout the whole volume, the bubbles are removed by a clearing field and the chamber is then ready to begin its next cycle.

2.3.1. The British and Cern Chambers

The British 1·5 metre chamber (30) was built in the early 1960's for use at the proton synchrotrons at CERN and at the Rutherford Laboratory, where it is at the present time. The Cern 2 metre chamber (31) was built a few years later and replaced the British chamber when the latter was moved to England.

Some of the parameters of the two chambers which are relevant to the problems of film analysis are shown in table 2.3.

Both chambers are divided lengthwise into three sections for purposes of illumination, which is provided by flash tubes. Uniformity of illumination throughout each region is achieved by a three-unit condenser system.

Each chamber has two opposite vertical windows, one being used for illumination, the other for photographing. This set-up is known as straight-through illumination, in contrast to the retroactive method used in some chambers, in which both light sources and cameras communicate with the chamber through the same (and only) window.

TABLE 2.3

BUBBLE CHAMBER PARAMETERS

		BNHBC	CERN HBC
Illuminated region:	length (cm)	140	177
	height (cm)	50	56
	width (cm)	50	50
Windows:	number	2	2
	length (cm)	150	218
	height (cm)	50	77
	thickness (cm)	16	17
Illumination:	no. of sources	3 x 3	3
	method	straight-through	straight-through
	"	dark-field	dark-field
	scattering angle	2^{o}	7^{o}
Cameras:	number	3	4
central plane demagnification		1:16	1:13.3
Film:	type	unperforated	unperforated
	width (mm)	35	50
no. of frames/film		2500	1500
Magnetic field:	central value (kgauss)	13.54	17.343
working temperature (^{o}K)		27	26
time delay (msec)		1.5	1.0

The intensity of the light scattered by a bubble falls off rapidly away from the forward direction, being about one-tenth of its forward value at an angle of 15° in hydrogen. Thus it is important to use a small scattering angle to get good contrast between the bubble image and the background. The British chamber uses a scattering angle of 2° (32) which is small enough for aberration effects to be important; this requires the use of monochromatic sources. The Cern chamber uses an angle of 7° (33) and also has monochromatic sources.

The bubbles can be detected either by observing the scattered light directly or by viewing the straight through beam out of which the bubbles have scattered some light. The former method, known as dark field illumination, is used in both the British and Cern chambers. The bubbles appear as bright points on a dark background; however the film as used for analysis is a negative so that the reverse is then true.

The cameras have to be far enough apart to give a stereoscopic angle sufficient for the accurate determination of the particle trajectories in space. Their axes must also be parallel, otherwise severe computational difficulties would occur in the reconstruction. They must therefore have wide angle lenses in order for each one to be able to view most of the chamber. The arrangement of the cameras in the two chambers with respect to the beam direction is shown in fig. 2.2.

On the inside of each window there are sets of reference marks in the form of crosses of various shapes and orientations.

FIG. 2.2

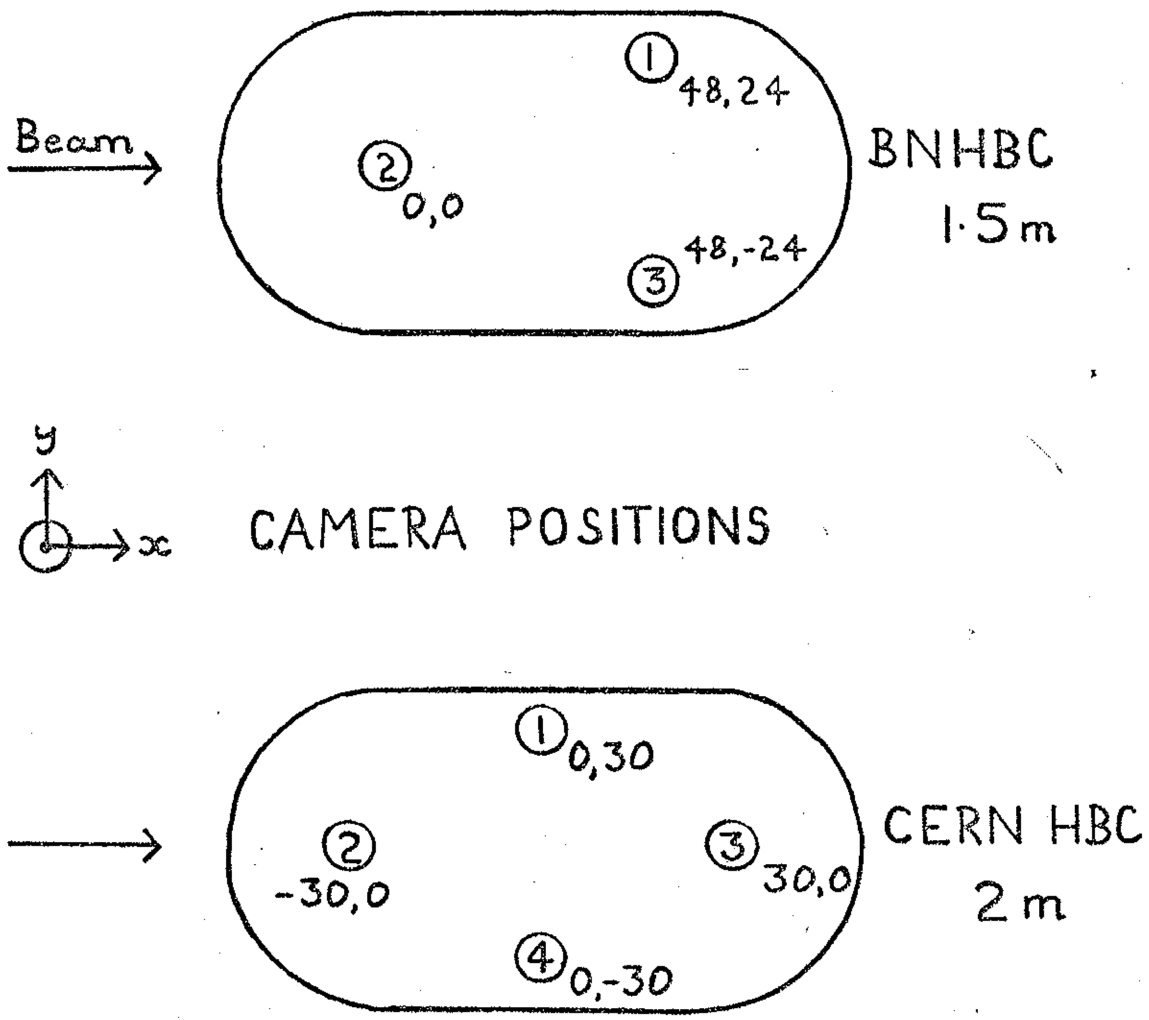

CAMERA POSITIONS

These fiducial marks define a chamber-based coordinate system to which the measurements made on the film are referred. There are also sets of reference marks on the camera gates.

A data panel which shows the current roll and frame number is recorded on the film alongside the chamber image.

2.3.2. Monitoring during a run

The density of bubbles along the path of a particle can be varied within wide limits by altering the degree of superheating. It is an important parameter since it is a function of the velocity of the particle. This means that a combination of measurements of track curvature and bubble density allow (in principle) a determination of the mass of the particle. In practice this is not always possible since the (empirical) relation between bubble density and velocity is of the form (34)

$$b = C/\beta^2, \tag{2.6}$$

where $\beta = v/c$ and C is a function of the thermodynamic properties of the liquid.

Thus, close to the relativistic limit $\beta = 1$, the difference in bubble density for particles of different mass is very small and is not easy to measure experimentally.

The bubble density which all tracks approach in this limit is known as minimum ionisation for that particular set of chamber conditions. Kaons of momentum 10 Gev/C have $\beta = v/c \doteq 0{\cdot}9988$

so that they represent minimum ionisation to within 1 part in 400. Because the thermodynamic conditions of the chamber will change slightly during a run, measured bubble densities are always compared with the density for a beam track on the same frame, so that the quantity C in equation (2.6) is eliminated.

A suitable bubble density for minimum ionising tracks is about 10-15 per centimetre. The pressure change during the chamber expansion is chosen to given a value in this range and this in turn determines the time interval required between the entry of the particles and the flash, i.e. the time required for the bubbles to grow to photographable size.

During a run the values of the pressure change and the time delay are checked at regular intervals. The bubble density is checked by counting the number of bubbles in a known length of track with the aid of a microscope; this is done for several beam tracks on the test-strip taken from the end of each roll (see section 2.2.2 for further details).

CHAPTER 3

DATA EXTRACTION

The following chapters describe how the information recorded on the film is extracted and put into a form ready to be used for the analysis of the K^-p strong interaction.

As mentioned at the end of the last chapter, there are two main types of information that can be obtained from a track, its curvature and its bubble density.

In the analysis of the more recent 10 Gev/c K^- exposures (experiments 12 and 13) the information on both curvature and bubble density is retrieved in a single process using a flying-spot device (35) to scan the frame and record the position of every bubble.

Before the development of this device to the stage where it could be used for routine analysis, the operations of curvature and bubble density determination were usually kept separate and this was the case with experiments 75 and 10. The measurement process described later in this chapter refers only to the former operation; the information from the bubble densities is introduced at a later stage by a visual inspection of the film and this will be discussed in the next chapter.

It is found to be more convenient to make an initial visual examination of the film (known as scanning) in which details of the interactions of interest for analysis are recorded, rather than to try and combine this with the measuring operation.

The general procedures used in the analysis are the same in each of the five collaborating groups but the exact details vary from group to group, since they depend on factors like manpower (both physicist and non-physicist) and the relative amounts of scanning, measuring and computing time available. Where specific details are described they refer to the methods of the London Group.

After the measurement stage, the raw data is put through a sequence of computer programs; these are described in the later parts of this chapter.

3.1 Scanning

Each roll of film is projected at about 10-15 times magnification and examined frame by frame for the types of interaction which are to be analysed. These scanning projectors need not be of high precision since no quantitative measurements are made on them.

One of the useful features of hydrogen bubble chambers is that the target nuclei are single protons; this makes it a lot simpler to analyse the interactions than if the target were a more complex nucleus of protons and neutrons. An interaction between a beam particle and a target proton is seen in the chamber as a beam track which ends at a certain point, from which begin other tracks caused by the charged particles produced in the interaction. In general there will be some neutral particles produced as well but these are undetected.

Since the K^- and the proton have electric charges -1, +1 respectively and since all known charged particles have only a single + or - charge, it follows that, assuming charge is conserved in the interaction, there must be equal numbers of positively charged and negatively charged particles produced.

Sometimes one of the charged tracks from an interaction may decay in the chamber, usually into one charged particle and one or more neutrals. This is observed as a kink in the trail of bubbles at the decay point.

Also a neutral particle may be seen to decay into charged particles (usually two) within the chamber volume. This appears as a V-shaped pair of tracks which points back towards the primary interaction in which the neutral particle was produced.

An interaction (usually called an event) is characterised by a three-digit number known as the topology. The first digit is the total number of charged tracks (prongs) coming from the event and can be 0, 2, 4, 6 ..... The second digit is the number of charged decays (kinks) and the third is the number of neutral decays (V^0's). These last two digits are usually 0 or 1, sometimes 2 but rarely higher. Topologies where the second and third digits add up to two or more, that is where there are two or more associated neutral or charged decays, are called rare topologies. If there are ten or more prongs the topology becomes a four-digit number; this is not very common.

The following information is recorded at the scanning stage, for each event:

i) roll, frame and event number. The event number is used to distinguish events on the same frame and increases from 1 in the downbeam direction.

ii) topology.

iii) scan number and scanner's number.

iv) an approximate indication of the position of the interaction point in the chamber.

v) if necessary, a sketch of the event and any special instructions to aid the measurer.

In experiment 75 this information was recorded on scanning sheets and the whole job of book-keeping was done manually. In experiment 10 a semi-automatic system was adopted, the details being recorded on specially designed cards which were later punched.

Each film is scanned completely twice, and then a comparison scan (the check-scan) is made in order to resolve the discrepancies between the first two scans. In experiment 75 the second scan was done by technical assistants and the other two by physicists; subsequently the first two scans were done by the assistants but the check-scan was still carried out mainly by physicists. Two views are used for each scan, a different pair for scans 1 and 2. On the whole events are only recorded if there are three good views available. In experiment 10, where there are four cameras, the film from camera 2 (situated towards the beam entry end of the chamber) is not used in the analysis. This is the best view to omit since it sees more of the beam track (whose momentum is known anyway) and less of the final particle tracks which have to be measured. In principle, all four views could be used but most measuring devices are set up to take a maximum of three. It is doubtful anyway whether the increase in precision would be worth the extra measuring effort involved.

The criteria used in scanning the film are summarised in table 3.1. Events are only recorded if they lie within certain defined regions of the chamber (called fiducial regions). Charged and neutral decays have larger fiducial regions. The choice of region for the primary interaction is a compromise: on the one hand it is advantageous to use as large a region as possible, simply to maximise the amount of data obtained; on the other hand, the tracks have to be long enough to get an accurate curvature measurement and also one does not want to allow too many of the neutral strange particles to escape from the chamber before decaying.

Except for the width of region definition in experiment 75, which just requires that an event is visible on cameras 1 and 3, all fiducial region definitions refer to camera 1.

TABLE 3.1

SCANNING AND MEASURING CRITERIA

		Experiment 75	Experiment 10
Views used:	scan 1	3,2	1,4
	scan 2	1,3	3,1
	measuring	1,2,3	1,3,4
Fiducial regions:	number	3	2
length definition		bright bands on film	fiducial marks
width "		event seen in 1,3	" "
length of region 1 (cm)		40.7	88
" " " 2 "		41.7	39
" " " 3 "		46	-
Beam track			
minimum length (view 1)(cm)		5 (initially 2)	fixed by region definition (about 15)
maximum angular acceptance		1°	1°
Topologies scanned			
region 1		all	all except 000
region 2		001,201,401	rares
region 3		rares	-
Topologies measured			
region 1		200,400,001,201,401*	all except 410,610,810,...
region 2		001,201,401	rares
region 3		rares	**

* The London and Vienna groups also measured and analysed topology 600

** The London group also measured and analysed topology 601.

3.1.1 Stopping tracks

One important piece of information which is passed on from scanner to measurer concerns stopping tracks. Because the proton is the only stable hadron, a particle which stops within the chamber volume and does not decay must be a proton. Quite often tracks end in the photograph because the particle has hit one of the windows. In this case the end point of the track and the set of fiducials on the inside of that window are coplanar so that the relative position of the end-point and these fiducials will be practically the same in all views. Thus to find genuine stopping tracks the scanner compares any end-point on the frame with each set of fiducials, e.g. by superimposing the views on the scanning projector; an end-point which does not match up with either set is a stopping point.

The advantage of looking for stopping protons is that there is an empirical relation between the range and the initial momentum of a given particle; the momentum may therefore be found from a range determination. This is particularly useful since a stopping proton track is often too short to get an accurate momentum measurement from its curvature.

When a stopping track is measured the operator takes the last bubble as one of the measured points and gives it a special label.

Apart from the interaction of K^- beam particles with protons, there are other "events" which occur in the chamber and give potentially useful information.

3.1.2. Secondary interactions

Each hadron produced in a primary interaction has a certain cross-section for undergoing a further collision with another target proton in the chamber. The probability of an interaction in a length L of a track is $\sigma\rho L N_0$, where ρ is the density of liquid hydrogen and N_0 is the Avogadro number. For $\sigma = 50\text{mb}$, $\rho = 0{\cdot}06$, $N_0 = 6{\cdot}10^{23}$, L = 120cm, this gives a probability of about 0·2 for a typical secondary track. An analysis of this secondary interaction may give some information as to the identity of the secondary particle and this, in turn, may be of some help in analysing the primary interaction.

i) Interactions of neutral secondaries

These look like V^0's but have an odd number of prongs. Unlike V^0's, there can be other neutral particles produced, so that the line of flight cannot be exactly determined. It is therefore not easy to be sure of the origin of these secondary neutral particles and they are ignored.

ii) Interactions of charged secondaries

These appear as secondary events on charged tracks from the primary interaction. If the track concerned is long enough and curved enough for a reasonably accurate momentum determination, it has not been considered worthwhile to measure the secondary interaction. In experiment 75 we did measure if the sagitta of the track was judged to be too small (there was no rigid limit). From the experience gained we decided that only elastic secondary scatters would be accepted. Consequently, in experiment 10, we did not measure them if they were obviously non-elastic; we also imposed a sagitta limit of 2mm in the chamber. For a 1 Gev/c track this corresponds to a length of about 17cm; the probability of an interaction before this is about 0·03.

3.1.3. K^- decays

A knowledge of the number of beam particles which decay in the chamber would enable an independent estimate of the total K^- flux to be made. The mean path length of a K^- before decay is $pc\tau/m$, where τ is the mean lifetime. For $\tau = 12.35$ nsec (2), c = 30cm/nsec and p/m = 20, this gives a length of about 74 metres, i.e. about 1 beam track in 37 will decay in the chamber.

In about 94·5% of its decays the kaon breaks up into a single charged particle and one or more neutrals. The angle between the incoming and outgoing charged tracks is usually quite small at high momentum and this makes these decays hard to see. The 5·5% represents decays into three charged pions (the so-called tau decay). The three pions are also strongly peaked in the forward direction but, being all visible, these decays are easier to see than the single-prong ones. We give them topology 300 and measure them as if they were normal interactions; this gives a measurement of the beam momentum which can be compared with that obtained from the RF separator parameters. A further advantage of using tau decays rather than single-prong decays is that they are a characteristic of the K^-; any pions in the beam will give rise to about twice as many single-prong decays as the same number of K^- but will give no three-prong decays.

Apart from these decays there will be a background of apparent odd-prong events. These are recorded at the scanning-stage in order to obtain an upper limit on their occurrence. Possible explanations for these anomalies can be divided into two categories, depending on whether there is an extra positive or an extra negative track.

i) <u>extra negative</u>

a) a δ ray is produced on one of the tracks very close to the apex of the event which is fast enough not to be identified as an electron by its ionisation.

b) there is a very slow proton which stops in a distance less than the bubble separation.

ii) <u>extra positive</u>

a) one of the secondary particles may have undergone an interaction very close to the primary event. Replacing the distance of 120cm used in the calculation in section 3.1.2 above by 1mm, gives the probability of this occurring for a given track as about 1/5000.

3.1.4 <u>Electron pairs</u>

These arise from the materialisation of γ-rays in the Coulomb field of a proton. The average interaction length for this process (called the radiation length) is 819cm in hydrogen.

The most likely origin in the chamber of an electron pair is the decay $\pi^0 \rightarrow 2\gamma$. Assuming an average visible path length of 120cm for the gammas the probability of a given one converting in the chamber is about 1/7, i.e. the probability of seeing both gammas from the decay is only 1/49, while the probability of seeing one is 12/49. These chances are too small to make it worthwhile measuring (or even noting) these electron pairs.

The opening angle of an electron pair is always practically zero. A V^o which happens to have a small opening angle can appear ambiguous with an electron pair at the scanning stage. To avoid losing any genuine V^o's we measure all apparent electron pairs when neither track can be identified as an electron by ionisation.

3.2 Measuring

Most of the measurements for this experiment have been carried out on one or other of the two National Measuring Machines belonging to the Imperial College group. The optics for these machines were designed by the Technical Optics group at the college and other parts were made commercially. In addition some of the measurements for experiment 75 were done on a less sophisticated but not much less accurate machine (called Hauser) which was built by members of the group.

The process of measuring involves making accurate determinations of various points on each of the three views of an event. A measurement is made by bringing the point to be measured into coincidence with a fixed mark on the projection screen. The operator then presses a button and the (x, y) coordinates of the point are punched out in binary-coded octal form on 5-track paper tape. Unless there are explicit instructions to the contrary, between 5 and 10 points are measured on each view for each track of the event; in addition measurements are made of the interaction point (called the production apex), any other special points (e.g. stopping points or apices of decays or secondary interactions), and four particular fiducial marks. The latter relate the measurements on the film to positions in the bubble chamber reference system. This procedure is repeated for the other two views of the event. The operator also sets up on dials various items of book-keeping information, e.g. roll, frame and event number, date, operator's number and measurement number (this distinguishes different measurements of the same event). This information is transferred to the paper tape before measurements begin. When a set of fiducials, a point, or a track, has been measured an identifying label is punched automatically by the machine.

On both National Machines the actual measurements are made by detecting the displacements of fringes in a Moiré fringe system produced by two diffraction gratings, one fixed to the machine and one on the movable stage. The least count corresponds to a displacement on the film of 2μ, that is, about 32μ and 27μ in the British and Cern chambers respectively (see table 2.3). The counters which record the displacements of the fringes due to movements in the x and y directions are set to fixed values when the first fiducial on a view is measured; at the end of the view the operator resets on this fiducial and compares the readings of the x and y counts with their initial values. If they disagree by more than about 6 counts the view is remeasured.

For x-direction displacements the film is moved parallel to its length; in the y direction it is the projection lenses which move. The movements are controlled by oil hydraulic rams; the x and y movements have velocities proportional to the components of a sine-cosine resolver, so that the resultant motion can be controlled by a single foot pedal. The direction of motion is determined by an arrow on the projection screen at the measuring point.

The optical systems of the two machines are somewhat different (32). One of them (called Bertha) has two screens, one (of magnification 9) covering the whole frame, on which the operator looks for the events, and a smaller one (of magnification 30) which shows the area around the point to be measured. The other machine (Willie) has a single screen of intermediate magnification.

There can be both random and systematic errors on the measurements from these machines. The random error has been determined (for Bertha) by repeated settings on the same fiducial and has a root-mean-square value of 4μ (on the film) (36). The systematic error was investigated by measuring about 30 points on an 8cm long accurately straight line exposed on a piece of film. On reversing the film and repeating the measurements any systematic curvature introduced is reversed. Comparison of the two sets of measurements indicated an introduced sagitta of 0.5μ; with the magnetic fields used in the present experiment this corresponds to momenta of about 40, 60 Gev/c respectively in the two chambers.

In preparing the data for the final analysis the events are treated independently. The overall aim is to identify the particles produced (including neutral particles which are not directly observed) and to obtain their vector momenta. With many events this aim is too ambitious for a hydrogen bubble chamber alone to achieve.

The process of computation is conventionally divided into several stages. This is partly because a single complete program would be too large and also because there often has to be intervention by a physicist before the final interpretation of an event can be made.

In this experiment the chain of programs developed in Cern is used. The programs are THRESH, GRIND, SLICE and SUMX; detailed descriptions of these can be found in reference 37. Thresh and Grind were run mainly on the Imperial College IBM 7090; Slice and Sumx were run on the Cern CDC 3400, CDC 6600 respectively.

Before data is ready for the first stage in this chain it has to be converted from paper tape to magnetic tape. At the same time checks are made to ensure that the correct numbers of fiducials, points and tracks have been measured on each view and that the labels and the basic book-keeping information are valid. This was done by programs PING and BIND for experiments 75 and 10 respectively. At a later stage, when the measuring machines were connected on-line to the group's PDP-6 computer, these checks were made in real time. This made it worthwhile making some rough checks on the actual measurements since the operator could be asked to repeat an unsatisfactory track immediately.

3.3 Geometric reconstruction

From the measurements made on each view Thresh (37-39) calculates the direction in space and the curvature of each track. It assumes that the tracks are segments of pure helices. This implies that the magnetic field is assumed to be constant throughout the chamber volume (it actually has a maximum variation from its central value of a few percent) and that the slowing down of the particle due to multiple Coulomb scattering is neglected. This slowing down is most serious for slow tracks and it is often necessary to measure only part of the way along such a track in order for Thresh to be able to reconstruct it satisfactorily.

The chamber-based frame of reference is shown in figure 3.1, which also shows the approximate positions of the four fiducials measured, as seen from a point in the centre of the camera system. The Z-axis points towards the cameras and the X-Y plane is the back of the front glass.

In order to perform the reconstruction of an event in space, Thresh has to be supplied with data on various features of the chamber. This data should be constant for all film taken during a single run and consists of the following items:

i) the coordinates of the cameras in the chamber reference system;

ii) the refractive indices and thicknesses of each of the optical media between the cameras and the back glass of the chamber;

iii) coordinates of the four measured fiducial marks as seen in each camera. These are given in the chamber reference system translated to the intersection of the optic axis with the front glass;

FIG. 3.1

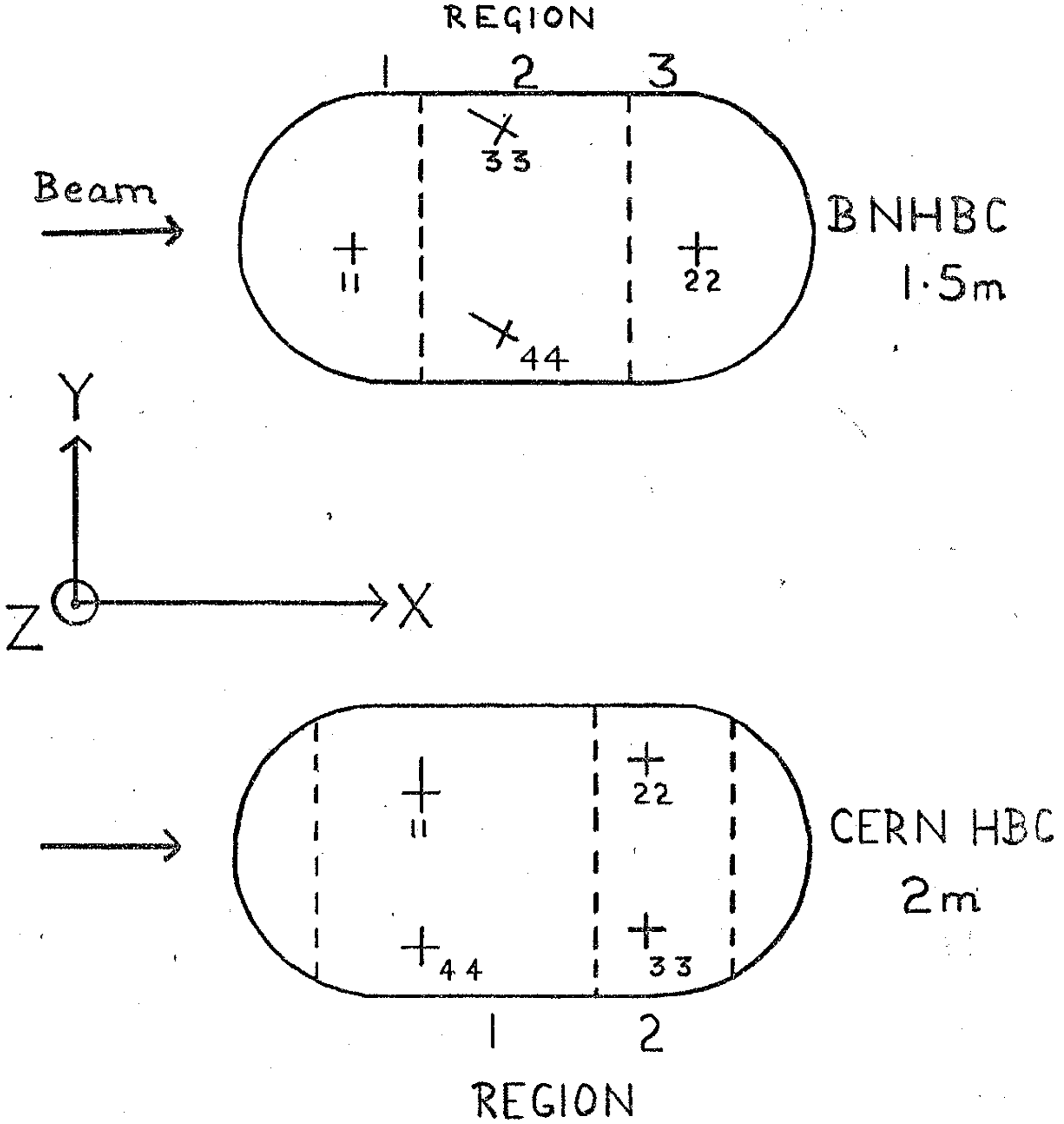
REGION
1
2
3
33
Beam
11
22
44
BNHBC
1·5m
Y
Z
X
11
22
44
33
CERN HBC
2m
1
2
REGION

iv) coefficients used for the correction of lens distortion and film tilt in the cameras;

v) some other general constants, for example, allowed tolerances for measured points and fiducials.

The values of some of these quantities are shown in tables 3.2 and 3.3. The fiducial and camera positions and the distortion corrections are determined from measurements of all fiducials (including the camera-based ones), together with measurements made on a grid of intersecting lines placed at various points in the chamber before it is filled with hydrogen. The final values of these constants are optimised using the program PYTHON (37).

The first stage in the reconstruction is to transform the raw film measurements (x, y) onto the Z = 0 plane of the chamber coordinate system. This transformation is assumed to be linear and is parametrised as:

$$\begin{aligned} X_i &= a_1 + a_3\, x_i + a_5\, y_i \\ Y_i &= a_2 + a_4\, x_i + a_6\, y_i \end{aligned} \tag{3.1}$$

where i runs over the 3 views. This corrects for translation and stretch of the film and for non-orthogonality of the measuring machine axes. The coefficients a_i are determined for each view by a least squares fit using both the measured fiducial positions and their known positions from the constants. With four fiducials measured this gives 8 equations for 6 unknowns.

TABLE 3.2

GEOMETRY CONSTANTS

		Experiment 75		Experiment 10	
Fiducial positions		X	Y	X	Y
F1	View 1	1.2476	0.3681	-22.947	-15.578
	" 2	3.7173	1.5997	-54.133	15.498
	" 3	1.2499	2.8446	-23.029	46.643
F2	" 1	64.2678	0.1530	-22.840	-50.771
	" 2	66.7768	1.3873	-53.963	-19.705
	" 3	64.2820	2.6435	-22.890	11.414
F3	" 1	28.4909	20.7865	39.705	-10.245
	" 2	18.8887	15.9782	8.577	20.833
	" 3	28.4781	11.2149	39.714	52.035
F4	" 1	28.5223	-9.8256	39.808	-45.432
	" 2	18.9519	-14.5830	8.672	-14.339
	" 3	28.5672	-19.4145	39.778	16.786
Distortion corrections			(all entries x 10^{-6})		
view 1	b_1, b_2	-681	8879	-788.99	-14025.95
	b_3, b_4	-2172	21948	-2351.72	-13264.28
	b_5, b_6	46295	-9793	-46504.68	30799.06
	b_7	-		309.49	
view 2	b_1, b_2	-2304	178	-1368.10	-4701.43
	b_3, b_4	763	23501	7919.94	-4148.45
	b_5, b_6	42707	-13351	14425.79	-5947.29
	b_7	-		662.97	
view 3	b_1, b_2	-4439	-5198	-844.53	-2187.44
	b_3, b_4	2157	10430	1159.26	-6947.05
	b_5, b_6	25801	-91	-1638.80	8946.26
	b_7	-		-489.78	

TABLE 3.3

GEOMETRY AND KINEMATICS CONSTANTS

	Experiment 75			Experiment 10		
Camera positions(cm)	X	Y	Z	X	Y	Z
view 1	47.9438	24.0003	141.8935	0.030	29.729	243.347
view 2	0.0043	0.0357	141.7864	30.068	-0.254	243.535
view 3	47.9892	-24.0505	141.7807	0.019	-30.257	243.284

General constants	Exp.75	Exp.10
THRESH		
Upper tolerance for fiducials (cm)	0.2	0.05
" " " labelled points (cm)	1.0	1.0
" " " ordinary points	0.2	0.2
Lower " " " "	0.05	0.05
Stereo ratio	8	8
Film-lens distance (cm)	18.6	18.6
GRIND		
Bubble density for $\beta = 1$ (cm^{-1})	15.0	14.0
Measurement error on film (cm)	0.0125	0.0075
Number of S.D.'s used in comparisons	3	3
Minimum errors on space points (cm)		
X, Y	0.03	0.03
Z	0.1	0.1
Maximum track length (cm)	150.0	160.0

Provided the final positions of the fiducials are within the specified tolerance the transformation (3.1) is applied to all measurements on the view. If not, the worst fiducial is discarded and the fit is repeated with the number of independent coefficients reduced to 4 by imposing orthogonality ($a_5 = -a_4$, $a_6 = a_3$). If one fiducial is still outside the tolerance the view is unacceptable. If less than 2 views of an event are acceptable the event is rejected.

The next step is to correct for film tilt and lens distortion in the cameras. To do this, both X and Y are multiplied by a fourth order polynomial in X, Y:

$$1 + b_1X + b_2Y + b_3XY + b_4X^2 + b_5Y^2 + b_6(X^2 + Y^2)^2 \qquad (3.2)$$

where the coefficients b_i are usually quoted as dimensionless parameters by removing the appropriate factors of the camera Z-coordinate. In (3.2) the first order terms correct for film tilt while the higher orders correct for lens distortion. Note that rotationally symmetric distortions would correspond to $b_3 = b_4 = b_5$, a condition which is not realised in practice.

In experiment 10 a further transformation was found to be necessary:

$$Y = Y + b_7X^2 \qquad (3.3)$$

As part of the process of reconstructing a track, Thresh associates with each measurement a reconstruction line. This is the part of the ray from that measured point to the camera concerned which lies in the chamber liquid. It is given by the relations

$$\begin{aligned} X &= F_x Z + G_x \\ Y &= F_y Z + G_y \end{aligned} \qquad (3.4)$$

where F_x, F_y, G_x, G_y are functions of the apparent position of the point in the $Z = 0$ plane and can be calculated. If a point is measured on two views its position in space is defined by the intersection of the corresponding reconstruction lines, or, since the lines will in general be skew because of errors, by their point of closest approach. If a point is measured on three views, the three reconstruction lines can be optimised to give the best coordinates for the point in space. This is the procedure followed for particular labelled points in the event such as the production apex or a stopping point. If the root-mean-square error on the coordinates obtained is larger than the tolerance the fit is repeated with one view less. If no combination of views is satisfactory the point is ignored.

The same procedure cannot be immediately applied to reconstruct points on tracks since the same space points are not measured on the different views. Instead the method of "near corresponding points" is used. The reconstruction lines are calculated for every measured point as before. The measurements on the view on which the track is most nearly seen as an orthogonal projection define the space points which will be reconstructed. A second view is chosen to ensure good stereoscopic conditions and the coefficients of the reconstruction lines of the required space points are determined by interpolation (sometimes extrapolation) from the known reconstruction lines on this view. When all points have been reconstructed in this way the first approximation to a helix is determined. The helix is described by:

$$X' = \rho(\cos\theta - 1) \tag{3.5}$$

$$Y' = \rho\sin\theta \tag{3.6}$$

$$Z' = \rho\,\theta\tan\lambda \tag{3.7}$$

where for convenience in computation, the coordinate system $(XYZ)'$ is obtained from (XYZ) by moving the origin to the starting point (A, B, C) of the track and rotating through an angle ϕ about Z so that Y' is the tangent to the track at (A, B, C). ρ is the radius of the cylinder on which the helix lies, λ is the dip angle (measured from the $X'Y'$ plane) and θ is the angular distance (measured in the $X'Y'$ plane) from the starting point to a point on the helix.* In this first approximation ρ, ϕ are determined from a least squares fit to the circle given by (3.5) and (3.6); λ is obtained by fitting to the straight line given by (3.7); the coordinates (A, B, C) of the starting point are taken from the point reconstruction or, if that was not successful, they are found by the method of corresponding points.

These parameters are used as starting values in the final least squares fit which consists of minimising the sum of squared deviations of the measurements from the projection of the fitted curve (on the film plane), the sum being over all measurements in all views. The parameters which are fitted are $1/\rho$, λ, ϕ, A (or B) and C.

* These angles ϕ and λ are not the same as those used in Grind. Equation (3.8) relates the two pairs of angles.

$1/p$ is used since it is expected to have a more Gaussian-like distribution than p, a property which is desirable in a least squares fit. One of the vertex coordinates has to be fixed since otherwise the point would be free to move along the track in the fit; in practice C is usually not as well determined as A, B so it is one of the latter pair which is fixed (the one which is the more sensitive to small variations in the parameters of the track in question).

Normally the fit converges below the required level within two of three iterations. The error matrix of the fitted parameters is then calculated; these are the so-called internal errors as they do not include uncertainties such as those due to multiple Coulomb scattering and therefore represent lower bounds on the true errors. The root mean square of the differences between measured and fitted points (usually called residuals) is a measure of the goodness of the fit. It has an approximate Poisson distribution with a modal value of about 8μ for the measuring machines used in this experiment.

Thresh outputs its results on magnetic tape in the form of binary records, one per event.

3.4 Kinematic fitting

Using values of the track parameters obtained in Thresh, Grind (37, 39, 40) imposes equations of conservation of energy and momentum at an interaction point with the aim of allowing restrictions to be placed on the possible identities of the particles participating in that interaction. The energy and momentum of a particle can be described by a suitable set of four parameters. The set used by Grind consists of the reciprocal of absolute value of the momentum (p), dip and azimuthal angles (λ, ϕ) and the mass (m), the first three of which correspond to the variables used in Thresh. For tracks reconstructed in Thresh, the value of p is obtained from the curvature and from a knowledge of the magnetic field (see below), while the two angles λ, ϕ are related to those used in Thresh by the relations:

$$\begin{aligned} \lambda_G &= \pm \lambda_T \\ \phi_G &= \phi_T \pm \pi/2 \end{aligned} \tag{3.8}$$

where $\pm$ refers to anti-clockwise and clockwise tracks respectively.

At an interaction point there are four constraint equations expressing energy-momentum conservation. These can be written

$$\sum P_x = \sum P_y = \sum P_z = \sum E = 0 \tag{3.9}$$

where the sum is over all particles participating in the interaction, the initial particles (beam and target) contributing with a negative sign. If there are less than four unknowns among the parameters of the particles the known parameters can be adjusted to give the best solution and a measure of the goodness of this fit can be obtained. The criterion for the best solution is that the quantity

$$X^2 = c^T G c \tag{3.10}$$

is a minimum, where $c_i = m_i - m^o_i$, m_i being the fitted values of the known parameters and m^o_i being the corresponding unfitted values. G^{-1} is the error matrix of the measured variables, that is, G^{-1}_{ii} is the variance of m_i and G^{-1}_{ij} is the covariance of m_i and m_j. The condition (3.10) is only strictly valid when the variables have Gaussian distributions and this is approximately true for the variables ($1/p$, λ, ϕ). If there are N unknown parameters at a vertex the quantity

$$n = 4-N \tag{3.11}$$

is called the number of degrees of freedom of the system. Three cases may be distinguished:

i) $1 \leq n \leq 4$ (or $N < 4$) In this case a fit is possible, as explained above, and one usually refers to it as an n-constraint (or n-C) fit;

ii) $n = 0$ ($N = 4$) Here there are an equal number of equations and unknowns and it is always possible to obtain a solution (though it may be unphysical). However there is no possibility of estimating the goodness of the solution. Although this is not a fit but just a calculation, it is usually called a zero-constraint fit. In this experiment no interpretations of events based on such fits have been accepted.

iii) $n < 0$ ($N > 4$) In this case there are more unknowns than equations and there is therefore no unique solution. This is referred to as a no-fit situation.

Variables in Grind are divided into three groups, depending on the sizes of their variances. Correlations between variables in different groups are assumed to be negligible.

i) Fixed variables These have very small variances, which are assumed to be zero. The masses of the particles usually fall into this class. This may seem strange since the mass is the one parameter which is never determined in Thresh. However, if the masses of the outgoing particles were left as unknowns it would only be possible to get a fit in the case of two- and three-particle final states with no unseen neutral particles. Instead it is possible to take advantage of the fact that, unlike the other three track variables which have continuous distributions, the masses form a fairly small set of discrete values, (about 16 in all). Moreover, applying the conservation of B, Y, Q and I at the strong interaction vertex severely restricts the number of possible combinations of particles and this number is further reduced by the knowledge that many of the allowed reactions are relatively uncommon and may be safely neglected. These properties make it feasible to attempt to fit, for each event, all possible sets of mass assignments, called hypotheses. For each hypothesis the masses are then fixed variables. This procedure has the disadvantage of neglecting the possibility of an unexpected occurrence. However such cases, if sufficiently unambiguous with any of the more likely possibilities, would probably be found in the small residue of events for which no satisfactory interpretation is found.

ii) Well measured variables These are derived from the variables which were successfully found by Thresh. They are denoted by m_i, with error matrix G^{-1}. The corrections to the m_i made during the fit are denoted by c_i.

iii) Unmeasured variables These arise in two ways. Firstly, Thresh may not always be able to reconstruct every parameter of the charged tracks. The most common case is a failure to reconstruct the curvature for a very short track; also sometimes the dip angle may not be obtained if it is large. The second situation concerns missing neutral particles. A hypothesis may be attempted with an unseen neutral particle of specified mass since, provided there are no other unknown parameters, a 1-C fit is possible.

This group of unmeasured variables can contain parameters which were reconstructed in Thresh but because of certain checks made by Grind are considered to be badly measured. Variables in this class are denoted by m_k', their error matrix by $(G'_{ke})^{-1}$ and the corrections to m'_k by C'_k. Elements of G'_{ke} referring to genuinely unmeasured variables are zero. This matrix is assumed to be diagonal since correlations between these parameters do not have much meaning.

While on the subject of unseen neutral particles, it is clear that Grind can never get a fit if there are two or more produced in a given event and so no such hypotheses are ever tried. Unfortunately at high energies a large proportion of the interactions fall into this category (about two-thirds in this experiment). This is one of the major deficiencies of a hydrogen bubble chamber since there is very little chance of seeing the gammas from the decay of the π^{o}, the most commonly produced neutral particle. In order to try and do some analysis on these no-fit events the following procedure is adopted. For a multi-neutral event up to four parameters can be calculated from the constraint equations. These are chosen to be the total momentum and energy for the neutral particle system, which is given the symbol Z^{o} and is subsequently treated on an equal footing with the other particles.

The constraint equations (3.9) can be written in the form:

$$f_v(m + c,\ m' + c') \ = \ 0 \qquad v = 1,\ 4V \tag{3.11}$$

where V is the number of vertices involved in the fit.

The problem is then to find the vectors c, c' such that (3.11) is satisfied and which minimise

$$X^2 \ = \ c^T Gc + (c')^T G'c' \tag{3.12}$$

Unfortunately the constraint equations are not linear functions of the chosen variables and this necessitates an iterative solution. If, after an iteration, the values of c, c' are $\bar{c}$, $\bar{c}'$, the next iteration is performed as follows: f_e is first expanded in a Taylor series about $\bar{c}$, $\bar{c}'$, neglecting second and higher order terms.

$$f_e(c,\ c') = f_e(\bar{c},\ \bar{c}') + B_{ei}(c_i - \bar{c}_i) + B'_{ek}(c'_k - \bar{c}_k') \tag{3.13}$$

where $B_{ei} = df_e/dc_i$, $B_{ek} = df_e/dc'_k$

Defining a vector x of Lagrangian multipliers, the function to be minimised can be written

$$X^2 = c^T Gc + (c')^T G'c' + 2xf \tag{3.14}$$

subject to

$$f(c,\ c') \ = \ Bc + B'c' + r = 0 \tag{3.15}$$

where $r = f(\bar{c}, \bar{c}') - B\bar{c} - B'\bar{c}'$.

Taking partial derivatives of X^2 with respect to c, c', x and equating to zero for the stationary condition gives

$$G_{ii}c_j \ + \ B^T_{vi}x_v \ = \ 0 \tag{3.16}$$

$$G'_{ke}c'_e + (B'_{vk})^T x_v = 0 \tag{3.17}$$

$$f(c, c') = B_{vi}c_i + B'_{vk}C'_k + r_v = 0 \tag{3.18}$$

where $i, j = 1, 2, \ldots\ldots n_c$ denote the well measured variables

$k, \ell = 1, 2, \ldots\ldots n'_c$ " " unmeasured "

$v = 1, 2, \ldots\ldots n_x$ " " constraint equations.

This is a system of $(n_c + n'_c + n_x)$ linear equations with an equal number of unknowns, c, c', x. From (3.16)

$$C = -G^{-1}B^T x \tag{3.19}$$

Substituting in (3.18) and subtracting tB', where t is a scalar, gives

$$- G_x^{-1} x + B'(1 - tB'G')C' + r = 0 \tag{3.20}$$

where $\quad G_x^{-1} = BG^{-1}B^T + tB'(B')^T$

This gives $x = G_x(B'(1 - tG')c' + r)$ (3.21)

assuming G_x exists (this can be shown).

Substituting in (3.17) gives

$$c' + (B')^T G_x r = 0 \tag{3.22}$$

where $K = (B')^T G_x B'(1 - tG') + G'$

Thus $C' = -K^{-1}(B')^T G_x r$ (3.23)

Then substitution in (3.21) gives x, then into (3.19) gives C, then into (3.14) gives X^2, which completes the iteration. The scalar parameter t is chosen so that $tB'(B')^T$ has about the same magnitude as $BG^{-1}B^T$; the final results are insensitive to wide variations in its actual value. After each step the residues of each of the constraint equations are examined, as are the values of the step size for each track (defined as the sum of the absolute values of the changes in the track variables in that step). If all these quantities are smaller than some specified limits the fit is considered to have converged. Provided the errors have been correctly assigned the minimum value of X^2 should be distributed as

$$F(X^2) = (X^2)^{\frac{1}{2}n-1}\ e^{-\frac{1}{2}X^2} / \ 2^{\frac{1}{2}n} \quad \Gamma(\tfrac{1}{2}n) \qquad (3.24)$$

where n is the number of degrees of freedom. Its actual value for a particular fit is a measure of the differences between the fitted and measured variables of the parameters. To provide a test of the goodness of the fit the probability of a fit giving a larger value of X^2 than that actually found is calculated in Grind.

Like Thresh, Grind requires certain items of data to be supplied. These are:

i) Specification of the hypotheses to be attempted for each type of event;

ii) details of the range-momentum relationship;

iii) values of the magnetic field at a set of grid points throughout the chamber;

iv) information on the labels for the various types of vertices and tracks given by Thresh;

v) parameters of the beam;

vi) convergence criteria;

vii) other general constants;

Values of some of these constants are given in tables 3.3 and 3.4.

The range-momentum relations are used by Grind to find the momentum of stopping tracks and in "swimming" the track variables from one point to another on the track. The latter facility is necessary to convert from centre of track variables given by Thresh and, in multi-vertex events

TABLE 3.4

KINEMATICS CONSTANTS

Beam constants		Experiment 75	Experiment 10
Reference point coordinates:	X	-30	-80
	Y	6	-3.5
	Z	-22	-24
Momentum (Gev/c)		10.00 ± 0.08	10.100 ± 0.040
Dip angle (mrad)		2 ± 6	1 ± 3
Azimuthal angle (mrad)		3148 ± 5	3174 ± 2
C_L	(see text for	-0.0004	0.00052
C_Y	explanation)	0.00046	0.00013
C_Z		-0.00311	-0.00171

Convergence criteria		
Max. no. of consecutive cut-steps	4	10
Max. no. of cut-steps in 1 hypothesis	30	40
Maximum no. (tight fit)	12	20
of iterations (loose fit)	10	15
Maximum residual of (tight fit)	0.0005	0.001
constraint equations (Gev)(loose fit)	0.01	0.01
Stability criterion for (tight fit)	0.001	0.001
track variables (loose fit)	0.02	0.02
Minimum probability	0.005	0.01
Matching factor t	0.00001	0.00001

where a charged track joins two vertices, to relate the parameters of this track at these vertices. In all multi-vertex events, fits at secondary vertices are performed first and, if successful, the parameters of the connecting tracks are used in the production vertex fit as if they were directly measured quantities. A further fit is carried out using all vertices simultaneously to get the final best values of the fitted variables. It can happen that this multi-vertex fit fails in which case the best values are taken from the primary vertex fit.

Because of the small curvature of beam tracks it is usually difficult to measure their momenta accurately. For this reason Grind is supplied with average values of beam track parameters, obtained by a separate measurement of a sample of long beam tracks having interactions on them near the end of the chamber (to exclude any muons from the sample). These so-called title values are specified with errors at a particular point D in the chamber and can then be swum from there to the point where the fit is made. For the momentum of the beam the title value is always imposed but for the dip and azimuthal angles a weighted mean of the title and measured values is taken provided they are consistent (within three standard deviations). The variations of beam angles with position in the chamber are also specified in the titles by the relations:

$$\begin{aligned} \lambda &= \lambda_o + C_Z(Z^1 - Z_D) \\ \phi &= \phi_o + C_Y(Y^1 - Y_D) + C_L L_D \end{aligned} \qquad (3.25)$$

where λ_o, ϕ_o are the title values specified at the point $D(X_D, Y_D, Z_D)$ and L_D is the track length from the plane $X = X_D$ to the measured apex. C_L, C_Y, C_Z are constants whose values are also given in the title block.

Grind normally accepts the binary tape written by Thresh as its input; it outputs a similar tape which now has several records per event. The first record is identical to the Thresh record so that a Grind output tape can be used as input to Grind again if necessary. Then there is a modified geometry record (including the modified values for the beam track) followed by one record for each successful fit giving the values of the fitted and unfitted parameters, their error matrices, the X^2-probability and some other quantities. The final record gives a summary of all attempted fits, both successful and unsuccessful.

Grind can also work in a mode called Grind Entry which accepts the input parameters of vertices and tracks from punch cards. This allows reconstructions from different measurements of the same event to be merged and is very useful for events in which different tracks have failed on each measurement.

3.5 Post-kinematics programs

For each successful fit Grind produces a punched card called a Slice card and a listing containing all quantities which may be needed in deciding the exact interpretation of an event. For experiment 10 these functions were carried out by a program AUTOGRIND which reads the Grind binary tape and makes many of the decisions about the fits automatically, thus reducing the work of the physicist to a minimum. This automatic decision-making is controlled by blocks of data in the same way as in Thresh and Grind. The details of the procedure used for selecting fits are described in the following chapter.

The Slice cards for the accepted fits are separated by hand from those for rejected fits and are used as input to the program Slice (37) in conjunction with the Grind binary tape. Slice finds the selected fits on this tape and calculates many quantities such as the effective masses of groups of particles, angles and momenta in both the centre of mass and laboratory frames of reference, transverse and longitudinal components of momentum and decay weights for strange particles. It writes all this information onto an output tape known as the Data Summary Tape (DST). This stage marks the end of the individual treatment of events and the analysis of the strong interaction reactions (which requires in general a large number of events of each type) can begin.

Histograms and scatter plots of interesting quantities on the DST are made using the program Sumx (37), which also has the facility (through CHARM routines) of calculating any additional quantities and plotting them too. An event can be included in, or omitted from, any desired plot as the result of a test on the value of any of its parameters.

CHAPTER 4

INTERPRETATION OF EVENTS

At high energies there may often be several possible interpretations of an event which are consistent with the kinematics. Since only one of these can be the true one it is important to be able to decide which one this is where ever possible. Only hypotheses for K^-p interactions which conserve B, Y, I and Q are attempted in Grind, since these quantum numbers are believed to be strictly conserved in all strong interactions. This means that additional baryons ($B \neq 0$) or strange particles ($S \neq 0$, where strangeness $S = Y - B$) can usually only be produced in pairs with equal and opposite values of B or S. The cross-sections for such reactions are known to be much smaller (by factors of about 400, 30 respectively (20)) than for reactions with just one strange particle and one baryon in the final state. For this reason the production of baryon-antibaryon pairs is neglected while the production of strange particle pairs is considered only for the rare topologies in which two or more strange particle decays are seen. These topologies are more complex to interpret and the methods for doing so will not be described here (41). At a later stage small samples of events of certain reactions involving the production of additional baryons or strange particles have in fact been isolated as a small background contribution from non-rare events on the DST (20). This is a much more economic procedure than attempting to fit these uncommon hypotheses for each individual event.

The restrictions described above imply the following, neglecting reactions with charged sigmas which have mostly not been measured:

i) negatively charged particles are either pions or kaons (no antiprotons);

ii) positive particles are pions or protons (no K^+);

iii) where there is an associated $\bar{K}^o$, all negatives are pions;

iv) where there is a Λ^o, all positives and negatives are pions.

The reasonableness of these restrictions is shown by the fact that only for a very few events is there definite evidence to the contrary.

At high energies the rest mass of a particle is small compared with its momentum and if the beam particle is a pion rather than a kaon it can often happen that the event will still give a fit to a K^- hypothesis. Estimates of the pion contamination were given in table 2.2. It was decided that they did not warrant the inclusion of any hypotheses with incoming pions.

4.1 Event-dependent criteria

A pair of error flags are defined for each track of an event in Thresh and Grind respectively. Normally these flags are set to zero but when any anomaly is detected for a track the corresponding flag (called an error-word) is set to a value which specifies the source of the difficulty. In general the more serious the trouble, the higher the error word. Before an event can be accepted, the error words for all its tracks (except for the beam for which title values can be imposed) must be less than certain chosen values. The conditions under which tracks are rejected in this way are:

in Thresh

i) if there is a complete failure of the track, either because there are not enough space points or because there is a bad circle fit in the first approximation (error word 4005);

ii) if there is a complete failure because less than two views are available (error word 4008);

or iii) if there is no convergence of the helix fit (error word 1000);

in Grind

i) if the differences between internal errors (given by Thresh) and external errors (calculated empirically by Grind in terms of the specified parameter fo) are greater than three standard deviations, for all three variables (p, λ, ϕ) of a single track (error word 100 + 40 + 20 = 160). There is a larger Grind error word (200) denoting tracks with no momentum measurement. This is permitted provided the track is too straight and/or short to allow such a measurement to be made accurately.

4.1.1. Ionisation information

For every charged track Grind calculates the expected ionisation from the momentum (fitted value for fits, unfitted values for no-fits). Any hypothesis having at least one track whose ionisation is inconsistent with that actually observed is discarded. In experiment 75 photographic prints were made of all measured events and these were examined to obtain the required ionisation estimates. In experiment 10 information on all tracks with an ionisation above minimum was coded on the scan card. This was punched and the information was processed through the book-keeping programs. At the Grind checking stage it was available to be used in deciding between competing hypotheses. By visual inspection of tracks it is possible to resolve relative ionisations of about 1·4 from minimum. Figure 4.1 shows the relative ionisations for π, K and p as a function of momentum. It can be seen that π and K can be distinguished up to about 0·8 Gev/c while for π and p the limit is about 1·5 Gev/c.

The use of the ionisation generally exhausts the possible information that can be obtained from individual events.

4.2 Event-independent criteria

To choose among any remaining hypotheses for an event it is necessary to establish (if possible) a set of criteria which when applied to a large sample of events will result in the true hypothesis being chosen as often as possible. The general basis for doing this is as follows. Suppose we have two sets of events, correctly assigned to hypotheses A and B respectively. Let (x_i) be a vector of variables each element of which can be a function of any of the parameters of the fit and let $A(x_i)$, $B(x_i)$ be the distribution functions over the vector space spanned by (x_i) for the events in A and B. Then, given another event E which has kinematic fits to both hypotheses A and B and for which (x_i) has the value (x_e), is it possible to assign the event to one or other of the hypotheses and, if so, with what confidence can this be done?

FIG. 4.1

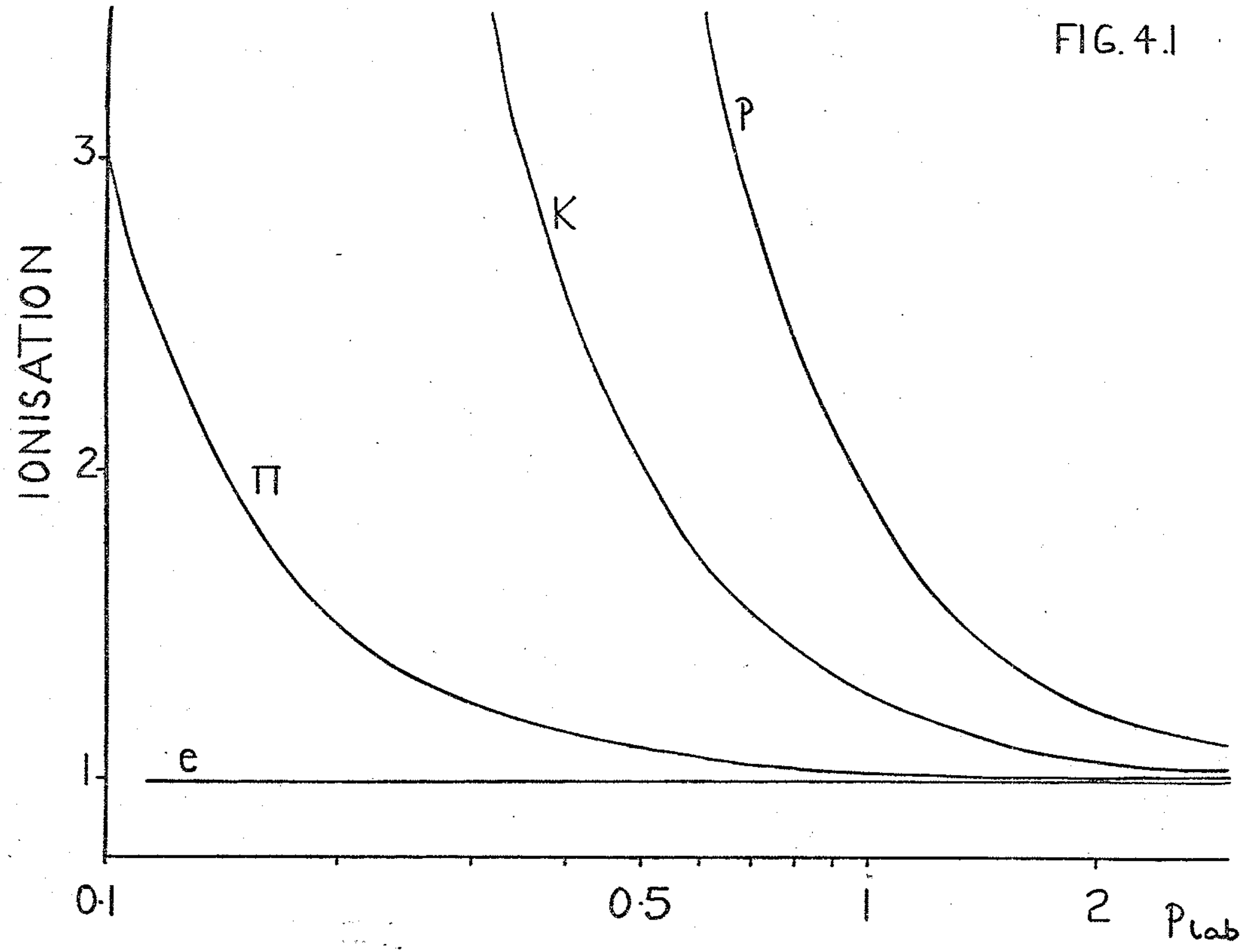

Three cases can be distinguished:

$$\begin{array}{lccc} \text{i)} & A(x_E) & \gg & B(x_E) \\ \text{ii)} & A(x_E) & \sim & B(x_E) \\ \text{iii)} & A(x_E) & \ll & B(x_E) \end{array} \qquad (4.1)$$

In cases i), iii) one of the hypotheses (A, B respectively) may be favoured over the other whereas in case ii) no definite preference can be shown. The actual divisions between the three cases depend on the level of confidence required in making the assignment of E to A or B. One should also consider the backings given to the two hypotheses for the event E, i.e. the probabilities that events from A, B would have likelihoods less than or equal to those for the event E. If both backings are small it may be that E belongs to neither A nor B.

A measure of the efficiency for separating events into hypotheses A, B using the variable set (x_i) is given by $(1 - I)$, where I is the overlap integral of the functions $A(x_i)$, $B(x_i)$:

$$I = \int A'(x_i).B'(x_i)dx_i \qquad (4.2)$$

where $A'(x_i) = A(x_i) / \sigma_A$ and $B'(x_i) = B(x_i) / \sigma_B$ are normalised to unity to restrict I to the range (0, 1). (These distribution functions are non-negative everywhere). For example if $A(x_i) = 0$ whenever $B(x_i) \neq 0$, i.e. if the functions are orthogonal, it will be possible to assign events to A or B with absolute certainty $(I=0)$. At the other extreme when the functions A', B' are identical, no separation can be achieved using the set (x_i) $(I = 1)$. Although A', B' are normalised to 1 in (4.2) it is important to use their absolute values (i.e. normalised to their respective cross-sections) in testing for conditions (4.1). This will automatically be the case if the prior information about events in A and B is taken from the experimental data.

The choice of the variable set (x_i) to use for a particular criterion is open to the experimenter. A good choice would be one for which the overlap integral I is as small as possible.

Sometimes a criterion involves a test on the parameters of a single fit (hypothesis A, say). In this case hypothesis B means hypothesis not-A and represents the combined effect of all other possible interpretations. In practice, criteria usually depend on sets (x_i) which contain only one or two elements. Also the case ii) in (4.1) is often artificially removed by choosing a certain x_i value (= x_o say) and forcing events into one or other of the hypotheses according to which side of x_o they lie. This is obviously convenient in that ambiguous classes of events do not have to be retained but for values of x_E near x_o, the confidence level for choosing the correct hypothesis may not be very high. A sensible choice might be to choose (x_o) such that $A(x_o) = B(x_o)$. Then events are always assigned to the hypothesis with the greater prior probability.

The criteria used in analysing the present experiment are summarised in table 4.1. Entries 1-4 in this table have been discussed earlier in the chapter. The first of these strictly comes into the category of the event-independent criteria described in this section since it depends on a prior knowledge of relative total cross-

TABLE 4.1

SELECTION CRITERIA

		Criterion for acceptance		
1) multi-baryon or multi-strange particle final states			neglected	
2) Thresh error-word for non-beam tracks			< 1000	
3) Grind " " " " " "			< 160 (except 200)	
4) consistency with observed ionisation			necessary	
		4-C fits	1-C fits	no-fits
5) χ^2-probability		> 1%	> 5%	-
6) if there are corresponding 1-C,4-C fits		accept	ignore	-
7) unseen Λ^o or Σ^o fit		-	ignore	-
8) missing mass squared:	π^o	-	(-0.12,0.10)	> 0.007
$(\text{Gev})^2$	$\overline{K}^o$	-	(0.10,0.35)	> 0.40
	n	-	(0.4,1.2)	> 1.15
	Λ^o	-	see 6)	> 1.56
9) proton lab. momentum:	2-prongs	none	< 2.0	< 2.0
(Gev/c)	4-prongs	none	< 3.0	< 3.0
	≥ 6-prongs	none	none	none
10) fitted $\overline{K}^o$ laboratory momentum:	2-prongs	-	> 2.0	-
	4- "	-	> 2.0	-
11) if probability is less than 1/3 of highest remaining probability		ignore	ignore	-
12) if still more than 3 interpretations		keep 3 highest probabilities		ambiguous class

The criteria are the same for experiments 75 and 10. Missing mass squared for no-fits refers to the stated particle plus additional neutral pions. (a, b) denotes a range of values within which the quantity must lie.

sections. This corresponds to choosing for (X_i) any reasonably well-behaved function of the fit parameters so that the distribution in (X_i) for the common types of reaction will be everywhere much higher than for rare reactions with additional baryon or strange particle pairs.

The remaining criteria 5-12 can be divided into three groups: 5, 6-10 and 11-12. Within these groups the criteria can be applied in any order without altering the overall effect although the order in the table is the most efficient one to use in practice. Not all criteria apply to all events, e.g. for 4-C fits 7-10 are not applicable while for no-fits 5-7, 10 and 11 are not relevant.

5) X^2-probability

This is a measure of the backing given to the hypothesis A for the event concerned. If the errors have been assigned correctly the probability distribution for a pure sample of events should be flat. If events of some other type B are misfitted to A the X^2 values will tend to be higher and so the probability distribution will be peaked towards lower values. Thus by choosing (X_i) = probability and making a cut at a suitable point one can remove a large number of misfits and not too many genuine ones. The limits chosen are 5% for 1-C or 2-C fits and 1% for 4-C or 3-C fits. This difference merely reflects the fact that the probability distribution for 1-C misfits is not so sharply peaked as that for 4-C misfits. It does not imply that a correct 4-C fit is statistically more reliable than a correct 1-C fit with the same probability for, as equation (3.24) shows, the number of degrees of freedom is taken into account when calculating the probability. Figure 4.2 shows the probability distributions for fits to the final state $pK^-\pi^+\pi^-$. These are mainly 4-C fits but there will be some 3-C fits in the sample mainly from events where the slow proton has undergone a secondary interaction. Fits with probability less than 1% have already been excluded (the height of the first bin in each histogram has been increased in the ratio 5:4 to allow for the reduced bin size). However the onset of the misfit peak can be seen in the sample from experiment 10; in the experiment 75 sample the distribution is peaked at high probabilities indicating that external errors have been somewhat overestimated.

6) <u>4-C fit preferred to corresponding 1-C fit</u>

By the corresponding 1-C fit is meant the hypothesis with the same assignments for the seen particles and an additional π^0. Due to the small mass of the π^0 it is fairly easy to get a 1-C misfit to a genuine 4-C event. However this spurious π^0 must necessarily have a small laboratory momentum since momentum is approximately conserved for the seen particles alone. Figure 4.3 shows the π^0 laboratory momentum ($= x_i$) distribution for accepted 1-C fits to the final state $pK^-\pi^0$. Any genuine 4-C events fitted to this hypothesis would show up as a peak just above zero.

7) <u>Unseen Λ^0 or Σ^0 neglected</u>

Reactions involving a neutral strange particle and no other

FIG. 4.2

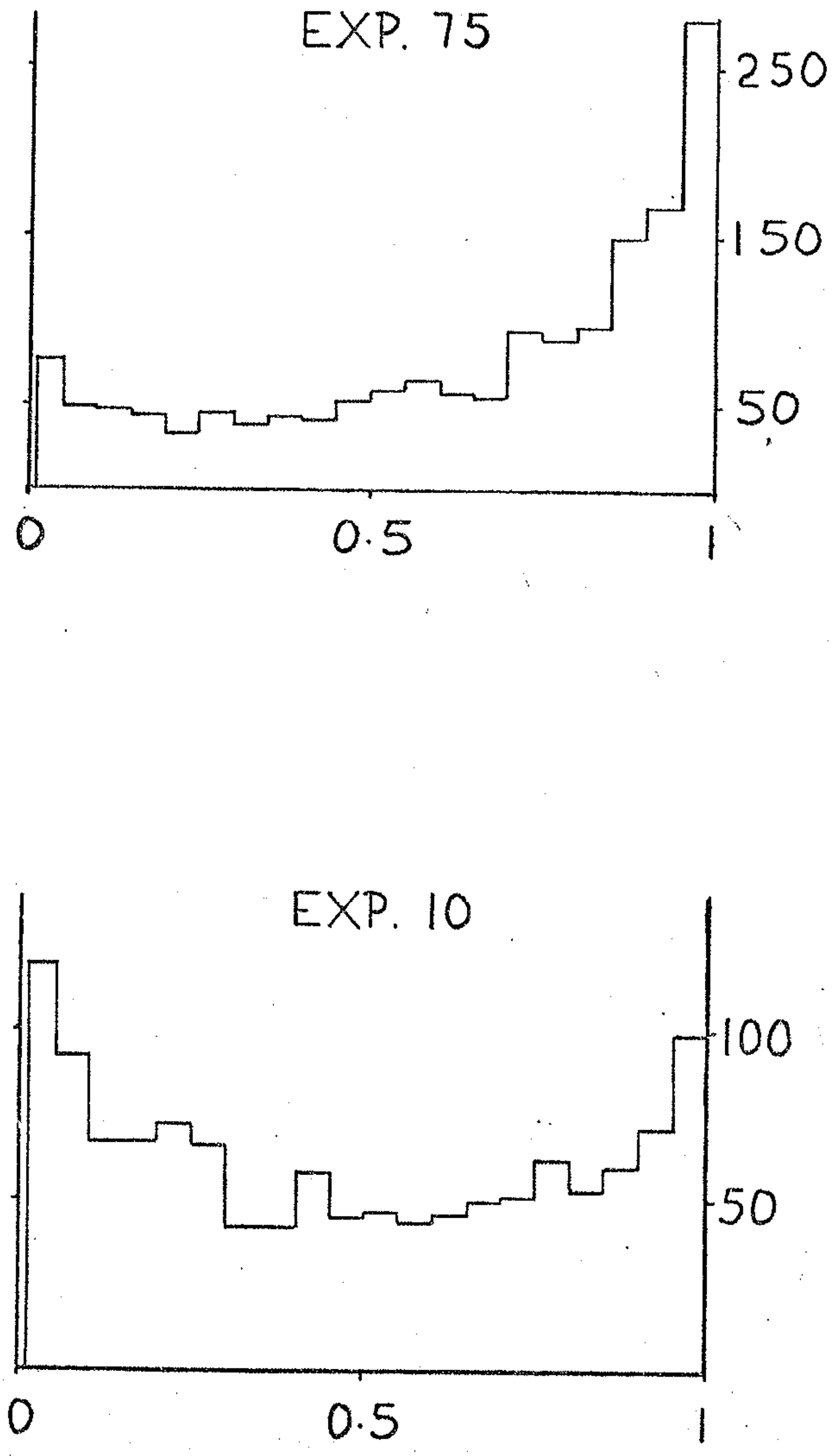

FIG. 4.3

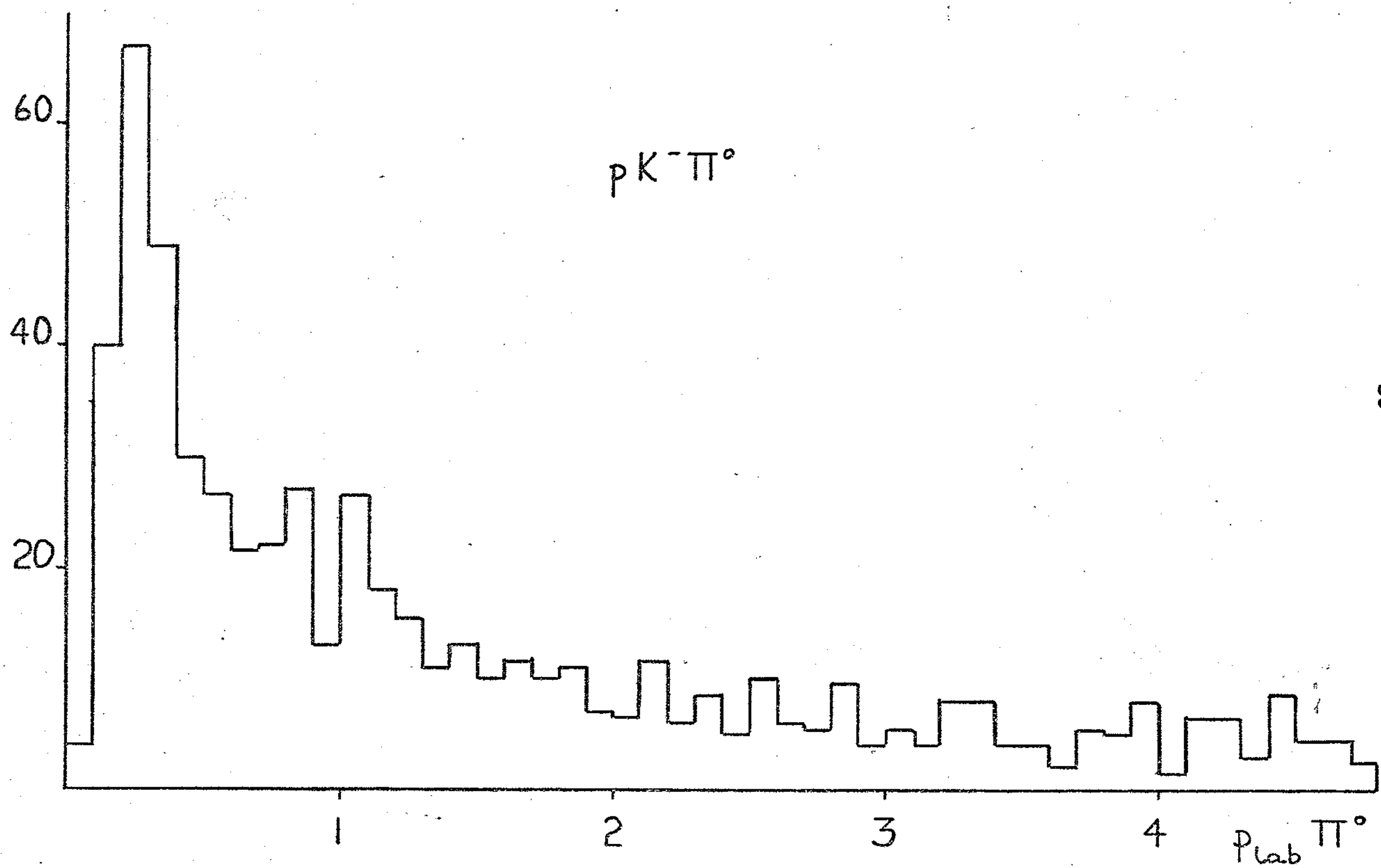

missing neutral particle can be fitted either as 4-C fits when the particle decays via a charged mode in the chamber or as 1-C fits when the decay is into neutrals or happens outside the chamber. The 4-C fits are not usually ambiguous with any other hypothesis and form a pure sample. The relative numbers in the two classes depend only on the well-known branching ratios into charged and neutral modes for the strange particle, with a correction for finite chamber size and for decays very close to the primary interaction point. The number of genuine 1-C fits can thus be calculated and compared with the number actually found.

In the case of missing neutral hyperons the numbers of 1-C fits found are about 20 times higher than expected and so both these hypotheses can be safely ignored. However the hypothesis with missing lambda is still retained in Grind to allow the calculation of the quantities for the corresponding no-fit hypothesis.

8) Missing mass square limits

The missing mass (MM) in an event is defined by the relation:

$$MM^2 = (\sum_i E_i)^2 - (\sum_i \underline{p}_i)^2 \qquad (4.3)$$

where the sum is over all the seen particles with the initial particles contributing with opposite sign. The missing mass can be interpreted as the invariant mass of the neutral particle system required to satisfy energy-momentum conservation. For events with a missing neutral particle of mass M the square of the missing mass given by (4.3) can be shown to be approximately Gaussian distributed about M^2, assuming that the main errors come from Gaussian errors in the individual momenta $\underline{p}_i$ (43). This seems to be realised in practice. The missing mass squared can be negative, for example, for a hypothesis which assigns pion tracks as heavier particles. No-fit events giving a misfit to a 1-C hypothesis with a missing neutral may be divided into two types:

i) those with the same assignments for all the seen particles but which have some neutral pions missing in addition to M. The missing mass squared for a system consisting of M and n π^0's has a broad distribution with threshold at $(M + nm_{\pi^0})^2$ within errors and a cut-off at high values due to the total energy available. The sum of such distributions for different values of n begins at $(M + m_{\pi^0})^2$ and to distinguish these no-fits from the corresponding fits it is necessary to be able to resolve this distribution from the Gaussian centred at M.

ii) those events with a different assignment for the charged tracks which cannot be distinguished from the correct assignment by ionisation. In this case the effect on the missing mass squared distribution of M is more complex and may also contribute as background in the Gaussian region and below.

The MMS limits for accepting fits with a missing π^0, $\bar{K}^0$ or neutron were chosen by examining the unselected missing mass squared distributions (x_i). Figure 4.4 shows the MMS distributions for selected events of topologies 200, 400 having one or more neutral pions missing (i.e. 4-C fits excluded). Each histogram shows the accepted 1-C fits (unshaded) and the no-fit events of category i) above (shaded). The position of the threshold for 2 π^0 production is indicated; it lies

FIG.4

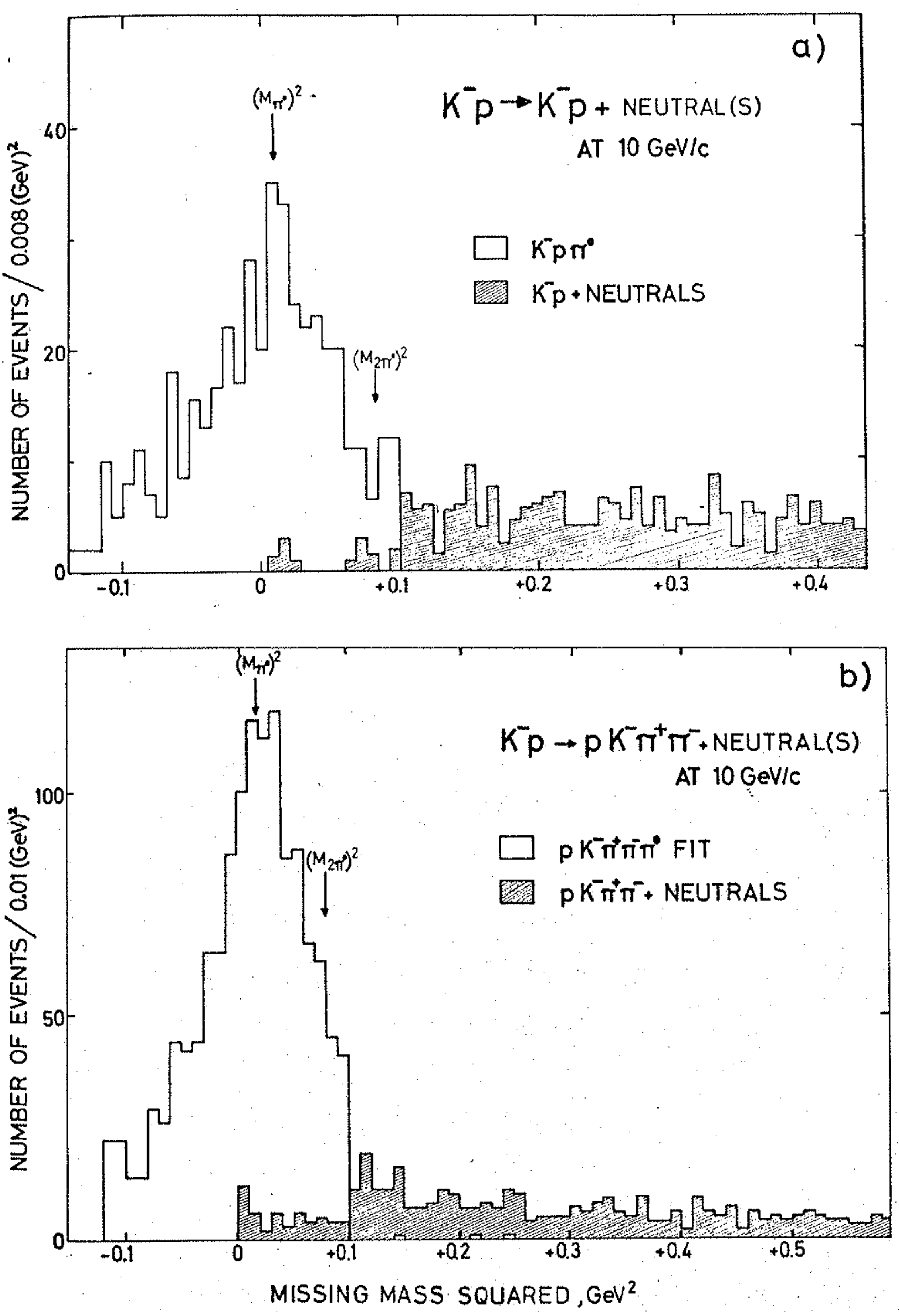

a)
$K^-p \rightarrow K^-p$ + NEUTRAL(S)
AT 10 GeV/c
$K^-p\pi^0$
K^-p + NEUTRALS
$(M_{\pi^0})^2$
$(M_{2\pi^0})^2$
NUMBER OF EVENTS / 0.008 (GeV)^2
0
20
40
-0.1
0
+0.1
+0.2
+0.3
+0.4
b)
$K^-p \rightarrow pK^-\pi^+\pi^-$ + NEUTRAL(S)
AT 10 GeV/c
$pK^-\pi^+\pi^-\pi^0$ FIT
$pK^-\pi^+\pi^-$ + NEUTRALS
$(M_{\pi^0})^2$
$(M_{2\pi^0})^2$
NUMBER OF EVENTS / 0.01 (GeV)^2
0
50
100
-0.1
0
+0.1
+0.2
+0.3
+0.4
+0.5
MISSING MASS SQUARED, GeV^2

within the range acceptable for a single π^{o}. However it is not too far from the upper limit of 0.10 GeV^2 and the number of incorrect 1-C fits accepted is probably small.

9) Proton laboratory momentum cut

Above about 1.5 GeV/C it is not possible to distinguish protons from pions by ionisation. However examination of the laboratory momentum distributions for p and π^+ in correctly assigned events shows that there are more high momentum positive pions than protons. This is in accordance with the dominance of peripheral reactions at high energies which allow only a small momentum to be transferred to the target proton. In higher multiplicity events there can be several π^+'s but no more than one proton so that one might have expected that a high momentum track would have even more chance of being a pion. However there is a stronger compensating factor from the dynamics of the interactions (which become somewhat less peripheral for the high multiplicities) so that the proton momentum distribution extends to higher values. Also the number of high momentum pions falls with increasing multiplicity. Cuts of 2 Gev/c and 3 Gev/c are used for 2-prongs and 4-prongs but no cut is applied for higher multiplicities. No cut is applied for 4-C fits since these are not usually ambiguous. Figure 4.5 shows the laboratory momentum distribution for the positive track in events identified as belonging to the final state $nK^-\pi^+$. In the same plot is shown the same distribution for the $p\overline{K}^{o}\pi^-$ reaction,

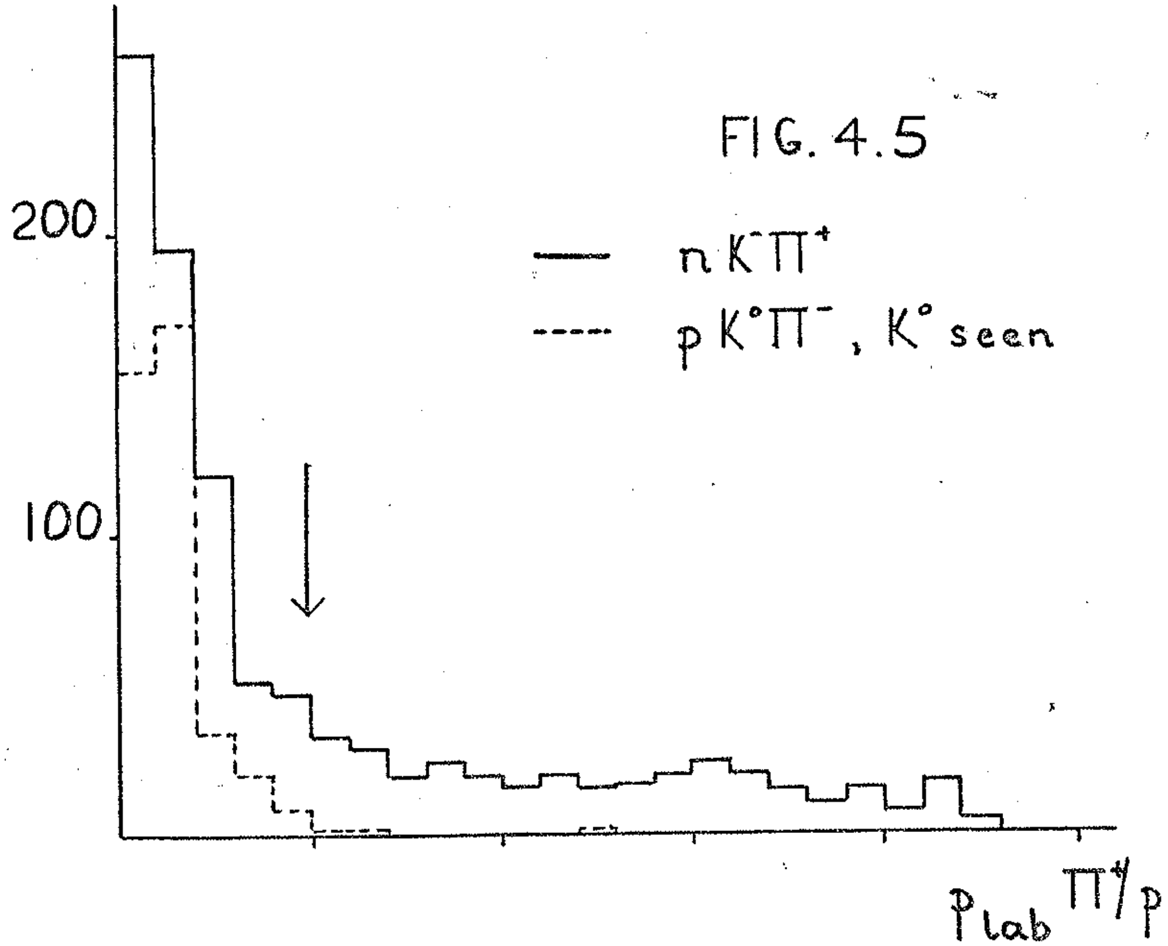
FIG. 4.5
200
100
$nK^-\pi^+$
$pK^0\pi^-$, K^0 seen
p_{lab} π^+/p

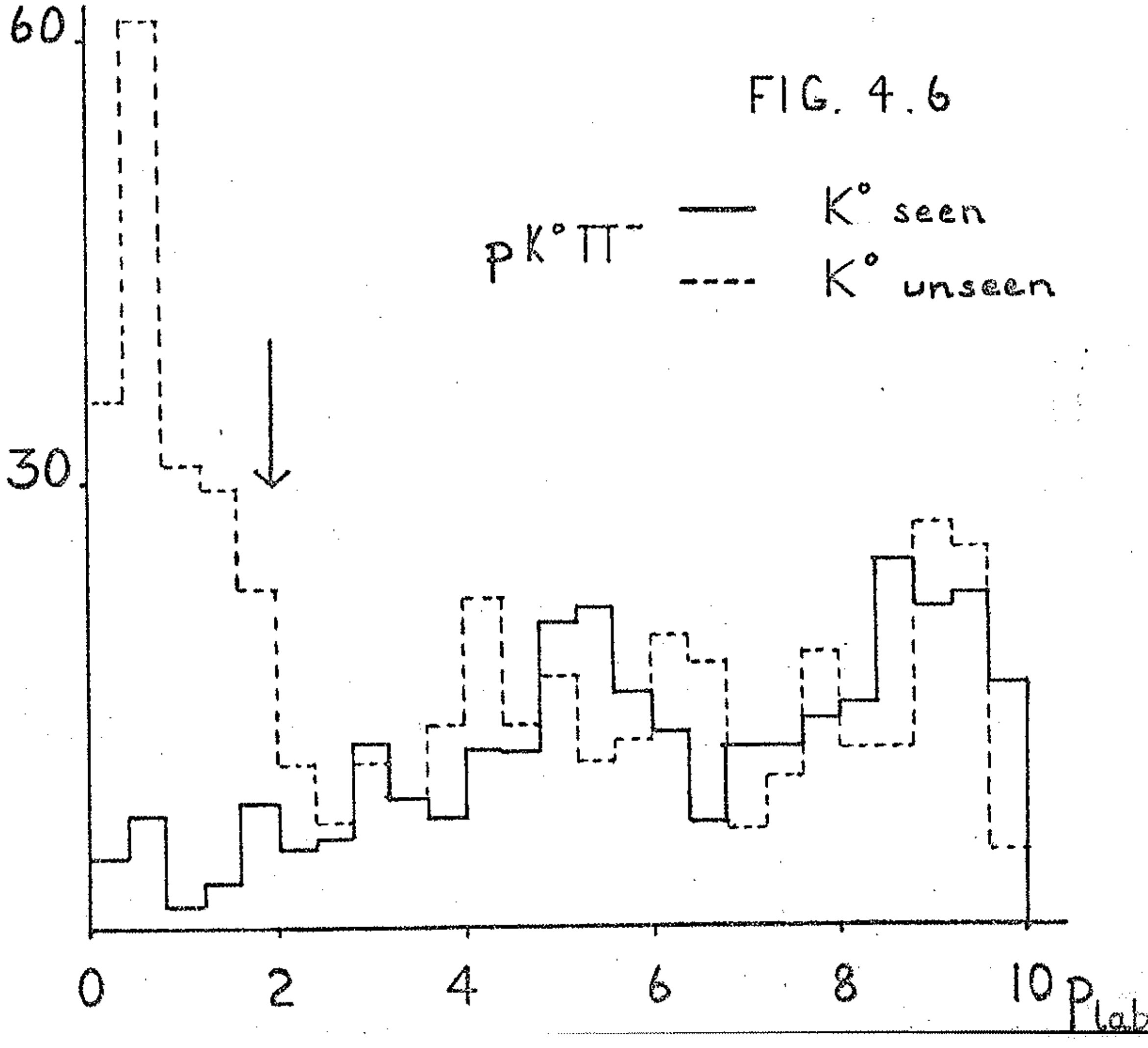
FIG. 4.6
60
30
$pK^0\pi^-$
K^0 seen
K^0 unseen
0
2
4
6
8
10
P_{lab}

obtained from the 4-C sample and normalised to the contribution expected from 1-C fits to $p\overline{K}^{o}\pi^{-}$. The relevant part is above 1.5 Gev/c where the positive track cannot be identified by ionisation. Of the 391 $nK^{-}\pi^{+}$ events in this region only 17 are expected to have come from misfitted $p\overline{K}^{o}\pi^{-}$ events. Given a choice between 1-C fits to these two hypotheses the pion one is favoured by about 5:1 for the momentum range 1·5 - 2·0 Gev/c. This is not considered sufficient to disregard the proton hypothesis but at 2 Gev/c, where the cut is made, the pion hypothesis is favoured by about 10:1 and this ratio goes up fast as the momentum increases.

10) Fitted $\overline{K}^{o}$ laboratory momentum cut

As explained in 7) the expected number of events with a fitted (i.e. unseen) $\overline{K}^{o}$ can be estimated from the number of events with $\overline{K}^{o}$ seen. The discrepancies between these pairs of numbers are not as severe as in the Λ^{o} case but the number of 1-C fits is still too high. The major source of misfits can be found by plotting for (xi) the $\overline{K}^{o}$ laboratory momentum for the two cases. Figure 4.6 shows this distribution for the pure sample of 4-C events $p\overline{K}^{o}\pi^{-}$ and also for an initial sample of 1-C fits to the same reaction. The latter is normalised to the former in the region above 2 Gev/c where they agree quite well but there is a large excess of fitted $\overline{K}^{o}$'s in the low momentum region. Thus 1-C fits with $\overline{K}^{o}$ momentum below 2 Gev/c are rejected (for 2- and 4- prongs) but no such cut is made for higher multiplicities.

11) 3:1 probability ratio

If two or more possible fits remain after the application of criteria 1-10 and the highest probability of one of these fits is P then any others with probabilities less than P/3 are rejected. Since the maximum probability P is 1, no fit with probability greater than 34% can be rejected in this way. This is an attempt to remove misfits from the tail of the misfit probability distribution. Suppose we have fits with probabilities p_A, p_B to hypotheses A, B for an event. Choosing for (xi) the pair of variables (p_A, p_B), the probability of hypothesis A being correct and of hypothesis B being incorrect is

$$A(p_A, p_B) \Big/ B(p_A, p_B)$$

which, if we neglect correlations between p_A, p_B and use the fact that $A(p_A)$, $B(p_B)$ are flat, reduces to

$$A(p_A).A(p_B) \Big/ B(p_A).B(p_B) \;=\; A(p_B) \Big/ B(p_A) \qquad (4.4)$$

Now $A(p_B)$, $B(p_A)$ are distributions of misfit probability so that they are peaked at low values of their respective arguments. Thus for an event with $p_A > 3p_B$, $A(p_B)$ will tend to be large and $B(p_A)$ will be small so that the ratio $A(p_B) \Big/ B(p_A)$ will be high and hypothesis A is preferred over B.

12) Restriction to three hypotheses per event

Slice accepts a maximum of 3 hypotheses for a single event. In the very few cases (only in the higher multiplicities) where more than 3 fits remain after applying all previous criteria, the 3 with the highest probabilities are selected. For no-fit events which have more than 3 possible interpretations there is no quantitative way of choosing between them. Instead all particles not definitely identified are assumed to be pions and the Slice card corresponding to this single no-fit hypothesis is selected. "AMBIG" is punched in a specified field on the card to differentiate such "undecided" no-fits from the "decided" ones of the same hypothesis.

4.3 Secondary fits

These are either strange particle decays or secondary interactions on charged tracks. For neutral strange particle decays the line joining the production and decay vertices determines the direction of the particle. Only its momentum is then unknown so that a 3-C associated fit is possible. If this fails a 1-C unassociated fit is attempted in which the direction is also left as an unknown. To be acceptable a V^0 must give an associated fit to the primary vertex. If a good unassociated fit is obtained on two measurements the V^0 is usually discarded. If a V^0 fits to the electron-pair hypothesis the latter is always accepted provided it is consistent with the observed ionisation. The event is recalculated without the electron pair if the fit was an associated one.

All other decisions concerning V^0 or secondary interaction fits are made in accordance with criteria 1-5 and 11 of table 4.1.

For multi-vertex events all decisions regarding the choice of fits are made on the single vertex fits but the Slice card for the corresponding multi-vertex fit is selected whenever this fit exists.

If an event has no interpretation which satisfies all the criteria, hypotheses can be accepted which slightly break one of the rules, e.g. momentum, probability or missing mass squared cuts.

In conclusion it should be noted that if there is an acceptable fit for an event, alternative no-fit interpretations are not considered. There is no justification for doing this except that in K^-p interactions this would lead to too many possibilities.

CHAPTER 5

CROSS SECTIONS

Since the amount of muon background in the beam is not well-known it is not possible to determine the overall normalisation for cross-sections by finding the total path length for all beam tracks.

As mentioned in Chapter 3 the tau decay of the K^- gives a measure of the total K^- path length but the total number of these decays is not large. This can however be used as a consistency check on the main method used which is to normalise to the total K^-p cross-section using results from counter experiments. (44). A total cross-section of 22.6 ± 0.2 mb is used for K^-p at 10.1 Gev/c.

5.1 Scanning corrections

To normalise to the total cross section value a careful scan is made for all events (except topology 000) in a restricted fiducial region. This region corresponds to the previously defined region 1 for both experiments 75 and 10. Some or all of the film is rescanned and from the numbers of events seen on either or both scans it is possible (with some simplifying assumptions) to estimate the number of events which have been missed by both scans. Suppose N_1 is the number of events of a certain type found only by scanner 1, N_2 the corresponding number for scanner 2 and N_{12} the number of such events found by both scanners. Then the total number found by either or both scanners is given by:

$$N = N_1 + N_2 + N_{12} \tag{5.1}$$

The aim is to estimate the total number of events of this type present (N_T). Let $\hat{e}_1$, $\hat{e}_2$ be defined by the relations:

$$\begin{aligned} \hat{e}_1 &= N_{12}\big/(N_2 + N_{12}) \\ \hat{e}_2 &= N_{12}\big/(N_1 + N_{12}) \end{aligned} \tag{5.2}$$

The denominators in these expressions are the total numbers of events found by scanners 2, 1 respectively. Therefore $\hat{e}_1$ represents the conditional probability of an event being found by scanner 1 given that it was found by scanner 2. Assuming that the two scans are independent, $\hat{e}_1$ ($\hat{e}_2$) is an estimator of the probability that an event is found by scanner 1 (2). The probability that an event will be found at all is:

$$\begin{aligned} \hat{e} &= \hat{e}_1(1-\hat{e}_2) + \hat{e}_2(1-\hat{e}_1) + \hat{e}_1\hat{e}_2 \\ &= 1 - (1-\hat{e}_1)(1-\hat{e}_2) \end{aligned} \tag{5.3}$$

Substituting for $\hat{e}_1$, $\hat{e}_2$ gives:

$$\hat{e} = N_{12}N\big/(N_1 + N_{12})(N_2 + N_{12}) \tag{5.4}$$

An estimate for N_T is then:

$$N_T = N/\hat{e} = (N_1 + N_{12})(N_2 + N_{12})\big/N_{12} \tag{5.5}$$

The errors on these quantities can be found by using the fact that the probability of scanner 1 finding exactly m events out of a total of M found by scanner 2 is given by the binomial distribution:

$$P(m) = M!\big/m!\,(M-m)!\;\; e_1^{\,m}\,(1-e_1)^{M-m} \tag{5.6}$$

This distribution has mean Me_1 and variance $Me_1(1-e_1)$, showing that $\hat{e}_1$ is an unbiased estimator of e_1 with variance $e_1(1-e_1)/M$. Thus

$$\begin{aligned} \mathrm{var}(\hat{e}_1) &= e_1(1-e_1)/(N_2 + N_{12}) \\ \mathrm{var}(\hat{e}_2) &= e_2(1-e_2)/(N_1 + N_{12}) \end{aligned} \tag{5.7}$$

From (5.3) this gives, by propagation of errors,

$$\mathrm{var}(\hat{e}) = (1-e_2)^2\ \mathrm{var}(\hat{e}_1) + (1-e_1)^2\ \mathrm{var}(\hat{e}_2) \tag{5.8}$$

This treatment of the efficiency problem assumes that there is a constant probability for finding each event in a particular scan. Because the probability is likely to vary with event topology these corrections are applied separately to each topology. Even so, there will still be some variation from event to event caused by the obscuring effect of other tracks, poor picture quality, the variation in angle of outgoing tracks and other similar factors. The validity of this assumption could be checked by making a third scan, since it predicts that the number of new events found should decrease by a constant factor from one scan to the next. The check-scan, in which the discrepancies between scans 1 and 2 are resolved, is not an independent scan but, if any additional events are seen at this stage, they are added to the sample. The number of such events does give a lower limit for the number that would have been found on a third scan.

The topology of an event is not a rigidly defined quantity since, for example, it is not always possible at the scanning stage to be certain that a V^o is associated with a particular event nor to be able to differentiate between electron pairs and strange particle decays. For calculating scanning efficiencies the topology of the final interpretation of an event is used, except for the unmeasured topologies 410, 610, 810, ... for which only scanning information is available. For purposes of cross section normalisation an event is said to be "seen" on a particular scan if its production apex is recorded. It does not matter if charged or neutral decays are missed as long as the information supplied by the two scanners for a given event is sufficiently similar to enable one to be sure that it is the same event they have seen.

Table 5.1 shows the scanning efficiencies (with errors) for the 6799 London events from experiments 75 and 10 used for the cross section normalisation. In addition there were two events of unusual topology, a 301 (definitely not a tau decay) and a 900. Possible explanations of such events were mentioned in chapter 3. In experiment 10 the scanning efficiencies were on the whole higher than in experiment 75, mainly due to the better quality of the photographs from the 2 metre chamber. Even so there are still some events for which the assumption of constant probability of being seen does not hold, as shown by the fact that 27 extra events were found during the check scan of experiment 10, whereas the calculated efficiencies predicted that only 8 events had been missed in both of the first two scans.

Provided the scanning efficiencies are close to 1 the simple minded calculation is probably not too unreasonable. However there are two situations in which it is certainly bad:

TABLE 5.1

SCANNING EFFICIENCIES FOR LONDON DATA

Topology	Efficiencies (%) scan 1	scan 2	overall	Total number of events seen
000	40.0 ± 12.6	16.2 ± 6.1	49.7 ± 11.2	46
001	92.4 ± 3.3	66.3 ± 4.9	97.4 ± 1.2	97
200	92.3 ± 0.6	86.3 ± 0.7	98.9 ± 0.1	2287
201	94.7 ± 0.9	91.2 ± 1.2	99.5 ± 0.1	619
210	88.5 ± 3.6	81.2 ± 4.2	97.8 ± 0.8	94
400	97.3 ± 0.4	94.8 ± 0.5	99.86 ± 0.02	1944
401	96.2 ± 0.9	91.7 ± 1.3	99.68 ± 0.03	460
410	93.6 ± 2.0	87.4 ± 2.6	99.2 ± 0.3	177
≥ 6-prong	96.8 ± 0.6	92.7 ± 0.9	99.77 ± 0.05	916
rare*	93.7 ± 2.5	86.4 ± 3.4	99.1 ± 0.4	157
others (301,900)	-	-	-	2
				6799
300(tau)*	84.6 ± 10.0	34.4 ± 18.4	89.9 ± 6.7	54
				6853

* the efficiencies for these topologies are calculated from the experiment 75 sample only.

i) for all events with topology 000 the scanning efficiency is very low (see table 5.1) as they can be easily obscured by other beam tracks. In experiment 10 they were not even recorded as they are, of course, useless for measurement since none of the final particles is seen. Fortunately one can make an accurate estimate of the number of such events in a way which is not possible with other topologies. Assuming the beam particle is a K^- there has to be a neutral strange particle in the final state for a zero-prong event. In practically all cases this will be either a $\overline{K}^o$ or a Λ^o (including Λ^o from Σ^o decays). In the cases when the strange particle decay is seen (topology 001) the scanning efficiency is higher because, although the primary interaction point is just as hard to see, when a V^o decay is seen which has no apparent origin the scanner always looks very carefully back along its approximate line of flight. When these 001's are analysed the separation between $\overline{K}^o$ and Λ^o events is quite clean and using the known charged/neutral branching ratios of these particles the number of 000 events can be estimated.

ii) for elastic scattering there is a serious scanning loss for low momentum transfers to the target proton and at high energies this is just where the cross section is highest. Below about $-t = 0.10$ $(Gev/c)^2$ there is a systematic loss of events, beginning at azimuthal angles (measured around the beam direction) for which the proton is moving towards or away from the cameras and extending to all azimuthal angles for values of $-t$ below 0.06 $(Gev/c)^2$ (corresponding to a proton range of about 7cm). Here $-t$ is the square of the 4-momentum transfer between the initial and final K^- or, equally well, between the target and final protons, defined by

$$t = (p_1 - p_2)^2 \tag{5.9}$$

where p_1, p_2 are the 4-momenta of the particles concerned.

This loss of events is corrected for in the following way (10). The fitted elastic events are divided into regions of t and the azimuthal angular distribution is plotted for each t-region. When there is a noticeable depletion for some azimuthal angles (which should be isotropically distributed for an unpolarised beam and target as in this experiment), this is corrected and at the same time the normal scanning efficiency correction is applied, also as a function of t. There still remains the very low $-t$ region where the azimuthal distribution is depleted at all angles. The assumption is made that the strong interaction K^-p elastic differential cross section is well-represented by an exponential in t. This is in good agreement with the data between $-t = 0.06$ and 1.0 and is theoretically expected to hold down to $-t = 0$. This fact is then used to correct for the final source of unseen elastic events by extrapolating the experimental distribution down to this point.

5.2 Normalisation

Having made all necessary corrections to the observed number of events the total expected number of interactions in the chosen region can be calculated. Table 5.2 shows the total (corrected) number of events in each topology and the corresponding partial cross section. The errors on these cross sections are calculated by combining the errors on the observed numbers of events (assumed to be Poisson distributed) with the uncertainty in the value of the total cross section used.

For the normalisation region the numbers of events corresponding to 1μb of cross section are 1·58, 1·40 for experiments 75, 10 and 2·97 overall. These numbers are not particularly useful for calculating the cross sections for particular reaction channels since, for some topologies, events were analysed from larger regions than that used for normalisation. Also the relative sizes of these regions were different in the two chambers. A better way is to use the topology cross section and to find, at any stage of the experiment, the ratio between the number of events of the required reaction to the total number of the same topology on the DST. Further corrections may be necessary before arriving at the final cross section (see following chapter). The above method has the advantage that the numbers of events in each topology which fail to get a successful interpretation are not required, provided it is reasonable to assume that these events are not biased towards particular reactions. Furthermore the cross section normalisation and the analysis of reactions are entirely separate operations so that new data can be added

TABLE 5.2

TOPOLOGY CROSS SECTIONS

Topology	exp.75	exp.10	total	cross section (μb)	average scanning efficiency (%)
000	691	717	1408	473 ± 17	54.0
001	409	414	823	277 ± 10	97.3
200	12684	11719	24403	8206 ± 110	88.0**
201	2985	2272	5257	1768 ± 21	99.7
210	433	424	857	288 ± 9	99.3
400	9567	8750	18317	6160 ± 86	99.95
401	2410	1981	4391	1477 ± 18	99.6
410	1050	791	1841	619 ± 16	99.6
600	4641*	2689	8607*	1962 ± 38	99.8*
601		441		322 ± 15	
610		443		323 ± 15	
800		278		203 ± 12	
801		29		21.1 ± 3.9	
810		61		44.5 ± 5.7	
10,00		12		8.8 ± 2.5	
10,01		3		2.2 ± 1.3	
10,10		3		2.2 ± 1.3	
$>$ 10-prong		7		5.1 ± 1.9	
rare	801	~500	~1301	437 ± 40	95.5
	35671	31534	67205	22600 ± 200	

1 event in region 1 (exp.75 + exp.10) $= 0.336 \pm 0.004$ μb

1 " " " 1 (exp.75 only) $= 0.634 \pm 0.006$ μb

1 " " " 1 (exp. 10 only) $= 0.717 \pm 0.006$ μb

* these entries are for all topologies with 6 or more prongs excluding rares

** this efficiency includes the effect of the unseen small angle elastic events.

to the DST without necessitating a recalculation of cross sections. This is an important point in the case of an experiment like the present one which continues over several years.

One might have expected a scanning bias similar to that described above for elastic scattering in the case of inelastic 200 events with a proton in the final state as these reactions also tend to have large cross sections when the momentum transferred to the proton is small. Examination of the relevant azimuthal angular distributions has shown that there is no serious loss of events in this way. This disagrees with the claim made by the Argonne-Northwestern collaboration for the existence of such a scanning loss in their K^-p experiments at 4.1 and 5.5 Gev/c (45). The presence or absence of a real dip at low $-t$ (as opposed to a bias) may have important theoretical significance.

A similar check was made to see if any events recorded as topology 300 (i.e. tau decays) could be 400 events with an unseen proton. Practically all events gave a good 4-C fit to the tau decay hypothesis so this was eliminated as a possible source of bias in the 4-prongs.

5.3 Normalisation check using tau decays

If n_i is the number of events of a process i observed during a time when N_K kaons are incident on a target with N_p protons per unit area, the cross section for the process i is given by

$$\sigma_i = n_i / N_K N_p \qquad (5.10)$$

The number of protons per unit area in a thickness d is given by

$$N_p = \rho N_o d \qquad (5.11)$$

where ρ is the density of liquid hydrogen and N_o is the Avogadro number.

N_K can be estimated from the number of kaon decays observed in the same thickness d of target, assuming an exponential decay law:

$$eN_K d = N_d (pc/m)(rt) \qquad (5.12)$$

where e is the scanning efficiency for the decays (of which N_d are seen), t is the mean K^- lifetime and r is the K^- branching fraction for the $\pi^+ \pi^- \pi^o$ mode. Included in the value of r (actual value 0.056) is a correction for single-prong K^- decays involving a π^o whose decay involves the production of a pair of electrons (Dalitz pair). If these electrons have momenta above about 200 Mev/c they will not be identifiable from pions by ionisation and so will simulate tau decays. The corrected value of r is 0.059.

Substituting (5.11) and (5.12) into (5.10) gives:

$$(\sigma i/ni) = (1/\rho No).(m/pc).(er/N_d t) \qquad (5.13)$$

The density of liquid hydrogen is known from the thermodynamic conditions of the chamber or it can be found by measuring the ranges of μ^+'s coming from the two-body decays of stopping π^+'s. All other constants can be found in reference (2) and give the result

$$(\sigma i/ni) = 0.213(e/N_d) \ \text{mb/event} \qquad (5.14)$$

The number of tau decays observed in region 1 for the London sample of experiments 75 and 10 was 54 with a scanning efficiency of about 90 $\pm$ 7%. Unfortunately no data are available on the tau decays found by the other groups. This then gives a value for the total cross section of:

$$\sigma_{tot} = 24.7 \pm 2.5 \text{ millibarns}$$

This is rather high compared with the accepted value of 22.6 $\pm$ 0.2 mb. Unless more decays can be used this method will remain rather unsatisfactory.

CHAPTER 6

BIASES IN THE REACTIONS STUDIED

The following reactions are the main ones to be discussed in the ensuing chapters. They are in fact the only reactions of the general types $K^-p \longrightarrow N\bar{K}\pi$, $N\bar{K}\pi\pi$ which are fittable, that is which have at most one unseen neutral particle. N stands for the nucleon i-spin doublet (p,n) while $\bar{K}$ is the kaon doublet ($\bar{K}^o$,K^-).

$K^-p \longrightarrow pK^- \pi^o$		1)
	$p\bar{K}^o \pi^-$, $\bar{K}^o$ fitted (unseen)	2a)
	$p\bar{K}^o \pi^-$, $\bar{K}^o$ seen	2b)
	$n\ K^- \pi^+$	3)
	$pK^- \pi^+ \pi^-$	4)
	$p\bar{K}^o \pi^- \pi^o$	5)
	$n\bar{K}^o \pi^+ \pi^-$	6)

In addition there are four unfittable reactions in these two general categories which may be referred to from time to time. They are listed here for completeness, together with the no-fit "reactions" into which they are classed. The $\bar{K}^o$'s in 7) and 10) are assumed to be seen.

$K^-p \longrightarrow n\bar{K}^o \pi^o$		(in $\bar{K}^o Z^o$)	7)
	$pK^- \pi^o \pi^o$	(in $pK^- Z^o$)	8)
	$nK^- \pi^+ \pi^o$	(in $K^- \pi^+ Z^o$)	9)
	$n\bar{K}^o \pi^o \pi^o$	(in $\bar{K}^o Z^o$)	10)

In future the pions in these final states will sometimes be denoted by their charges alone, e.g. $pK^- + -$ for reaction 4). Table 6.1 shows the numbers of fits allocated to reactions 1) - 6) for experiments 75, 10 and 75 + 10. In all there are 5571 events which give unique fits to these reactions after the criteria have been applied while 562 events are ambiguous between two hypotheses. In some cases the ambiguity is with a reaction not included in 1) - 6) which explains why the numbers do not balance. There were only 6 fits to these reactions which corresponded to triply ambiguous events. Of these the 3 in reaction 1) are due to a wrong selection of fits while the 3 in reaction 4) may be genuine ambiguities. It can be seen that the criteria have been fairly efficient in allocating a single hypothesis to each event. What is not clear is how often the selected hypothesis is the correct one and most of this chapter is devoted to a discussion of this.

Given a sample S of events which purport to be examples of a certain reaction, one may distinguish the following sub-sets:

i) the genuine (good) events (SG).

ii) the misidentified (bad) events (SB)

iii) the ambiguous events which are actually good events (SAG).

iv) " " " " " " bad " (SAB)

In addition there is the set:

v) the good events which have been excluded from the sample. (S_G')

The complete set of genuine events of the reaction is given by:

$$S_T = S_G + SAG + S_G^1 = S - (S_B + SAB) + S_G^1 \qquad (6.1)$$

TABLE 6.1

FITS ASSIGNED TO REACTIONS 1) - 6)

	pK^- o	$p\bar{K}^0$ −	$p\bar{K}^0$ −	nK^- +	pK^- + −	$p\bar{K}^0$ − o	$n\bar{K}^0$ + −
	1)	2a)	2b)	3)	4)	5)	6)
topology	200	200	201	200	400	201	201
no. of constraints	1	1	4	1	4	1	1
exp.75: unique	395	202	184	523	1056	519	318
ambiguous	101	96	-	10	488	9	2
total no. of fits	496	298	184	533	1544	528	320
total no. of events	445.5	250	184	528	1300	523.5	319
with decay wt.	-	-	214.07	-	-	577.04	361.34
av. decay wt.	-	-	1.163	-	-	1.102	1.133
exp. 10: unique	344	164	81	476	970	220	112
ambiguous	67	70	2	1	282	3	-
total no. of fits	414*	234	83	477	1255*	223	112
total no. of events	378.5	199	82	476.5	1111	221.5	112
with decay wt.	-	-	89.91	-	-	237.04	120.4
average decay wt.	-	-	1.096	-	-	1.070	1.075
75 + 10: unique	739	366	265	999	2033	739	430
ambiguous	168	166	2	11	772	12	2
total no. of fits	910*	532	267	1010	2808*	751	432
total no. of events	824	449	266	1004.5	2420	745	431
with decay wt.	-	-	303.98	-	-	814.08	481.74
average decay wt.	-	-	1.143	-	-	1.093	1.118

* these totals include 3 triply ambiguous fits (i.e. 1 event equivalent.)

Provided that the actual set S is the major contribution to the ideal set S_T one may write

$$N_T = N(1 - N_B/N)(1 - NAB/N)(1 + N_G{}^1/N) \qquad (6.2)$$

where N_i is the number of fits in the set S_i.

In practice the events in these subsets are not known individually but the numbers of events in each set may be estimated from relevant distributions. This means that the true cross section σ_T for the process may be found since this depends only on the total number of events and not on any individual event characteristics. The cross section σ for the observed sample S will in fact have its true value σ_T if

$$(1 - N_B/N)(1 - NAB/N)(1 + N_G{}^1/N) = 1 \qquad (6.3)$$

If the corrections to N are small this condition becomes

$$N_B + NAB = N_G{}^1 \qquad (6.4)$$

i.e. "bad" events included = "good" events lost. A trivial solution is $N_B = NAB = N_G{}^1 = 0$ which corresponds to the ideal sample S_T. In fact the relation (6.4) is exact as the approximations made in deriving it have cancelled out. It is an obvious result and could of course have been written down immediately.

The various stages at which biases can enter the given sample S will be discussed and, where possible, quantitative estimates of N_G, $N_G{}^1$, NAG, NAB and N_B will be made. If particular reactions are not specified the estimates can be considered to apply to all relevant reactions equally.

6.1 Unseen events (contributes to N_G^1)

Some events will always be missing from the sample because they are never seen at the scanning stage. The large losses in the 000 topology and in elastic scattering are not relevant to the study of reactions 1) - 10). For other types of event the simple-minded efficiency calculation predicts a very small number of missed events and it is hard to believe that there are not more events lost than this. Indeed some evidence was presented for this in the last chapter and it seems likely that a partial third scan would show that the assumption of equal visibility for all events of a given topology was not valid. Further scans of samples of the film might enable the true cross section to be obtained as the sum of an infinite series along similar lines to the method used by Derenzo and Hildebrand in their study of muon decay (46). The form of this series would not be a geometric progression as in the ideal case when there is a constant ratio between the numbers of new events found on successive scans but would be one whose terms decreased somewhat more slowly than those of the geometric series.

If these deficiencies were the same for all topologies it would not affect cross sections determined by normalisation to a known value. However they are likely to be more pronounced for a topology like 200 than for, say, 600 and they will also be biased towards events with tracks which are either short and slow, strongly dipping, or very fast and produced at small angles. The contribution to the lost events N_G^1 will however probably be small compared with that from other biases.

6.2 Rejected events (contributes to $N_G^{\,1}$)

There is always a residue consisting of events which fail to get acceptable interpretations even after repeated measurements. A breakdown of a sample of 425 such events from the London data of experiment 75 is shown in table 6.2. If these events are random samples from their respective topologies no bias will be introduced by their absence from the DST and for cross section purposes the number of such events does not need to be known for they have already been counted in the scanning totals. However certain types of event may preferentially fall into one of these rejected categories.

The unmeasurable events consist of those which could not be measured because of poor film quality, the obscuring effect of other tracks or damage to the film on one or more views. Also included are events in which a π^0 has decayed by the Dalitz pair mode and only one of the electrons can be distinguished. (If both electrons can be identified the event can be measured as normal with the two electron tracks omitted). Dalitz pairs will not occur for reactions with no missing π^0's (e.g. 4-C fits).

Events giving zero-constraint fits usually have a secondary interaction on one of the tracks close to the vertex so that its momentum is unmeasurable. This group will be biased towards events with slow tracks as these have larger cross sections for secondary interactions. The repeated failure of a track in the geometric reconstruction happens most frequently for slow and/or dipping tracks. These last two classes probably introduce only a small bias.

TABLE 6.2

BREAKDOWN OF UNSUCCESSFUL EVENTS

	TOPOLOGY				
	200	201	400	401	ALL
unmeasurable	48	29	50	36	163
zero-constraint fits	31	21	48	14	114
geometry failure	12	17	22	13	64
non-associated V^0	-	27	-	20	47
MM^2 negative	13	5	10	1	29
more than 1 baryon or strange particle	1	3	-	4	8
	105	102	130	88	425

It is often difficult to get an associated fit for a V^o which is within a few centimetres of the production apex. Short decay lengths are more likely to occur for slow V^o's so this may introduce a noticeable bias.

The next category in table 6.2 contains events which give a large negative missing mass squared for all hypotheses compatible with the observed ionisation. The reason for this is not entirely understood and it is possible that these events might be biased towards particular reactions. Finally there are a small number of events which are positively identified as multibaryon or multistrange particle final states.

6.3 <u>Correct hypothesis not attempted</u> (may contribute to N_G^1 and N_B)

If the correct hypothesis for an event has not been attempted in Grind the event may have another acceptable interpretation and be placed in the sample S. There are several situations where this arises:

i) As mentioned in chapter 4 fits are not attempted which require more than one strange particle or baryon in the final state because the cross sections for these processes are known to be small. Unlike the sample of such reactions discussed in 6.2 some of these events will <u>not</u> be positively identifiable and may therefore be accepted with an alternative interpretation. A background of about 1 event in 30 could be expected from this source (in all reactions). (N_B/N = 3%)

ii) Section 6.2 mentioned the situations where one or both electrons from a Dalitz pair are identifiable. If both have a momentum above 200 Mev/c they will be indistinguishable from pions and the event may have another acceptable interpretation. This bias can contribute to both N_B and N_G^1 since in addition the hypothesis of the actual reaction will not have been tried. A reaction involving the production of m neutral pions will give rise to Dalitz pairs in 1.17 m per cent of the cases. The probability of having two Dalitz pairs is very small (even for m = 10 it is only about 0.6%). Events with Dalitz pairs are not likely to give a fit and so will probably be classed as no-fits.

(for 1-C fits with missing π^o, $N_G^1/N = 1\%$)

(for no-fits, $N_G^1/N = 2\%$, $N_B/N = 1\%$)

iii) A very similar situation exists in the case of V^o's which decay so close to the production apex that they cannot be resolved from it at the scanning stage. The event will then be interpreted as having two additional prongs. The momentum balance is not affected in this wrong interpretation but the energy balance will be when one tries a strangeness conserving hypothesis. It seems likely that there will be a small background from such events in the samples of most reactions. The loss of events from the V^o reaction is corrected for. (see section 6.7).

iv) No fit is accepted which requires a missing Λ^o or Σ^o. The number of genuine fits which are rejected in this way can be estimated from the numbers of events where the Λ^o is seen. In experiment 75 there were 82 events of the reaction $\Lambda^o + -$ in the 201 topology in a region about double that used for the 200 topology. Thus, assuming 1/3 of the decays are not seen, and taking the worst case where all these events fit the reaction $nK^- +$, 20 out of the 528 events of the latter reaction obtained in experiment 75 may be expected to be mis-identified. The other lambda reactions will only contribute substantially in the no-fit samples.

(for reaction 3, $N_B/N = 4\%$)

v) No hypotheses are tried for the case of pions or antiprotons in the beam. Estimates of the background from these particles were given in table 2.2. Their total cross sections on protons at 10 Gev/c are 26.5, 54.0 mb. respectively (44) so that the contaminations are effectively increased by factors of 1.2 and 2.4 as far as the number of interactions produced is concerned. The antiproton contamination is expected to be quite small. An independent check of this can be made using the results from reactions involving anti-lambda production (11). Reactions where $\Lambda^o \Lambda^o \bar{\Lambda}^o$ or $\Lambda^o \Lambda^o$ decays are seen are most likely to be initiated by K^- but when $\Lambda^o \bar{\Lambda}^o$ is seen antiprotons could also be responsible. For K^- reactions involving no charged particles (i.e. no sigmas) the predicted ratios of these events from visibility arguments is

$$\Lambda^o \Lambda^o \Lambda^o : \Lambda^o \Lambda^o : \Lambda^o \bar{\Lambda}^o = 2 : 1 : 2$$

in experiment 75 (these are the numbers of events), Whereas the observed ratio is 2 : 2 : 2. Thus there does not seem to be any sizeable contribution from antiprotons. Assuming a cross section of 1 mb for $\bar{p}p \longrightarrow \Lambda^0 \bar{\Lambda}^0$ + neutrals, 1 seen event would correspond to a $\bar{p}$ contamination of 0.1%. It will also be rather harder for $\bar{p}$ interactions to give fits to K^- interactions than for π^- since the π and K have a much smaller mass squared difference. The chance of an event being caused by a pion depends on the topology. For events with an associated V^0 the chance of K^- being the beam particle is enhanced by about 3:1 (22%, 7%) whereas events without V^0's are favoured for pions by a factor of 1.2 (93%, 78%). Pions may often give fits (even four constraint ones) to kaon hypotheses.

(for V^0 topologies, N_B/N = 1%)

(for non-V^0 " , N_B/N = 7%)

6.4 Correct hypothesis failed to fit (contributes to N_G^1 and N_B)

Sometimes the fit to the genuine hypothesis for an event may fail. This is noticed most often for 4-C events where the missing mass squared and missing energy are close to zero (with small errors) making the event unacceptable as a no-fit. A sensitive test for the presence of such events is to examine the quantity MP_x - ME (47). The reason for the failure to fit may be a small error in the geometry constants. This would be likely to cause more trouble for 4-C fits because they are the most highly constrained. If it did occur also for 1-C fits it would be harder to pick out the individual events concerned since they would probably have values of the missing mass and energy compatible with a no-fit hypothesis.

6.5 Correct hypothesis rejected by criteria (contributes to $N_G^{\ 1}$, N_B)

The criteria applied in deciding between various interpretations of an event were listed in table 4. The probability cut-off gives $N_G^{\ 1}$ = 1%, 5% respectively for 4-C and 1-C fits if the distribution for genuine events is flat. The bias due to the inclusion of bad events is hard to estimate. The distribution shown in figure 4.2 for reaction 4) is the only one for the reactions studied where any peaking is seen at low values just above the cut-off. However most of the results presented for this reaction will involve only the experiment 75 sample where the probability distribution looks reasonable. It does seem as if there could be substantial impurities in the experiment 10 sample unless there is another explanation for the low probability peak.

The criterion which prefers a 4-C fit over the corresponding 1-C fit may affect the pair of reactions 2b) and 5) and also reactions 1), 4) and the reactions pK^-, pK^- + -o respectively, the latter two not being among the main ones studied here. Figure 4.3 showed the π^o laboratory momentum distribution for reaction 1) and there was seen to be very little overlap with the 4-C reaction; the same is true for reactions 2b), 4) and 5) (not shown).

The missing mass squared distributions are shown in figures 6.1 - 6.4 for the following pairs of reactions. In each pair both reactions have the same assignment for the seen particles but the first reaction has a single missing particle while the second has additional neutral pions. The plot for the first pair has already been shown in figure 4.4 for the experiment 75 data. The others are for the combined data of the two experiments.

Table 6.3	1-C fit	no-fit	N_G^1/N	N_B/N
(fig. 4.4)	$pK^- \circ$ (1)	$pK^- Z^o$ (8)	4%	14%
(fig. 6.1)	$p\overline{K}^o - \circ$ (5)	$p\overline{K}^o - Z^o$ (11)	2%	4%
(fig. 6.2)	$p\overline{K}^o -$ (2a)	$p - Z^o$ (12)	6%	3%
(fig. 6.3)	$nK^- +$ (3)	$K^- + Z^o$ (9)	9%	16%
(fig. 6.4)	$n\overline{K}^o + -$ (6)	$\overline{K}^o + - Z^o$(13)	3%	14%

(reactions 11 - 13 are defined for the first time here).

All the plots have reasonably Gaussian shaped peaks except for figure 6.3. This is probably due to the inclusion of a large number of no-fits because the maximum of the distribution has been shifted upwards from the neutron mass squared (0.88 Gev^2) to about 1.02 Gev^2. The other distributions all peak close to the mass squared for the relevant missing particle. The percentage of "bad" events included can be estimated by reflecting the lower half of the peak (where the contamination is expected to be small) onto the upper half and finding the difference between the folded and original distributions. The percentage of good events lost can be found by calculating the contribution to the integral of the Gaussian from the region above the missing mass cut. The values are shown in table 6.3. The assignments N_G^1, N_B will of course be reversed if one is considering the bias in the sample of no-fits caused by the events from the fittable reactions. In this case the value of N will become the total of the no-fit sample.

FIG. 6.1

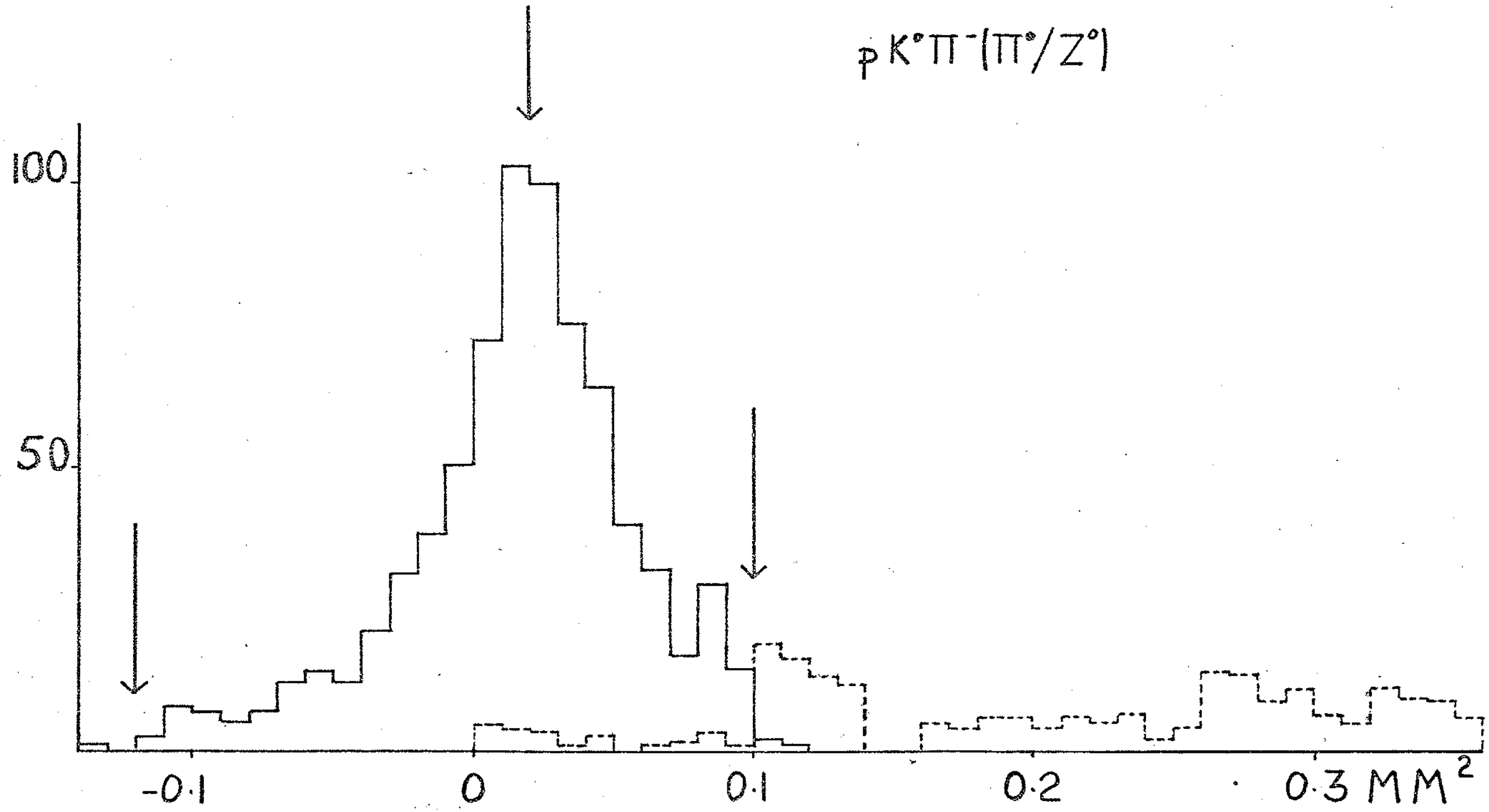

FIG. 6.2

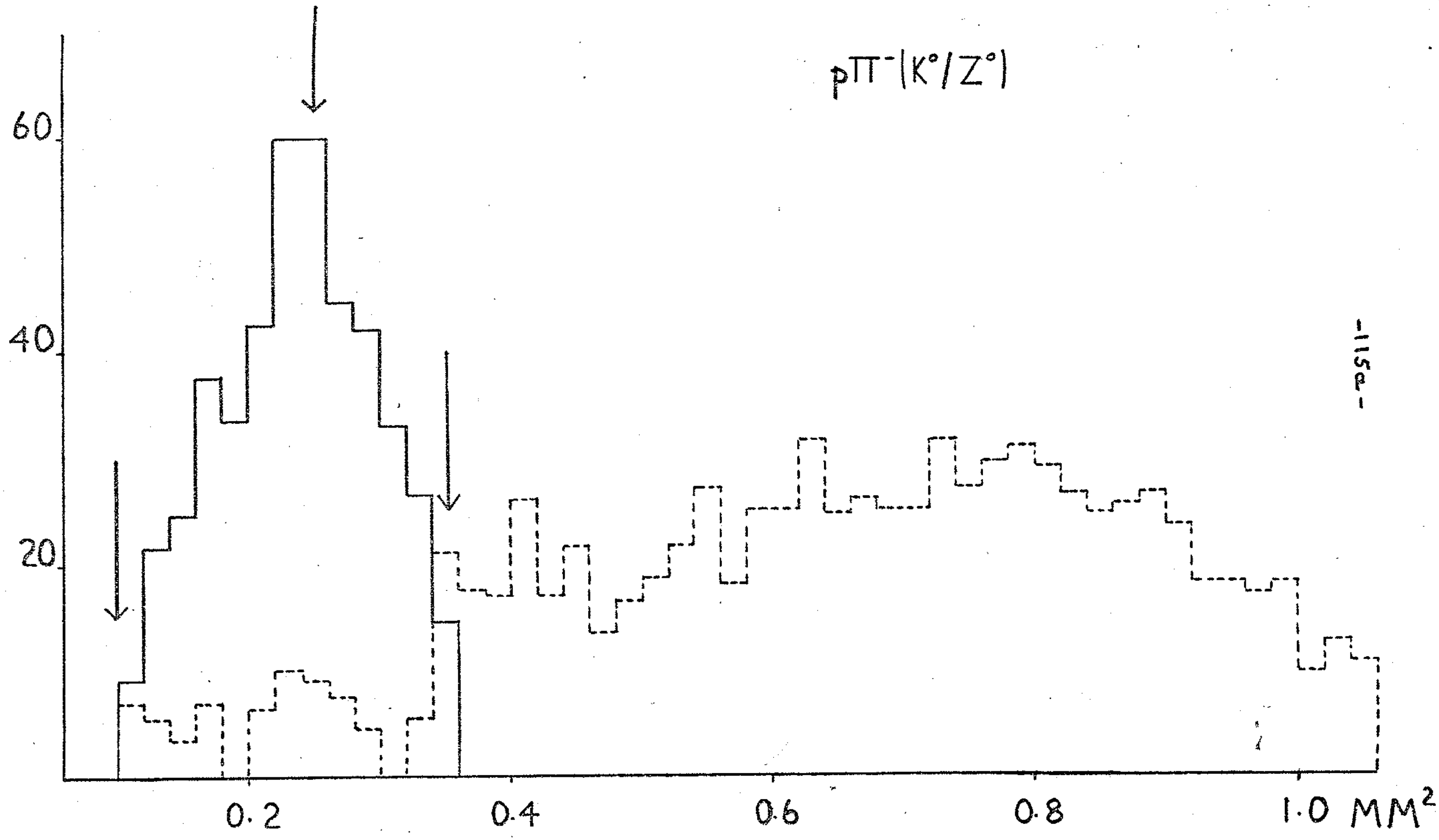

FIG. 6.3

$K^-\pi^+(n/Z^\circ)$

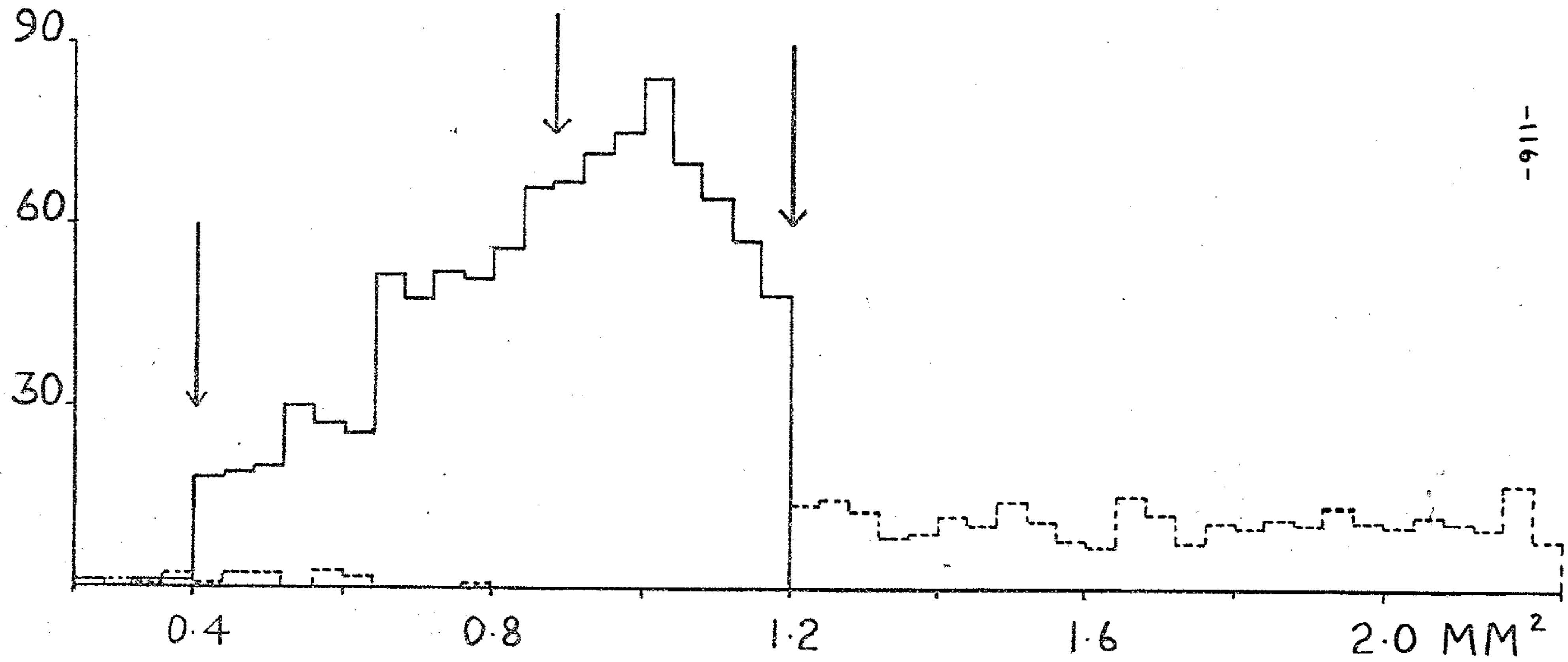

FIG. 6.4

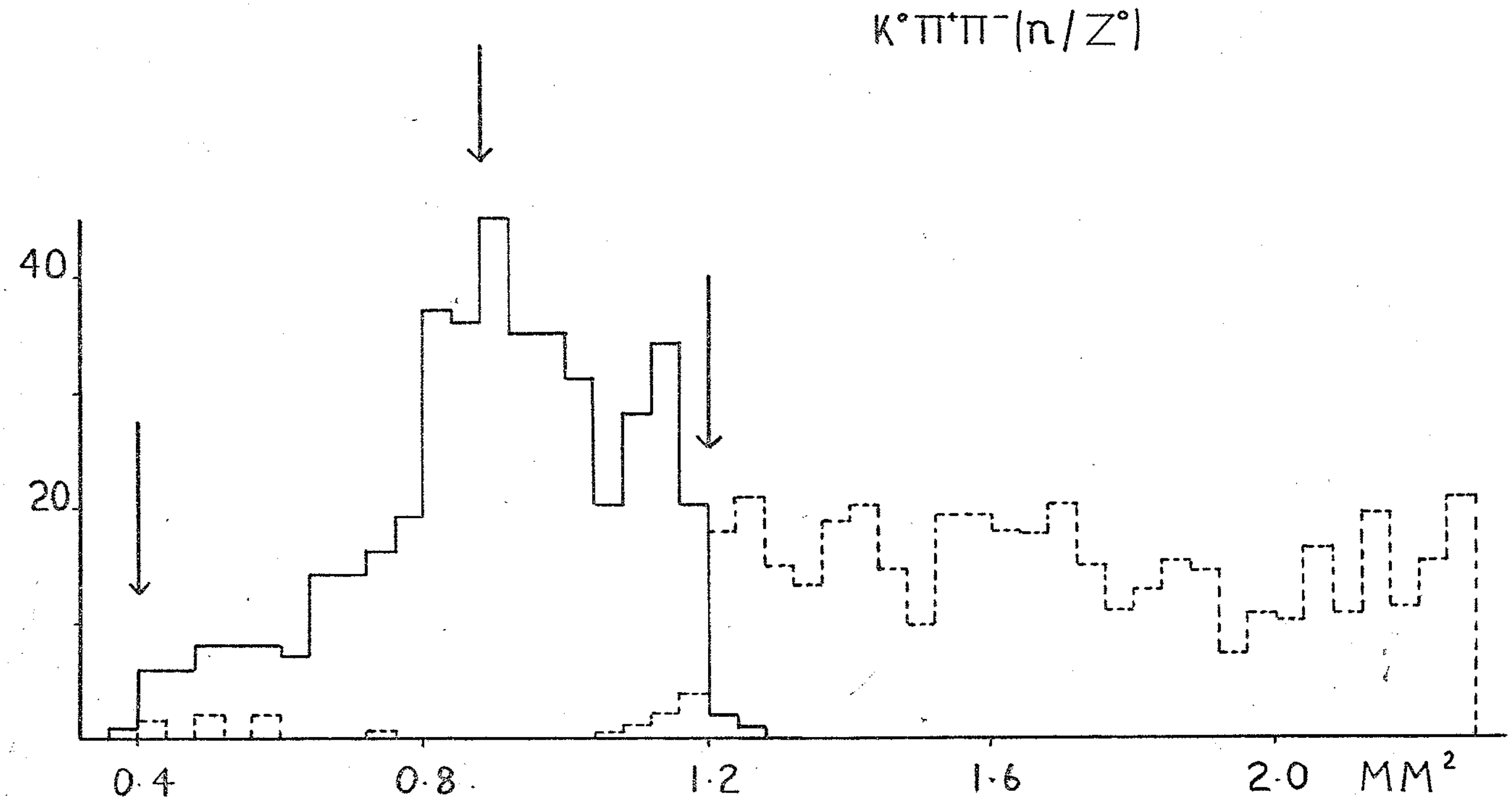

Application of the proton laboratory momentum cut can have caused genuine events to be lost from the final states containing a proton (reactions 1, 2a, 5) and also wrong events may have been assigned to reactions with a neutron in the final state (3, 6). On the whole, though, most of the events with fits rejected by this criterion are assigned as no-fits. Assuming reaction 2a is typical of the first set, the numbers of fits lost can be found from the number of 4-C fits to the same reaction which have protons of momentum greater than 2 Gev/c. In experiment 75 this number was 2 out of a total of 184 events. Assuming 1/3 of the $\overline{K}^0$'s are seen, one expects 2 such events in the smaller fiducial region which would have been rejected wrongly by the criterion.

$$(N_G^1/N = 1\%, N_B/N = 0\%).$$

The effect of the unseen $\overline{K}^0$ laboratory momentum cut can be estimated in a similar manner. This results in a loss of good events from reaction 2a). From a sample of 20 fits to reaction 2a) which had a $\overline{K}^0$ momentum of less than 2 Gev/c, 16 were reassigned to the no-fit reactions 8) or 12) while the other four were ambiguous (3 with reaction 3, 1 with reaction 1) and so the alternative fit was accepted for each. The 4-C reaction 2b) has 15 events out of 184 with $\overline{K}^0$ momentum below 2 Gev/c so that a similar number is expected to have been wrongly excluded from 2a) because of the cut.

$$(N_G^1/N = 7\%, N_B/N = 0\%)$$

6.6 Correct hypothesis ambiguous (contributes to N_{AG},N_{AB})

In the case of ambiguous events where one of the hypotheses is the correct one it may be possible in many cases to determine the correct assignment by comparing the properties of the ambiguous fits to those of the unique samples of the same reactions. In such cases one does at least know that there is a bias since both hypotheses cannot be correct. One common procedure with ambiguous events is to weight them in proportion to the cross sections for the two reactions. This means choosing f in the range (0, 1) such that

$$\begin{aligned} N_{AB} &= f(N_{AB} + N_{AG}) \\ N_{AG} &= (1-f)(N_{AB} + N_{AG}) \end{aligned} \qquad (6.5)$$

Where ambiguous events have been plotted with unique events in this experiment they have been given half-weights since the cross sections of the competing processes are usually of the same order. This was only intended as a temporary measure to be used until enough events were obtained to study the ambiguities in more detail.

No ambiguity exists between fits corresponding to different topologies so that in discussing the ambiguities in reactions 1) - 6) there are three categories to consider, namely topologies 400, 201 and 200.

i) 400 ambiguities (reaction 4)

As can be seen from table 6.1 there are a substantial number of fits to this reaction which are ambiguous. Since this gives a 4-C fit the corresponding 1-C fits have been rejected if they existed so that the only possible ambiguity is between different fits to the same reaction. This arises because there are two positive tracks and two negative tracks and the tracks of each pair have different particle assignments (p/π^+ and K^-/π^- respectively). Thus if the kinematic situation is such that more than one of the four permutations gives rise to a fit and if the tracks whose particle assignments differ are above the limit for identification by ionisation the fits will be ambiguous. Since this occurs for K^-/π^- above about 750 Mev/c but for p/π^+ only above 1.5 Gev/c and since protons preferentially have quite low momenta, almost all of the ambiguities in this reaction will be of the K^-/π^- type. This is an internal ambiguity so that the cross section for the process is unaffected by the choice of the weighting factor f.

If 1, 2 denote the tracks which are ambiguous and MP_i, MM_i are the values of the missing momentum and missing mass for the hypothesis i then energy conservation requirements in the two cases lead to the relation

$$(p_1^2 + m_K^2)^{\frac{1}{2}} + (p_2^2 + m_\pi^2)^{\frac{1}{2}} + (MP_i^2 + MM_i^2)^{\frac{1}{2}}$$
$$= (p_1^2 + m_\pi^2)^{\frac{1}{2}} + (p_2^2 + m_K^2)^{\frac{1}{2}} + (MP_j^2 + MM_j^2)^{\frac{1}{2}} \qquad (6.6)$$

The momentum conservation equations require that MP_i, MP_j must be nearly equal and if fits are obtained to both hypotheses i, j the values of MM_i^2, MM_j^2 must be compatible with zero (no missing particle). This occurs when p_1, p_2 are approximately equal so that, on a plot of p_1 against p_2 for all fits to reaction 4), the ambiguous events will be situated close to the $p_1 = p_2$ line and above the lines

$p_1 = p_2 = 750$ Mev/c.

ii) <u>201</u> (reactions 2b, 5, 6)

The first of these reactions gives a 4-C fit and has essentially no ambiguities. The two ambiguous fits are either due to mistakes in applying the criteria or to ambiguity with the 4-C reaction Λ^o + - . Reactions 5), 6) do have a few ambiguities either with each other or possibly with Λ^o + - o. Since the negative track in these events is always assumed to be a pion, the ambiguity between 5) and 6) is between p and π^+ and can therefore only occur for momenta between the identification limit of 1.5 Gev/c and the momentum cut at 2 Gev/c.

iii) <u>200</u> (reactions 1, 2a, 3)

This topology has more ambiguities than the 201 topology since there is no restriction on the identity of the negative track. From table 6.1 one can see that the main ambiguity is between 1) and 2a) as one would expect since these differ in the assignment of the negative track. Reaction 3) is only allowed to be ambiguous with the others for events where the positive track has a momentum in the range 1.5 - 2.0 Gev/c. One might have expected more ambiguities between 1) and 3) than between 2a) and 3) since the former pair do at least have a K^- in common. However it is not clear whether the slight excess of ambiguities in 1) (101 over 96) is significant in this respect. For events ambiguous between 1) and 2b) energy conservation gives the relation

$$(p_1^2 + m_K^2)^{\frac{1}{2}} + (p_2^2 + MM_i^2)^{\frac{1}{2}} = (p_1^2 + m_\pi^2)^{\frac{1}{2}} + (p_2^2 + MM_j^2)^{\frac{1}{2}} \qquad (6.7)$$

where 1, 2 refer to the negative and neutral particles which give rise to the ambiguity.

Suppose hypothesis i corresponds to reaction 1) and that its missing mass $MM_i = m_\pi$. Then, neglecting the mass differences within the pion and kaon I-spin multiplets, $MM_j = m_K$ so that the other hypothesis will also give a fit in the centre of its missing mass distribution. Thus missing mass squared cuts would not have been very effective in separating these hypotheses which may be why such a lot remain ambiguous.

6.7 Correct hypothesis unique (represents the N_G part of the sample)

This is hopefully the major contribution to the total sample available for most reactions. Having accepted the correct interpretation for these events it is important to know what biases, if any, are present in the values of the fitted parameters of the event and whether the sample itself is an unbiased one from all events of the reaction.

The title values for the beam track should have large enough errors for most genuine beam tracks to have an equal chance of fitting. Histograms of the momentum, dip and azimuth for the beam track taken from a sample of four-constraint fits indicate that this is so (not shown).

Any bias caused by an error in the knowledge of the magnetic field value can be detected by a shift of the peak in the unfitted mass of the $\overline{K^0}$ determined by measuring its decay into two pions. This was found to be centred at the accepted mass value (not shown).

In bubble chamber experiments it is normal to impose chosen (external) errors on the measured quantities at the kinematics stage because the internal errors obtained from the scatter of points about the fitted trajectory have statistical fluctuations from one track to another and also because there are additional factors which are not taken into account in these internal errors. Examples of these factors are multiple Coulomb scattering, uncertainties in the geometry constants and possible turbulence in the chamber liquid. The reasonableness of the imposed errors may be checked by the flatness of the chi-squared probability distributions. Figure 4.2 shows these for the reaction $pK^- + -$ in experiments 75 and 10. The first of these is fairly typical of all reactions in experiment 75 in that it is peaked at high values showing that the external errors have been overestimated. The other 4-C reaction 2b) has a very similar distribution while the 1-C reactions have an even larger peak at high values. In experiment 10 the distributions for 4-C fits are peaked at both ends while for 1-C fits they are fairly flat with a slight rise at high probabilities.

A more sensitive test is provided by the stretch function for a variable x defined by

$$S(x) = (x_f - x_m)/(dx_f^2 - dx_m^2)^{\frac{1}{2}} \qquad (6.8)$$

where f, m refer to the fitted and measured (unfitted) values of x. The stretch function should be a unit Gaussian if there are no systematic errors (which would shift the mean) and if the random errors have been correctly estimated (otherwise the variance would be different from unity). Distributions of these quantities for the momentum and angles of tracks in a sample of 4-C fits from experiment 75 are shown in references 41 and 42. They are consistent with the expected behaviour.

Some of the biases present in the sample of accepted fits due to the loss of genuine events (N_G^1) have been discussed in earlier sections of this chapter. For events involving a seen strange particle decay there is an additional bias due to the events of the same reaction in which the decay takes place outside the chamber. This will cause a loss of events where the strange particle has a high momentum and therefore more chance of escaping from the chamber before decaying. For neutral strange particles there is also the possibility of decay into neutral particles but this does not bias the sample since it obviously makes no difference if this unobserved decay occurs inside or outside the chamber. For reactions with no other neutral particle missing it is still possible to get a 1-C fit and, in principle, the sum of the two classes should equal the total sample for the reaction. However the 1-C fits are much more subject to contamination as has been indicated above. Also where there is another neutral particle missing, the event can only be fitted when the strange particle decay <u>is</u> seen. Thus in both cases it is advantageous to correct the samples for the decays which are lost. This is done by weighting each observed event by the inverse of the probability of the observed V^o decaying within the visible region of the chamber. A correction is also applied for V^o's which are not detected because they are too near the production apex (see section 6.3). A minimum length of 3mm is used for this (projected onto the film plane). It would perhaps have been more satisfactory to correct also for the events where the V^{o} was seen but did not give an associated fit because it was too near the apex (see section 6.2). The necessary cut-off to use could have been found from the lifetime plot of the strange particles from the successful events.

The weight W used is given by

$$1/W = \exp(-\,\mathrm{Lmin}/L_o \cos\lambda) - \exp(-\,\mathrm{Lmax}/L_o) \qquad (6.9)$$

where Lmin = the minimum observable length (3mm), Lmax is the potential length over which the decay could have been seen (i.e. the distance along the line of flight to the edge of the illuminated region) and L_o is the length corresponding to a particle with the mean lifetime t and is given by

$$\mathrm{Lo} = \beta tp/m \qquad (6.10)$$

where β is the velocity of the particle (c = 1). Strictly speaking the decay weight W should also contain contributions from all possible positions of the apex within the fiducial volume. This can be important for cases when Lmax is very small because (6.9) can then lead to a very large weight. This occurs when the distance of the production apex from the edge of the visible volume is small compared with the distance Lo for the particle concerned. An upper limit for the allowed weight is imposed in Slice but this does not affect the reactions discussed here since there is always a substantial distance between the end of the fiducial region for the production apex and the edge of the chamber. The average values of the decay weights in each reaction are shown in figure 6.1. The values for experiment 10 are in each case less than those for experiment 75. This simply reflects the fact that the choices of the fiducial regions mean that there is a relatively larger volume for observing the decays in the 2 metre chamber.

For just the same reasons the sample of events assigned to reaction 2a) will be biased towards the fast $\overline{K}^{o}$'s. An analogous weight could be calculated for these events but this is probably a negligible bias compared with the uncertainties already present in this sample. These uncertainties can be investigated by taking events from reaction 2b) and refitting them to reaction 2a) by discarding the measurements of the V^{o} tracks. This was done for a sample of 23 of the four constraint events with the following results (after applying the usual criteria

Unique fits to reactions 2a)	13 events
Ambiguous fits to reactions 2a), 1)	3 "
Unique fits to reaction 1)	3 "
No acceptable fit	4 "
	23 "

From the totals for reaction 2b) in table 6.1 it can be calculated that the expected number for 2a) is 432. Normalising the above results to this number we get contributions of 244, 56, 56, 75 for the four categories. The observed numbers for the first two categories can be found from table 6.1 and are 366 and 83. The observed numbers for the other two categories are unknown.

We can then deduce the following for reaction 2a):

$$N_G/N = 244/449 = 54.3\%$$

$$N_B/N = 122/449 = 27.2\%$$

$$N_{AG}/N = 56/449 = 12.5\%$$

$$N_{AB}/N = 27/449 = \underline{6.0\%}$$

$$\underline{\underline{100.0\%}}$$

$$N_G^1/N = 56 + 75/449 = 29.2\%$$

These are to be compared with the estimates obtained in sections 6.1 - 6.6 for this reaction. There is some measure of consistency but the earlier estimates seem to be a little on the low side especially when it is realised that they are not all independent. For example there is a very strong correlation between the X^2-squared probability and the missing mass squared for 1-C fits as the value of X^2 obtained after the first iteration in Grind can be shown to be given by (48):

$$X^2 = (MM_i^2 - m_i^2/dMM_i^2)^2 \qquad (6.11)$$

where m_i is the mass of the missing particle. This is probably a good enough approximation to the final value of X^2 to preserve most of this correlation between X^2 and MM^2. An experimental verification of this has been given for the reaction $\pi^- p \longrightarrow n + + + - -$ at 6Gev/c (49).

There are a few additional points which have some bearing on the biases present in the data.

Many quantities like probability, missing mass squared, missing energy, laboratory momenta and error of the missing mass squared have been examined both in one and two dimensional plots for the data from the separate groups and no significant differences have been found. Up till now all groups have used measuring machines of similar accuracies.

Distributions of the (X, Y, Z) coordinates of the apices of accepted events are as expected, namely isotropic in X and approximately Gaussians in Y and Z (reflecting the beam profile).

Some events in the final states containing a K^- will not appear in the topology 200 because the K^- has decayed in the chamber. In principle a weighting could be used to correct for these events but due to the relatively long lifetime of the K^- this weight would be always close to 1. For kaon momenta of above 500 Mev/c the fraction which decay within a distance of 1 metre is approximately 1/7.5 p and since most K^- particles have momenta in the range 5 - 10 Gev/c in the reactions studied this fraction is only about 1/50.

The chance of an unassociated V^o giving an associated fit to an event in the chamber may be estimated as follows. The V^o can be assumed to have an origin outside the visible volume and to give an associated fit if it passes within a distance of an event apex which is of the order of the measurement accuracy for reconstructed points. V^o's with no observable origin are seen once in every 7 - 8 frames whereas the number of events measured per frame is about 2/3. This gives a probability for a chance association of about 10^{-5} which is negligible for reactions with cross sections of greater than 1 μb.

Further selections which are made later to isolate specific reactions involving resonance production will in some cases improve the purity of the samples.

CHAPTER 7

MASS DISTRIBUTIONS AND RESOLUTION

The most striking features of reactions 1) - 6) involve the $K\pi$ and $K\pi\pi$ groups of particles. (Strictly speaking these are $\overline{K}$'s (s = -1) and not K's (s = +1) but the bar will be omitted when there is no possibility of confusion). The presence of detailed structure in these systems can most readily be seen by examining effective mass histograms. The effective mass M of a system of n particles is defined by the relation

$$M^2 = (\sum_i E_i)^2 - (\sum_i \underline{p}i)^2 \qquad (7.1)$$

This mass M may be considered to be that of the "particle" which is kinematically equivalent to the group of n particles but in general this has no direct physical significance. In certain cases however the group of n particles may have come from the decay of a resonant state with well-defined mass M and this state may be considered to be a particle in the same sense as nucleons, kaons and pions, the particles which are directly detected in the bubble chamber. The only difference between a resonance like M and the other particles mentioned is that M has a high enough mass to be able to decay by the strong interaction whereas there are no states of lower energy available for the other particles which have the same quantum numbers for all the observables which are conserved in a strong interaction. Therefore these particles are either stable (as in the case of the proton) or decay via some other type of interaction which requires less quantum numbers to be conserved. These other interactions are the electromagnetic (I-spin violating) and the weak (I-spin,strangeness and parity violating). The very different relative strengths of these interactions are related to the lifetimes of the particles whose decays they cause. Typical times are 10^{-23}, 10^{-16} and 10^{-10} seconds for the strong, electromagnetic and weak interactions. The distances travelled by a relativistic particle in these times are about 3.10^{-13}, 3.10^{-6} and 3 cm respectively. Thus weakly decaying particles travel a detectable distance before decaying whereas the others effectively decay at their point of production as far as can be ascertained experimentally. However there is a difference between the electromagnetic and strong decays in that the former occur at a relatively large distance (hundreds of atomic diameters) from their production whereas the strong decays occur within the range of the strong interaction which produced the primary event. This means that the decay products of the resonant state may be affected by other particles produced in the event, that is the state does not necessarily decay independently but can be influenced by these final state interactions. The lifetime of a particle or resonant state is related by the uncertainty principle to the inverse of the width of its mass distribution. For a weakly decaying particle the width is much smaller than the error in the mass determination and so is never directly observed. This is not so for the strongly decaying states which have observed widths ranging from about 10 to a few hundred Mev. For widths much larger than this the concept of the state as a particle which is produced and then decays become rather vague. The mass distribution for the decay of a pure resonant state is expected to have the following form, usually known as a relativistic Breit-Wigner distribution (50, 51)

$$\frac{d\sigma}{dM^2} = \frac{d\sigma_s(M)}{\pi} \quad \frac{M_o \; \Gamma_i(M)}{(M_o^2 - M^2)^2 + M_o^2 \, \Gamma_T^{\,2}(M)} \qquad (7.2)$$

where M_o is the mass of the resonance, $\Gamma_T(M)$ is its width and $\Gamma_i(M)$ is the partial width for the decay mode i defined by

$$\Gamma_i = f_i \; \Gamma_T \qquad (7.3)$$

where f_i is the fraction of all the decays that occur through the mode i. In (7.2) $d\sigma_s(M)$ is the cross section for the production of a stable particle of mass M which the resonant cross section approaches in the limit of zero width (i.e. a stable particle). The width $\Gamma(M)$ is a function of the mass and for a two-particle decay can be written in the form (51)

$$\Gamma(M) = \Gamma_o(q/q_o)^{2\ell+1}(\rho(M)/\rho(M_o)) \qquad (7.4)$$

where q is the momentum of both of the decay products in the rest frame of M, Γ_o, q_o are values at $M = M_o$ and $\rho(M)$ is only a slowly varying function of M.

In most cases the dominating part of (7.2) is the denominator of the second factor which, when M is close to M_o, may be written

$$4M_o^2 \left((M_o - M)^2 + \Gamma_T^2 (M_o)/4 \right) \qquad (7.5)$$

which gives a Breit-Wigner distribution in M (instead of M^2) The width Γ_T is then the full width of the peak at half the maximum height.

If processes other than the production of the resonance give rise to effective masses in the resonance region there will be a background under the Breit-Wigner shape. Under certain circumstances the two amplitudes (resonance and background) may interfere.

At lower energies (incident momenta around 2-4 Gev/c) the effective mass distributions of groups of particles which did not contain resonances were fairly well represented by the prediction of the statistical theory (52). This assumed that the interaction between hadrons was so strong that a statistical equilibrium was attained among all states compatible with the known conservation laws. The relative probability of a given final state was then assumed to be proportional to the phase space available for this state, that is the matrix elements for all final states were taken to be constant.

Unfortunately this model does not provide a good description of the non-resonant parts of the effective mass distributions in the present experiment. While it is still satisfactory in the higher multiplicities (6-prongs and above) it gives a very poor description of the background processes in the lower multiplicities. In the absence of any better solution in these cases the background in a resonance region is estimated by extrapolation of the observed distribution outside the resonance in a smooth way. This will be referred to as a smooth hand-drawn background.

7.1 <u>$K\pi$ systems</u>

Figure 7.1 shows the effective mass distributions for the ($K\pi$) system in reactions 1), 2a), 2b) and 3. The purest sample of events is that for 2b) and two peaks are clearly resolvable at masses of about 900 and 1400 Mev and with widths of about 50 and 150 Mev

FIG. 7.1

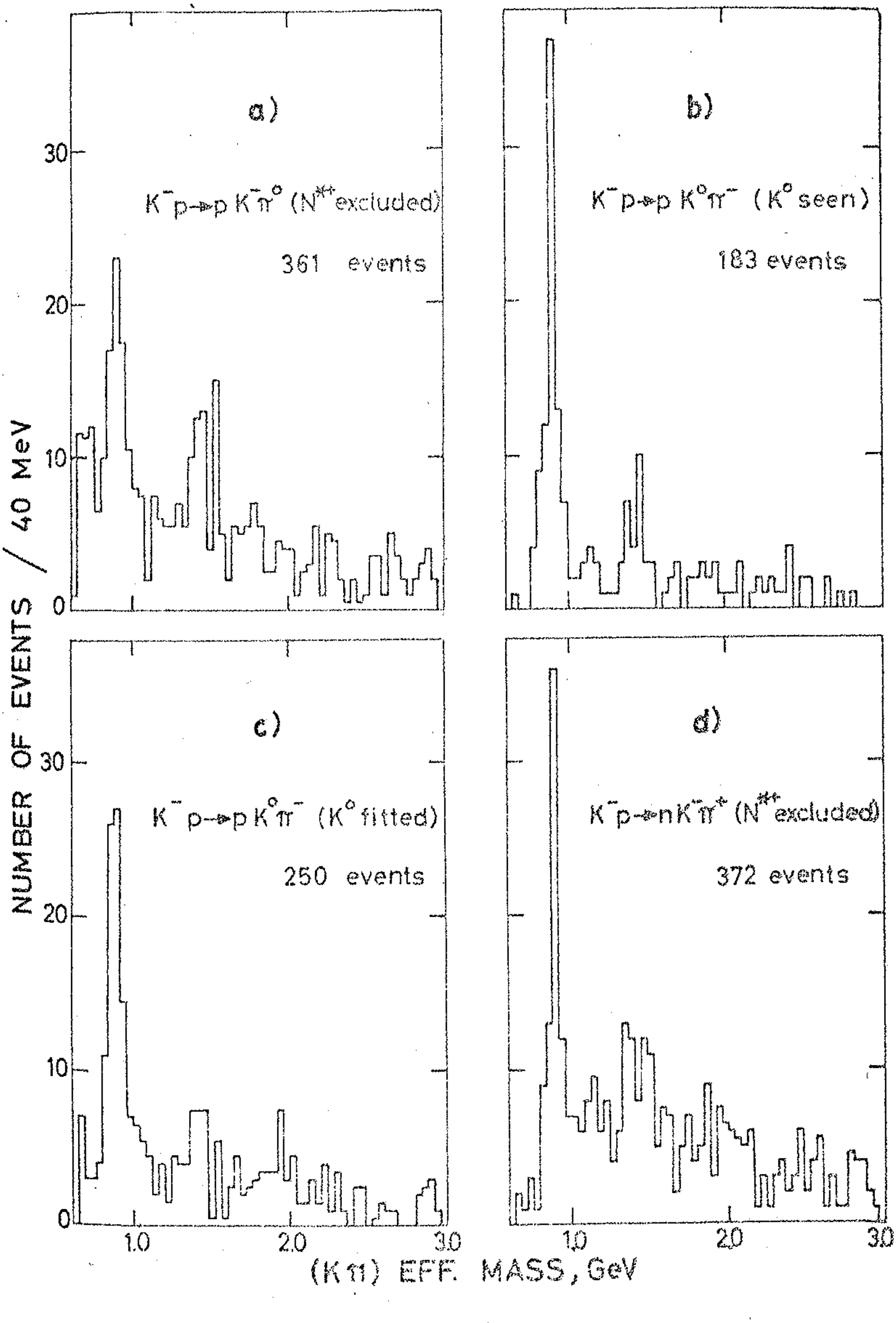
a)
K⁻p→p K⁻π° (N** excluded)
361 events
b)
K⁻p→p K°π⁻ (K° seen)
183 events
c)
K⁻p→p K°π⁻ (K° fitted)
250 events
d)
K⁻p→n K⁻π⁺ (N** excluded)
372 events
NUMBER OF EVENTS / 40 MeV
0
10
20
30
1.0
2.0
3.0
(Kπ) EFF. MASS, GeV

respectively. The same peaks can be seen in the other three plots but in 1) and 3) the backgrounds are larger and in 2a) the second peak is not too well resolved. Both these peaks correspond to well established resonant states having been first reported in 1961 and 1965 (53, 54). They are referred to as the K*(890) and the K*(1420) where the numbers are their approximate mass values in Mev. Since the only other particle present is a nucleon these states are produced in reactions of the general form

$$K^- p \longrightarrow pK^{*-} \tag{7.6}$$

$$nK^{*0} \tag{7.7}$$

where the K* subsequently decays into a K and a π. Reactions of this type where two initial particles give rise to two final particles are the simplest to describe theoretically and are therefore an obvious starting point in the study of strong interactions. When one of the particles is unstable (as in the present case) the reaction is usually called quasi two-body. The background under the peaks and in the other parts of the $K\pi$ mass distribution comes from other competing processes which lead to the same final states 1) - 3). These processes could involve the production of resonances between one of the other two pairs of particles ($N\pi$ or NK) or they could lead directly to the three particle final state. Examination of the (NK) effective mass distributions shows no significant production of any resonances (these would be Y_0^*'s or Y_1^*'s if present). Figure 7.2 shows the (nK^-) mass plot for a small sample of events of reaction 3); the corresponding plots for reactions 1) and 2) are very similar. The $N\pi$ mass distributions show peaks due to the N*(1236) in reactions 1) and 3) (charge state = +1) but not in reaction 2) (charge = 0).

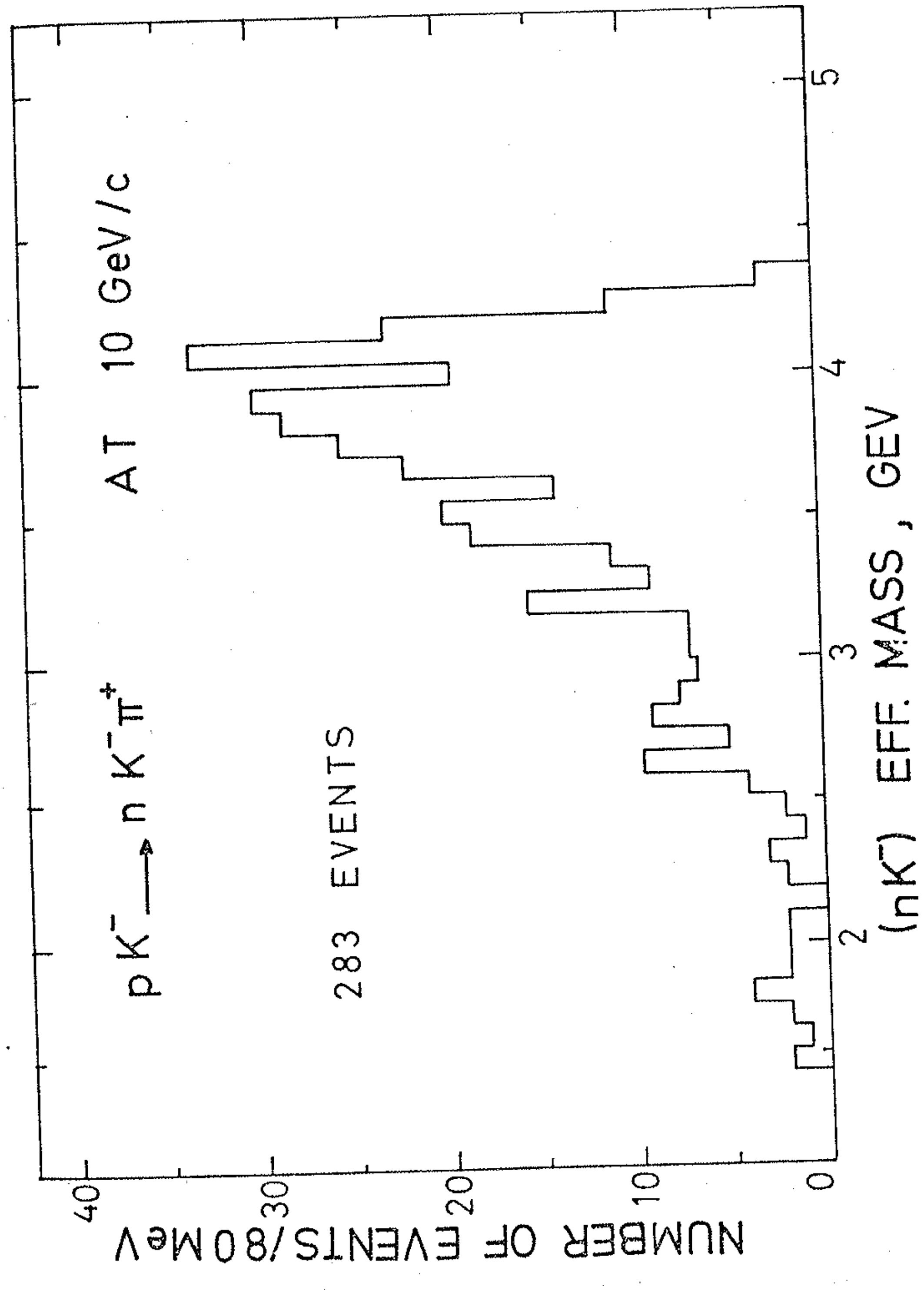
$pK^- \longrightarrow nK^-\pi^+$ AT 10 GeV/c
283 EVENTS
NUMBER OF EVENTS/80 MeV
0
10
20
30
40
2
3
4
5
(nK^-) EFF. MASS , GEV

If the processes of K* and N* production in 1) and 3) are assumed to be independent then they cannot occur simultaneously in one event since both involve the pion in the reaction. It therefore follows that the purity of the K* samples can be improved by removing events which lie in the N* peak provided there is not much kinematic overlap between these two classes of event. This has been done in figure 7.1 using the mass region 1.12 - 1.34 Gev for excluding N* events and is a further example of the kind of criterion described in chapter 4 where (xi) is now chosen as $\left(M(K\pi), M(N\pi)\right)$.

To obtain the best estimates of the masses and widths of the two K*'s the combined ($K\pi$) mass distribution for reactions 2b) and 3) was fitted to the superposition (without interference) of two Breit-Wigner distributions of the form (7.2) and a smooth hand-drawn background. These two reactions are used since the momenta of the particles contributing to the K* are directly measured whereas in the other two reactions either the K or the π is a fitted particle. It should be noted that these two reactions contain K*'s in different charge states (-1, 0 respectively). The mass values for these states are expected to differ slightly (by a few Mev) due to SU(2)-violating interactions which cause mass splitting within the I-spin multiplets. The results of the fit are shown in table 7.1 and figure 7.3 shows the fitted curve superimposed on the combined histogram; the dotted curve represents the background contribution. Also shown in the table are the accepted world average values taken from reference 2. The observed masses are seen to be compatible with these values but the observed widths are greater, especially for the K*(1420). This is because they contain

TABLE 7.1

FITTED VALUES OF MASSES AND WIDTHS

Resonance	Mass (Mev)	Width (Mev)	World average values M		Reactions fitted
K*(890)	893 ± 4	58 ± 7	*895.6 ± 0.6	50.1 ± 0.8	2b), 3)
K*(1420)	1423 ± 21	175 ± 57	1409 ± 4	96 ± 7	2b), 3)
K*(1320)	1325 ± 6	186 ± 15	Not well-known		4), 5)
	1335 ± 6	196 ± 16			all **
L(1800)	1785 ± 12	127 ± 43	1775	-	4), 5)
	1789 ± 8	132 ± 28			all **

* This value is the average of the neutral and negative charge states.

** The reactions used in this fit are given in chapter 8 (section 8.4.3)

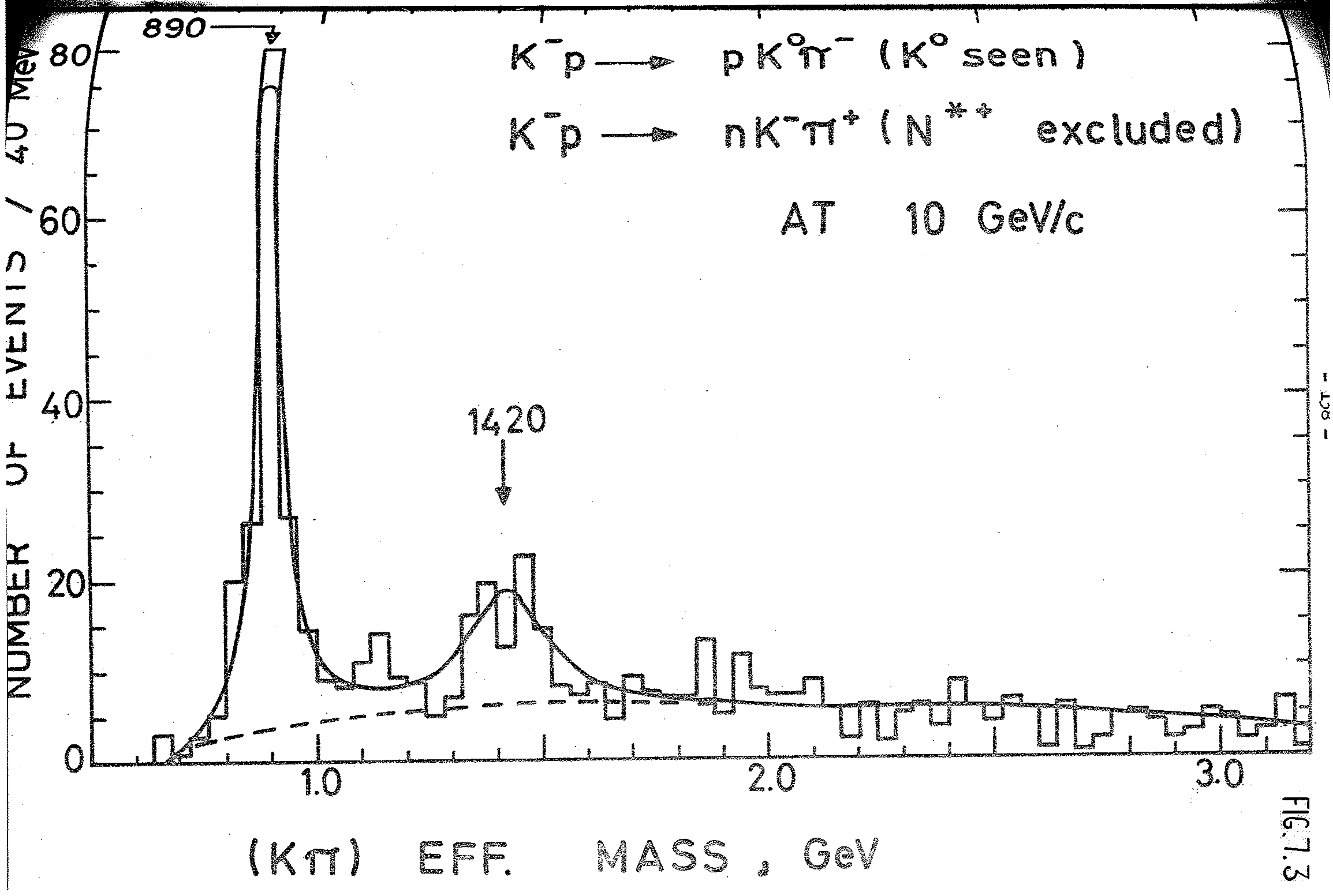
890
80
60
40
20
0
NUMBER OF EVENTS / 40 MeV
$K^-p \longrightarrow pK^0\pi^-$ (K^0 seen)
$K^-p \longrightarrow nK^-\pi^+$ (N^{*+} excluded)
AT 10 GeV/c
1420
1.0
2.0
3.0
($K\pi$) EFF. MASS, GeV

FIG. 7.3

contributions from the experimental mass resolution as well as from the natural widths of the resonances. This does in fact mean that the distribution no longer has a true Breit-Wigner shape since each mass value will be a sample of one from a Gaussian distribution whose width is a measure of the error on that mass value. However it seems that this effect can be taken account of to a first approximation by using a Breit-Wigner distribution of greater width.

So far the mass spectra for all decay modes of these two K*'s have been examined except for $K^{*o} \longrightarrow K^o o$ which occurs in the no-fit reaction 7). In a no-fit reaction there is no information available about the individual particles which make up the multi-neutral system Z^o. Thus the only effective masses which can be calculated are for groups of particles which contain either all or none of the missing neutrals. In the case of reaction 7) it is not possible to calculate the $(K^o o)$ mass since there is also a neutron missing.

7.2 Methods of fitting

The general problem in fitting is as follows. Given a function $f(\underline{x}_i, \underline{a})$ where $\underline{x}$ is a set of values of observables for an event i and $\underline{a}$ denotes a set of unknown parameters describing the theoretical function f, it is required to find the set $\hat{\underline{a}}$ which give the best agreement between $f(\underline{x}_i, \underline{a})$ and the experimental data for a sample of n events. The most general method for doing this is that of maximum likelihood. The combined probability of observing the n sets of data, assuming they are independent, is

$$P(\underline{x}) = \prod_{i}^{n} f(\underline{x}_i, \underline{a})\, d\underline{x}_i \qquad (7.8)$$

The likelihood of the parameter set $\underline{a}$ given the observed values $\underline{x}$ is defined by

$$\ell(\underline{a}, \underline{x}) = \prod_{i}^{n} f(\underline{x}_i, \underline{a}) \qquad (7.9)$$

where the factor $\prod_{i}^{n} d\underline{x}_i$ has been dropped since it is independent of $\underline{a}$ and will not therefore affect the maximisation of ℓ with respect to $\underline{a}$. It is often more convenient to maximise the logarithm of ℓ rather than ℓ itself. Since log x is a monotonically increasing function of x this will also not affect the estimate $\hat{\underline{a}}$. Also in practice standard computer programs exist which minimise functions of several parameters. Maximisation of a function is trivially equivalent to minimising its negative so that the function which is actually used is

$$-\log\ \ell(\underline{a}, \underline{x}) = -\,L(\underline{a}, \underline{x}) = -\sum_{i}^{n} \log f(\underline{x}_i, \underline{a}) \qquad (7.10)$$

(Note that now any function independent of $\underline{a}$ may be added to L without affecting the maximum likelihood estimate.) If $f(\underline{x}_i, \underline{a})$ is a simple enough function of the parameters $\underline{a}$ (it should have no more than a quadratic dependence on them), the maximum likelihood condition may sometimes be found by direct differentiation. This will not be so if the parameters have restricted ranges and the likelihood function has a stationary maximum outside the allowed range. In most cases direct calculation is not possible and an iterative procedure is necessary.

It may be shown that the maximum likelihood estimate $\hat{\underline{a}}$ has the following properties:

i) it is a sufficient estimator of $\underline{a}$ provided one exists, that is the method exhausts all possible information about $\underline{a}$ which can be found from the data $\underline{x}$.

ii) it is an efficient estimator if there is one, that is the estimate $\underline{a}$ is the most accurate one allowed by the Cramer-Rao inequality (55).

Further in the limit $N \longrightarrow \infty$

iii) it is always an efficient estimator;

and iv) near its maximum it approximates to a multi-Gaussian distribution in the parameters $\underline{a}$ so that confidence limits on a parameter can be found from its width with respect to that parameter.

The main disadvantages of the method are that only one maximum will be found even when the function may contain several comparable ones, that for small values of n it may not be unbiased or efficient and that there is no criterion for deciding on the "goodness" of the estimate. Also the maximisation may be rather slow.

Another commonly used method for fitting is that of least squares (this was mentioned in chapter 3 in the discussion of the kinematics program). The maximum likelihood method does reduce to the problem of least squares in the case of Gaussian variables but the latter method can be more economic because the data can be grouped into bins, though of course some information is lost when this is done.

The X^2 method also has the advantage of enabling confidence limits to be placed on the fit itself as well as on the individual parameter values since X^2 has a known probability distribution. It thus enables different hypotheses to be compared. In this connection it could be used in conjunction with the maximum likelihood method to compare solutions to different theoretical functions.

Most of the fits to the data of this experiment have used the maximum likelihood method.

7.3 $(K\pi\pi)$ systems

Because of the additional pion these are a little more complex than the $(K\pi)$ systems since one has the possibility of resonance production in two and/or three-body effective mass distributions. If a resonance is observed in a three-particle system it could decay into these three particles directly or it might decay first into two particles, one of which then undergoes a further decay into two particles. A single resonance may have decay modes of both these types.

Figure 7.4 shows the $(K\pi\pi)$ mass distributions for reactions 4), 5) and their sum. As in the $(K\pi)$ case two peaks are clearly seen but here their mass values are roughly 1300 and 1800 Mev. Their widths are about 150 and 100 Mev respectively but are more difficult to estimate by eye because the background under the peaks is larger than that in the $(K\pi)$ distributions. The shaded histograms contain the events for which the square of the four-momentum transfer from the

FIG. 7.4

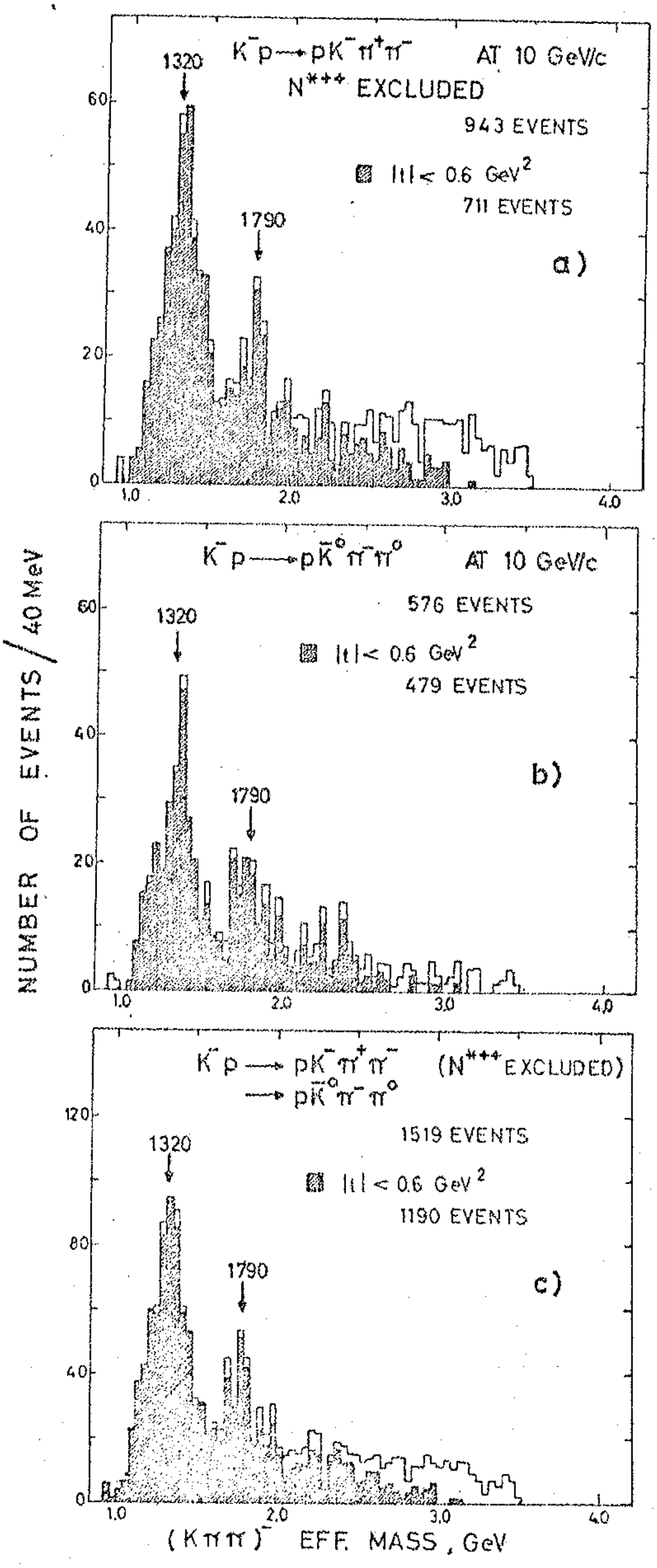
K⁻p → pK⁻π⁺π⁻ AT 10 GeV/c
N*⁺⁺ EXCLUDED
943 EVENTS
|t| < 0.6 GeV²
711 EVENTS
1320
1790
a)
K⁻p → pK̄°π⁻π° AT 10 GeV/c
576 EVENTS
|t| < 0.6 GeV²
479 EVENTS
1320
1790
b)
K⁻p → pK⁻π⁺π⁻ (N*⁺⁺ EXCLUDED)
→ pK̄°π⁻π°
1519 EVENTS
|t| < 0.6 GeV²
1190 EVENTS
1320
1790
c)
NUMBER OF EVENTS / 40 MeV
(Kππ)⁻ EFF. MASS, GeV

initial target proton to the final proton (or equivalently from the initial K^- beam particle to the final ($K\pi\pi$) system) is less than 0.6 $(Gev/c)^2$. Figure 7.5 shows the same plot for reaction 6) and a striking difference can immediately be seen for there are no sharp peaks in the distribution (the significance of the double peaked curve drawn above this histogram will be explained later). The small number of events in this reaction is not because it is analysed using only part of the data. In fact the fiducial volumes used for this reaction are exactly the same as for reaction 5) since both come from the 201 topology. Also both 5) and 6) contain a K^o so that the proportions of events lost due to unobserved decays will also be about the same in the two cases.

As in the $NK\pi$ reactions we choose to eliminate events in the region of any clear resonance involving the proton and one or more of the other three particles. The mass distribution of the (p+) system in reaction 4) shows a strong signal from $N^{*++}(1236)$ (see figure 7.6) There is also some evidence for resonances in the mass region 1.4 - 1.8 Gev of the (p+ -) mass spectrum in the same reaction but these will often be associated with events where M(p+) is in the $N^{*++}(1236)$ region and so will be automatically excluded once the latter is removed. Figure 7.7 shows the two dimensional plot of M(p+) against $M(K^- + -)$ for reaction 4). It can be seen that most of the N^{*++} events correspond to ($K\pi\pi$) masses which are above the region of the two observed peaks. (1.3 - 1.8 Gev). Finally there is no sign of any Y* resonances in any of the mass distributions (pK^-), (pK^-+) or (pK^--). Figure 7.8 shows the first of these and the positions of some of the known Y_o^*

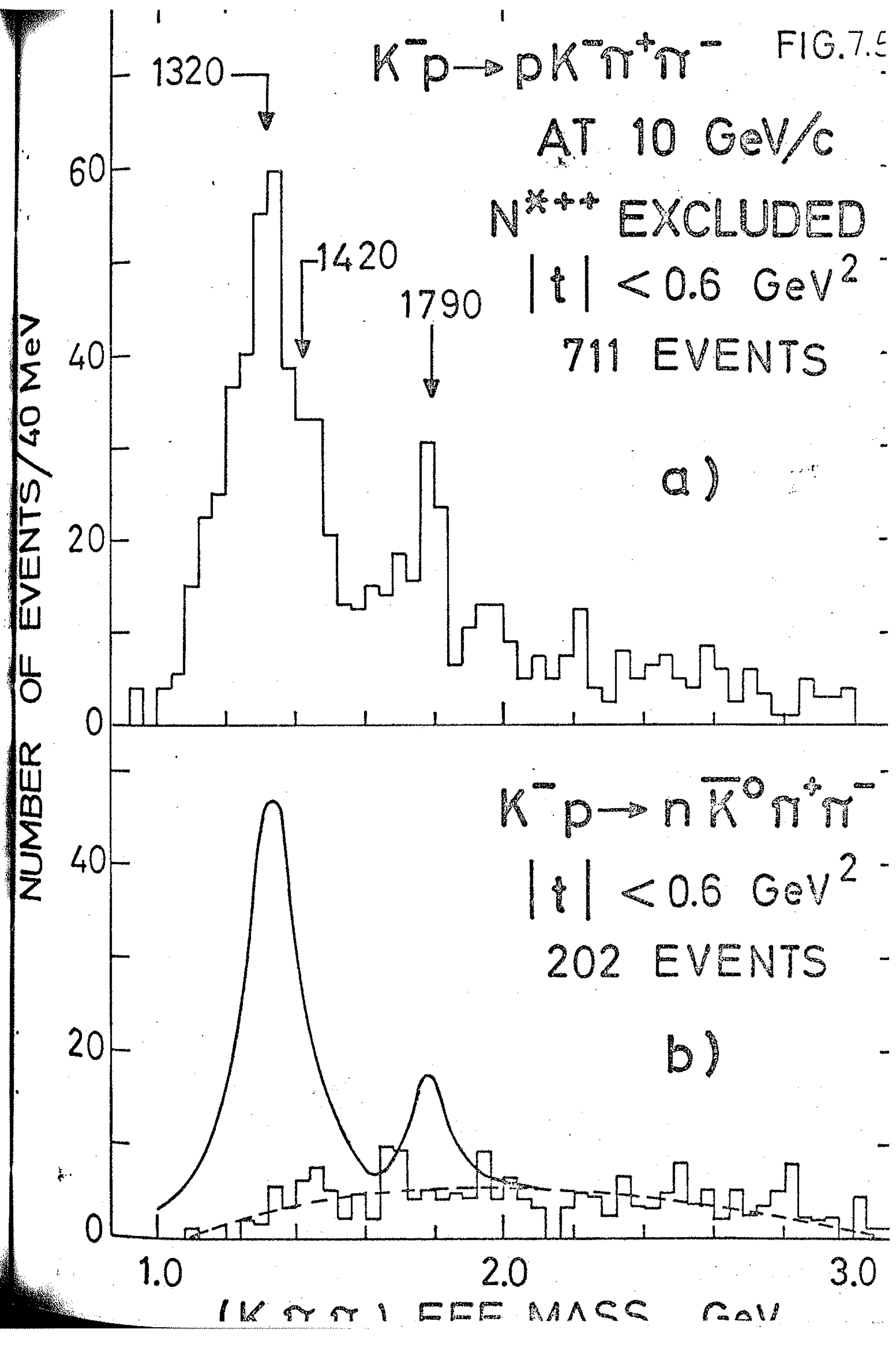
FIG.7.5
1320
1420
1790
K⁻p → pK⁻π⁺π⁻
AT 10 GeV/c
N*⁺⁺ EXCLUDED
|t| < 0.6 GeV²
711 EVENTS
a)
K⁻p → n K̄⁰π⁺π⁻
|t| < 0.6 GeV²
202 EVENTS
b)
NUMBER OF EVENTS/40 MeV
60
40
20
0
1.0
2.0
3.0
(K π π) EFF MASS GeV

FIG. 7.6

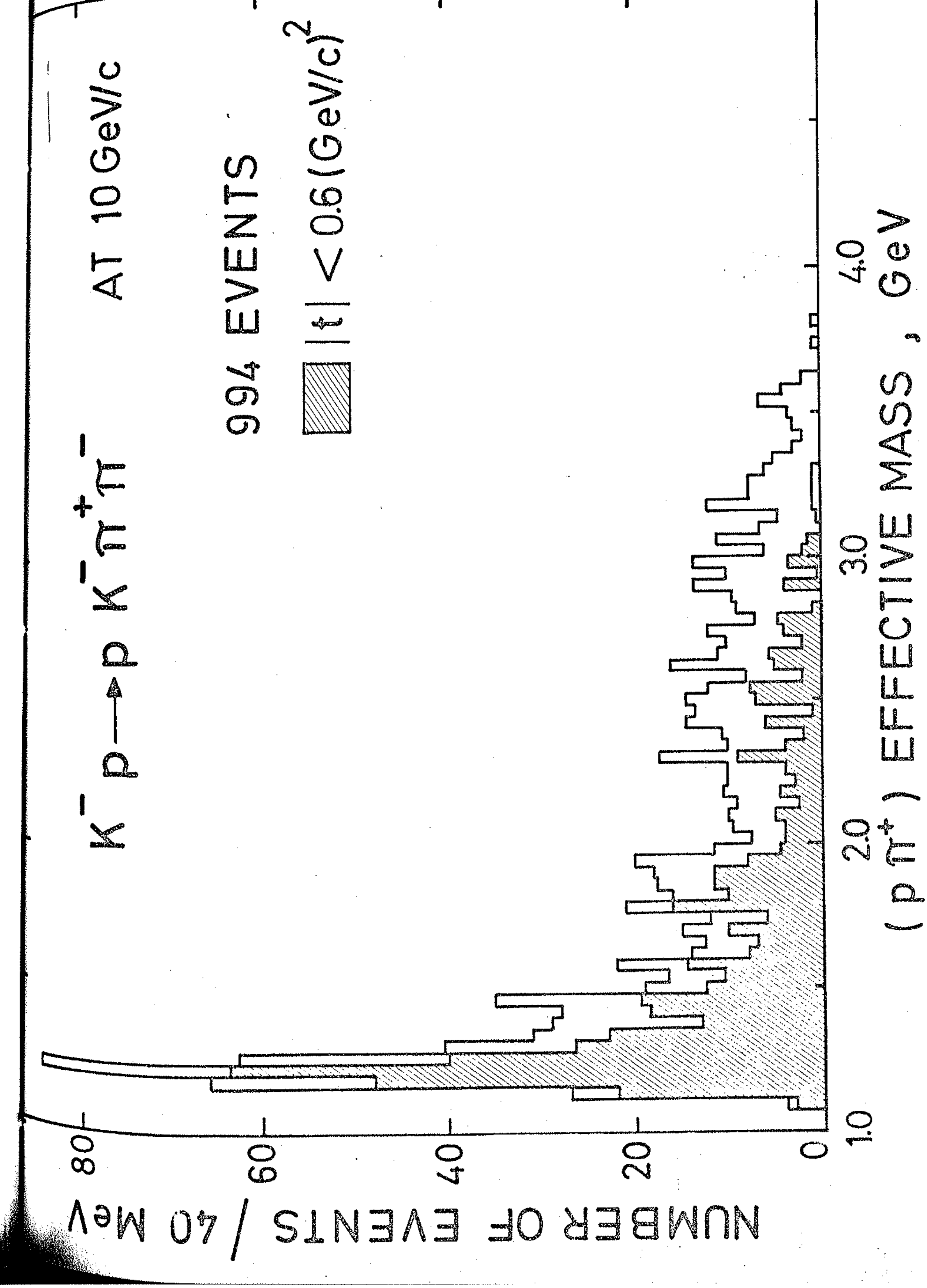
$K^- p \to p K^- \pi^+ \pi^-$ AT 10 GeV/c
994 EVENTS
$|t| < 0.6 (GeV/c)^2$
NUMBER OF EVENTS / 40 MeV
0
20
40
60
80
1.0
2.0
3.0
4.0
$(p\pi^+)$ EFFECTIVE MASS , GeV

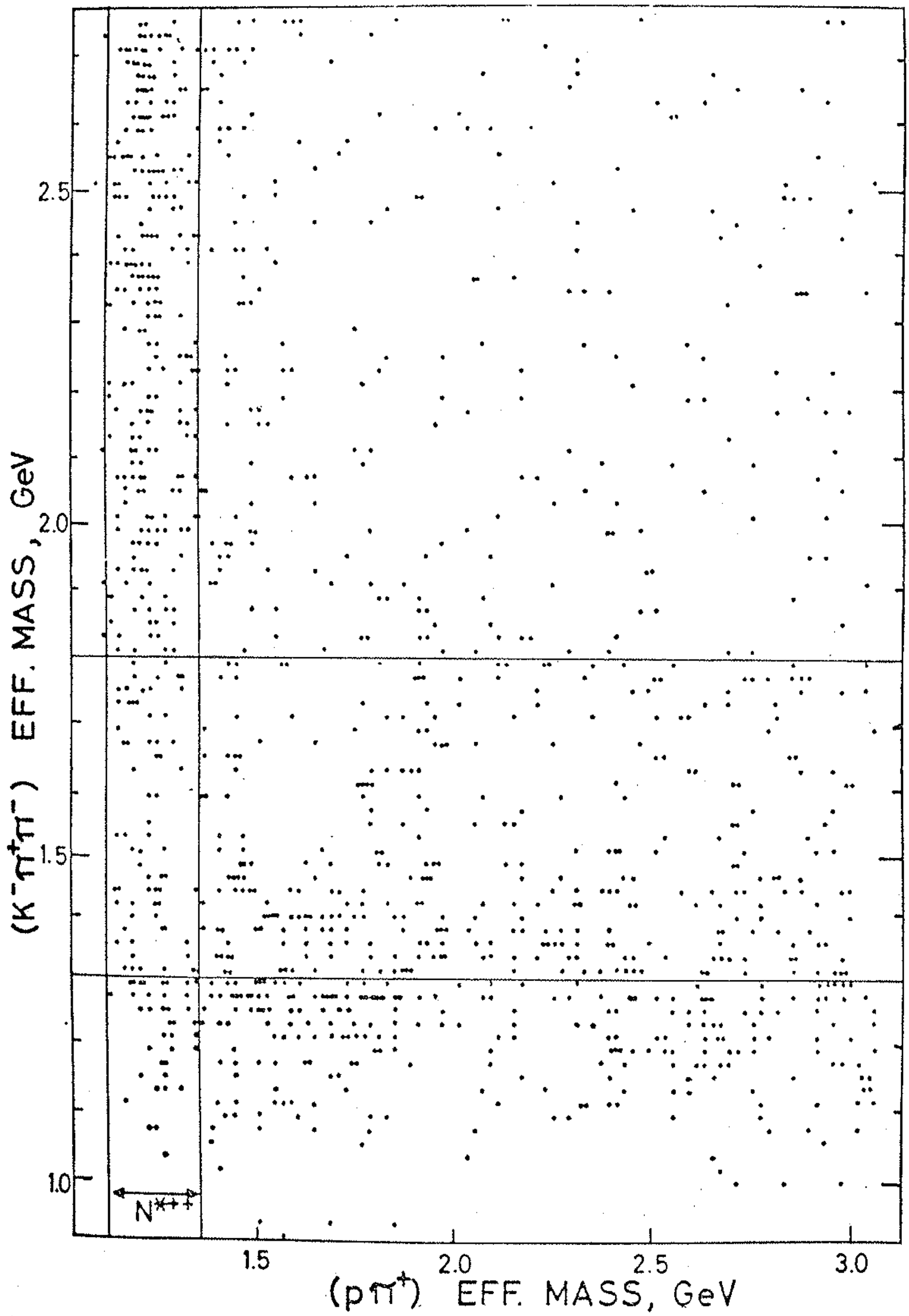

$(K^-\pi^+\pi^-)$ EFF. MASS, GeV
2.5
2.0
1.5
1.0
N^{*++}
1.5
2.0
2.5
3.0
$(p\pi^+)$ EFF. MASS, GeV

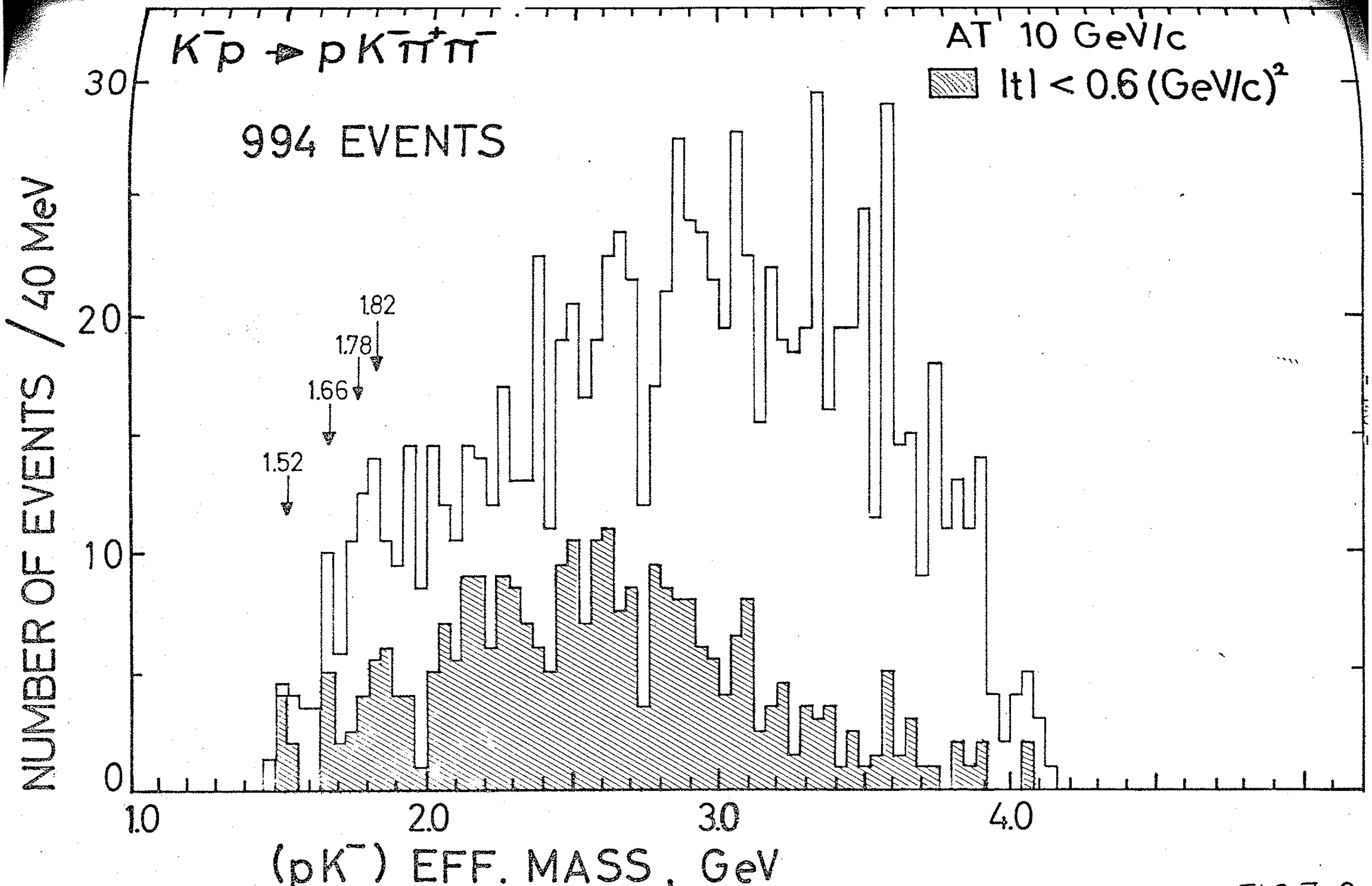
$K^-p \rightarrow pK^-\pi^+\pi^-$
994 EVENTS
AT 10 GeV/c
$|t| < 0.6\ (GeV/c)^2$
1.52
1.66
1.78
1.82
NUMBER OF EVENTS / 40 MeV
0
10
20
30
1.0
2.0
3.0
4.0
(pK^-) EFF. MASS, GeV

FIG 7.8

and Y_1^* resonances are indicated by the arrows. The shaded part is for events with momentum transfers (to the pK^- system) less than 0.6 $(Gev/c)^2$ which might be expected to enhance any resonant signal that was present. The next two figures (7.9 and 7.10) show the Chew-Low plots for reactions 4) and 5), that is plots of the $(K\pi\pi)$ mass against the momentum transfer to the $(K\pi\pi)$ system. (Actually the original Chew-Low plots used mass squared rather than mass (56).) These plots show that the peaks at 1.3 and 1.8 Gev are produced peripherally, that is with predominantly very small values for the momentum transfer t. (Since the value of t is always negative in the physical regions of all the processes studied, the symbol t will be used from now on to refer to the absolute value of the momentum transfer, unless stated otherwise.) The peaks do not seem to be produced any more peripherally than the background as can be seen from the mass regions below 1.3 Gev and between 1.5 and 1.6 Gev. There is however a general tendency for the peripherality to decrease as the $(K\pi\pi)$ mass increases. The effect of selecting events with t less than 0.6 $(Gev/c)^2$ can be seen to remove very few events from the peak regions. These cuts do however remove quite a substantial number of events from the $(K\pi\pi)$ mass region above 2 Gev and so help to reduce the overall peak/background ratio.

The lower of the two peaks will be referred to as $K^*(1320)$ although it is unlikely to be due to a single resonance. A peak in this mass region was first reported by Almeida et al. in 1965 (57).

FIG. 7.9

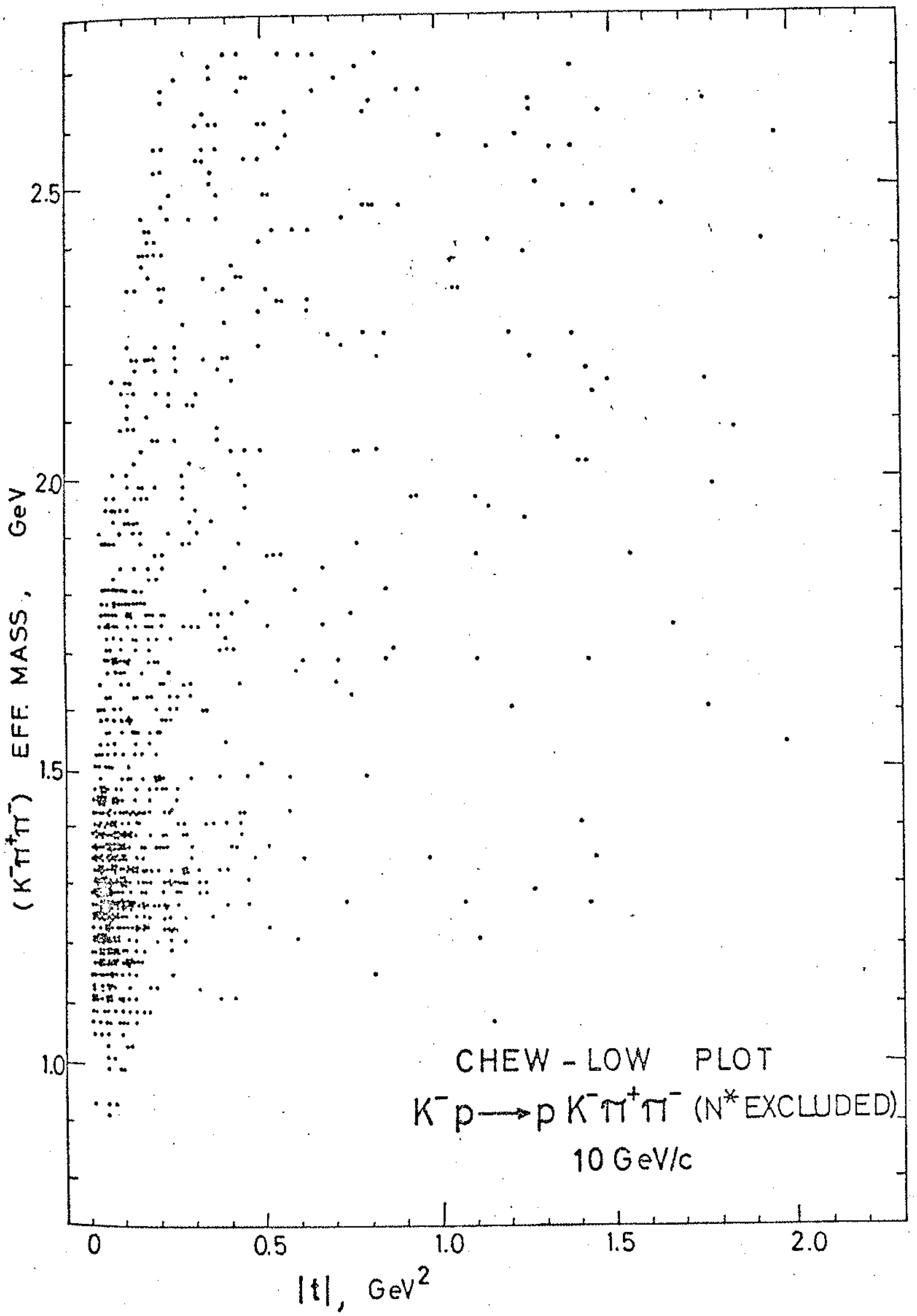

DM 30905

FIG. 7.10

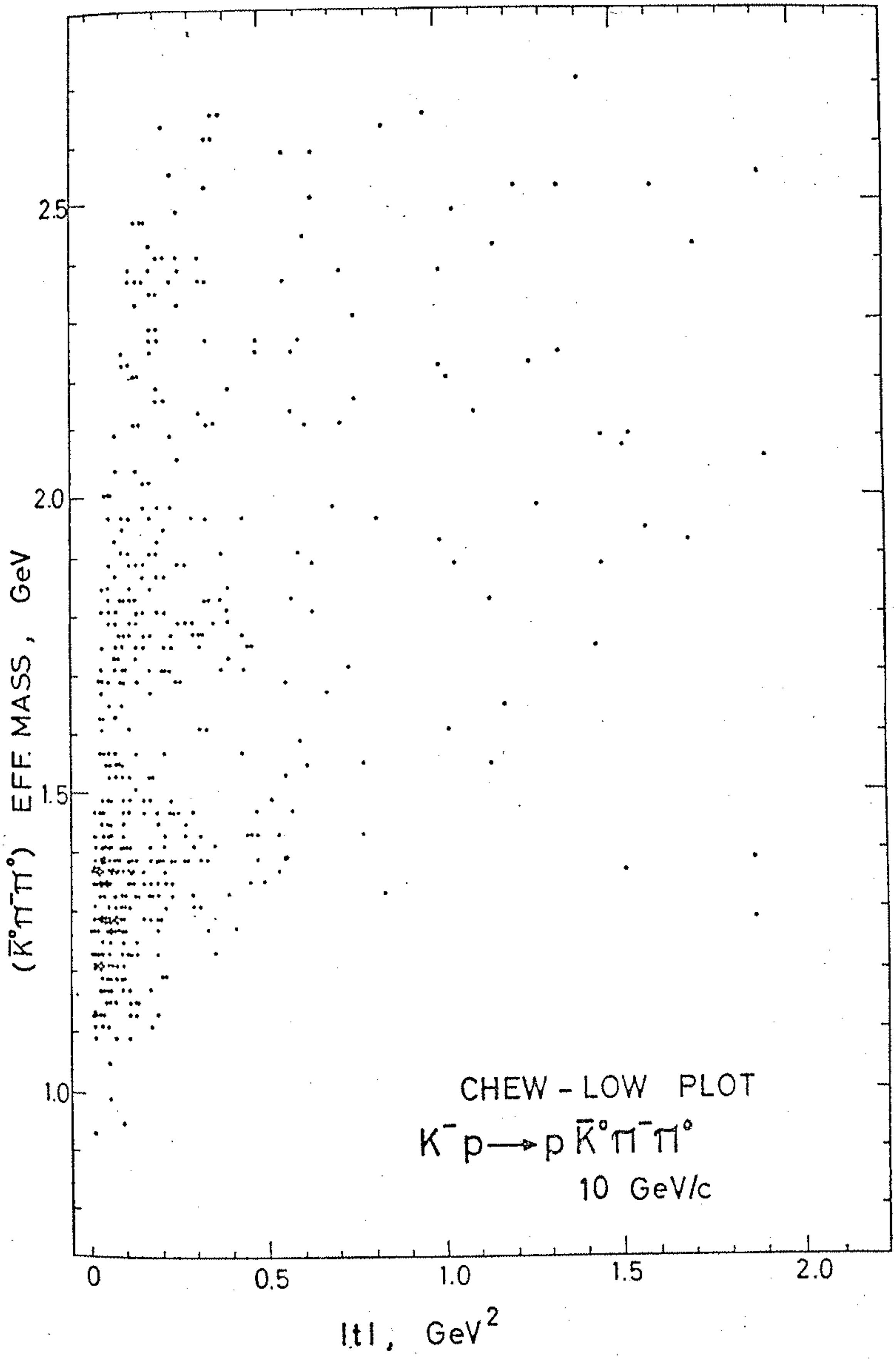

DR 30805

Since then many experiments have found peaks at different mass values in the range 1.2 - 1.4 Gev and there may well be two or more resonances in this region. However it should be noted that some experiments have been explained without the need for any resonance (e.g. (58)).

The higher of the two peaks was observed for the first time in the present experiment and was called the L-meson (9). This was perhaps an unwise choice as this name had previously been used generically for all the lighter particles like the pion and the muon (59) and, more importantly, the symbol L has now been reserved for meson resonances with I = 3/2, should any ever be discovered (2). (The resonance observed here will be shown to have I = 1/2 - see chapter 8). Since the first report of the L-meson, peaks in the same mass region have been seen in several other experiments; the available data is consistent with there being no more than one resonance in the peak. In the last year a very high statistics experiment analysed by one of the Berkeley groups has given a non-resonant interpretation for the L(60). However their peak is a lot broader and flatter than the ones in figure 7.3 which certainly helps in such an interpretation. The latest data from the 10 Gev/c K^- experiment has about 6000 events in reaction 4) and about 1650 in reaction 5), that is increases of factors of about $4\frac{1}{2}$ and 3 respectively over that shown in figure 7.3. The L-peak seems just about as sharp as before.

Both the K*(1320) and the L are produced in reactions of the general form (7.6) but, unlike the K*(890) and K*(1420) they do not appear to be produced at all in reactions like (7.7). The combined distribution from reactions 5) and 6) is fitted to a sum of two Breit-Wigner distributions and a smooth hand-drawn background. The general shape of this background is suggested by Deck-type calculations (61) (see later). Since the K*(1320) peak is probably not due to a single resonance the fit to a Breit-Wigner is not very meaningful. However it does at least provide a parametrisation of the data. The results of the fit are shown in table 7.1 and the fitted distribution is shown in figure 7.11. The shaded events in this distribution correspond to the small dotted curve sitting on the horizontal axis of the plot at about 1400 Mev. This curve represents the contribution from the known $K\pi\pi$ decay modes of the K*(1420) (mainly K*(890) but some $K\rho$). This contribution is calculated from the $K^*(1420) \rightarrow K\pi$ decay observed in reactions 1) and 2) assuming equal branching ratios into $K\pi$ and $K\pi\pi$ (the most recent compilation gives values in the ratio 1.11 ± 0.19 (2) . Only 32 events are removed by this correction. The K*(1420) signal is relatively small in reactions 4) and 5) compared with reactions 1) and 2) since the total cross sections for 4) and 5) are substantially higher, but in some experiments a separate peak due to the K*(1420) has been resolved in the $(K\pi\pi)$ mass distribution. Since the K*(1420) is also produced with a neutron in reaction 3) there should also be a signal from its $(K\pi\pi)$ decay mode in reaction 6). In figure 7.5 the small peak near 1400 Mev is consistent with the signal expected from the K*(1420) as shown by the small dotted curve.

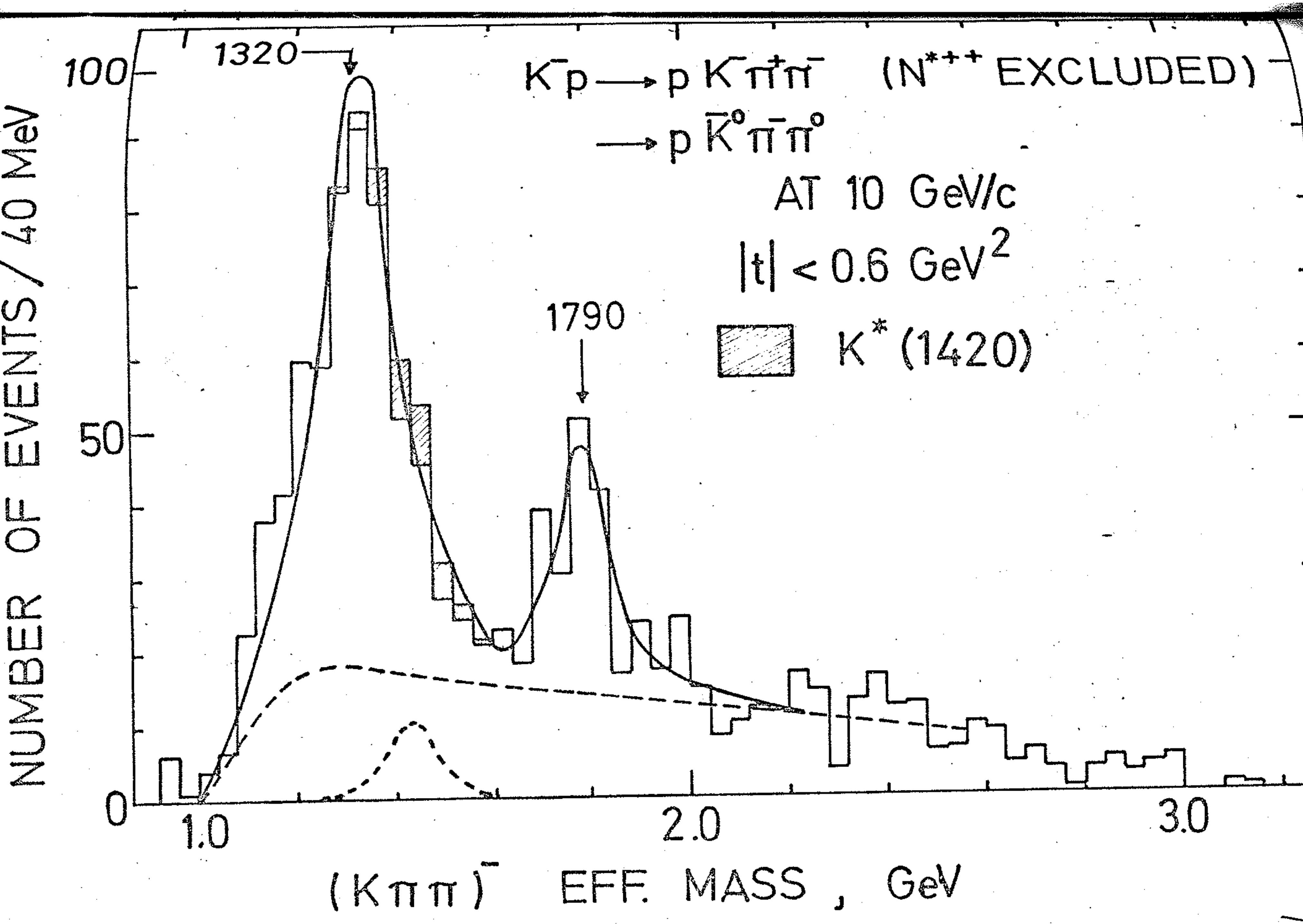

1320
1790
$K^-p \longrightarrow pK^-\pi^+\pi^-$ (N^{*++} EXCLUDED)
$\longrightarrow p\bar{K}^0\pi^-\pi^0$
AT 10 GeV/c
$|t| < 0.6$ GeV^2
$K^*(1420)$
NUMBER OF EVENTS / 40 MeV
0
50
100
1.0
2.0
3.0
$(K\pi\pi)^-$ EFF. MASS , GeV

FIG. 7.11

One might expect the two resonances (if that is what they are) observed in reactions 4) and 5) to be seen also in the ($K\pi\pi$) mass spectra for reactions 8) and 12). Reaction 8) contains a different decay mode (K^-oo) but 12) simply corresponds to events of reaction 5) where the K^o has not been seen to decay. Assuming that the Z^o in these reactions represents ($\pi^o\pi^o$) in 8) and ($K^o\pi^o$) in 12) the effective masses of the ($K\pi\pi$) systems can be calculated. These no-fit reactions will certainly contain some contributions from final states where Z^o includes additional neutral pions so there is likely to be a larger background in these distributions than in those for the fitted channels. Figure 7.12 shows the distribution for the sum of reactions 8) and 12). A clear peak is seen in the 1300 Mev region and there is some indication of a peak near 1800 Mev. The background under these peaks is relatively large as expected.

As mentioned earlier in connection with the no-fit reaction 7) it is not possible to calculate the ($K\pi\pi$) effective masses in no-fit channels which also have a missing neutron since the contributions of this neutron and the missing mesons to Z^o cannot be separated. This applies also to reactions 9) and 10). However since we see no important structure in the (K^o + -) mass distribution of reaction 6) it is unlikely that the corresponding distributions for reactions 9) and 10) would be any more interesting.

In order to see whether the K*(1320) and L(1800) decay directly into three particles ($K\pi\pi$) or via intermediate two-body states one can replot the distributions including only events where the mass of

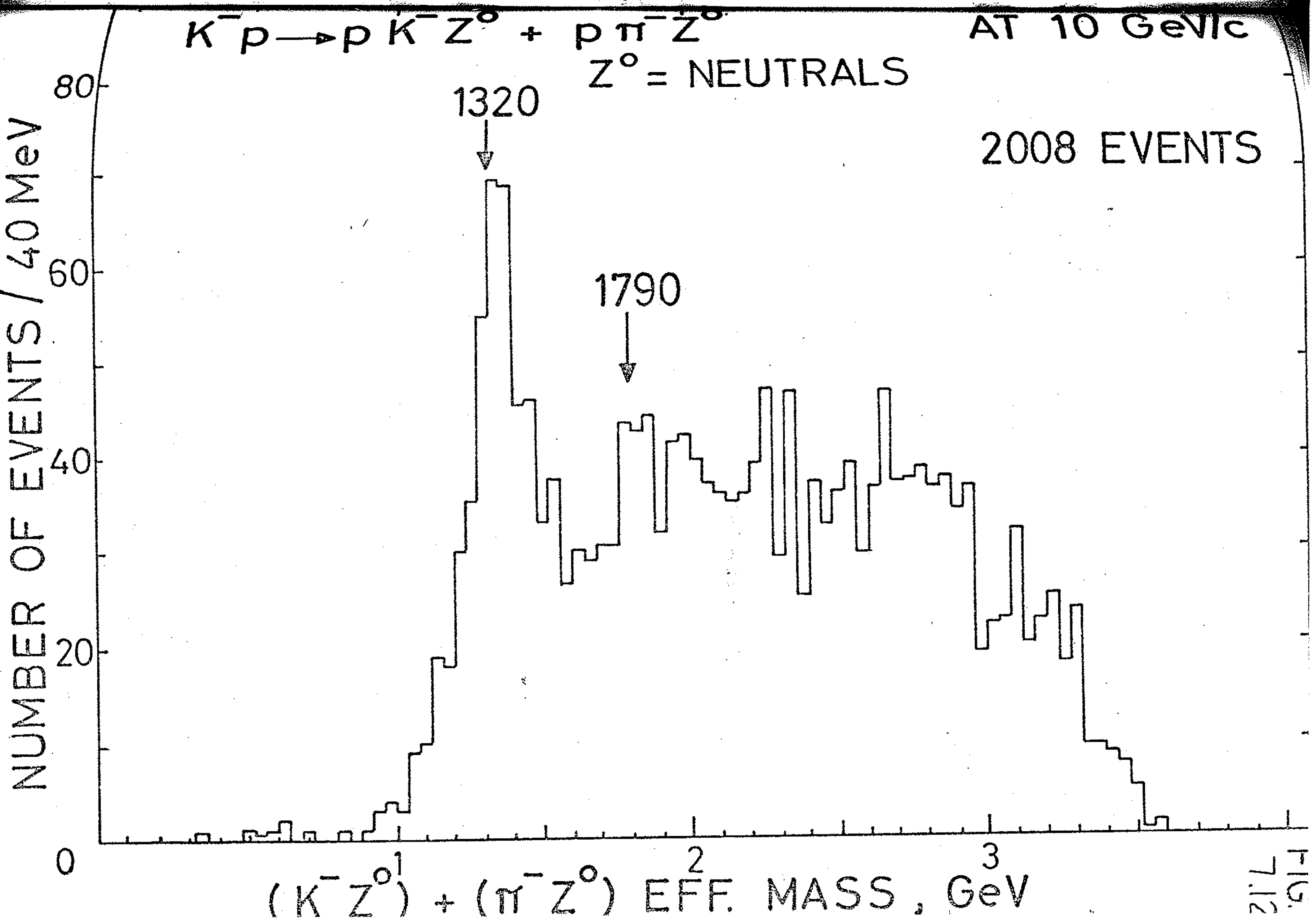
K⁻p → p K⁻ Z° + p π⁻ Z°
Z° = NEUTRALS
AT 10 GeV/c
2008 EVENTS
1320
1790
NUMBER OF EVENTS / 40 MeV
0
20
40
60
80
1
2
3
(K⁻ Z°) + (π⁻ Z°) EFF. MASS , GeV
FIG. 7.12

pair of particles in the $(K\pi\pi)$ system lies in the region of an observed two-body resonance. The most likely candidates for these two-body resonances are K*(890) and K*(1420), both of which are present in the $(K\pi)$ mass distributions for reactions 4) and 5) (see figures 7.13 - 7.15) and $\rho(760)$ which is a $\pi\pi$ resonance and is also produced in 4) and 5) (figures 7.16 and 7.17). It should be noted that reaction 5) contains contributions from both K^{*-} and K^{*0} (890 and 1420). Figure 7.18 shows plots of the $(K\pi\pi)$ mass distributions for samples of reactions 4) and 5) with the requirement that K*(890) or $\rho(760)$ are present. The mass regions used for making these selections are shown in Table 7.2. An inspection of these plots suggests that the K*(1320) is observed in $K\rho$ and $K^*(890)\pi$ decay modes in both reactions. The signals from the L are much weaker especially in the $K^*\pi$ modes of reaction 5). However it must be emphasised that the selection of two-body resonances using mass bands includes some non-resonant background and excludes resonance events in the tails of the Breit-Wigner distributions. More precise results on the observed decay modes will be obtained by a quantitative analysis of the K*(1320) and L(1800) mass regions (see chapter 8).

7.4 Mass resolution

As mentioned in section 7.2 the fitted widths of the K*(890) and K*(1420) resonances are larger than the accepted values for the natural widths of these states due to the broadening introduced by

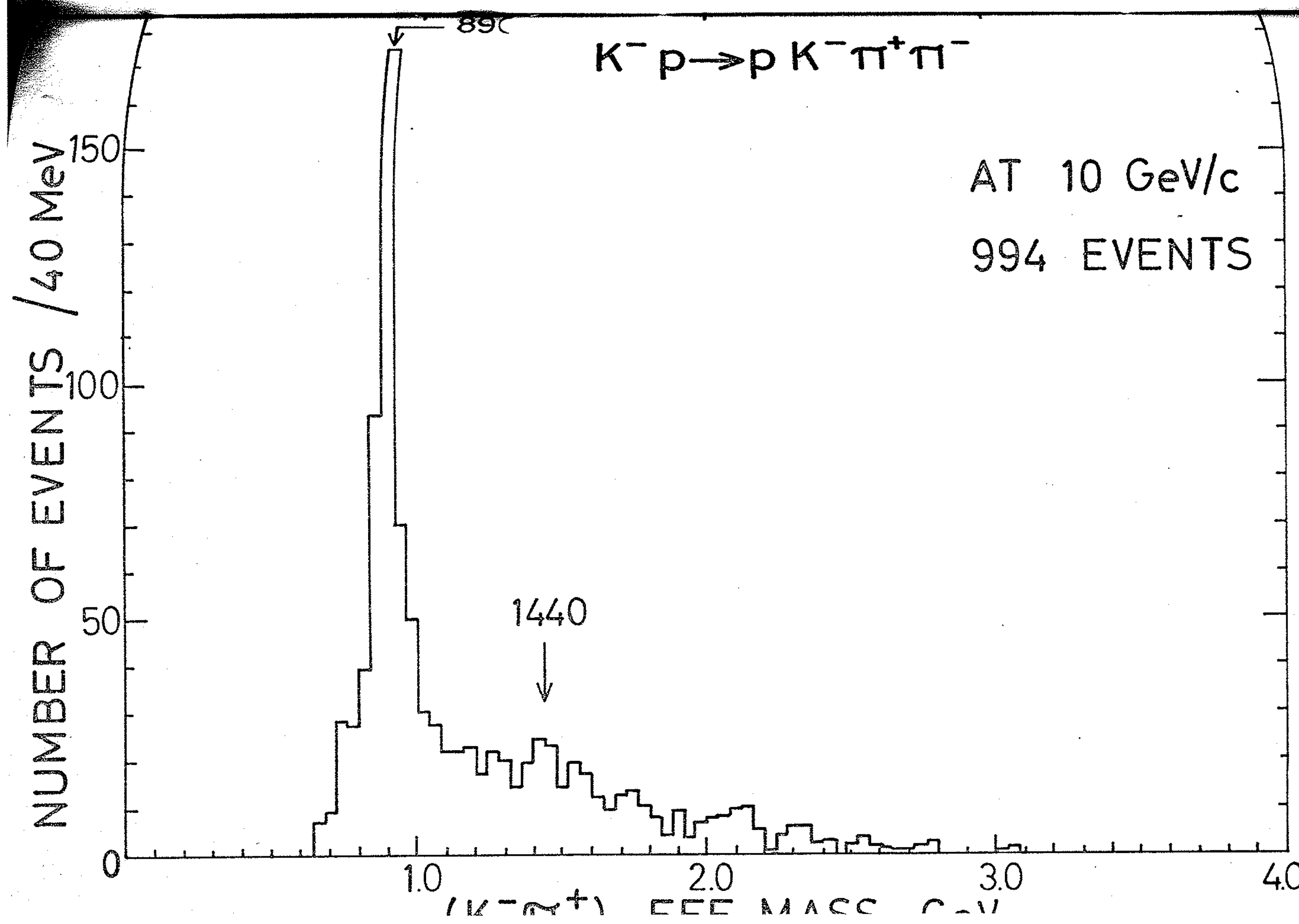

$K^- p \rightarrow p K^- \pi^+ \pi^-$
AT 10 GeV/c
994 EVENTS
890
1440
NUMBER OF EVENTS /40 MeV
0
50
100
150
1.0
2.0
3.0
4.0

FIG. 7.13

FIG. 7.14

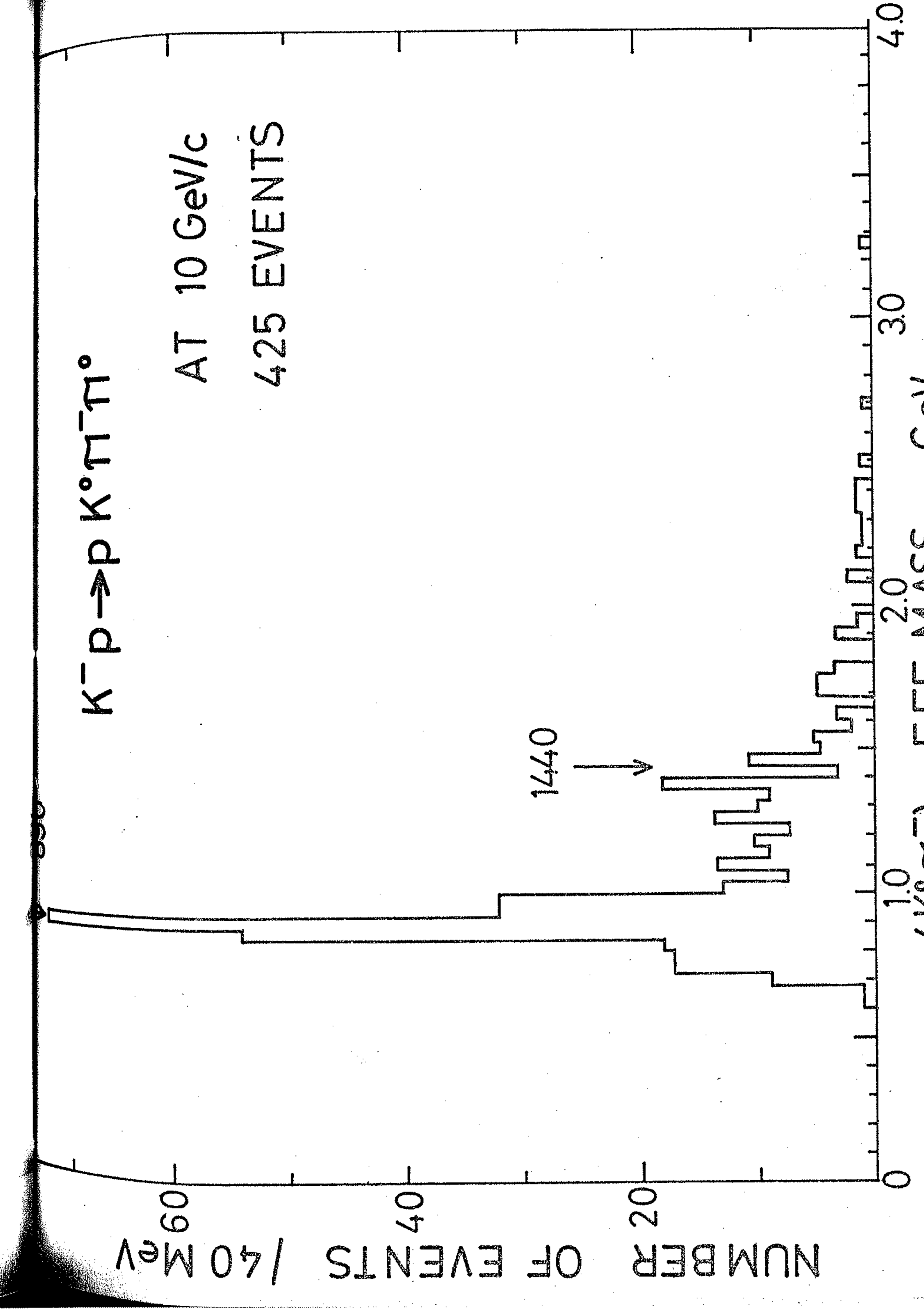
$K^- p \rightarrow p K^\circ \pi^- \pi^\circ$
AT 10 GeV/c
425 EVENTS
1440
NUMBER OF EVENTS /40 MeV
0
1.0
2.0
3.0
4.0
20
40
60

FIG. 7.15

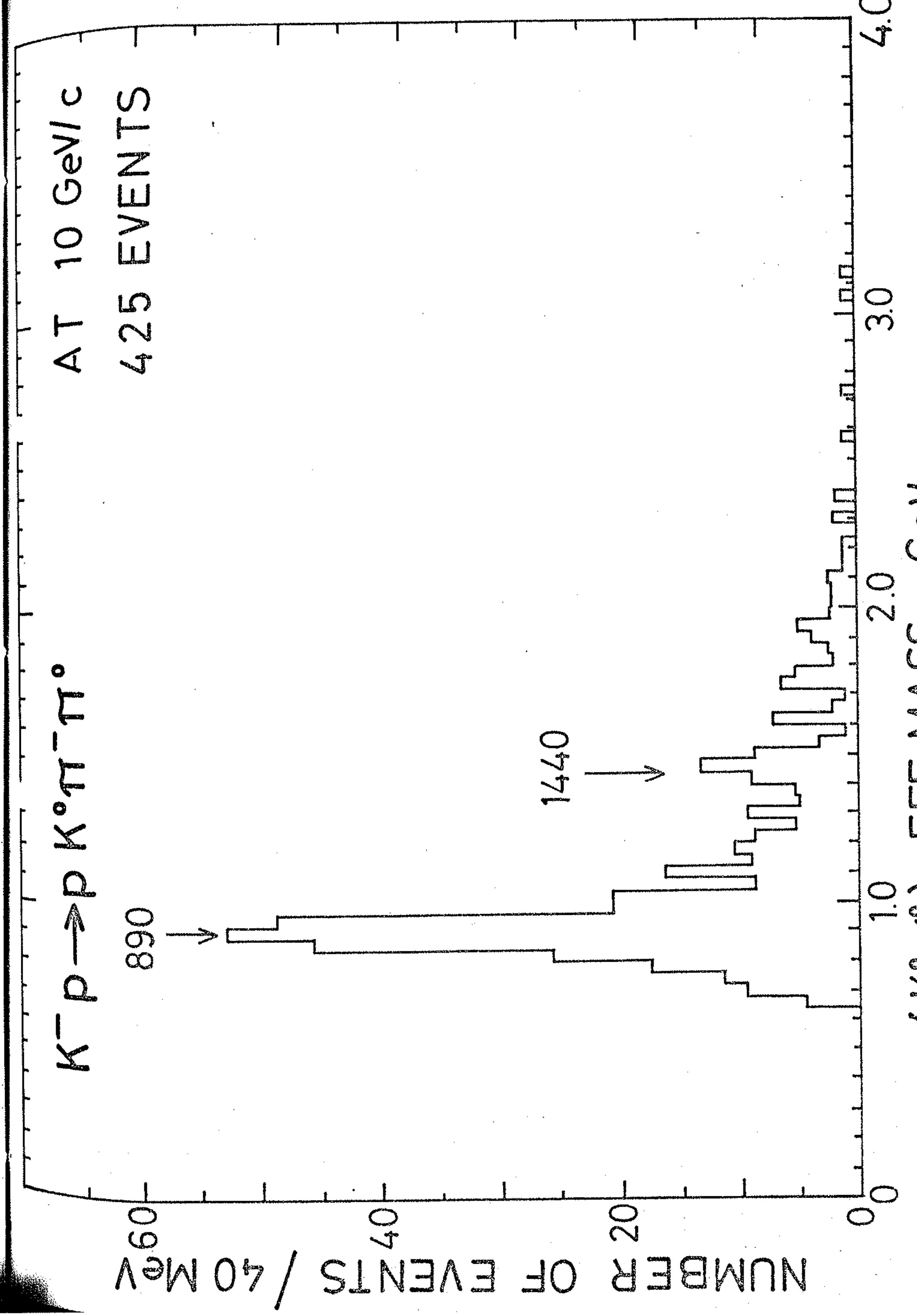
K⁻p → pK°π⁻π°
AT 10 GeV/c
425 EVENTS
890
1440
NUMBER OF EVENTS / 40 MeV
0
20
40
60
0
1.0
2.0
3.0
4.0
EFF MASS
GeV

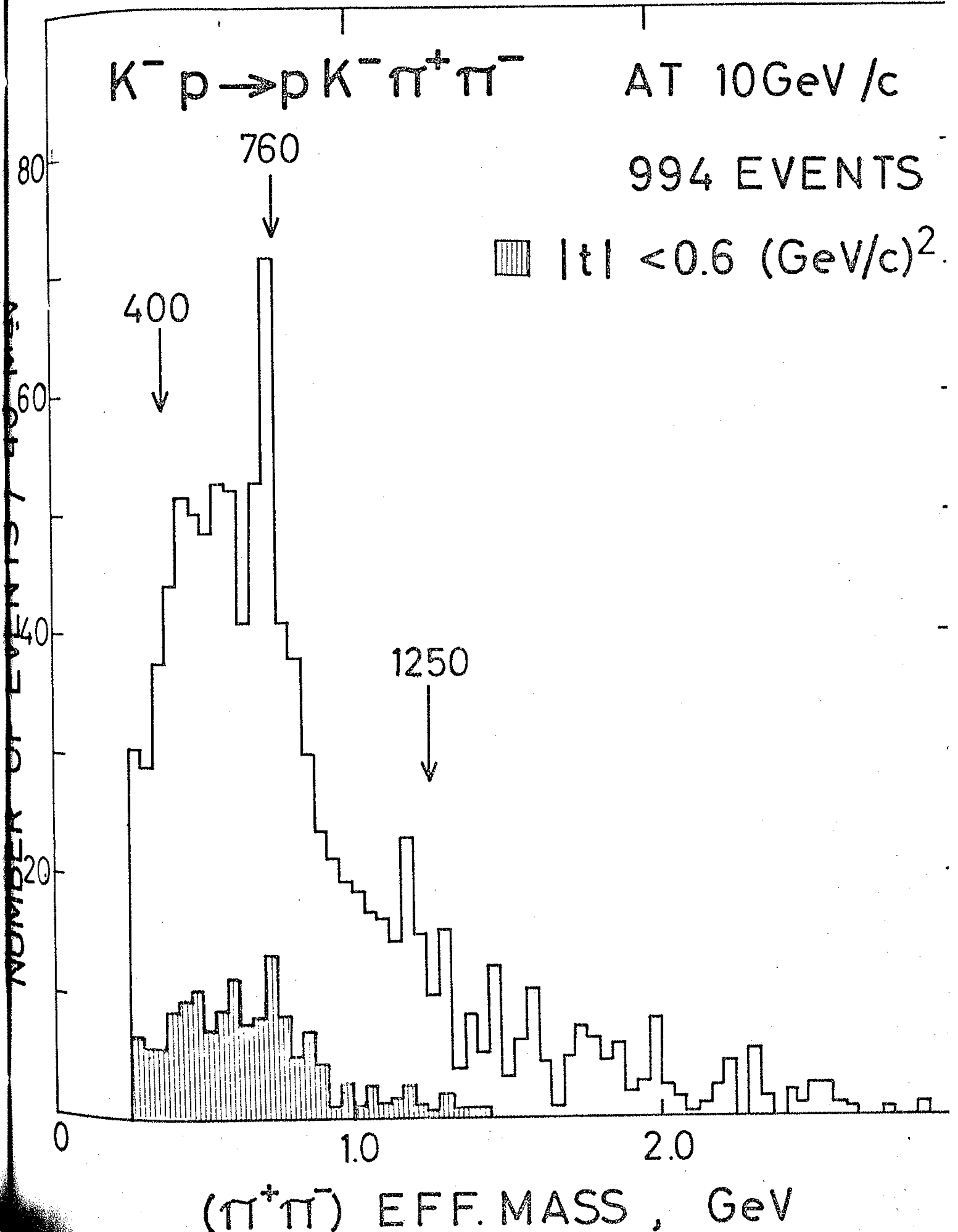
K⁻p → pK⁻π⁺π⁻ AT 10GeV/c
994 EVENTS
|t| <0.6 (GeV/c)²
760
400
1250
NUMBER OF EVENTS / 40 MeV
80
60
40
20
0
1.0
2.0
(π⁺π⁻) EFF. MASS, GeV

FIG. 7.17

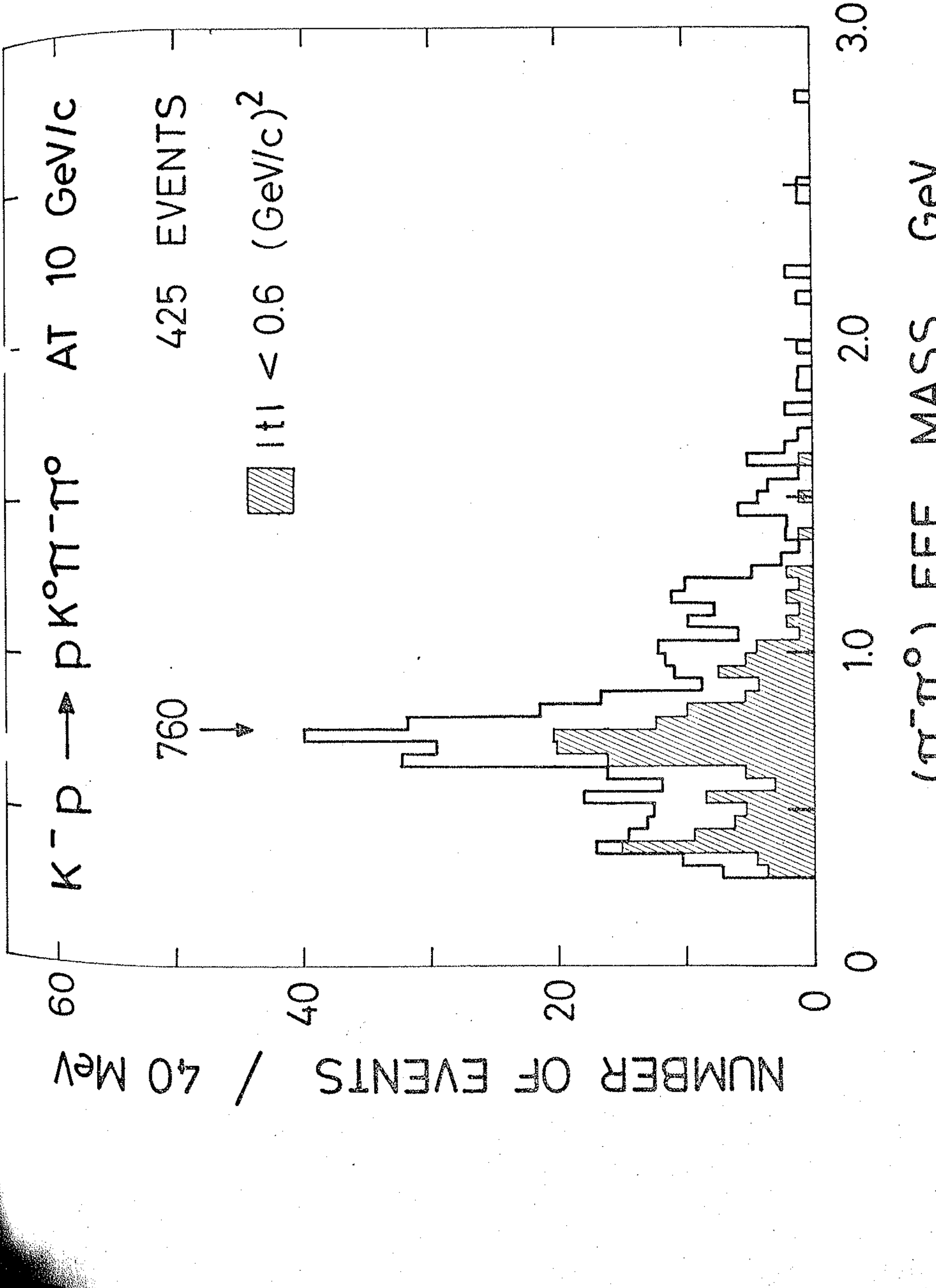
K⁻p → pK°π⁻π° AT 10 GeV/c
425 EVENTS
|t| < 0.6 (GeV/c)²
760
0
1.0
2.0
3.0
(π⁻π°) EFF. MASS , GeV
0
20
40
60
NUMBER OF EVENTS / 40 MeV

FIG. 7.18

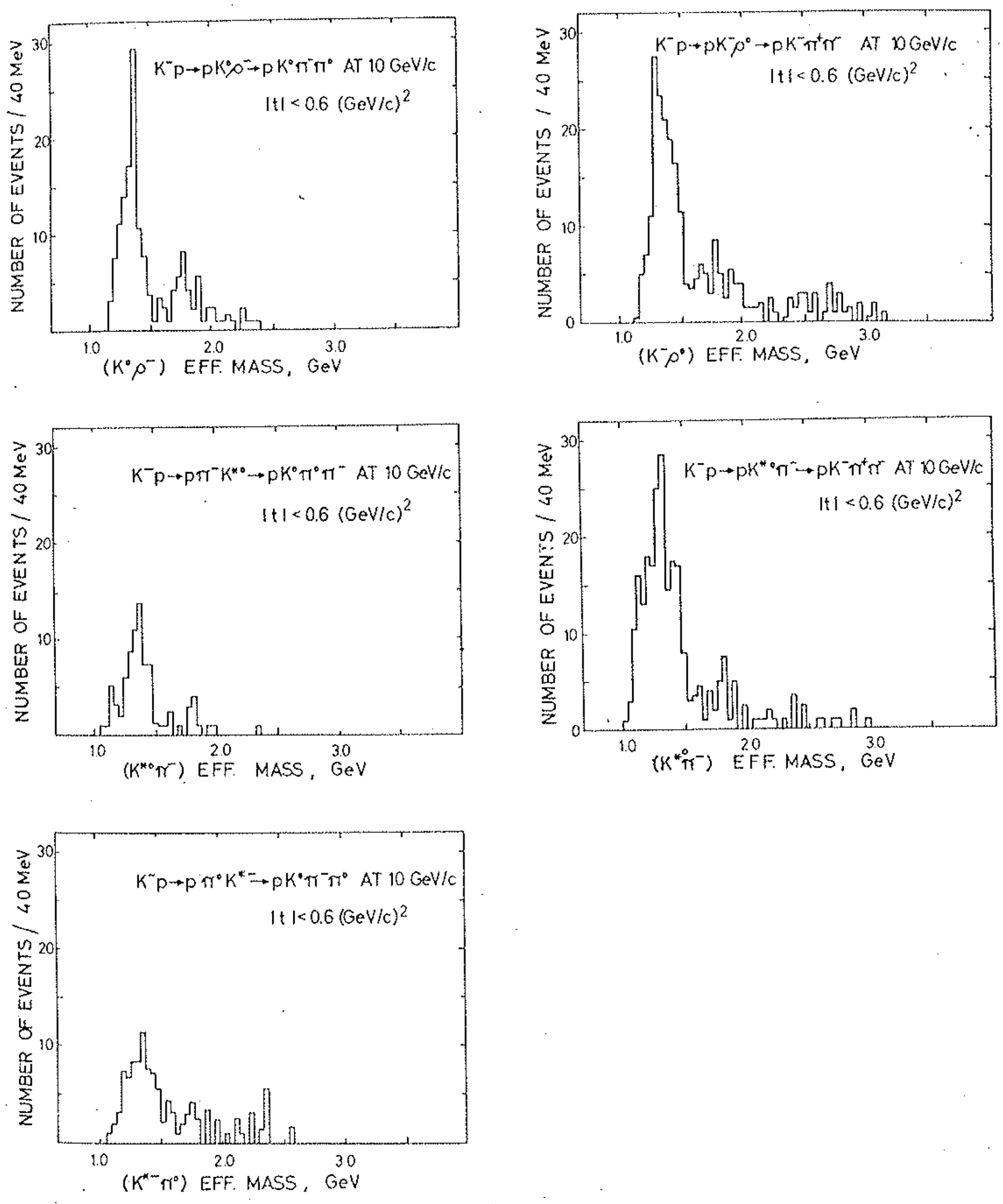

NUMBER OF EVENTS / 40 MeV
K⁻p→pK°ρ⁻→pK°π⁻π° AT 10 GeV/c
|t| < 0.6 (GeV/c)²
(K°ρ⁻) EFF. MASS, GeV
K⁻p→pK⁻ρ°→pK⁻π⁺π⁻ AT 10 GeV/c
|t| < 0.6 (GeV/c)²
(K⁻ρ°) EFF. MASS, GeV
K⁻p→pπ⁻K*°→pK°π°π⁻ AT 10 GeV/c
|t| < 0.6 (GeV/c)²
(K*°π⁻) EFF. MASS, GeV
K⁻p→pK*°π⁻→pK⁻π⁺π⁻ AT 10 GeV/c
|t| < 0.6 (GeV/c)²
(K*°π⁻) EFF. MASS, GeV
K⁻p→pπ°K*⁻→pK°π⁻π° AT 10 GeV/c
|t| < 0.6 (GeV/c)²
(K*⁻π°) EFF. MASS, GeV

TABLE 7.2

MASS LIMITS USED FOR SELECTING OR REMOVING WELL-KNOWN RESONANCES

Resonance	Mass range (Gev)
$N^{*++}(1236)$	1.12 - 1.34
$K^*(890)$	0.82 - 0.96
$K^*(1420)$	1.3 - 1.5
ρ^o	0.62 - 0.88
f^o	1.15 - 1.35
η^o	0.5 - 0.6
ω^o	0.75 - 0.81

TABLE 7.3*

MASS LIMITS USED FOR STUDYING PARTICULAR RESONANCES

$K^*(890)$	0.82 - 0.96	
$K^*(1420)$	1.3 - 1.5	
$K^*(1320)$	1.00 - 1.55	wide limits (used for Dalitz plot analysis)
L(1800)	1.6 - 2.2	

* The resonance to background ratios for these samples have not been calculated, contrary to the statement made in the text.

the experimental errors. In order to estimate the real widths of any newly discovered resonances it is obviously important to know the sizes of these experimental uncertainties and what effect they will have on the observed width of a resonance.

The most direct way of finding the error on an effective mass value is to calculate it by error propagation from the known errors on the track parameters, assuming that these have been correctly estimated. The expression for a two-body effective mass M_{12} is

$$M_{12}^2 = (E_1+E_2)^2 - (\underline{p}_1+\underline{p}_2)^2 = m_1^2+m_2^2 + 2E_1E_2 - 2p_1p_2 \cos\theta 12 \quad (7.11)$$

This gives

$$M_{12}^2 dM_{12}^2 = (E_2\beta_1 - p_2\cos\theta_{12})^2 \, dp_1^2 + (E_1\beta_2 - p_1 \cos\theta_{12})^2 \, dp_2^2$$
$$+ p_1^2 p_2^2 \sin^2\theta_{12} \, d\theta_{12}^2 \quad (7.12)$$

where θ_{12} is the angle between the particles 1 and 2. The mass resolution for 4-prong 4-C fits was calculated to be about 10 Mev, and for 4-prong 1-C fits about 17 Mev (at a mass of about 1.4 Gev).

A more empirical approach is to select a reaction in which a particle is produced which has a width which is negligible (or at least small) compared with the mass resolution. The observed peak should then approximate to a Gaussian whose width is the mass resolution. This method suffers from the drawback that the resolution itself is a function of the mass and also depends on whether the particles concerned in the mass combination are all observed or whether one is a fitted particle. Thus the use of a known narrow peak to determine the resolution gives a result which is only really applicable to a mass combination with the same approximate Q-value (assuming it to have come from the decay of a resonance) and with the same number of constraints in the fit. Figure 7.19 shows the production of the ω^o meson in the (+ -o) effective mass distribution of the reaction.

$$K^- p \longrightarrow pK^- + - o \tag{7.13}$$

The ω^o has a natural width of only 12.7 Mev which is not quite negligible compared to the experimental resolution but is the smallest of all strong interaction decay widths. The resolution derived from the observed width of the ω^o peak in this reaction is consistent with that obtained by direct calculation. In 4-C fits the narrowest resonance produced is the K*(890) which has a natural width of 50 Mev. From the observed width of 58 $\pm$ 7 Mev for this resonance in reactions 2b) and 3) combined one might expect a resolution of about 30 Mev in two-prong events if the approximation quoted by Ficenec et al. (62) is correct

$$\Gamma_{obs}^2 = \Gamma_o^2 + (dM)^2 \tag{7.14}$$

where Γ_{obs} is the observed width and Γ_o is the natural width.

For (+ -) mass distributions an estimate of the resolution could be obtained by taking the two pion tracks from observed K^o decays, adding them to the tracks at the primary vertex and refitting to the new hypothesis which will now be strangeness non-conserving. The width of the (+ -) effective mass distribution for the tracks which were taken from the K^o decay will give a measure of the resolution to be expected in such a distribution. A similar method can be used for $(p\pi)$ mass distribution by treating Λ^o decays in an analogous way.

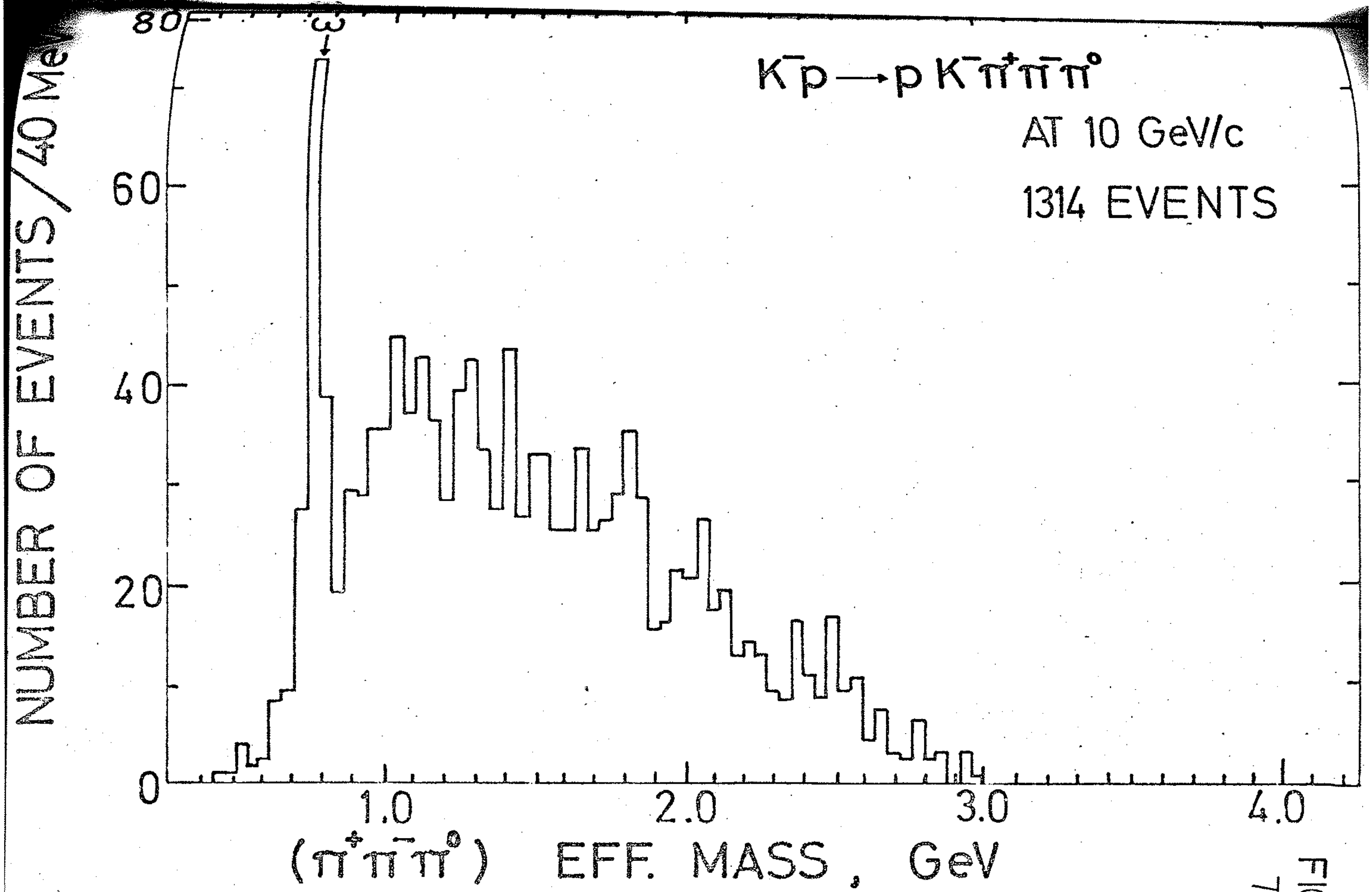
$K^-p \rightarrow pK^-\pi^+\pi^-\pi^0$
AT 10 GeV/c
1314 EVENTS
ω
NUMBER OF EVENTS / 40 MeV
0
20
40
60
80
1.0
2.0
3.0
4.0
$(\pi^+\pi^-\pi^0)$ EFF. MASS , GeV

FIG. 7.1.

To improve the mass resolution in a given plot it is permissible to use only particularly well-measured events. For events of reaction 4) where the proton stops in the chamber and so has its momentum determined accurately the $(K\pi\pi)$ mass, which is just the missing mass to the proton in the reaction, is reduced to about 8 Mev. However such a selection may bias the sample towards certain types of process.

7.5 Possibility of other resonances

In view of the large number of non-strange meson resonances reported in various bubble chamber experiments and in the Cern Missing Mass and Boson spectrometer experiments, and because of the success so far of SU(3) in classifying particle states into multiplets containing both strange and non-strange members, it would not be surprising to find ~~many~~ more $Y = -1$ kaonic resonances in the $(K\pi)$ or $(K\pi\pi)$ systems.

An examination of the plots shown in this chapter shows a few peaks which may become significant when more data is available.

i) in reaction 1) (figure 7.1) there is quite a large peak just below the K*(890). This is almost certainly due to a bias in the assignment of these events but the exact explanation is not known at present. It is unlikely to be a $(K\pi)$ resonant state because it is not seen in the four-constraint reaction 2b).

ii) in figure 7.3 there is a slight hump between the K*(890) and K*(1420) peaks centred at about 1140 Mev. A very similar peak was reported by Crennell et al. in a K^-n experiment at 3.9 Gev/c (63).

Provided the total number of events in the sample is large the number n which fall into a certain bin of a histogram will be approximately Poisson distributed, that is its variance will be equal to n. If n^1 is the number of events expected in that bin for the null hypothesis, the variate $(n^1 - n) / \sqrt{n}$ may be taken to be normally distributed.

Using the dotted background in figure 7.3 as the null hypothesis the significance of the 1140 peak is about 4 standard deviations in the centre bin and about 5 standard deviations if 3, 5 or 7 bins are used. This is the same level of significance as the peak reported in the Brookhaven experiment (63). However from the fitted curve in figure 7.3 it can be seen that quite a large contribution to this peak comes from the tails of the K*(890) and K*(1420) and compared with this curve the significance of the centre peak is only about 2σ. Also no peak is observed in this mass region in reactions 1) or 2a) but the mass resolution is certainly poorer in these reactions which might smear out the effect of a peak. The most recent data (including results from most of experiment 12 as well as from 75 and 10) shows slight bumps of about 2σ significance in reactions 1) and 3) but these are centred at about 1200 Mev. Thus there seems to be no evidence at present for a $(K\pi)$ resonance in this mass region at 10 Gev/c.

In connection with the significance of such peaks it is interesting to note that, using an estimate for the total number of effective mass histograms published, it has been calculated that the numbers of 3, 4 and 5 standard deviation fluctuations which should be observed in one year are about 1000, 25, 0.25 respectively (64). Thus even a 4σ effect, which has a probability of less than 1 in 10^4 of being exceeded by chance may not in itself suggest the existence of a resonant peak. For comparison the significances of the K*(890) and K*(1420) peaks in figure 7.3 are about 34 and 10 standard deviations respectively, each calculated for 5 bins.

iii) Although there is a slight excess of events around 2 Gev in figure 7.3 this is not very significant and no evidence is seen in this experiment (even with the increased data) for any $(K\pi)$ resonance above the K*(1420).

iv) There is no evidence for any peaks in the $(K\pi\pi)$ mass distributions except for those already mentioned. This is true for both the original and the new data.

7.6 Splitting of the K*(1420)

Great interest has been aroused over the last few years following the discovery of a splitting in the mass peak of the A2 meson in the Cern Missing Mass Spectrometer experiment (65). This splitting was reconfirmed by the same group using a different experimental arrangement (the so-called Boson Spectrometer) and has also been seen in bubble chamber data (66). Apart from the obvious explanation of two resonances in the same mass region (these would have to be interfering to fit the data but this is not unlikely since they could have the same spin-parity) the suggestion was put forward that one might be seeing the effects of a new kind of S-matrix singularity, namely a double pole or dipole (67). If this is the case one might expect a similar splitting in other members of the 2^+ nonet, in particular the K*(1420). Figure 7.3 does show a dip in the central bin of the K*(1420) peak and this dip is contributed to by both the reactions 2b) and 3), as can be seen from figure 7.1. However the significance of this dip is only about 1 standard deviation. Stronger dips can be seen in the K*(1420) region for reactions 1) and 2a) in figure 7.1 but these are two bins (80 Mev) lower than the corresponding dips in reactions 2b) and 3). In the latest data even these dips have completely disappeared. Thus there is no evidence for a splitting of the K*(1420), a conclusion also reached by Davis et al. (68) whose mass distribution also has a dip at the centre of the K*(1420) peak.

7.7 Samples for further study

As mentioned earlier, processes containing two bodies (particles or resonances) in both the initial and final states are the easiest to treat theoretically. For this reason it is important to be able to select samples of events from the observed reactions in order to isolate sub-reactions of the form (7.6) and (7.7), where the K* refers to any one of the four resonances 890, 1420, 1320 and 1800. This is done by taking a slice of the effective mass distribution containing the resonance in question. The choice of mass limits to use necessitates a compromise between including enough events to make the analysis statistically meaningful and taking a narrow slice to improve the resonance to background ratio, which will be largest at the centre of the peak assuming the background is reasonably smooth. There will always be background events included in the slice and resonant events lost from the tails of the Breit-Wigner distribution. The cross section for a sub-process involving resonance production is not affected since it can be found from the area of the fitted Breit-Wigner distribution. Table 7.3 shows the mass regions used for selecting the samples for further study. Also given are the values of N_G^1, N_B where the notation is that introduced in chapter 4 to describe the purity of samples of events.

As mentioned in chapter 1 there are two complementary aspects in the study of high energy strong interaction processes. One is the elucidation of the quantum numbers of the observed resonant states and the other is a determination of their production mechanisms. Since the quantum numbers of the K*(890) and K*(1420) are mostly well-established the main emphasis will be on their production. For the K*(1320) (sometimes called the Q peak) and the K*(1800) (or L peak) the situation is sufficiently unknown to make the determination of the quantum numbers an important task whereas the study of the production mechanisms for these states is still at an early stage.

CHAPTER 8

DETERMINATION OF QUANTUM NUMBERS

8.1 Baryon number and hypercharge (B, Y)

In strong interactions these two additive quantum numbers appear to be strictly conserved. The observed decays of the four resonances discussed in the last chapter must occur by a strong interaction because of their relatively large widths and so they all have

$$B = 0 \quad \text{(i.e. they are mesons)}$$

$$\text{and} \quad Y = -1 \quad \text{(or alternatively } S = -1 \text{ since } S = Y - B\text{)}$$

8.2 Isotopic spin (I)

The concept of isotopic spin or I-spin was originally introduced to describe the similarity (except for charge) of the proton and the neutron (69). Nowadays many groups of particles having similar properties and differing only in their charges are known and each of these groups constitutes an I-spin multiplet. The meaningfulness of this grouping lies in the fact that the strong interaction is believed to be invariant under SU(2), the Lie group of rotations in I-spin space, that is to say, the I-spin quantum number is conserved in strong interactions. The breaking of the SU(2) degeneracy of the mass spectrum is then ascribed to the electromagnetic interaction which is obviously not I-spin invariant since its strength depends very much on the charges of the particles involved.

The charge and hypercharge of all known hadrons are related to the third component of the isotopic spin by the Gell-Mann-Nishijima relation (70)

$$Q = I_3 + Y/2 \tag{8.1}$$

Since Q is always integral and $Y = -1$ for $\bar{K}$'s, I_3 must be half-integral. The possible values of I_3 for a state with total I-spin I are I, I - 1, ..., -(I - 1), -I. Thus for states with $Y = -1$ (K^*'s) the possible values for I are 1/2, 3/2, 5/2, ... Pions have $Y = 0$ so that I could be 0, 1, 2 ..... and nucleons have $Y = +1$ which gives 1/2, 3/2, 5/2 ...... as possible I-spin values.

Since the only particles which have ever been observed in these three multiplets are $(\bar{K}^o, K^-)$, (π^+, π^o, π^-) and (p, n) respectively it is firmly established that

$$I(K) = 1/2, \quad I(\pi) = 1 \text{ and } I(N) = 1/2$$

8.2.1 Relations between production amplitudes

The possible values of total I-spin for the following states are:

$K\pi$: $I = 1/2$ or $3/2$

$K\pi\pi$: $I = 1/2$, $3/2$ or $5/2$

KN : $I = 0$ or 1

The K^-p system (which is the initial state used in the present experiment) is a mixture of the states with I = 0 and I = 1 and can be decomposed into these states using SU(2) Clebsch-Gordan coefficients as follows:

$$(K^-; p) = (1/2, -1/2; 1/2, +1/2)$$
$$= (1/\sqrt{2})\{(1,0) + (0, 0)\} \qquad (8.2)$$

where the pairs of numbers correspond to (I, I_3) values. The I = 1 and I = 0 parts of the initial (K^-p) state may be considered independently since they are orthogonal. Consider the general reaction

$$K^-p \longrightarrow K^*N \qquad (8.3)$$

The following table shows the possible I-spin structures of the final state in this reaction which are consistent with I-spin conservation. (I_3 is just an additive quantum number since (8.1) relates it to two other additive quantum numbers).

TABLE 8.1

I	I_3	I(K*)	I_3(K*)	I(N)	I_3(N)
1	0	1/2 or 3/2	$\pm$ 1/2	1/2	$\pm$ 1/2
0	0	1/2	$\pm$ 1/2	1/2	$\pm$ 1/2

There are three things to note from this table:

i) the value I = 5/2 listed earlier as a possibility for a $(K\pi\pi)$ system does not appear. This is obvious since a final state consisting of such a state and a nucleon could only have a total I-spin of 2 or 3 whereas the initial state has components with

$I = 0$ and 1. Thus an $I = 5/2$ state cannot be produced in a reaction like (8.3) by an I-spin conserving interaction.

ii) $I(K^*) = 3/2$ occurs only for the case when the intial state has $I = 1$. This part of the initial state may be decomposed in the following way in terms of an $I = 3/2$ K^* and a nucleon:

$$(1, 0) = (1/\sqrt{2}) \left\{(3/2, +1/2; 1/2, -1/2) - (3/2, -1/2; 1/2, +1/2)\right\}$$
$$= (1/\sqrt{2}) \left\{(K^{*0}_{3/2}, n) - (K^{*-}_{3/2}, p)\right\} \tag{8.4}$$

This gives the following relation between the cross sections for these processes

$$\frac{\sigma(K^-p \longrightarrow nK^{*0}_{3/2})}{\sigma(K^-p \longrightarrow pK^{*-}_{3/2})} = 1 \tag{8.5}$$

This relation holds not only for the total cross-sections for these reactions but for their differential cross sections into any particular part of phase space, down to the level at which the effects of the electromagnetic mass splitting within the multiplets become important.

iii) $I(K^*) = 1/2$ can be formed with a nucleon both from the $I = 0$ and $I = 1$ components of the initial state. For each of these states one can formally write down similar decompositions to (8.4). However since both these states (0, 0), (1, 0) lead to the same set of final states they will in general interfere and no relation corresponding to (8.5) will hold for $K^*_{1/2}$ (see however section 8.2.3 for derivation of such relations using additional assumptions).

8.2.2 Relations between decay amplitudes

One can derive a further class of I-spin relations by examining the decays of each of the K* states. Table 8.2 shows all possible decay modes of the type $K\pi$ or $K\pi\pi$ for both I = 3/2 and I = 1/2 K*'s.

TABLE 8.2

I	I_3	Q	$K\pi$	$K\pi\pi$
3/2	+3/2	+1	K^o+	K^o + o, K^- ++
1/2,3/2	+1/2	0	K^o o,K^-+	K^o + -, K^- + o, K^o oo
			(7) (3)	(6) (9) (10)
			(1) (2)	(4) (5) (8)
1/2,3/2	-1/2	-1	K^-o,K^o-	K^- + -, K^o - o, K^- oo
3/2	-3/2	-2	K^- -	K^- - o, K^o - -

Notice that the bottom half of the table is obtained exactly from the top half by the transformation $I_3 \longrightarrow -I_3$. Only the two middle lines of the table correspond to the reactions so far discussed; the top and bottom rows are included for completeness and will be referred to later. The numbers between the middle lines correspond to the reactions in which the various charge states are seen. All reactions from 1) - 10) occur showing that all possibilities were written down earlier in the list of reactions to be studied.

The various decay modes for a given (I, I_3) state shown in table 8.2 may be related using Clebsch-Gordan coefficients. Where there is only one possible decay mode the relations are trivial.

For the $I_3 = \pm 1/2$ $(K\pi)$ states one can derive the relations shown in table 8.3. For the case of 3-body decays it is only possible in general to derive triangular inequalities between the various rates but if the decay occurs via two consecutive two-body decays one can obtain equalities of the kind shown in table 8.3 for each of the two-body decays. Possible intermediate states for such cascade decays of higher K*'s are $K^*(890)\pi$, $K^*(1420)\pi$ and $K\rho(760)$. The relative rates for the first of the two sequential decays into one of these three intermediate states are given by table 8.3 with K replaced by K*(890) or K*(1420), or π replaced by ρ as necessary. (This assumes I = 1/2 for these two K*'s and I = 1 for ρ) The rates for the second step in the overall decay can again be obtained from table 8.3 with the additional information that the charge states of the ρ have only a single decay mode each ($\rho^{\pm} \longrightarrow \pi^{\pm} o$, $\rho^{o} \longrightarrow + -$). The relative contributions of these decay modes to the six $(K\pi\pi)$ final states are shown in tables 8.4 and 8.5 where K* stands for either the (890) or the (1420) resonance. The pairs of particles shown in brackets are those which form the two-body resonance in the intermediate stage of decay. The third particle in such a situation is often called the bachelor particle. For the $K^*\pi$ decays there are 8 entries in the table for the six possible final states since one final state in each group contains two possible intermediate K* states.

In the case of decay into three particles without the assumption of an intermediate two-body state the amplitudes for decay into one of the three possible charge states (for either $I_3 = + 1/2$ or $- 1/2$) can be expressed in terms of two independent amplitudes.

TABLE 8.3

RELATIVE $K\pi$ DECAY RATES

I_3	Ratio	$I(K^*) = 1/2$	$I(K^*) = 3/2$
+ 1/2	$\frac{K^o\ o}{K^-\ +}$	1/2	2
- 1/2	$\frac{K^-\ o}{K^o\ -}$	1/2	2

TABLE 8.4

RELATIVE $K^*\pi$ DECAY RATES (K* = 890 or 1420)

$I_3 = +1/2$	$(K^o\ -)+$:	$(K^-\ o)+$:	$(K^-\ +)o$:	$(K^o\ o)o$
I = 1/2	4	2	2	1
I = 3/2	2	1	4	2
$I_3 = -1/2$	$(K^-\ +)-$:	$(K^o\ o)-$:	$(K^o\ -)o$:	$(K^-\ o)o$
I = 1/2	4	2	2	1
I = 3/2	2	1	4	2

TABLE 8.5

RELATIVE $K\rho$ DECAY RATES

$I_3 = +1/2$	$K^o(+\ -)$:	$K^-(+\ o)$:	$K^o\ (o\ o)$
I = 1/2	1	2	0
I = 3/2	2	1	0
$I_3 = -1/2$	$K^-(+\ -)$:	$K^o(-\ o)$:	$K^-\ (o\ o)$
I = 1/2	1	2	0
I = 3/2	2	1	0

This is true for any value of the total I-spin of the $(K\pi\pi)$ system and implies that the three amplitudes satisfy a linear relation, from which a triangle inequality can be derived. For example, for a $(K\pi\pi)$ system in the state $(1/2, -1/2)$ one may write:

$$\begin{aligned} A_1(K^- + -) &= (1/\sqrt{3})\, T_o + (1/\sqrt{6})\, T_1 \\ A_2(K^- \; o \; o) &= -(1/\sqrt{3})\, T_o \\ A_3(K^o - o) &= \qquad\qquad\quad (1/\sqrt{3})\, T_1 \end{aligned} \tag{8.6}$$

where the two independent amplitudes T_o, T_1 correspond to the situations where the $(\pi\pi)$ sub-system is in a state of total I-spin 0, 1 respectively. One could equally well choose as the independent amplitudes those for which the $(K\pi)$ system had definite I-spin but this is usually not so convenient as the symmetry properties of the amplitudes are not so obvious. The amplitudes (8.6) satisfy the relation

$$A_2 = -A_1 + A_3/\sqrt{2} \tag{8.7}$$

from which the following triangle inequality can be derived between the three cross sections:

$$\left|\tfrac{1}{2}\sigma_3 - \sigma_1\right| \leqslant \sigma_2 \leqslant \tfrac{1}{2}\sigma_3 + \sigma_1 \tag{8.8}$$

For the case of a $(K\pi\pi)$ system in a state $(3/2, -1/2)$ the corresponding relation is

$$\left|2\sigma_3 - \sigma_1\right| \leqslant \sigma_2 \leqslant 2\sigma_3 + \sigma_1 \tag{8.9}$$

The inequalities (8.8) and (8.9) hold for the general differential cross sections for the reactions. If the amplitudes (8.6) are integrated over all phase space the contribution of the interference term between T_o and T_1 in the first amplitude vanishes because it is antisymmetric under interchange of the two pions. This gives the following equality between the total cross sections for these final states:

$$N_2 = N_1/2 - N_3/4 \qquad (8.10)$$

where an additional factor of two is included to take account of the fact that there are two identical particles in the second reaction. For I = 3/2 the corresponding relation is

$$N_2 = N_3/2 - N_1/4 \qquad (8.11)$$

These reactions may not be much use as a test of I-spin because the second final state corresponds to a no-fit channel. However, if the I-spin of the ($K\pi\pi$) system is known in some other way, (8.10) or (8.11) can be used to calculate the total cross section for the (K^- oo) mode in terms of those for the other two modes in the case of a direct decay into ($K\pi\pi$). Relations (8.6) - (8.11) hold also if the decay proceeds via a two-body intermediate state (e.g. $K^*(890)\pi$) but in such cases those derived earlier in tables (8.4) and (8.5) are stronger since they hold for the differential cross sections,not just for the total cross sections.

8.2.3 Relations between production amplitudes requiring assumptions about the production mechanism

In section 8.2.1 we wrote down the possible states of total I-spin for the initial state (K^-p) and the final state (K^*N). In the case where only one value of I-spin was common to the two states we were able to derive relation 8.5 but a similar relation could not be derived when two I-spin values were shared because of the possibility of interference. We could have reached exactly the same conclusions by taking either of the other two pairings of the four external particles as is shown by the following table in which k denotes the (unknown) I-spin of the K*.

TABLE 8.6

(i)	I_i	I_f	(f)
(K^-p)	0, 1	$k \pm \frac{1}{2}$	(K^*N)
(pN)	0, 1	$k \pm \frac{1}{2}$	(K^-K^*)
(K^-N)	0, 1	$k \pm \frac{1}{2}$	$(p\,K^*)$

(Note that in the second and third cases the pairs consist of one ingoing and one outgoing particle.) Table 8.6 is particularly trivial in the present case since 3 out of the 4 external particles have the same I-spin (one-half) so that the values of I_i, I_f are the same for all 3 cases. This will not be so, for example, in $\pi^- p \rightarrow XN$ where the corresponding table is (x = I-spin of X):

TABLE 8.7

(i)	I_i	I_f	(f)
(π^-p)	1/2, 3/2	$x \pm \frac{1}{2}$	(XN)
(pN)	0, 1	$x \pm 1$, x	(π^-X)
(π^-N)	1/2, 3/2	$x \pm \frac{1}{2}$	$(p\,X)$

However the number of I-spin values common to (i) and (f) will be the same whichever of the 3 cases is used, as can be seen by substituting particular values for x.

Although we have done nothing more yet than make a formal expansion of I-spin amplitudes in 3 different ways, the 3 cases are obviously analogous to the description of a two body into two body reaction using the Mandelstam invariant variables s, t and u (71), defined by

$$
\begin{aligned}
s &= (p_a + p_b)^2 = (p_c + p_d)^2 \\
t &= (p_a - p_c)^2 = (p_b - p_d)^2 \qquad (8.12) \\
u &= (p_a - p_d)^2 = (p_b - p_c)^2
\end{aligned}
$$

s- channel

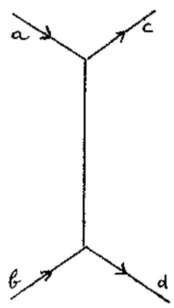

t-channel

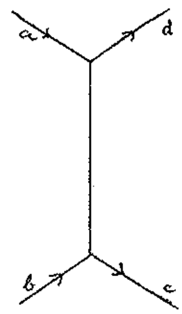

u-channel

To give dynamical significance to tables 8.6 and 8.7 one can interpret the common values of I-spin in the three cases as being those of the states which are exchanged in the s, t and u channels respectively. For certain ranges of the variables s, t, u the dynamical description of the reaction using one of the 3 channels may be particularly simple in the sense that only a few sets of quantum numbers (at most) are exchanged.

These regions are:

i) for the s-channel, the low energy region (about 0.5 - 2 Gev/c);

ii) " " t- " , high energy forward scattering;

iii) " " u- " , " " backward " .

Previously we could not derive relations between cross sections for processes where two possible values of total I-spin could be exchanged. If we know (or assume) that only states with a single value of I-spin contribute to the exchange in a particular reaction we are then able to derive relations analogous to (8.5). Such relations are necessarily weaker since they depend on knowledge of (or assumptions about) the production mechanism. They are probably most useful for investigating the exchanged I-spin when the I-spins of the external particles are all known but they can be used for finding an unknown external I-spin if one has sound knowledge of the production mechanism.

For the reactions studied here the relevant channel is the t-channel since the K* and the final nucleon are mainly produced peripherally with respect to the beam and target particles (in that order).

We get for the production of $K^*_{1/2}$, assuming either pure $I = 0$ or pure $I = 1$ exchange,

$$\frac{\sigma(nK^{*o}_{1/2})}{\sigma(pK^{*-}_{1/2})} = \begin{array}{ll} 0 & (\, I = 0 \text{ exchange}) \\ 4 & (\, I = 1 \quad " \quad) \end{array} \qquad (8.13)$$

As before these relations hold for the differential cross sections, neglecting electromagnetic mass splitting effects.

8.2.4 Tests for I-spin of observed resonances

It is not possible to determine the experimental value of the ratio

$$p = \frac{\sigma(nK^{*o})}{\sigma(pK^{*-})} \qquad (8.14)$$

for any of the four K* resonances observed because there is no way of calculating the contributions to the numerator from the no-fit channels 7), 9) and 10). However it can be seen that corresponding pairs of decay modes in table 8.2 transform into one another under $I_3 \longrightarrow -I_3$ and this means that any relation derived for p will also hold for individual pairs of decay modes. In particular the ratios that can be tested are

$$p_1 = \frac{(K^- +)}{(K^o -)} \quad \text{for } K^*(890) \text{ and } K^*(1420) \qquad (8.15)$$

and $$p_2 = \frac{(K^o + -)}{(K^- + -)} \quad \text{for } K^*(1320) \text{ and } L(1800) \qquad (8.16)$$

Experimental values for these ratios using total cross sections are shown in table 8.7. The use of the total cross section to test relations which hold generally for the differential cross section may not give very precise tests since a lot of information will have been lost in the integration. However such a test does use all events in the reaction which compensates a little by reducing the statistical errors. The experimental values presented here are calculated from effective mass plots, using double the usual Poisson errors to take account of systematic errors due to the estimation of the background. Better

TABLE 8.7

EXPERIMENTAL PRODUCTION RATES

K*	(890)	(1420)	(1320)	(1800)
observed value of p_1 or p_2	0.6 ± 0.2	1.4 ± 0.4	0.0 ± 0.1	0.1 ± 0.2
expected values:				
I(K*)= 3/2	1	1	1	1
(I = 1 exchange) I(K*)= 1/2	4	4	4	4
(I = 0 ") I(K*)= 1/2	0	0	0	0

TABLE 8.8

DECAY RATES INTO ($K\pi$)

	(K^{o} −)	(K^{-} o)
(observed) K*(890)	1	0.6 ± 0.1
K*(1420)	1	0.7 ± 0.3
(expected) I = 3/2	1	2
I = 1/2	1	0.5

values will be obtained later by more quantitative methods. For channels with a $\overline{K^o}$ the distributions corrected for decay weight have been used and an additional factor of 2.91 is used to correct for the long-lived K_2^o component and the neutral decays of the K_1^o (ref. 2).

From the observed values of p_1, p_2 the following deductions can be made:

i) the small value of p_2 for both K*(1320) and L(1800) strongly rules out the assignment I = 3/2 for these states (relation 8.5). They must therefore have I = 1/2 in which case (8.13) suggests that they are produced entirely by I = 0 exchange. Figure 7.5 (see chapter 7) shows the two relevant distributions. The curve drawn above the lower histogram shows the signal expected if the peaks had I = 3/2. The absence of such peaks is by far the most conclusive evidence for the assignment I = 1/2 in both cases.

ii) for the K*(890) I = 3/2 seems unlikely but for K*(1420) the value of p_1 is compatible with 1 which means that I = 3/2 cannot be ruled out on these grounds alone. Of course p_1=1 does not imply that I = 3/2 since all values from 0 to 4 are possible for an I-spin one-half resonance produced by both I = 0 and I = 1 exchanges. Assuming the I-spin is 1/2, the values of p_2 suggest that the larger contribution to the production of both these resonances is from I = 0 exchange.

Tests for I-spin using the decays of the resonances may be made using those final states in tables 8.3 - 8.5 which occur in fitted channels. The experimental numbers are shown in tables

8.8 - 8.10 and have been normalised to the four-constraint reaction in each case. Table 8.8 strongly suggests I = 1/2 for K*(890) and K*(1420) which is the accepted assignment for these two well known resonances. In table 8.9 the K*(1320) $\longrightarrow$ K*(890)π decay mode gives good agreement with I = 1/2. The K*(890)π and K*(1420)π decay modes for the L(1800) also seem consistent with I = 1/2 except that there appears to be more K^{*-}(890) than K^{*o}(890). This is particularly noticeable when plots of (Kπ) masses are made for different slices of the (K^oo -) mass distribution. Below 1700 Mev both charge states of the K*(890) are observed although the (K^o -) peak is narrower because of the smaller experimental resolution when both particles are observed. Above 1700 Mev (i.e. in the L-region <u>and</u> beyond) the 890 peak in (K^- o) has virtually disappeared. For a (K^oo -) system in a pure I = 1/2 state the amplitude is purely antisymmetric on exchange of the two pions. This cannot therefore explain the observed behaviour which requires the presence of an I = 3/2 amplitude. Such a contribution may possibly come from one or more of the processes which constitute the background.

A departure of <u>both</u> the (K^o o)- and (K^o -)o rates from their expected values relative to (K^- +)- in such a way that they remain equal is compatible with a pure I = 1/2 amplitude as it could be explained by interference between two modes leading to the same final state. This does not appear to be happening for either the K*(1320) or the L(1800), at least at the level of these initial approximate calculations. (It should be noted that in the original paper on the L-meson (9) the theoretical predictions for the K*(890)π decay

TABLE 8.9

DECAY RATES INTO K*

			$(K^- +)-$	$(K^o\ o)-$	$(K^o\ -)o$
(observed)	K*(1320) $\longrightarrow$	K* (890)π	1	0.6 ± 0.1	0.7 ± 0.1
	L(1800) $\longrightarrow$	K* (890)π	1	0.3 ± 0.2	0.7 ± 0.3
	L(1800) $\longrightarrow$	K*(1420)π	1	-	0.3 ± 0.2
(expected)		I = 3/2	1	0.5	2
		I = 1/2	1	0.5	0.5

TABLE 8.10

DECAY RATES INTO $K\rho$

		$K^-(+ -)$	$K^o(- o)$
(observed)	K*(1320)	1	1.0 ± 0.2
	L(1800)	1	1.1 ± 0.4
(expected)	I = 3/2	1	0.5
	I = 1/2	1	2

rate ratio

$$\frac{(K^- +) - \text{plus } (K^o\ o)-}{(K^o\ -)o}$$

were incorrectly given as 4 and 1 for I = 1/2, 3/2. From table 8.4 or 8.9 it can be seen that the correct values are 3 and 0.75 respectively).

For the $K^-\rho^o$ decays of the K*(1320) and the L(1800) there appears to be an anomaly because the observed values seem to be inconsistent with the expectation for I = 1/2. (They are actually consistent with I = 3/2 but since we have already shown this assignment to be unacceptable it can be safely ignored from now on.) A ratio of about 1:1 between the two ($K\rho$) decay modes in the Q-region (1200 - 1400 Mev) has also been observed in a K^+p experiment at 9 Gev/c (72). (The decay of a strangeness + 1 K* has exactly the same features as an S = -1 system with all particles changed to antiparticles.) Two explanations were suggested for this effect. The first involved interference between K*(890) and ρ from the competing decay modes since some parts of phase space are populated by both these decays. However Bowler (73) has since shown that the expected ratio is 2:1 irrespective of the relative phases and magnitudes of the two decay amplitudes. The other possibility is that an I = 0 $\pi\pi$ resonance (ϵ) is partly responsible for the (+ -) peak; it cannot of course contribute to the (o -) peak which has no I = 0 component and this might explain the observed ratio. Although there is as yet no absolutely conclusive evidence for the existence of such a resonance in the ρ^o region, many experiments have postulated one in order to explain certain anomalies, notably the asymmetry in the decay of the ρ^{o}. Also several analyses of the s-wave $(\pi^{+}\pi^{-})$ phase shift using the reaction $\pi^{-}p \longrightarrow \pi^{+}\pi^{-}n$ find a value near 90° in the region of 720 Mev which suggests there might be a resonance there (2). If so, its width would be well over 100 Mev. In the Veneziano model (74) an $I = 0$, $J^{P} = 0^{+}$ $\pi\pi$ resonance would correspond to the first daughter of the ρ and is expected to occur at about the same mass. In this connection it is interesting to note that an application of the four-point Veneziano model to the decay $Q^{-} \longrightarrow K^{-} + -$ correctly predicts the observed 1:1 ratio (75). This model would also predict a similar contribution to the same decay of the L(1800) which might then explain the observed "ρK" ratio of 1.1 ± 0.4.

If a wide ε^{o} resonance is contributing to the (+ −) peak for $(K^{-} + -)$ systems in the Q-region one might expect the apparent ρ^{o} peak to differ in mass or width from that seen in corresponding $(K^{o} - o)$ systems. Such an effect was seen in the 9 Gev/c K^{+} experiment (72), where the (M, Γ) values for the ρ peak were (720, 180) and (760, 80) in the two cases. These values are to be compared with the accepted values of (765, 125), bearing in mind the fact that production of pion pairs with masses in the upper half of these peaks is restricted by the available phase space. Figure 8.1 shows the relevant distribution for the Q-region (1260 - 1370 Mev) using the most recent data of the present experiment. The distributions peak at 734, 742 Mev respectively but this difference is probably not very significant. However the (+ −) peak does seem to be wider in spite of the fact that the experimental resolution for M(+ −) is smaller than for M(− o).

FIG. 8.1

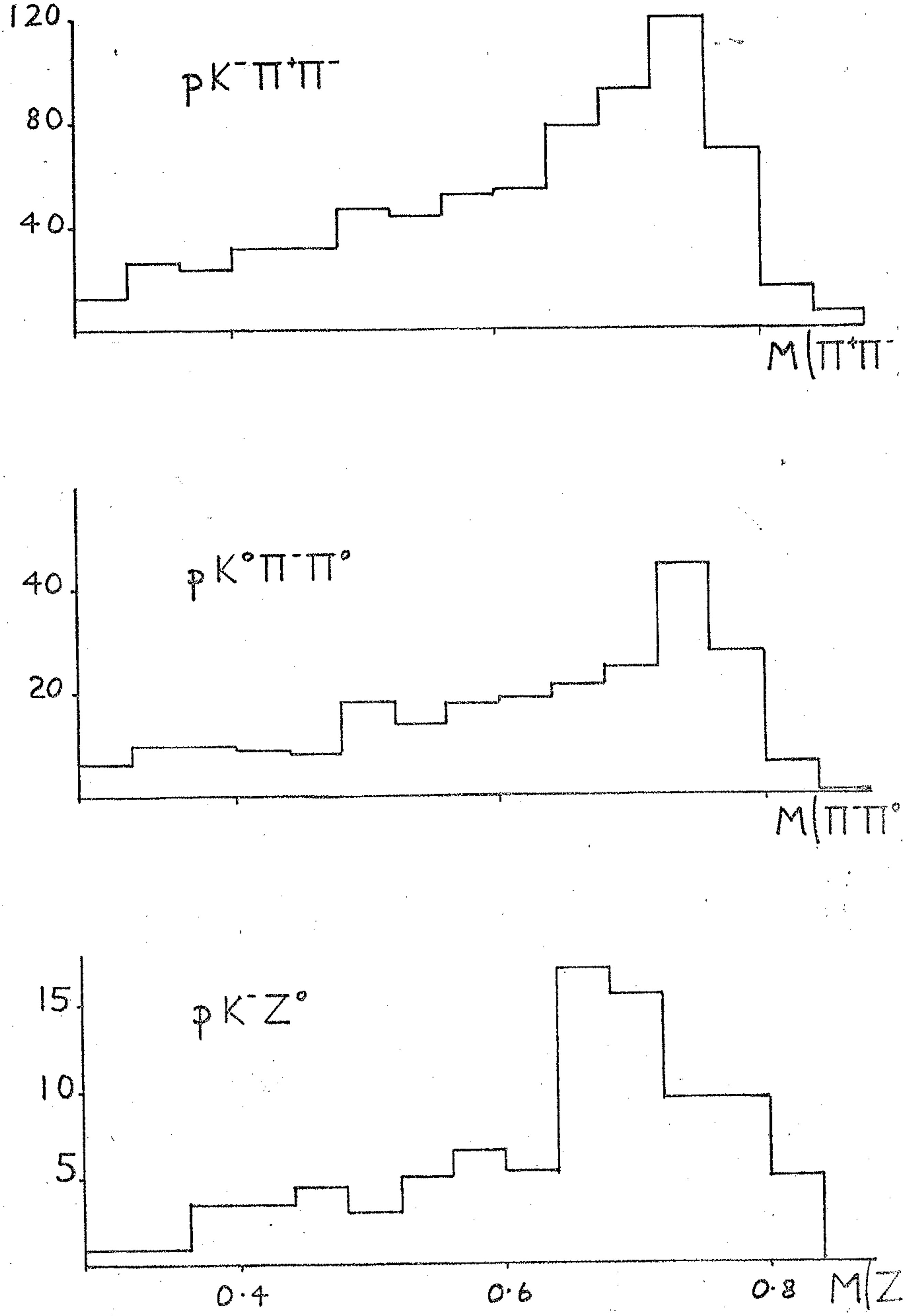

The best place to look for a direct signal from the ϵ^o is in the (o o) decay mode since the ρ coupling to this channel vanishes. Unfortunately such a decay necessarily implies a no-fit situation in a hydrogen bubble chamber experiment which is one of the reasons why the existence of the resonance has been hard to confirm or refute. The mass of the Z^o combination in no-fit events of the type pK^-Z^o peaks at about 650 Mev but has a long tail extending to about 2.5 Gev. In fact only about 40% of these events have Z^o masses below 900 Mev so it seems reasonable to assume that a large proportion of these are $\pi^o\pi^o$ events. The third plot in figure 8.1 shows the Z^o mass distribution for events with $M(K^-Z^o)$ in the region of the K*(1320). There is some evidence for a peak at about 655 Mev, that is, lower than the ρ mass, which could possibly explain the slight decrease in mass observed in the (+ -) distribution for the (K^- + -) system. The size of this peak, when combined with the expected ratio of 2 for the (+ -)/(o o) decay rate ratio of ϵ^o and subtracted from the observed (+ -) distribution, gives a very approximate value of 1.9 ± 0.6 for the genuine (ρK) ratio in the charge states K^o(- o) and K^-(+ -).

8.3 Spin and parity (J^P)

Every elementary particle has a well-defined spin and parity and in all interactions angular momentum is believed to be conserved. Parity conservation holds for strong interactions. The "stable" particles (i.e. those stable against a strong decay) which are directly detected in the bubble chamber have $J^P = 0^-$ (mesons) or $1/2^+$ (baryons), with the single exception of the Ω^- which probably has $J^P = 3/2^+$. Actually the spins have only been directly measured for the pion (neutral and positive states only) and the nucleon; the spin assignments for the other stable particles have been deduced from their decays into pions and nucleons, assuming that angular momentum conservation holds in these weak processes. It is interesting to note that Selleri has proposed a different allocation of spins to the strange particles, namely $J(K) = 1/2$, $J(\Lambda) = 1$, $J(\Sigma) = 1$ and $J(\Xi) = 3/2$ (76). Their decays can then be explained by assuming that a $\Delta J = 1/2$ selection rule operates. This puts J and I on a similar footing since the corresponding rule for I is known to hold approximately in such decays. It also has the advantage of automatically incorporating the $\Delta S = 1$ rule which has an independent existence in the usual scheme. At first sight these assignments would seem to be incompatible with SU(3) symmetry in which multiplets contain particles with the same J^P. However spin dependent forces could account for the SU(3) breaking since in Selleri's scheme the hypercharge, which is usually considered to be responsible for the SU(3) breaking (77), is related to the spin by the following relations:

$$\begin{aligned} Y &= -2(J-1) \quad \text{for the baryon octet} \\ Y &= -2J \qquad\quad\; \text{for the meson octets} \end{aligned} \tag{8.17}$$

Leaving aside this intriguing possibility, which awaits direct experimental test, one can obtain some restrictions on the possible values of J^P for resonances which decay (either directly or in two or more steps) into $K\pi$ or $K\pi\pi$.

8.3.1 $K\pi$ system

One can build up higher spin states from two pseudoscalar ($J^P = 0^-$) particles by combining them in a state of relative orbital angular momentum ℓ ($\ell = 0, 1, 2, ...$). Strictly speaking this is only valid non-relativistically since the spin and orbital parts of an angular momentum cannot be separated in a Lorentz invariant way. However the results obtained can always be rigorously proved without recourse to this separation.

From a knowledge of angular momentum wave functions one can easily show that an orbital angular momentum ℓ contributes a factor $(-)^{\ell}$ to the overall parity of the system. Thus the spin and parity of a $(K\pi)$ system with orbital angular momentum ℓ is given by:

$$(0^-, \ell, 0^-) \longrightarrow \quad J = \ell \;;\; P = (-)^{\ell} \tag{8.18}$$

Only one-half of all possible J^P values for a boson system are generated in this way namely 0^+, 1^-, 2^+, 3^-, ... This sequence is called the natural parity series. The complementary sequence 0^-, 1^+, 2^-, 3^+, ... is called the unnatural parity series and states with these J^P values cannot decay into two pseudoscalar particles.

8.3.2 $K\pi\pi$ systems

From the result of the last section any two of the three particles must be in a relative state of natural parity. Taking the natural parity series term by term and adding the third particle in an orbital momentum state L relative to the first pair gives the following possibilities:

$$(0^+, L, 0^-) \longrightarrow \quad J = L; \; P = (-)^{L+1} \qquad (8.19)$$

i.e. $0^-, 1^+, 2^-, 3^+, \ldots\ldots$

$$(1^-, L, 0^-) \longrightarrow \quad J = 1; \; P = + \text{, if } L = 0 \qquad (8.20)$$

i.e. 1^+

$$\longrightarrow \quad J = L \pm 1, L \; ; \; P = (-)^L \text{, if } L \neq 0 \qquad (8.21)$$

i.e. $(2^-, 1^-, 0^-)$, $(3^+, 2^+, 1^+)$, ...

Similarly $(2^+, L, 0^-)$ gives 2^-, $(3^+, 2^+, 1^+)$, $(4^-, 3^-, 2^-, 1^-, 0^-)$, ... Rearranging these sequences in order of increasing J one has $0^-, 1^+, 1^-, 2^+, 2^-, 3^+, 3^-, \ldots\ldots$ and it is clear that for any spin greater than zero states of both parities occur. Only 0^+ is absent so that such a decay is forbidden for a 0^+ state.

8.3.3 J^P determinations of the observed resonances

The two $(K\pi)$ resonances observed (890 and 1420) must belong to the natural parity series since they decay into two pseudoscalars. The spin-parity of the K*(890) has been well-established as 1^- since the first suggestion of this assignment in 1962 (78). For the K*(1420) the assignment $J^P = 2^+$ is preferred although 3^- has not yet been completely ruled out (79). Sufficient data to make a useful addition to the spin-parity information on the 1420 have only recently become available in the present experiment and an analysis has not yet been carried out.

The spin-parity assignments of the two $(K\pi\pi)$ resonances (1320 and 1800) are not so well-known and it is mainly with a determination of these that the rest of this chapter will deal. One method used is to analyse the distribution of events on the Dalitz plot (80) of the $(K\pi\pi)$ system as a function of the mass of that system. This has been done by fitting the theoretical Dalitz plot densities for various spin-parity values (up to $J = 3$) using the maximum likelihood method. The assignment 0^+ has not been tried since we have seen that this is forbidden for a $(K\pi\pi)$ resonance. The transition matrix elements used in the theoretical amplitudes were expressed using the tensor formalism of Zemach (81); the exact expressions used for these matrix elements are given in reference 82 and are fully relativistic. The decay modes considered were $K^*(890)\pi$, $K\rho$ and direct $(K\pi\pi)$ for both resonances, and in addition $K^*(1420)\pi$ for the L-meson. The background under the resonances was assumed to have contributions from the same components.

The need for all these components was demonstrated by a preliminary first-approximation fit in which spin-parity was not considered. The two-body decays were described by Breit-Wigner bands on the Dalitz plot with isotropic angular distributions and possible interferences were neglected. The Dalitz plots for successive 100 Mev slices of $(K\pi\pi)$ mass were analysed by maximum likelihood and the contributions of each mode found are plotted against the $(K\pi\pi)$ mass in figures 8.2 and 8.3 (for reactions 4) and 5) respectively). It can be seen that each of the modes considered shows peaks near 1300 Mev and 1800 Mev in at least one of the reactions.

DECAY RATES OF $K\pi\pi$

$K^-p \to pK^-\pi^+\pi^-$ (N^{*++} EXCLUDED) AT 10 GeV/c

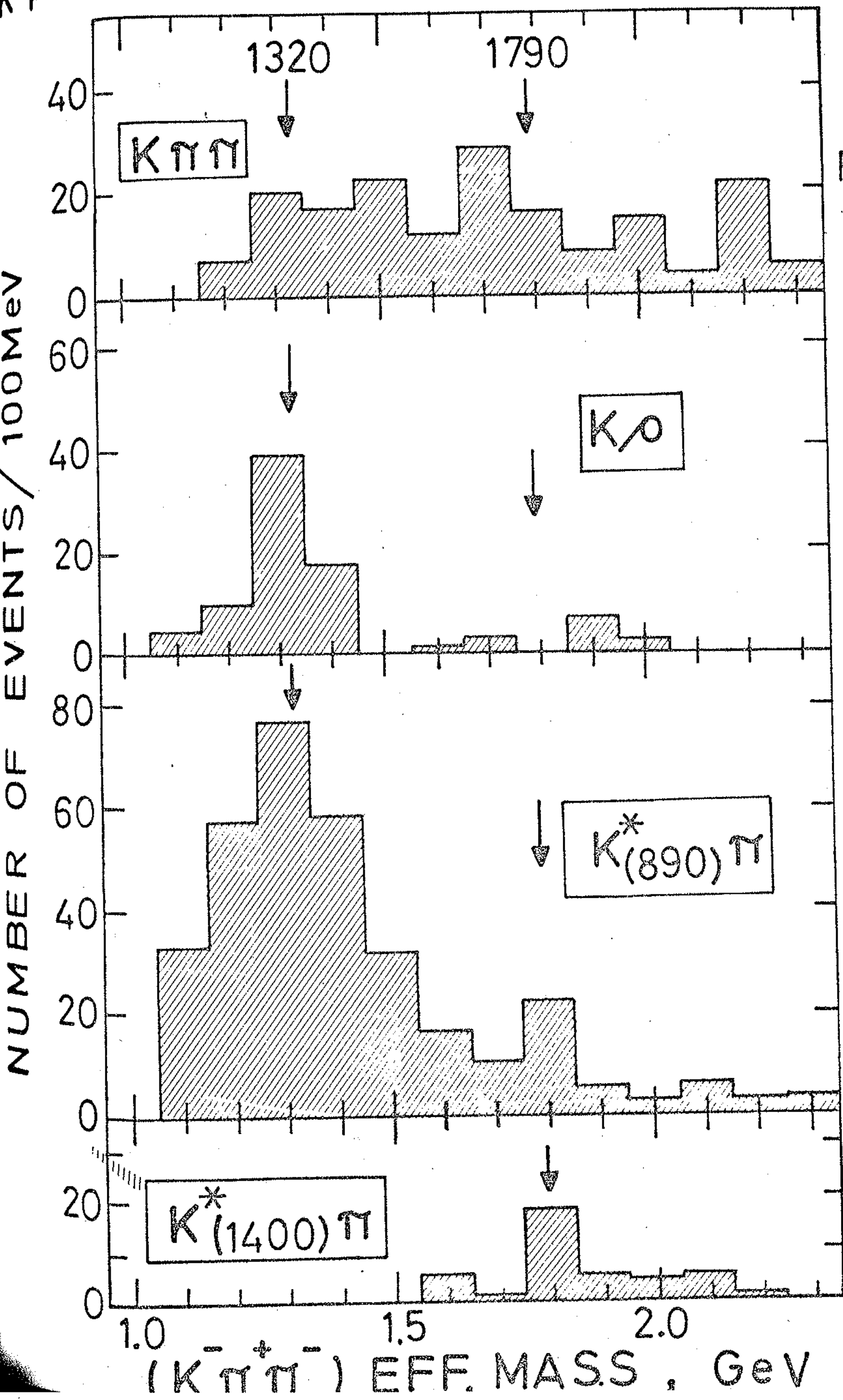

FIG. 8.7

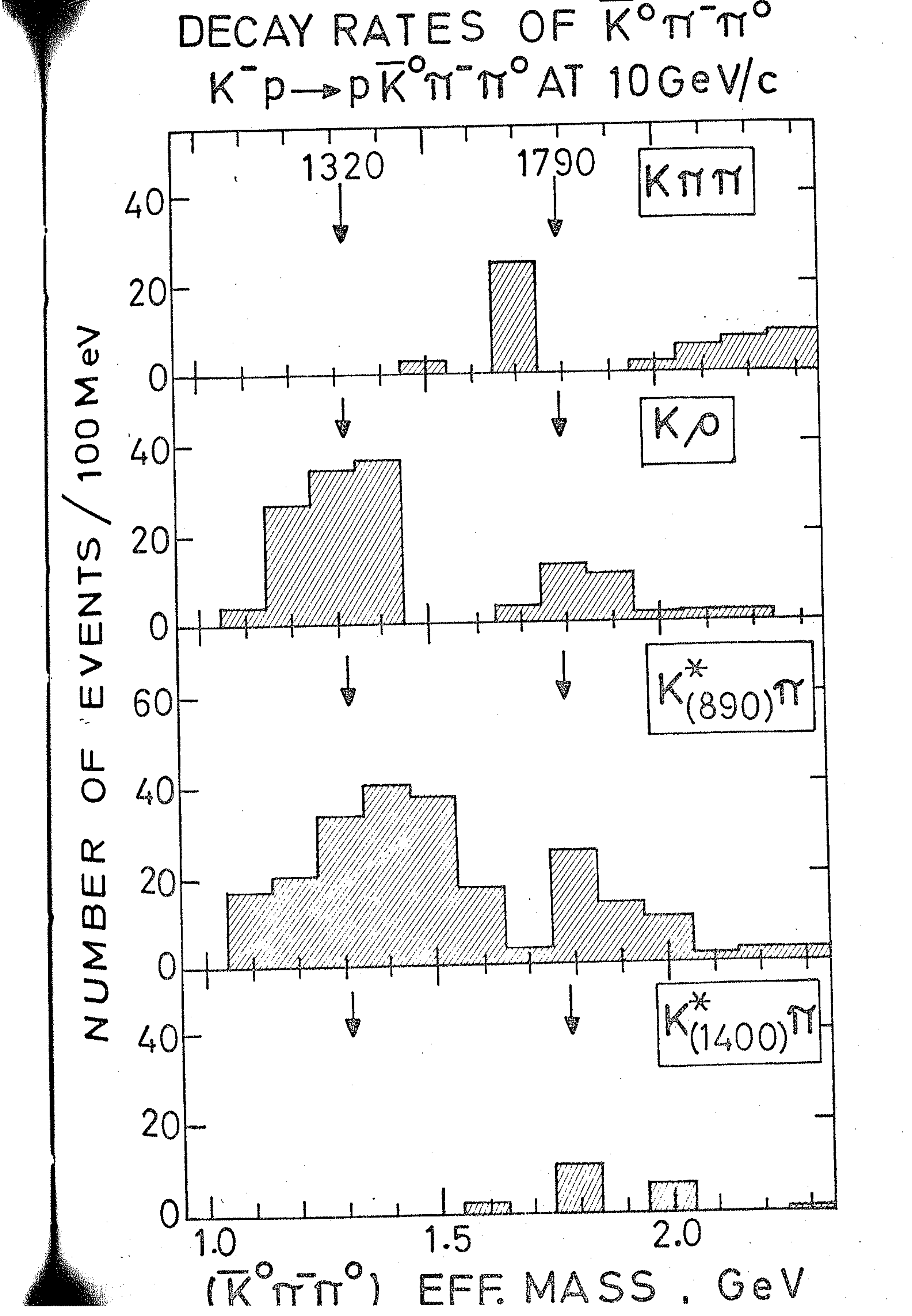

DECAY RATES OF $\bar{K}^0\pi^-\pi^0$
$K^-p \rightarrow p\bar{K}^0\pi^-\pi^0$ AT 10 GeV/c
1320
1790
$K\pi\pi$
$K\rho$
$K^*_{(890)}\pi$
$K^*_{(1400)}\pi$
NUMBER OF EVENTS / 100 MeV
0
20
40
60
1.0
1.5
2.0
$(\bar{K}^0\pi^-\pi^0)$ EFF. MASS , GeV

For the main fits wide limits are used for both resonances (see table 7.2) so as to include substantial amounts of the neighbouring background regions. This enables the background contributions to be better determined than they would be if narrow regions had been chosen. As in the plots shown earlier a t-cut is applied at 0.6 $(\mathrm{Gev/c})^2$ and events in the $N^{*++}(1236)$ region are removed in reaction 4). Figures 8.4 and 8.5 show the Dalitz plots for rather narrower regions around the observed peaks. Each plot is of $M^2(\pi\pi)$ against $M^2(K\pi)^0$ and includes events from both reactions.

The logarithm of the likelihood function used in the fits is given by:

$$L(J^P, a, b) = \sum_i^{(4)} \log \frac{d_i^{(4)}}{\iiint d_i^{(4)} dm\, dwde} + (4 \longrightarrow 5) \quad (8.22)$$

$$\text{where } d_i^{(j)} = \sum_k^{res} a_{kj} \left| M_{kj}^{res} (J^P, m_i, w_i, e_i) \right|^2 F^{res} (m_i)$$

$$+ \sum_k^{bgd} b_{kj} \left| M_{kj}^{bgd} (m_i, w_i, e_i) \right|^2 F_{kj}^{bgd} (m_i) \quad (8.23)$$

$$= \frac{d^3\sigma}{dmdwde}$$

$d_i^{(j)}$ is the Dalitz plot density distribution, m is the $(K\pi\pi)$ mass and w, e are the energies of the two pions in the $(K\pi\pi)$ rest system; j = 4,5 refers to the reactions 4), 5) and i runs over the events in these reactions. M_{kj}^{res}, M_{kj}^{bgd} are the matrix elements for the decay component k in reaction j for resonance and background respectively. F^{res}, F^{bgd} describe the $(K\pi\pi)$ energy dependence of the resonance and background components and are related to the production process. Finally, a_{kj}, b_{kj} are the parameters to be fitted.

FIG. 8.4

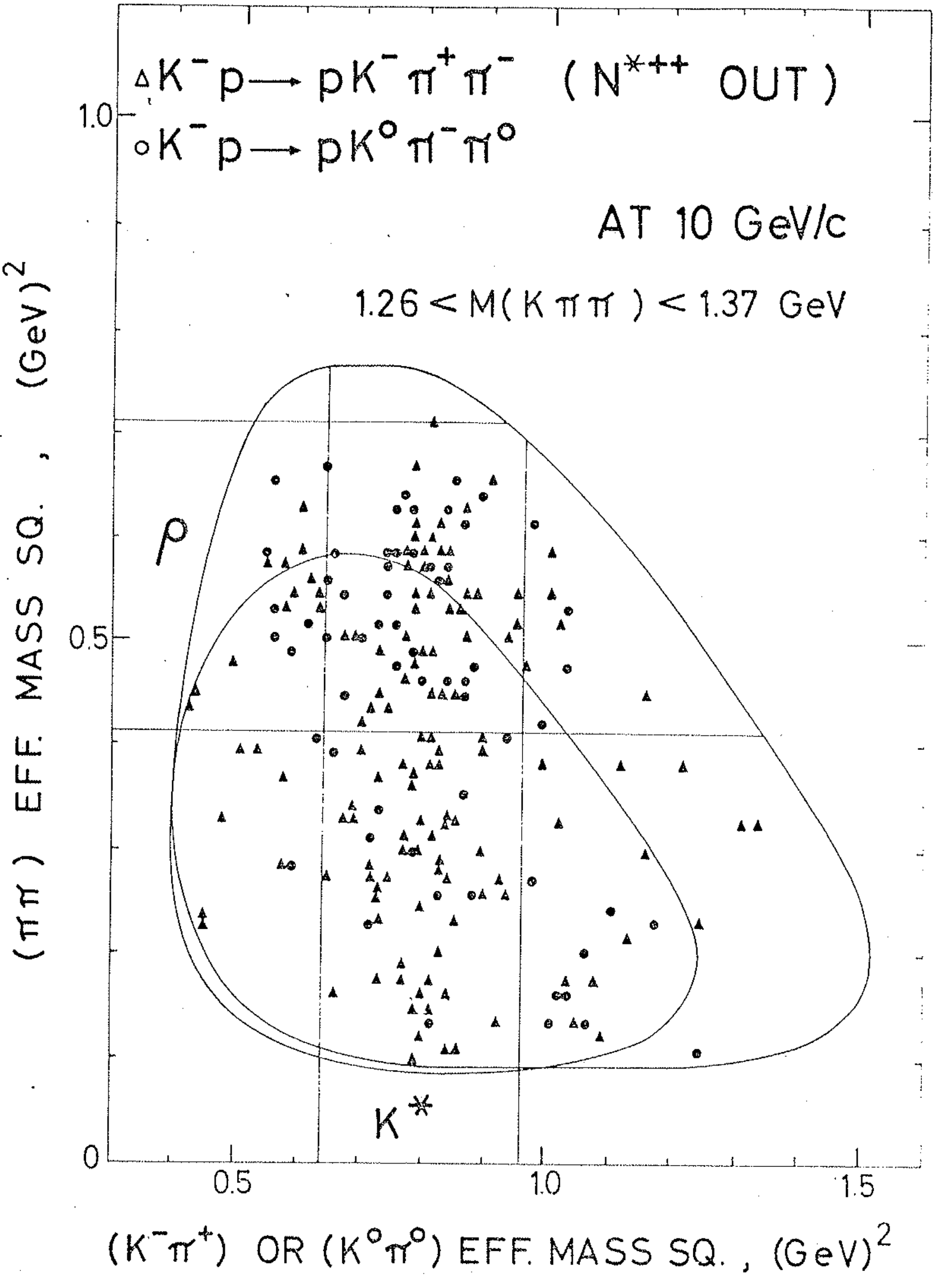
△ K⁻p → pK⁻π⁺π⁻ (N*++ OUT)
○ K⁻p → pK°π⁻π°
AT 10 GeV/c
1.26 < M(Kππ) < 1.37 GeV
ρ
K*
1.0
0.5
0
0.5
1.0
1.5
(ππ) EFF. MASS SQ. , (GeV)²
(K⁻π⁺) OR (K°π°) EFF. MASS SQ. , (GeV)²

FIG. 8.5

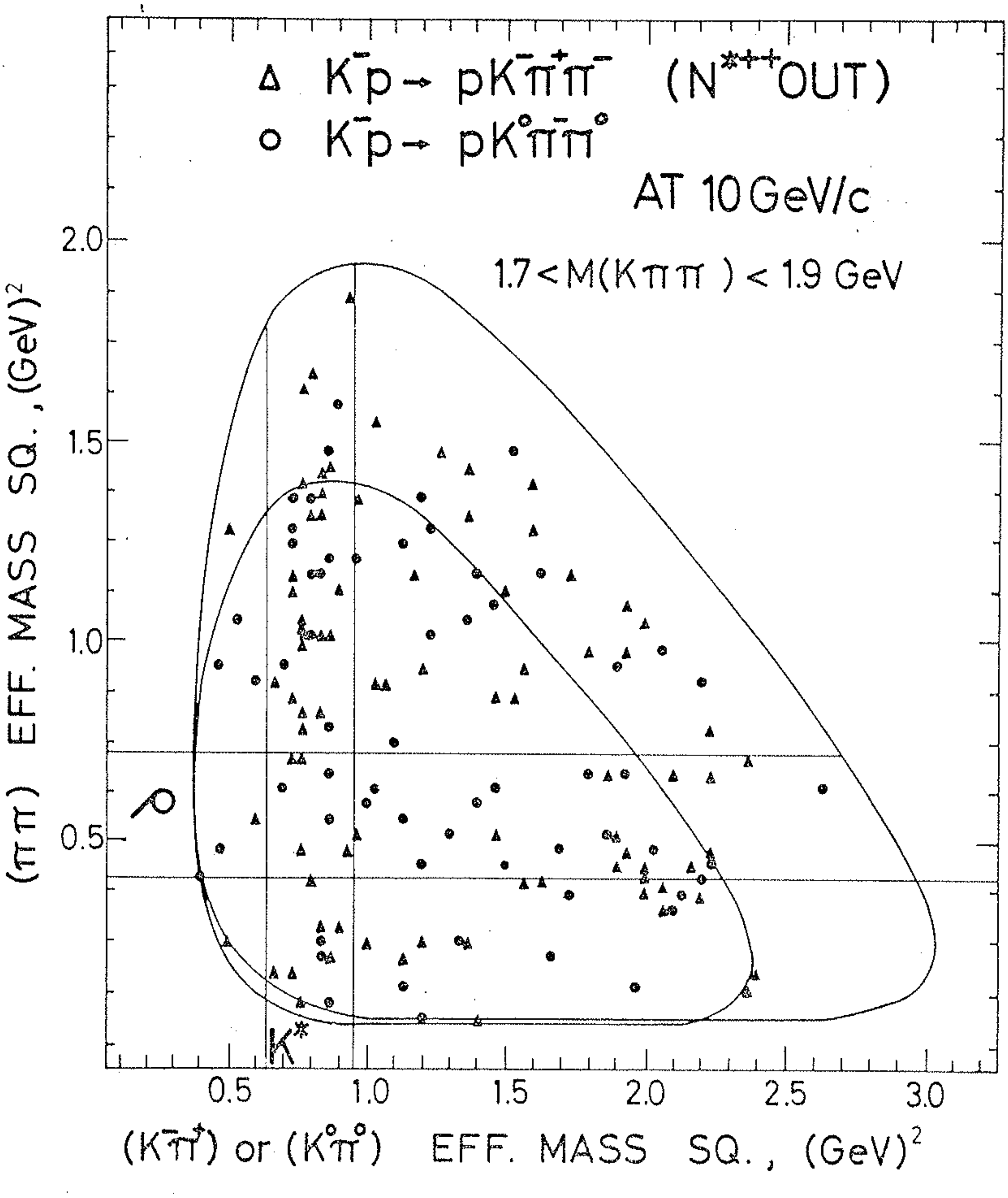
Δ $K^-p \rightarrow pK^-\pi^+\pi^-$ (N^{*++} OUT)
o $K^-p \rightarrow pK^0\pi^-\pi^0$
AT 10 GeV/c
1.7 < M(Kππ) < 1.9 GeV
ρ
K*
2.0
1.5
1.0
0.5
0.5
1.0
1.5
2.0
2.5
3.0
(ππ) EFF. MASS SQ., $(GeV)^2$
$(K^-\pi^+)$ or $(K^0\pi^0)$ EFF. MASS SQ., $(GeV)^2$

Some of the a_{kj} are related for a given I-spin of the whole system. The I-spins of both resonances were assumed to be one-half except that the assignment $J^P = 2^-$ was also tried for the L-meson assuming $I = 3/2$. The results of these fits are shown in tables 8.11 and 8.12 for the K*(1320) and L(1800) respectively. The values of the likelihood function were actually negative and an arbitrary number has been added to give the values shown. As mentioned in the last chapter this does not affect the maximum likelihood condition.

The J^P assignments giving the largest likelihoods are 1^+ for both resonances. However for the L-meson, the likelihoods for $J^P = 2^-$ and 3^+ are hardly less and must be considered as possible values. It can be seen that the analysis has achieved a separation between the natural and unnatural series of spin-parity assignments but that assignments within these series are not much separated from each other. This merely reflects the fact that the Dalitz plot distribution tends to have a similar general form for J^P values in the same series (82) (except $J = 0$). For example, distributions along K*(890) bands vanish at the centre for $J^P = 0^-$ and at the ends for $J^P = 1^-$ or 2^+. The observed distributions do not appear to vanish either at the centre or at the ends and are more in agreement with a J^P of 1^+ or 2^-. The unnatural parity series is preferred for both K*(1320) and L(1800). The single fit with $I = 3/2$, $J^P = 2^-$ for the L has a low likelihood. This confirms in a more quantitative way the preference for $I(L) = 1/2$ obtained above from a consideration of relative decay rates.

To test the goodness of the fit a chi-squared test was carried out using the results of the two fits which gave the highest

Table 8.11

J^P	Value of likelihood FCT.	Resonance $K\pi\pi$	Resonance $K\rho$	Resonance $K^{*}(890)\pi$	Resonance $K^{*}(1420)\pi$	Background $K\pi\pi$	Background $K\rho$	Background $K^{*}(890)\pi$	Background $K^{*}(1420)\pi$	Channel
1^+	821.2	20.2 19.5	10.5 15.6	36.9 27.3	10.7 7.9	60.4 14.1	5.5 18.9	26.6 44.6	24.4 0.0	$K^-\pi^+\pi^-$ $\bar{K}^0\pi^-\pi^0$
2^-	821.0	24.6 26.1	8.4 12.4	33.8 25.0	9.4 6.9	62.2 14.2	5.0 18.4	27.1 44.8	24.6 0.0	$K^-\pi^+\pi^-$ $\bar{K}^0\pi^-\pi^0$
3^+	820.6	23.9 24.2	9.1 13.5	33.3 24.7	10.6 7.8	63.1 12.7	4.7 18.6	26.6 46.2	23.8 0.0	$K^-\pi^+\pi^-$ $\bar{K}^0\pi^-\pi^0$
0^-	816.0	40.2 43.4	0.0 0.0	11.9 8.8	9.1 6.8	50.7 2.0	11.6 27.3	45.5 59.4	25.8 0.0	$K^-\pi^+\pi^-$ $\bar{K}^0\pi^-\pi^0$
2^+	812.9	5.4 25.8	4.4 6.5	27.3 20.2	9.2 6.8	85.5 20.7	4.7 17.2	33.3 48.8	25.3 1.8	$K^-\pi^+\pi^-$ $\bar{K}^0\pi^-\pi^0$
3^-	812.1	4.8 23.7	5.6 8.3	26.4 19.6	9.0 6.7	83.8 18.8	4.6 17.1	33.8 50.1	27.0 3.6	$K^-\pi^+\pi^-$ $\bar{K}^0\pi^-\pi^0$
1^-	811.8	5.7 21.3	6.5 9.7	27.4 20.3	7.4 5.5	77.8 17.0	6.3 18.1	34.1 52.7	29.8 3.2	$K^-\pi^+\pi^-$ $\bar{K}^0\pi^-\pi^0$
2^- $I=3/2$	810.9	40.6 36.3	5.1 1.9	16.9 31.3	3.0 5.6	52.6 18.3	7.1 24.2	39.5 30.2	30.3 0.0	$K^-\pi^+\pi^-$ $\bar{K}^0\pi^-\pi^0$

Table 8.12

τ^P	Value of likelihood FCT.	Resonance			Background			Channel
		$K\pi\pi$	$K\rho$	$K^*(890)\pi$	$K\pi\pi$	$K\rho$	$K^*(890)\pi$	
1^+	648.7	95.9	45.1	162.7	10.4	0.0	90.8	$K^-\pi^+\pi^-$
		0.0	70.4	126.9	9.3	0.0	56.4	$\bar{K}^o\pi^-\pi^o$
2^-	634.0	83.0	22.7	198.1	20.6	18.3	62.3	$K^-\pi^+\pi^-$
		7.5	35.4	154.5	0.0	38.9	26.9	$\bar{K}^o\pi^-\pi^o$
C^-	572.0	177.6	0.0	126.2	0.0	53.1	48.1	$K^-\pi^+\pi^-$
		98.9	0.0	98.4	0.0	37.4	28.3	$\bar{K}^o\pi^-\pi^o$
1^-	567.9	127.9	77.1	98.8	12.9	0.0	88.3	$K^-\pi^+\pi^-$
		0.0	120.3	77.0	6.2	0.0	59.6	$\bar{K}^o\pi^-\pi^o$
2^+	542.3	128.7	23.1	151.9	11.5	16.2	73.5	$K^-\pi^+\pi^-$
		42.7	36.1	118.5	0.0	37.4	28.4	$\bar{K}^o\pi^-\pi^o$

likelihood values. The binning of the events used for the test was varied randomly and a mean value of X^2 was found; this was done because the number of events per bin was not always large enough to make the X^2-test reliable for a given choice of bins. For the K*(1320) 1^+ solution the average value of X^2 was 85 ± 8 for 47 degrees of freedom which corresponds to a probability of 0.1% for a more extreme result. For the L-meson (also the 1^+ solution) the average X^2 was 39 ± 5 for 28 degrees of freedom which gives a 7% probability. The small probability in the former case may be partly due to the description of the $(K\pi\pi)$ mass spectrum in terms of a single Breit-Wigner distribution when in fact there may be more than one resonance present.

The conclusions from the above analysis are that both peaks have spin greater than zero and unnatural spin-parity. The fit also gives the contributions of the various decay modes considered. These will be shown in the next section when other decay modes have been discussed.

8.4 Search for additional decay modes

So far we have only discussed $(K\pi)$ decay modes for the K*(890) and K*(1420) and $(K\pi\pi)$ modes for the other two resonances. These states may have other decay modes and a determination of the relative contributions of the various modes for a certain resonance provides one of the important sources of information on its properties. To be able to do this it is necessary to search for all possible decay modes arising from the production of the resonance in a particular reaction. In the present case the reactions are quasi two-body ones where the only other particle in the final state is a nucleon. The observation (or absence) of other decay modes may also give additional information on the quantum numbers of the state. A search for decay modes arising from different production reactions may also give indications of the possible quantum numbers but is not relevant for finding the decay branching ratios.

If the decays are strangeness conserving they will lead to final states of the form $(K + m\pi)$, possibly in more than one step due to resonance formation at an intermediate stage. The maximum numbers of pions allowed by energy conservation are 2, 6, 5 and 9 for resonances near 890, 1420, 1320 and 1800 Mev respectively. Although they may be allowed by energy considerations, decays into a large number of final particles are likely to be suppressed since the phase space distribution for a system containing all particles in the final state except one rises only slowly from its zero value at threshold. For the L-meson there is also the possibility of a decay into $(K\bar{K}\bar{K} + m\pi)$ where m can be 0, 1 or 2. Radiative decay modes have not been considered.

8.4.1. $K^*(890)$

An upper limit for the only possible mode (other than $K\pi$) can be obtained from the number of events observed in the 890 Mev region of the $(K\pi\pi)$ mass distributions. In the latest data (experiments 75, 10 and 12) the mass region 860 - 920 Mev of the $(K^- + -)$ distribution contains 6 events; no events are seen in the same regions of the $(K^0 - o)$ or $(K^- \; o \; o)$ mass distributions. These numbers as they stand do not satisfy either of the relations (8.8) or (8.9) which are expected to hold for pure $I = 1/2$ or $I = 3/2$ amplitudes which suggests that both may be present. Consistency with both relations can best be achieved (within errors and neglecting interference) if 2 of the 6 events are from the $I = 1/2$ part of the amplitude, bearing in mind the fact that the number of events in $(K^0 - o)$ has to be multiplied by about 2.4 to correct for both the unseen K^0 decays (a factor of 3) and the slightly larger mean fiducial volume for these events (a factor of 0.8). This gives an upper limit of 0.4 μb (at the 95% confidence level) for $K^{*-}(890)$ production with subsequent decay into $(K\pi\pi)$. Using the total cross section of 92 ± 9 μb for the same reaction with $(K\pi)$ decay one obtains,

$$R = \frac{K^{*-}(890) \longrightarrow K\pi\pi}{K^{*-}(890) \longrightarrow \text{all modes}} < 0.4\%, \text{ with 95\% confidence} \qquad (8.24)$$

For the neutral K^* only one of the three charge states $(K^0 + -)$ is accessible to study and no events are seen in the $K^*(890)$ mass region. Assuming that all three charge states have equal weight the upper limit (95% confidence) for the $(K\pi\pi)^0$ decay is about 4 μb, whereas the cross-section for $(K\pi)^0$ decay is 58 ± 10 μb. Thus the upper limit on the branching ratio is not as restrictive as that obtained in (8.24). The only previously reported experimental value of R is an upper limit of 0.2% (83). The $(K\pi\pi)$ decay is strongly suppressed by phase space and by the p-wave centrifugal barrier. Among theoretical estimates (84), Sweig has obtained a ratio of 0.002% using ρ-meson dominance and SU(3) couplings.

8.4.2 K*(1420)

We have already used the known $(K\pi\pi)$ branching ratio to subtract the (unresolved) contribution of the $K^{*-}(1420)$ from the $(K\pi\pi)^-$ mass distributions (see fig. 7.11). Also the small peak in the region of 1400 Mev seen in the neutral $(K^0 + -)$ mass combination of reaction 6) (see fig. 7.5) was previously stated to be consistent with the known decay rates of the K*(1420). Other decay modes of this resonance are likely to be seen better in neutral charge states since in the negative charge states we know there may be a contribution from the nearby K*(1320). The results of a search for decays into $(K + m\pi)$ for values of m up to 6 are shown in table 8.13. The search in the higher multiplicity events used the combined data of experiments 75, 10 and 12. For a final state consisting of K and m pions there are (m + 1) possible charge states and when the total charge is zero only one of these charge states corresponds to a fitted channel. To correct for the unfittable channels it is assumed that all charge states have equal cross-sections. It would perhaps have been more reasonable to weight each charge state by an

TABLE 8.13

DECAY MODES OF K*(1420)

m	Data used	Decay into	No.of events	$\sigma(\mu b)$	Branching ratio (%)
1	75	$K^- +$	42 ± 7	39 ± 7	57 ± 17
2	"	$K^0 + -$	14 ± 3	30 ± 5	43 ± 13
3	"	$K^- + + -$	< 1	< 2.5	< 3.6
4	75, 10, 12	$K^0 + + - -$	< 1	< 1.6	< 2.3
5	"	$K^- + + + - -$	< 1	< 0.8	< 1.1
6	"	$K^0 + + + - - -$	< 1	< 2.8	< 4.0
3	75, 10	$K^- \omega^0$	< 17	< 6	< 11
3	75, 10, 12	$K^- \eta^0$	< 5	< 2	< 4

I-spin coefficient (85) before assuming equality but the approximation used is probably fairly reasonable bearing in mind the other uncertainties present.

The quoted values for the $(K\pi)$ and $(K\pi\pi)$ branching ratios are consistent with the accepted values given in reference 2. The statistics do not justify a separation of the $(K\pi\pi)$ mode into contributions from $K^*(890)\pi$ and $K\rho$. The other two modes reported in ref. 2 for the $K^*(1420)$ are $K\omega^0$ and $K\eta^0$. Since both the ω^0 and η^0 decays involve at least one neutral particle they will never be observed in a fitted channel for the overall neutral charge state. The upper limits quoted in table 8.13 for these two modes are obtained from the negative charge state (to be discussed in the following section). As expected no evidence for the production of $K^*(1320)$ or L(1800) was found in the neutral charge states examined.

8.4.3 K*(1320) and L(1800)

Figure 8.6 shows the combined $(K\pi)^-$ mass distribution for reactions 1), 2a) and 2b). There is no trace of any peaking near 1320 or 1800 Mev. The most likely cause of this suppression is angular momentum conservation which forbids a $(K\pi)$ decay for a state with unnatural spin-parity. This is consistent with the Dalitz plot analysis which gave a preference for unnatural J^P in both cases.

The results of a search for other modes are given in table 8.14. All decays into $(K + m\pi)$ for values of m up to 6 are considered except that there are no data at present available for events with 8 charged prongs. Where there are two-body decay modes

FIG. 8.

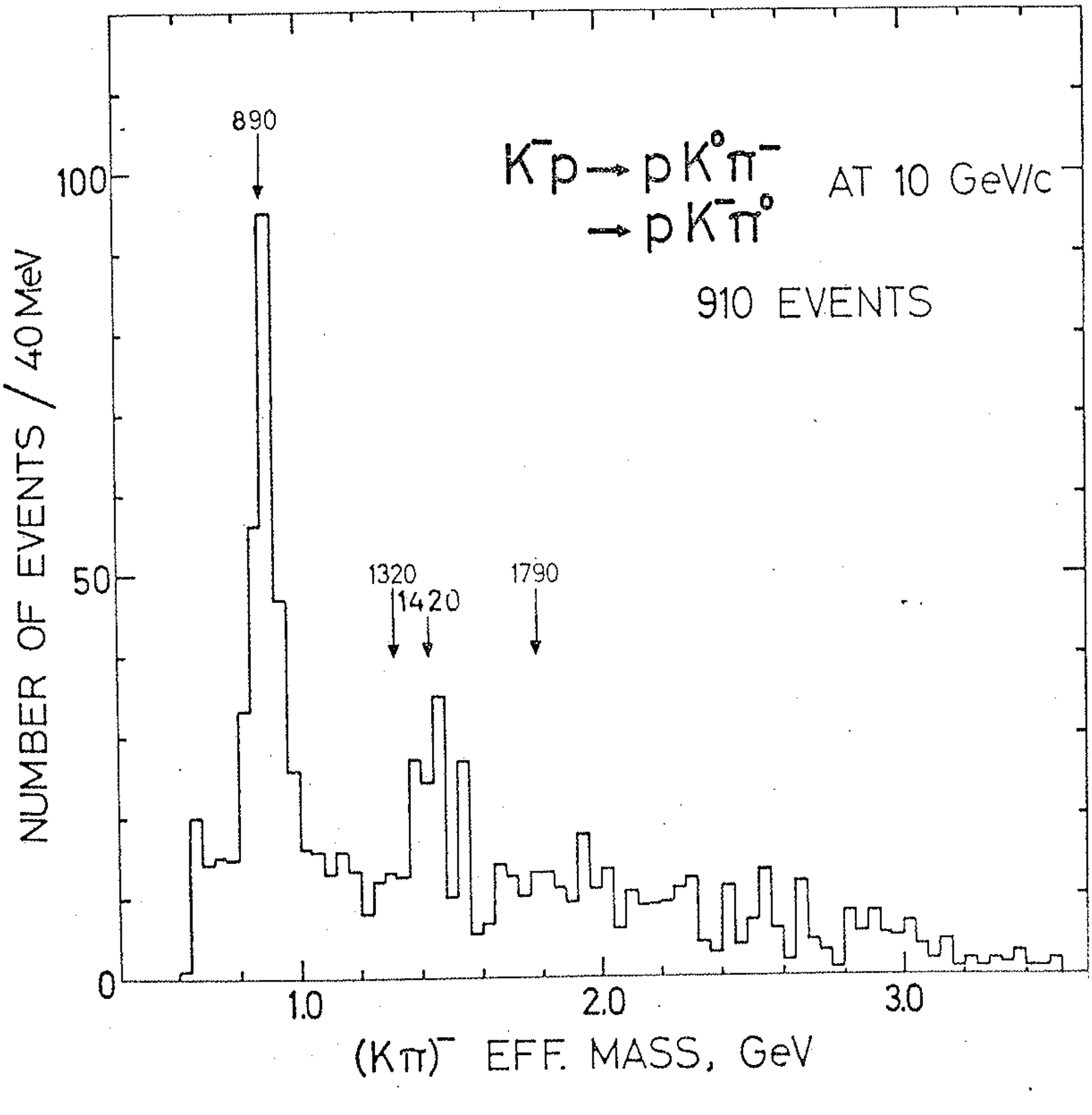

890
$K^-p \rightarrow pK^0\pi^-$ AT 10 GeV/c
$\rightarrow pK^-\pi^0$
910 EVENTS
1320
1420
1790
100
50
0
1.0
2.0
3.0
NUMBER OF EVENTS / 40 MeV
$(K\pi)^-$ EFF. MASS, GeV

TABLE 8.14

SEARCH FOR ADDITIONAL DECAY MODES OF K*(1320) AND L(1800)

m	Data used	Decay mode	Threshold (Mev)	No. of events observed K*(1320)	L(1800)
1	75	$K^- o$, $K^o -$	635	< 12	< 12
2	"	$K^- + -$, $K^o - o$	770	see tables 8.11 & 8.12	
"	"	$K^- o\ o$			
"	75,10	$K^- f^o$	1745	-	< 5
3	75,10,12	$K^- + - o$	910	55 ± 30	100 ± 30
		$K^- \eta^o$	1045	< 5	6 ± 4
		$K^- \omega^o$	1280	55 ± 30	32 ± 20
		$K^{*o}(890)\rho^-$	1655	-	< 12
		$K^{*-}(890)\rho^o$	"	-	< 15
		$K^o + - -$	910	< 3	< 15
		$K^{*-}(890)\rho^o$	1655	-	< 5
		$K^o - o\ o$	910	< 15	< 15
(4)		$K^{*-}(890)\eta^o$	1440 ($\eta^o \rightarrow$ neutrals)	-	< 13
4		$K^- + + - -$	1050	< 1	< 10
		$K^o + - - o$		< 1	< 7
		$K^{*-}(890)\eta^o$	1440 ($\eta^o \rightarrow$ charged)	-	< 2
		$K^{*-}(890)\omega^o$	1670	-	< 5
5		$K^- + + - - o$	1185	< 1	< 3
		$K^- X^o$	1455	-	< 3
		$K^o + + - - -$	1185	< 1	< 1
6		$K^o + + - - - o$	1325	-	< 1

No details available at present for the mass spectra ($K^- + - o\ o$) and ($K^o + - - o\ o$)

involving intermediate resonance production estimates are given of their contributions. In no-fit channels resonance combinations cannot be selected unless the missing neutral system (Z^o) is wholly within or wholly without the combination required. A particular no-fit channel will in general contain contributions to ($K + m\pi$) final states for various values of m depending on the number of neutral pions present. Since it is not possible to separate the contributions of these various final states it is assumed that the missing neutral system contains the minimum number of neutral particles. From the (m + 1) possible charge states of the form ($K + m\pi$) this leaves just 3 for each value of m (greater than 2) where one can search for decays.

The only positive evidence for other decay modes is into the charge state (K^- + - o). This mass distribution is shown in figure 8.7 with events in the N^{*++} region removed. There appears to be a significant peak near 1800 Mev. When events with t less than 0.6 $(Gev/c)^2$ are selected the higher mass part of the distribution is reduced a great deal and the peak, which is only slightly reduced, is thereby much more significant (about four standard deviations). This behaviour is very similar to that of the L-meson peak seen in the ($K\pi\pi$) channels and thus it seems reasonable to suppose that we have observed a new decay mode of the L.

In the (+ - o) mass distribution of the same reaction we have already mentioned the existence of a peak due to the ω^o when discussing the mass resolution (see figure 7.19). Figure 8.8 shows the (K^- + - o) mass distribution for events where the mass of the (+ - o) system lies in the ω^o region. As well as a clear peak

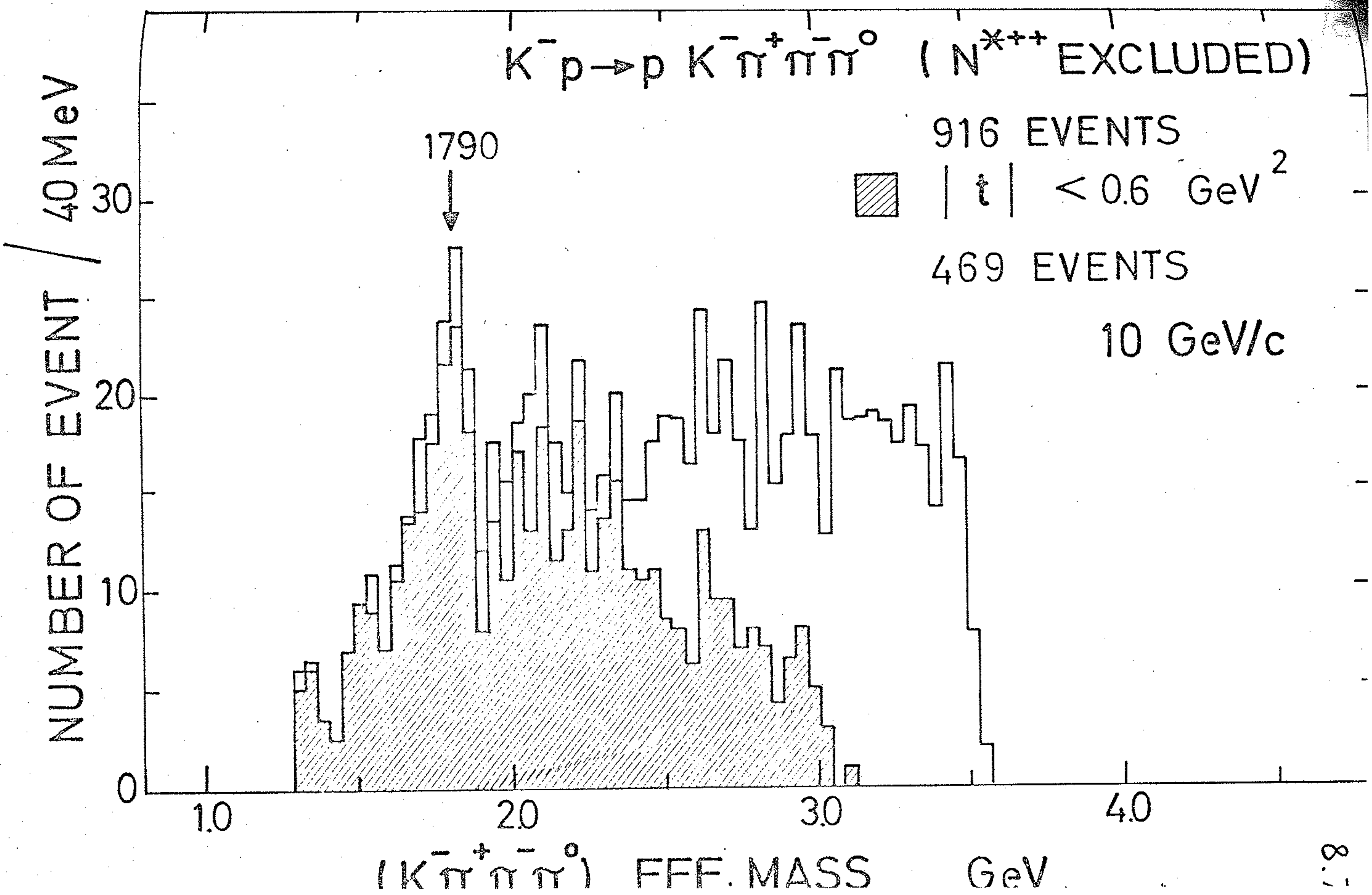
$K^-p \to p K^- \pi^+ \pi^- \pi^o$ (N^{*++} EXCLUDED)
916 EVENTS
$|t| < 0.6$ GeV^2
469 EVENTS
10 GeV/c
1790
NUMBER OF EVENT / 40 MeV
0
10
20
30
1.0
2.0
3.0
4.0
$(K^- \pi^+ \pi^- \pi^o)$ EFF. MASS GeV

8.7

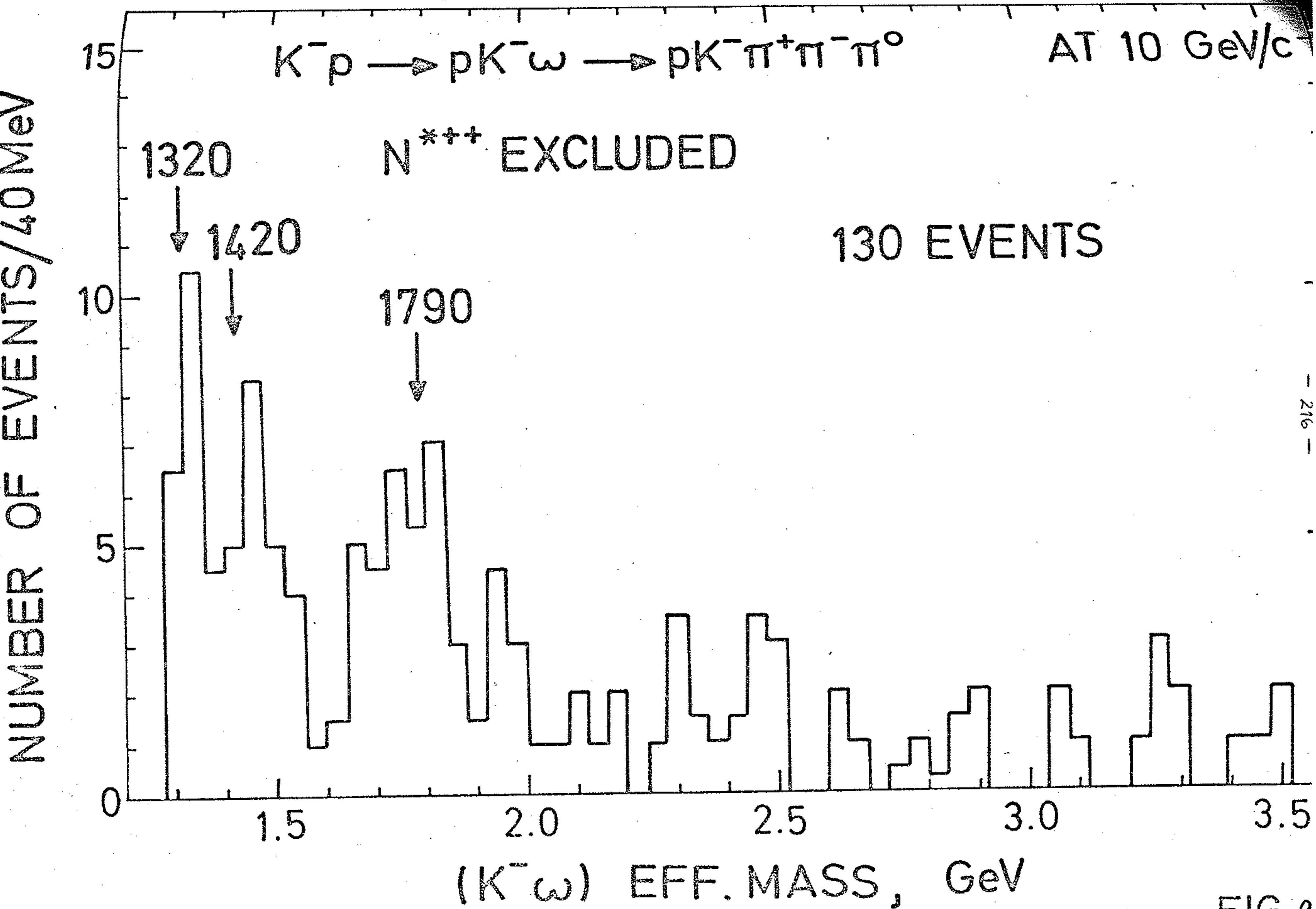

$K^-p \rightarrow pK^-\omega \rightarrow pK^-\pi^+\pi^-\pi^o$
AT 10 GeV/c
N^{*++} EXCLUDED
130 EVENTS
1320
1420
1790
NUMBER OF EVENTS/40MeV
0
5
10
15
1.5
2.0
2.5
3.0
3.5
$(K^-\omega)$ EFF. MASS, GeV

FIG.8

near 1800 Mev there also seems to be a peak around 1300 Mev which could possibly be due to the K*(1320). It should be noted that figure 8.7 contains data from experiments 75 and 10, which is approximately double the sample used for figure 8.6 for this particular reaction. The estimates quoted in table 8.14 are obtained from a much larger sample and show that there is a significant amount of L-decay into (K^- + − o) which is not via ω^o while the peak for the K*(1320) is consistent with being entirely associated with ω^o.

We expect contributions to the (K + 3π) mass spectra arising from the decay mode K*(1420)π of the L, where the K*(1420) subsequently decays into (K$\pi\pi$), rather than via the (Kπ) decay mode which was involved in the Dalitz plot analysis. From the fitted branching ratio one can calculate the expected numbers of events for each of the four (K + 3π) charge states. By adding an extra I = 1/2 K* decay to the decay rates given in table 8.4 and neglecting interferences one obtains:

$$(K^- + - o) : (K^o + - -) : (K^o - o\ o) : (K^-\ o\ o\ o)$$
$$= 12 : 8 : 6 : 1 \qquad (8.25)$$

For the first three of these four charge states the expected numbers of events (after correction for V^o visibility and fiducial volume differences) are:

54 ± 40, 15 ± 10, 12 ± 8

whereas the observed numbers (ω^o events having been removed) are:

74 ± 30, < 15, < 15

Thus the 1800 Mev peak is consistent with being the sum of the $K^-\omega^o$ decay mode and part of the K*(1420)π decay mode. (From the ($K^-\omega^o$) mass spectrum one can also obtain a rough upper limit of about 10% on the K*(1420) branching ratio into $K\omega^o$, as mentioned in the previous section).

If the peaks in figure 8.8 really represent the decays of the Q and the L then they necessarily have I = 1/2 since the ω^0 has zero I-spin. The angle ψ between the perpendicular to the ω^0 decay plane and the outgoing K^- (measured in the $K^-\omega^0$ rest frame) serves as an analyser of the spin-parity of the $(K^-\omega^0)$ system. Figure 8.9 shows the distribution of cos ψ for events with $M(K^-\omega^0)$ between 1.7 and 1.9 Gev. If this peak is really due to the L-meson the background seems quite small. A spin-parity of 0^- would give a $\cos^2\psi$ distribution while 1^-, 2^+, ... would give a $\sin^2\psi$ one. The chi-squared probabilities for these two hypotheses ($\cos^2$ and $\sin^2$) are 0.04% and 0.1% respectively whereas the observed distribution is consistent with isotropy (probability = 98%). Thus this tends to support the previous conclusion that L has spin greater than zero and unnatural parity. Also shown in figure 8.9 is the distribution of the cosine of the Jackson angle θ (see chapter 9 for the definition of this angle). Although this distribution depends on the production mechanism the non-isotropy suggests that the spin is non-zero. In this connection it should have been mentioned earlier that the Dalitz plot distribution is independent of the production mechanism, that is, independent of the polarisation of the resonance.

The following observations concerning the possible quantum numbers of the K*(1320) and L(1800) can be made from a consideration of the decay modes investigated (see table 8.15)

i) All modes except those involving π or ρ imply I = 1/2 (if seen).

ii) Decays into $K\eta^0$ and KX^0 are not expected for the same reason as $K\pi$ is not expected, that is, because both η^0 and X^0 are believed to be pseudoscalars.

FIG. 8.9

DECAY ANGLE DISTRIBUTION

$K^-p \longrightarrow K^-p\,\omega$ (N^{*++} EXCLUDED)

$\hookrightarrow \pi^+\pi^-\pi^0$

1.7 GeV < $K^-\omega$ < 1.9 GeV

24.8 EVENTS

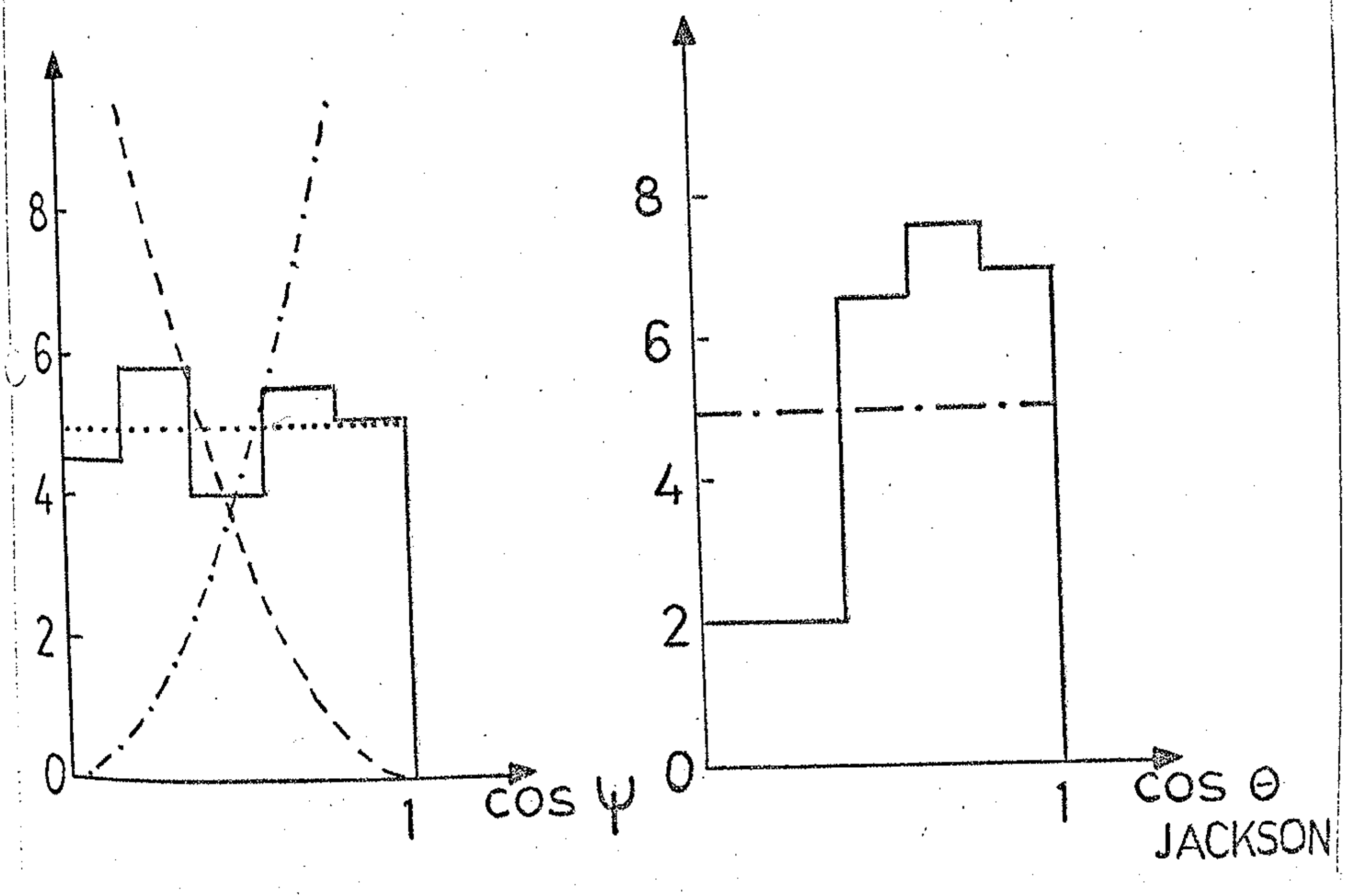

iii) Decays which have a small Q-value (that is, for which the decaying state is only just above threshold) are likely to have the smallest allowable orbital angular momentum because decays with higher values of L will be suppressed by the centrifugal barrier. For the K*(1320) the decay modes $K\rho$ and $K\omega^{o}$ have Q-values of about 60, 41 Mev respectively. Assuming they are in a relative S-wave this means that $J^{P} = 1^{+}$ for the K*(1320). Similarly for the L(1800) the decay mode Kf^{o} (Q = 40 Mev) would imply $J^{P}(L) = 2^{-}$.

The final results for the K*(1320) and L(1800) branching ratios are shown in table 8.15. The cross sections shown are those obtained from the Dalitz plot analysis with additional contributions from the $(K\pi\pi)$ decay of the K*(1420) and from the $(K\omega^{o})$ decay mode. To obtain an independent estimate of the total cross sections the combined $(K + m\pi)^{-}$ mass distribution (m = 1, 2, 3) from reactions 1), 2), 4), 5), 8) and 12) together with $p(K^{-} + - o)$ and $p(K^{o} + - -)$ is fitted to the sum of four Breit-Wigner distributions and a smooth background. The masses and widths of the K*(890) and K*(1420) are fixed at the values obtained earlier from the fit to the sum of reactions 2b) and 3) (see chapter 7). The distribution and the fitted curve are shown in figure 8.10 in which the K*(1420) peak is not resolved because of its relatively small cross section. The fitted values for the masses and widths of the K*(1320) and L(1800) are shown in table 7.1 together with the values obtained earlier (with which they are consistent). Since all reactions in which the Q and L peaks are seen are included in figure 8.9 the areas under the Breit-Wigner distributions represent their total production cross sections. The values obtained are $513 \pm 70 \mu b$ and $169 \pm 34 \mu b$ which are to be compared with those obtained from the sum of the individual branching ratios, namely $575 \pm 72 \mu b$ and $165 \pm 39 \mu b$ respectively. The two sets of values

TABLE 8.15

DECAY MODES OF K*(1320) AND L(1800)

Decay mode	K*(1320) (μb)	K*(1320) %	L(1800) (μb)	L(1800) %
$K\pi\pi$ (direct)	127 ± 43	22 ± 8	48 ± 20	29 ± 13
$K\rho$	119 ± 19	21 ± 4	19 ± 14	12 ± 9
$K^*(890)\pi$	322 ± 55	56 ± 12	58 ± 15	35 ± 12
$K^*(1420)\pi$	-	-	32 ± 25	19 ± 15
$K\omega^0$	7 ± 3	1 ± 0.5	8 ± 4	5 ± 3
TOTAL	575 ± 72	100	165 ± 39	100
(KE^0)*		10 ± 2		5 ± 4
$K\pi$	< 7	< 1	< 7	< 1
$K\eta^0$	< 2	< 0.3	< 3	< 2
KX^0	-	-	< 2	< 1
$K\phi^0$	-	-	< 8	< 5
$K^*(890)\eta^0$	-	-	< 1	< 1
$K^*(890)\omega^0$	-	-	< 2	< 1
$K^*(890)\rho^0$	-	-	< 4	< 3
Kf^0	-	-	< 5	< 3

* This contribution (if it exists) is already included in the $K\rho$ decay rate (see section 8.3)

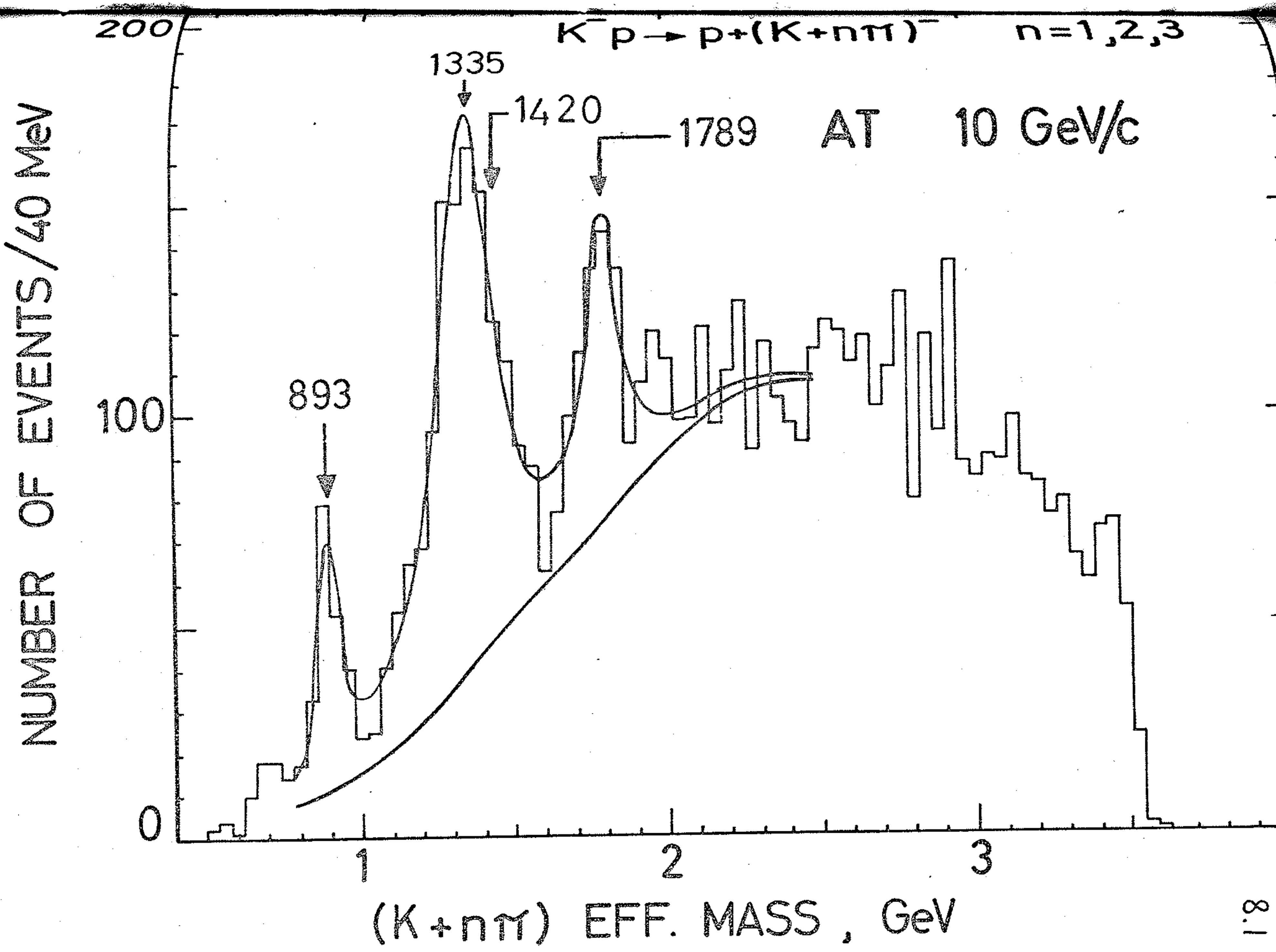
K⁻p → p+(K+nπ)⁻ n=1,2,3
AT 10 GeV/c
1335
1420
1789
893
NUMBER OF EVENTS/40 MeV
200
100
0
1
2
3
(K+nπ) EFF. MASS , GeV

FIG. 8.1

are consistent, especially in view of the fact that the single Breit-Wigner fit to the Q-peak is not too satisfactory.

8.5 SU(3) quantum numbers

Since the discovery of the Ω^- hyperon (86) gave the first conclusive evidence that SU(3) was an approximate symmetry of the strong interactions it has been natural to try and assign the known resonant states to SU(3) multiplets. Although the basic irreducible representation of SU(3) is a multiplet of three (triplet) the multiplets found to occur in nature for meson systems are either singlets ($\underline{1}$) or octets ($\underline{8}$).

Assuming that the SU(3)-breaking interaction transforms like hypercharge, the Gell-Mann-Okubo (GMO) mass formula (77, 87) can be derived for the states in an irreducible representation. This assumption is based on the experimental observation that particles in the same I-spin multiplet (that is with the same hypercharge) have almost equal masses whereas there are relatively large mass splittings between states with different hypercharge. For meson octets the GMO relation leads to the sum rule:

$$4M^2(K) = 3M^2(\eta) + M^2(\pi) \tag{8.26}$$

where K, η, π refer to the members of the 0^- octet or to the corresponding members of other octets. In general (8.26) is not always satisfied because it often happens that SU(3) singlets and octets with the same spin-parity occur in the same mass region. This then allows the possibility of mixing between the singlet state and the $I = Y = 0$ octet state since these have identical sets of quantum numbers. Mixing will occur if their mass separation is less than or of the order of the typical mass splitting within an octet (200 - 400 Mev). In this case the physically observed states (w, ϕ) are linear combinations of the singlet and octet states (So, Io) and are usually expressed in terms of a mixing angle θ :

$$\begin{aligned} w &= S_o \cos\theta + I_o \sin\theta \\ \phi &= -S_o \sin\theta + I_o \cos\theta \end{aligned} \tag{8.27}$$

The quark hypothesis, which assigns fractional internal quantum numbers (B, Q, Y) to the three states of the basic triplet, was introduced to explain the occurrence of singlets and octets and the absence of other multiplets (3, 89). This idea was extended further to imply that hadrons are bound states of real quarks (90) and there have been many experiments which have attempted to observe isolated quarks (see chapter 1). The three quark states are usually labelled (p, n, λ) as they have the same I-spin structure as the particles proton, neutron and lambda respectively. Their values of B, Q and Y are given by:

$$q_i(B, Q, Y) = \begin{matrix} p(+1/3, +2/3, +1/3) \\ n(+1/3, -1/3, +1/3) \\ \lambda(+1/3, -1/3, -2/3) \end{matrix} \tag{8.28}$$

Given I_3, only two of (B, Q, Y) are in fact independent since the Gell-Mann-Nishijima relation (8.1) is satisfied. The meson states are assumed to be bound states of a quark-antiquark ($q\bar{q}$) system and higher spin states are obtained by the excitation of orbital angular momentum between the two quarks. There may also be radial excitations but these are not considered here. The sets of $(q\bar{q})$ states obviously give rise to a nonet structure which, with SU(3)- invariant interactions, is reducible to an octet and a singlet $(\underline{3} \otimes \bar{\underline{3}} = \underline{8} \oplus \underline{1})$. The absence of other possible representations $\underline{10}$, $\overline{\underline{10}}$ and $\underline{27}$ is explained by the fact that they would require bound states of the form $(qq\bar{q}\bar{q})$. These so-called exotic states are assumed to be suppressed relative to the $(q\bar{q})$ states.

A nonet may be described in spectroscopic notation by the symbol $^{2S+1}L_J$ where L represents the orbital angular momentum (S, P, D, F, G, ...), J is the total spin and S is the total Pauli spin (quarks have intrinsic spins of one-half). Since q, $\bar{q}$ have opposite intrinsic parities the overall parity is given by:

$$P = (-)^{L+1} \tag{8.29}$$

The charge conjugation (C) parity for the neutral non-strange (NNS) members of the multiplet is:

$$C = (-)^{L+S} \tag{8.30}$$

so that the G-parity (91) is:

$$G = C(-)^I = (-)^{L+S+I} \tag{8.31}$$

The average nonet mass is expected to increase with L so that the states of lowest mass should correspond to L = 0, for which there are just two nonets, $^1S_0$ and $^3S_1$, with $J^{PC} = 0^{-+}$ and 1^{--} respectively. These correspond to the pseudoscalar and vector meson nonets which were quite well established as SU(3) multiplets before the quark model was proposed. For higher values of L there are always just four nonets since parallel quark spins (S = 1) lead to $J = L \pm 1$, L (triplet state) while antiparallel quark spins (S = 0) lead only to J = L (singlet state). Table 8.16 shows the $(q\bar{q})$ spectrum for values of L up to 4. From this it can be seen that 0^{--} (special case) and all states with $P = -C = (-)^J$ are absent. Such states are called exotics of the second kind to distinguish them from the exotic states mentioned above. No states are known which have these "forbidden" J^{PC} assignments which is additional support for the $(q\bar{q})$ model. The other well-established nonet is the tensor nonet ($J^{PC} = 2^{++}$). This could be assigned to either $^3P_2$ or $^3F_2$ but the former is more likely since it is expected to be lower in mass.

We have seen earlier that $J^P = 1^+$ (axial vector) is the preferred assignment for the K*(1320) peak while 2^- (pseudotensor) seems likely for the L(1800), although the latter could be 3^+ (or even higher in the unnatural parity series). From table 8.16 it can be seen that for each value of L (greater than zero) there are two unnatural parity nonets with the same spin (J = L) but with opposite C-parity for their NNS members. As usual the pairs of I = Y = 0 states in each nonet can be mixings of the pure octet and pure singlet states. However these states (and the I = 1, Y = 0 states) will be well-defined for each nonet separately since they have different G-parity. This is not so for the K* states because they are not eigenstates of G and there can therefore be mixing between

TABLE 8.16

QUARK-ANTIQUARK BOUND STATES

L	TRIPLET			SINGLET
0	$^3S_1$	-	-	^1S_o
	1^{--}	-	-	0^{-+}
1	$^3P_2$	$^3P_1$	^3P_o	$^1P_1$
	2^{++}	1^{++}	0^{++}	1^{+-}
2	$^3D_3$	$^3D_2$	$^3D_1$	$^1D_2$
	3^{--}	2^{--}	1^{--}	2^{-+}
3	$^3F_4$	$^3F_3$	$^3F_2$	$^1F_3$
	4^{++}	3^{++}	2^{++}	3^{+-}
4	$^3G_5$	$^3G_4$	$^3G_3$	$^1G_4$
	5^{--}	4^{--}	3^{--}	4^{-+}

notation: $^{2S+1}L_J$

J^{PC}

the states K_A, K_B which belong to the nonets whose NNS members have $C = \pm 1$. Since the difference in mass between such nonets is expected to be small one might expect that this mixing would be quite substantial and that this would complicate the study of these K*'s. However there is a difference between this kind of mixing and the singlet-octet mixing which suggests that the $K_A - K_B$ mixing may be fairly small. In the SU(3) scheme one can define, by analogy with the G-parity for I-spin, two other parities G_u, G_v connected with U-spin and V-spin respectively (92). These spins are associated with the other two SU(2) subgroups of SU(3) which will be denoted $SU(2)_u$ and $SU(2)_v$. In particular the multiplets with V = 0, 1 are V_o^o and (K^-, $V_1{}^o$, K^+) where

$$(V_o{}^o, V_1{}^o) = \tfrac{1}{2}\begin{pmatrix} 1 & -\sqrt{3} \\ \sqrt{3} & 1 \end{pmatrix} (I_o^o, I_1^o) \quad \text{(here } X_i^j \text{ denotes} \tag{8.32}$$

a state with total X-spin of i and third component j.) The G-parity is given by:

$$Gv = C(-)^V \tag{8.33}$$

In the SU(3)-symmetric limit all three parities G, Gu and Gv are conserved so that, for example, the charged K_A, K_B states, which are eigenstates of Gv with opposite eigenvalues (± 1) do not mix. This is in contrast to singlet-octet mixing which persists even in the SU(3) limit because the two I = Y = 0 states share the same (relevant) quantum numbers. Thus in the real world where SU(3) is broken one might still expect that the $K_A - K_B$ mixing is small whereas one has no reasons in the SU(3) scheme alone for expecting any particular amount of singlet-octet mixing. For (unmixed) kaon states belonging to octets with definite C-parity one can derive relations between various decay modes on the assumption of Gv-parity conservation (93) that is, assuming invariance under the SU(2)v subgroup of SU(3). This is clearly a weaker assumption than assuming full SU(3) invariance since, although it follows from the latter, it obviously does not itself imply SU(3) invariance. Nevertheless some useful relations may be very easily obtained.

In the decay

$$K_1^{*-} \longrightarrow K_2^{*-} + V_i^o \tag{8.34}$$

the conservation of Gv-parity requires that V_i^o is V_o^o or V_1^o according as $C_1C_2C_3$ is even or odd, C_1, C_2, C_3 being the C-parities of the nonets to which the states K_1^*, K_2^* and V_i^o belong. This follows from the fact that the kaon states have Gv = $-C_1$, $-C_2$ while V_o^o, V_1^o have Gv = $\pm C_3$ respectively. (Strictly speaking we should only refer to the C-parity of the NNS members of a nonet but we can define the C-parity <u>of a nonet</u> to mean just this.)

If octet-singlet mixing is neglected, use of (8.32) leads to the relation

$$\frac{R\ (K_1^* \longrightarrow K_2^*\ I_o)}{R\ (K_1^* \longrightarrow K_2^*\ I_1)} = 1 \text{ or } 1/9 \tag{8.35}$$

for $C_1C_2C_3$ = odd, even respectively. This relation involves the total rates for the decay mode indicated, that is, there is an additional factor of three in the denominator to include the two modes $K_2^{*-}\ I_1^o$ and $K_2^{*o}\ I_1^-$ (see table 8.3). In practice octet-singlet mixing may be neglected for the 0^- nonet, since η, η^1 are almost pure octet and singlet states respectively, but not for the vector or tensor nonets. In any case, one can use (8.27) to write

$$
\begin{aligned}
V_o^o &= \tfrac{1}{2}(\omega \sin\theta \quad + \quad \phi\cos\theta \; - \; \sqrt{3}\, I_1^o) \\
V_1^o &= \tfrac{1}{2}(\sqrt{3}\,\omega \sin\theta + \sqrt{3}\,\phi \cos\theta \; + \; I_1^o) \\
S_o^o &= \qquad \omega \cos\theta \; - \; \phi \sin\theta
\end{aligned}
\tag{8.36}
$$

The singlet and octet have the same C-parity so that S_o and V_o have the same G_v since both are V-spin singlets (S is of course a singlet in both I-spin and V-spin so that its indices can refer to either). Thus in the decay leading to the state V_1 ($C_1C_2C_3$ odd) we get immediately the following relation between overall decay rates:

$$K_2^* I_1 : K_2^* \phi : K_2^* \omega = 1 : \cos^2\theta : \sin^2\theta \tag{8.37}$$

In the case where $C_1C_2C_3$ is even there are also contributions from the decay into the SU(3) singlet state S_o, that is, the final state may be written as $a_8V_o + a_oS_o$, where a_8, a_o are the relative proportions of V_o, S_o.
($a_8^2 + a_o^2 = 1$) In this case we get:

$$K_2^*I_1 : K_2^*\phi : K_2^*\omega = 9 : (\cos\theta - \frac{2a_o}{a_8}\sin\theta)^2 : (\sin\theta + \frac{2a_o}{a_8}\cos\theta)^2 \tag{8.38}$$

As a consistency check, putting $a_o = 0$ and $\theta = 0$ in these last two relations, we recover the two cases of (8.35).

If full SU(3) invariance is assumed from the start all possible decays into a given pair of multiplets are related. The relative rates given in table 8.17 are obtained from the tables of SU(3) Clebsch-Gordan coefficients given in reference 94. The relevant case here is the product of two octets which has the following decomposition into irreducible representations:

TABLE 8.17

DECAY RATES FOR $K_1^* \longrightarrow \underline{8}_2 + \underline{8}_3$ ASSUMING SU(3) SYMMETRY

DECAY MODE $\underline{8}_2$ $\underline{8}_3$	$C_1C_2C_3 = +1$ (even)	$C_1C_2C_3 = -1$ (odd)
$K_2^* (I_1)_3$	$9/20 \ \lvert H\rvert^2$	$1/4 \ \lvert M\rvert^2$
$K_2^* \phi_3$	$\lvert H\cos\theta_3/\sqrt{20} + L\sin\theta_3\rvert^2$	$1/4 \ \lvert M\rvert^2 \cos^2\theta_3$
$K_2^* \omega_3$	$\lvert -H\sin\theta_3/\sqrt{20} + L\cos\theta_3\rvert^2$	$1/4 \ \lvert M\rvert^2 \sin^2\theta_3$
$(I_1)_2 K_3^*$	$9/20 \ \lvert H\rvert^2$	$1/4 \ \lvert M\rvert^2$
$\phi_2 K_3^*$	$\lvert H\cos\theta_2/\sqrt{20} + K\sin\theta_2\rvert^2$	$1/4 \ \lvert M\rvert^2 \cos^2\theta_2$
$W_2 K_3^*$	$\lvert -H\sin\theta_2/\sqrt{20} + K\cos\theta_2\rvert^2$	$1/4 \ \lvert M\rvert^2 \sin^2\theta_2$

Notation:

Subscripts 2, 3 denote the two final multiplets; 1 denotes the multiplet containing the decaying K* state. H, M are the octet-octet amplitudes in the two cases $C_1C_2C_3 = \pm 1$ and K, L are the octet-singlet amplitudes corresponding to the SU(3) singlet states $(S_o)_2$, $(S_o)_3$ respectively. The mixing angles between these two singlets and the corresponding octets are θ_2, θ_3. I_1 denotes the I = 1, Y = 0 octet triplet state.

The relative amounts of singlet and octet contributions in the $C_1C_2C_3 = +1$ case are given in terms of the notation used in (8.38) by:

$$H/K\sqrt{20} = -\left(\overset{a_8/2a_0}{\cancel{98/290}}\right)$$

or the same with L replacing K for the other octet-singlet pairing.

$$\underline{8} \otimes \underline{8} = \underline{27} \oplus \underline{10} \oplus \underline{\overline{10}} \oplus \underline{8} \oplus \underline{8}' \oplus \underline{1} \tag{8.39}$$

The appearance of $\underline{8}$ and $\underline{8}'$ on the right hand side implies two distinct couplings between an octet and a pair of octets. For meson systems these correspond to the cases in which $C_1C_2C_3$ is even or odd respectively. The upper and lower halves of table 8.17 each contain information derived earlier using only $SU(2)_v$ invariance. The extension to full SU(3) invariance relates the top half of the table to the bottom half, which is conveniently measured by the ratio between the $K_2^*(I_1)_3$ and $(I_1')_2K_3^*$ decay rates (2, 3 denote the two final octets). If octets 2 and 3 are the same then the two halves of the table are identical and SU(3) gives no extra relations.

The relative rates in table 8.17 have been calculated assuming constant matrix elements for the decays, that is, only the Clebsch-Gordan coefficients have been considered. In practice this will not be correct because of SU(3) breaking interactions. These may be taken account of to first order by using the physical mass values to calculate a phase space factor of the form p^{2l+1}, where p is the momentum of each of the decay products in the rest frame of the resonance and is given by:

$$p = \lambda^{\frac{1}{2}}(m_1^2, m_2^2, m_3^2)/2m_1 \tag{8.40}$$

where the function λ is defined by:

$$\lambda(x, y, z) = (x - y - z)^2 - 4yz \tag{8.41}$$

The mixing angles used have been calculated from the most recent world average values for particle masses (2). Relations (8.26) and (8.27) lead to the following expression for θ :

$$\tan^2\theta = \frac{M^2(\phi) - M^2(I_o)}{M^2(I_o) - M^2(\omega)} \tag{8.42}$$

where $M^2(I_o)$ is obtained from the GMO formula

$$M^2(I_o) = \frac{4M^2(K^*) - M^2(I_1)}{3} \tag{8.43}$$

As is customary for mesons, mass squared values have been used in the calculation though this cannot be rigorously justified (95). This procedure does at least seem consistent with the fact that in relativistic field theories the squared mass has the same status for boson fields as does the mass in the case of fermion fields (96). However the original motivation for using M^2 was to improve the agreement with the GMO mass formula in the case of the pseudoscalar nonet. Since then the vector and tensor octets have been found to violate the GMO formula quite strongly and it is now customary to attribute even the small violation in the 0^- octet to $\eta - \eta'$ mixing. Thus the original reason is no longer present and it is an open question whether M, M^2 or any other power of M should be used (97). This question is open to experimental test and the decay rates of higher resonances is one situation in which such a test may be possible.

The values of the mixing angles obtained are:

$$\begin{array}{lll} \text{for the } 0^- \text{ nonet} & : & 10^\circ 39' \\ 1^- \quad " & : & 39^\circ 47' \\ 2^+ \quad " & : & 33^\circ 6' \end{array} \tag{8.44}$$

The variation of these angles as a function of the power of the mass used in their determination is discussed in reference 97. The vector and tensor nonet mixing angles are fairly insensitive to the power used but the pseudoscalar angle varies quite rapidly. For a linear mass relation the angles are $23^{\circ}30'$, $36^{\circ}58'$ and $31^{\circ}42'$ respectively. The fact that the angle for the 0^{-} nonet is higher in this case whereas the other two angles have decreased is because in the former case it is the lower mass particle (η) which is assumed to be mainly octet. This is a natural assumption since the η very nearly satisfies the GMO formula. In the other two nonets there is clearly a large mixing effect and there is no particular reason within the SU(3) framework for preferring an angle of θ to one of $(\pi/2 - \theta)$. However there are reasons outside SU(3) for preferring the smaller angle. The most general mass Lagrangian for a meson nonet contains four terms whose relative contributions are in general unknown (98). To first order in mass splitting the nonet contains four distinct mass values (e.g. ρ, K*, ω, ϕ) which is just enough to determine the four coefficients in the Lagrangian. If some theoretical ansatz is made which ignores one term (or more) in the Lagrangian, the use of the four physical mass values will allow one (or more) sum rules to be obtained. Schwinger deduced the following sum rule for the vector meson nonet from a field-theoretic starting point (99).

$$(\phi - \rho)(\omega - \rho) = \frac{4}{3}(K^* - \rho)(\phi + \omega - 2K^*) \qquad (8.45)$$

where the symbols represent mass squared values. This relation is well satisfied for the vector nonet and also for the corresponding particles in the tensor nonet. (It is not satisfied for the 0^{-} nonet). Okubo also gave an ansatz in which two of the terms in the general mass Lagrangian were omitted (100). This leads to the two sum rules

$$\rho = w \tag{8.46}$$

$$\rho + \phi = 2K^* \tag{8.47}$$

Again these are well satisfied for the vector and tensor nonets. They correspond to a mixing angle given by:

$$\tan\theta = 1/\sqrt{2} \tag{8.48}$$

which gives $\theta = 35^{o}18'$. This makes it more reasonable to choose ϕ and f^1 as the states with the larger octet contribution since this leads to the mixing angles given in (8.44) which are fairly close to Okubo's "ideal" value. Perhaps more importantly, the same mixing angle (8.48) can be derived from SU(6) symmetry, whereas Okubo did not base his ansatz on any sound theoretical foundations.

The decay rates available experimentally for testing the relations derived above in the case of the K*(1320) and L(1800) are shown in table 8.18. The C-parities of the final nonets are well-known (see table 8.16) so that the tests allow in principle a determination of C_1, the C-parity of the nonet to which the resonance in question belongs. Decays into two pseudoscalars are not included in the table since it is likely that they are forbidden by the unnatural spin-parity of the parent. All possible modes of the types $1^- + 0^-$ and $1^- + 1^-$ are considered although some have their threshold above the mass of the K* (indicated by dashes in the table). This is true for <u>all</u> modes of the form $2^+ + 0^-$, except for the $K^*(1420)\pi$ decay of the L(1800), so that these decays can give no information on C_1. The values of l used for calculating the phase space factors are $l = 0$ (s-wave) for the K*(1320) $\longrightarrow 1^- + 0^-$ decays (assuming $J^P = 1^+$ for the 1320), $l = 1$ (p-wave) for the $L \longrightarrow 1^- + 0^-$ decays and $l = 1$ for the $L \longrightarrow 1^- + 1^-$

TABLE 8.18

COMPARISON OF CORRECTED DECAY RATES WITH $SU(2)_V$ AND SU(3) PREDICTIONS

K*(1320)		Observed rate (%)	P.S. factor	Corrected rate	Predicted rates $C_1 = +1$	$C_1 = -1$	Conclusions
0^-1^-	$K\rho$	21 ± 4	0.216	97 ± 18	1	9	$C_1 = +1$ inconsistent
	$K\phi$	-	-	-	-	-	$C_1 = -1$ consistent
	$K\omega$	1 ± 0.5	0.187	5 ± 3	0.41	0.41	
1^-0^-	$K^*\pi$	56 ± 12	0.350	160 ± 34	1	9	$\frac{K\rho}{K^*\pi} = 0.6 \pm 0.2$
	$K^*\eta$	-	-	-	-	-	
	$K^*\eta^1$	-	-	-	-	-	

L(1800)

0^-1^-	$K\rho$	12 ± 9	0.608	20 ± 15	1	9	$C_1 = \pm 1$ both consistent
	$K\phi$	0 ± 2.5	0.231	0 ± 11	0.59	0.59	within errors
	$K\omega$	5 ± 3	0.578	9 ± 5	0.41	0.41	$\frac{K\rho}{K^*\pi} = 0.4 \pm 0.4$
1^-0^-	$K^*\pi$	34 ± 12	0.715	48 ± 17	1	9	$C_1 = +1$ inconsistent
	$K^*\eta$	0 ± 0.3	0.220	0 ± 1	0.97	0.97	$C_1 = -1$ consistent
	$K^*\eta'$	-	-	-	-	-	
1^-1^-	$K^*\rho$	0 ± 1.2	0.090	0 ± 13	9	1	$C_1 = \pm 1$ both consistent
	$K^*\phi$	-	-	-	-	-	
	$K^*\omega$	0 ± 0.6	0.071	0 ± 8	0.41	0.41	

decays (assuming $J^P = 2^-$ for the L). The observed rates are quoted as percentages of the total decay rate; the rates after correction for SU(3) breaking are quoted in an arbitrary scale. For the $C_1C_2C_3 = +1$ case where there are complications due to coupling to the SU(3) singlet state (see relation 8.38) the predicted rates in table 8.18 have been calculated on the assumption that (a_o/a_8) is zero. That this is not unreasonable can be seen from the fact that combining the $K_2^*\phi$ and $K_2^*\omega$ rates in (8.38) leads to a relation which is independent of the mixing angle, namely:

$$K_2^*I_1 : (K_2^*\phi + K_2^*\omega) = 9 : 1 + (2a_o/a_8)^2 \qquad (8.49)$$

Assuming for the moment that $C_1C_2C_3 = +1$, the experimental rates in table 8.18 require (a_o/a_8) to be not too large and are consistent with it being zero. Furthermore, the conclusions drawn from table 8.18 would not be changed if this ratio was left as a free parameter.

From the comparison between observed and predicted rates it can be seen that C = -1 is strongly preferred for the nonets to which the K*(1320) and the L(1800) belong. In the former case it is the $K\rho/K\omega$ ratio which is the vital one; in the case of the L the sensitive ratio is $K^*\pi/K^*\eta$. Thus the preferred nonet assignments for these two states are:

$J^{PC} = 1^{+-}$ for the K*(1320)

$J^{PC} = 2^{--}$ for the L(1800)

Since two nonets with $J^P = 1^+$ and two with $J^P = 2^-$ are expected in the quark model, it is important to consider the possibility that the observed mass peaks contain both these states. Figure 8.11 shows the $(K\pi\pi)$ mass distribution plotted in narrower bins (10 Mev wide). This might be expected to show some evidence of fine structure in the peak regions if there were really two resonances present. In the Q region there does appear to be some tendency towards two peaks centred at about 1285 and 1335 Mev, especially in the $(K^- + -)$ contribution where the mass resolution is expected to be better (shaded events). These peaks are not very significant and represent deviations from a smooth background of only about 3, 2 standard deviations respectively. The most recent data containing the results of experiments 75, 10 and 12 shows somewhat better evidence for separated peaks at 1290, 1380 and 1460 Mev. However these are seen only in the $(K^0 - o)$ spectrum, whereas the traces of structure in $(K^- + -)$ have been smoothed out by the new data, indicating that they were not statistically significant. Thus the only conclusion from the present experiment alone is that there is no discernible structure in the Q peak.

Structure has however been reported in some other experiments. The LRL group of Goldhaber first reported a separation of the expected K*(1420) signal from the rest of the Q peak in the 4.6 Gev/c experiment (110). Since then several other experiments have resolved the K*(1420) (101, 102b, 109, 111) but since its cross-section is known to decrease at high energy compared to that of the rest of the Q peak, its non-resolution in such experiments is not a serious problem, especially in view of the fact that its contribution can be calculated from the $(NK\pi)$ final states. Apart from the K*(1420) a splitting

FIG. 8.11

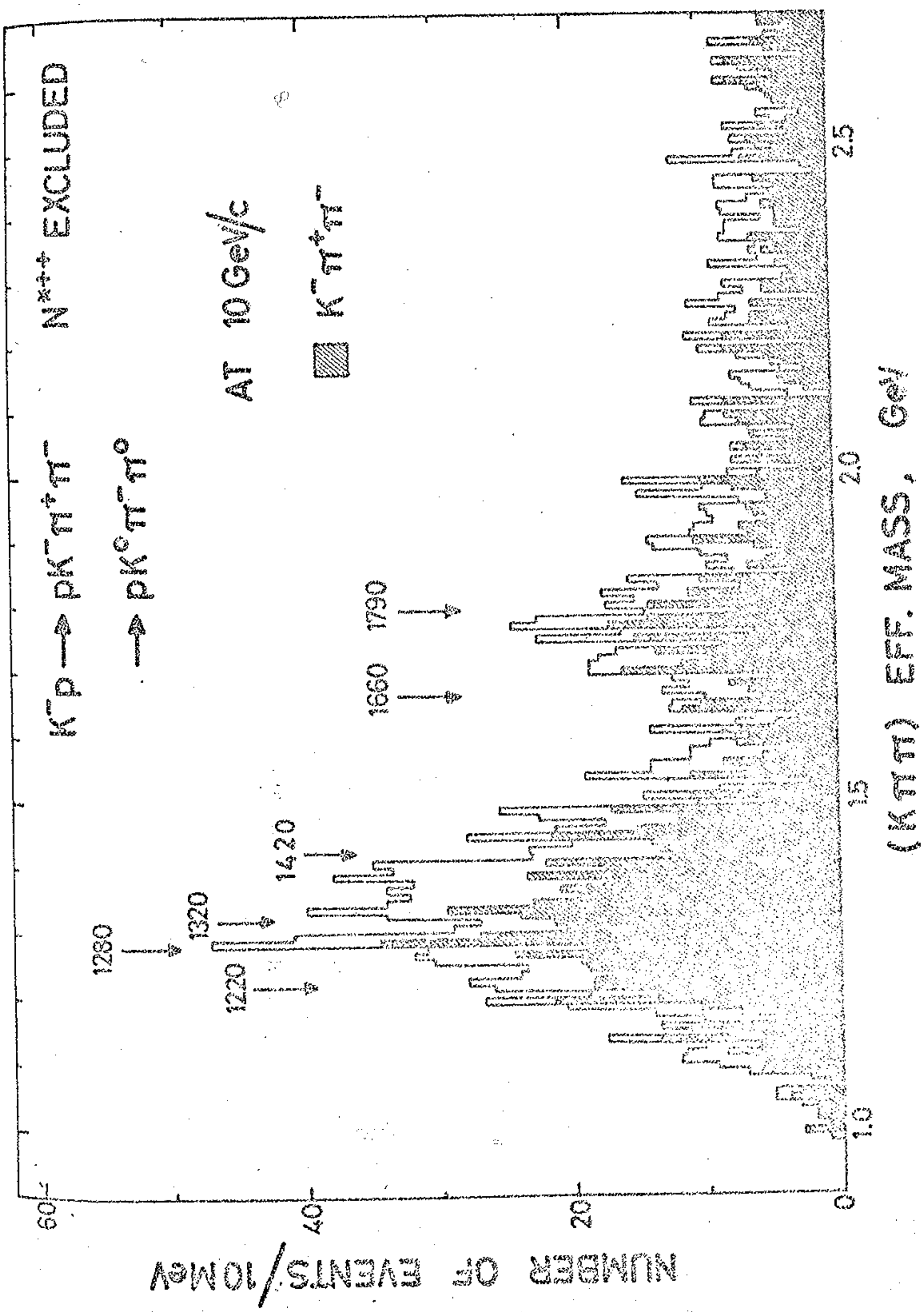
$K^-p \rightarrow pK^-\pi^+\pi^-$
$\rightarrow pK^0\pi^-\pi^0$
N^{*++} EXCLUDED
AT 10 GeV/c
$K^-\pi^+\pi^-$
1220
1280
1320
1420
1660
1790
0
20
40
60
1.0
1.5
2.0
2.5
($K\pi\pi$) EFF. MASS, GeV
NUMBER OF EVENTS/10 MeV

of the Q peak has been reported in the K^+p experiments at 5, 9 and 10 Gev/c (111, 114, 115) but no significant splitting is seen in other experiments, including the one with the most data at present (116). The positions of some of the reported peaks are indicated above the histogram in figure 8.11.

If there are two resonances in the Q-region it is likely that they both have $J^P = 1^+$ since all experiments favour this assignment. Assuming no interference one might expect relative branching ratios which were intermediate between the predictions for $C = \pm 1$ nonet members. The observed $K\rho/K\omega$ ratio for the Q peak, which seemed more consistent with a $C = -1$ assignment, would be reduced if some of the $K\rho$ mode was in fact $K\epsilon^0$. This possibility was discussed in the last chapter as an explanation of the discrepancy in the SU(2)-predicted branching ratios of the $K\rho$ mode. However such a change would make worse the already poor agreement with the SU(3)- predicted decay ratio $K\rho/K^*(890)\pi$ (see table 8.18).

In figure 8.11 there is no evidence for any fine structure in the L region, nor has any been reported in the other experiments which observe a peak in the same mass region. The assignment $C = -1$ is preferred for the L because of the large $K^*(890)\pi$ $/K^*(890)\eta$ decay rate ratio. The $K\rho/K^*(890)\pi$ ratio is again smaller than 1, the value required by SU(3) symmetry, although it has a large error. Better agreement with SU(3) would be obtained if the $K^*(890)\pi$ rate had been somewhat overestimated and this would, at the same time, reduce the $K^*\pi$ $/K^*\eta$ ratio. But even with the largest decrease of $K^*\pi$ consistent with maintaining the $K\rho/K^*\pi$ ratio compatible with

1 (about a factor of 4 change) the C = - 1 assignment will still be strongly favoured.

Thus in spite of the possibility of there being more than one state present in the Q peak (as shown by other experiments, but admittedly at different energies), the Q peak observed in the present experiment does not seem to have a strong contribution from K* states belonging to C = + 1 nonets. The L peak is also consistent with no contribution from C = + 1 states.

8.5.1 <u>Possible existence of higher multiplets</u>

If the K*(1320) and L(1800) are members of SU(3) nonets, one might expect to find the non-strange states required to complete these nonets in roughly the same mass region. The 0^-, 1^- and 2^+ nonets seem to be satisfactorily assigned, the only slight worries being the split A_2 and the E-meson at 1422 Mev. For the latter, spin-parity 0^- is preferred and it therefore has no place in an already complete 0^- nonet. However it is possible that E could be accommodated in the first radial excitation of the 0^- nonet, although one would not have expected such a state to have quite such a low mass (118). This leaves three of the four L = 1 nonets to be accounted for. The situation here has changed very little since the survey by Dalitz at the Philadelphia Conference in 1968 (118).

After a period when each was out of favour as a resonant state the A1(1070) and B(1235) seem now to be well-established (they have I = 1, G = $\pm$ 1 respectively). 1^+ is the favoured spin-parity assignment in both cases so that they are good candidates for the 1^{+-} and 1^{++} nonets. For the I = 1 member of the 0^{++} nonet the $\delta(962)$ seems a reasonable choice; this state is possibly also responsible for the $(K\bar{K})$ enhancement seen at 1016 Mev, just above the $K\bar{K}$ threshold.

The most likely mass for the $1^{++}K^*$ state (we are assuming here that K*(1335) is assigned to 1^{+-}) is about 1240 Mev. This is consistent with the mass of the C-meson, first seen several years ago in $\bar{p}p$ annihilations at rest and recently confirmed (119), and also with the $(K\pi\pi)$ peaks with masses of 1230 $\pm$ 15, 1260 $\pm$ 10 Mev observed in K+p interactions (111, 114). The scalar K* state may have a mass of about 1100 Mev. There have been somewhat contradictory claims for the production of a $(K\pi)$ resonance in this region (see chapter 7 and references 63, 120). However perhaps the best evidence comes from a $(K\pi)$ phase shift analysis carried out using data from the reaction $K+p \longrightarrow K^+\pi^-N^{*++}$, which is known to occur by pion exchange. This predicts a rather wide resonance at 1100-1200 Mev (121).

The situation is not so good in the case of the Y = I = 0 states. The D(1285), which is mainly seen decaying into $(K\bar{K}\pi)$ in $\bar{p}p$ annihilations and has G = C = + 1, is fairly well-established and has a favoured spin-parity of 1^+. There is also the <u>new</u> H-meson at 1000 Mev reported by Goldhaber (122) at the 1969 Lund Conference which has G = C = - 1 and could have $J^P = 1^+$. There is no good evidence for any other 1^+ states with I = 0 although it is just possible that the E-meson might be one since some experiments favour this assignment. $I = 0$ states tend to be a little harder to observe since they occur only in $I_3 = 0$ states which also contain contributions from $I = 1$ resonances. Also states with unnatural spin-parity and positive G-parity are forbidden to decay into either 2 or 3 pions. Thus the most likely decays would be 4π or $K\bar{K}\pi$ and this too makes such states more difficult to study. For the 0^+ I-spin zero states there is one good candidate, the S*(1060). The sigma (or ϵ^0) $\pi\pi$ resonance for which many indications exist but for which there is no absolutely conclusive evidence has a mass which has been variously estimated as anything from 300 to 800 Mev. With the other assignments for the 0^+ nonet this could not be the remaining $I = 0$ state because the following inequality, derived from (8.26) would not be satisfied:

$$\frac{3\omega + \rho}{4} \leqslant K^* \leqslant \frac{3\phi + \rho}{4} \qquad (8.50)$$

(The symbols refer to the squares of the masses and ω is assumed to be the lighter of the two singlet states). The lower and upper limts in (8.50) if ϵ^0 is used are 774 and 1036 Mev compared with the K* mass of about 1100 Mev. If anything, the K* mass would seem to be above 1100 Mev rather than below (121). More simply, ϵ^0 is not acceptable because S*(1068) is below the mass of the pure octet $I = 0$ state as given by the GMO formula (1142 Mev) and thus the other $I = 0$ state must lie above this. There is still one possibility for this state, namely an enhancement seen in three experiments, two in $M(4\pi)$ at 1410 Mev (123) and one in $M(K_s K_s)$ at 1440 Mev (124).

The $K_s K_s$ decay requires the state to have natural spin-parity and $C = +1$ while 4π would imply $G = +1$, that is, if these are different decay modes of the same state it has $I = 0$. Spin-parity 0^+ is preferred over 1^- and 2^+ by Bettini et al.

The possible states belonging to the $L = 0$ and $L = 1$ $(q\bar{q})$ nonets are shown in table 8.19. All the well-established resonances below 1520 Mev are included, as are many of the not so certain ones. The only reported states which do not appear are the $\epsilon^0(700)$, as mentioned above, three exotic states (two with $I = 3/2$, $Y = 1$ and one with $I = 2$, $Y = 0$) for which the evidence is not very convincing in view of the fact that there are as yet no well-established exotics (125), and finally the $A_{1.5}$ (1175).

The situation in the case of the $L = 2$ $(q\bar{q})$ states is somewhat more speculative. For the $I = 1$ states there are two complementary sources of data, bubble chamber experiments and the Cern missing mass spectrometer experiments. The latter reported four states (R1-R4) in the mass region 1600-1900 Mev which are seen in the negative charge state so that they must have $I = 1$ (or 2). Unfortunately the G-parities of these states cannot be determined. Bubble chamber experiments have also reported several states in this region but one of the difficulties here is that they are often observed in the neutral charge state which means that the I-spin cannot be found although the G-parity can. Thus it is sometimes hard to match up the results of the two types of experiment. Spin-parity determinations from decay distributions are difficult for all experiments and have not often been attempted.

TABLE 8.19

POSSIBLE ASSIGNMENTS FOR L = 1 AND L = 2 $(q\bar{q})$ NONETS

L = 1

I	J^{PC} =	2^{++}	1^{++}	0^{++}	1^{+-}
$\frac{1}{2}$		$K^*(1409)$	$K_c(1243)$	$K^*(1100)$	$K^*(1335)$
1		$A_2(1300)$	$A_1(1070)$	$\delta(962)$	$B(1235)$
0		$f(1264)$	$D(1288)$	$S(1062)$	$H(991)$
0		$f'(1514)$	$E(1422)$	$4\pi(1438)$	?

L = 2

I	J^{PC} =	3^{--}	2^{--}	1^{--}	2^{-+}
$\frac{1}{2}$		$K^*(1720)$?	$L(1789)$	$K^*(1852)$	$K^*(1660)$
1		$\rho_N(1663)$	$\rho(1714)$	$\rho(1830)$	$\pi_A(1634)$
0			$\phi(1650)$		$\phi(1750)$?
0			$\phi_A(1830)$		

Only one of the four L = 2 nonets has C = + 1 ($J^{PC} = 2^{-+}$) and a good candidate for its I = 1 state is $\pi_A(1640)$ (also called A_3) which has G = - 1 and a preferred spin-parity of 2^-. The $\rho_N(1660)$ or g-meson is a 2π state and therefore has natural spin-parity. Bose statistics considerations require it to have odd spin and negative parity. Crennell et al. (126) prefer $J^P = 3^-$ from the observed $\pi\pi$ scattering angle distribution so it seems likely to belong to the 3^{--} nonet. The η or $\rho(1830)$ has G = + 1 but could have I = o or 1. If it has I = 1 it could correspond to the R_4 peak at 1820 Mev. In this case it would have C = - 1 and we might reasonably assume it to belong to the 1^{--} nonet since there seems to be a tendency for the MMS set-up to observe only natural parity states. For example the $\rho(1^-)$ and $A_2(2^+)$ are seen but the $A_1(1^+)$ and $B(1^+)$ are not. This could possibly be connected with the fact that the MMS does not observe resonances at very low t-values and states of unnatural parity tend to be produced at smaller t-values than natural parity ones. A bubble chamber experiment studies all t-values in an unbiased way, except for possible scanning biases at <u>very</u> small t. The best candidate for the remaining I = 1 state is the $\rho(1710)$, which could however be the 4π decay of the g-meson although their masses seem to be quite well separated (1714 ± 7, 1663 ± 11 Mev respectively). In the 11 Gev/c experiment two enhancements are seen in the 4π spectrum, a narrow one in $\omega^0\pi$ at 1630 Mev and a broad one in $\rho\pi\pi$ at 1700 Mev (127). It seems likely that the first of these is a decay of the g while the other may be a different state, the ρ (1710), which has the correct G-parity for filling the remaining gap in the $I = 1$ states.

In the case of the K* states we first assign L(1800) to the 2^{--} nonet on the basis of the present experiment. The 5 Gev/c K^+ experiment report a K*(1660) which seems to have a definite $K^*(1420)\pi$ decay mode (111). Since the threshold for such a decay is at about 1560 Mev we would expect this to be an s-wave decay which would mean that K*(1660) could be assigned to the 2^{-+} nonet. There is a slight worry here since the same experiment has some indication of a $K\pi$ decay, seen in constructive interference with N^{*++}. If this is genuine it would imply natural parity, that is, presumably $J^P = 2^+$ with a p-wave $K^*(1420)\pi$ decay. The same group also report a peak at 1850 Mev which they do not claim as definite evidence for a new resonance because it is very close to the maximum of phase space at that energy. However this coincides in mass with a 3 standard deviation peak at 1852 $\pm$ 8 Mev reported in a Missing Mass Spectrometer run using a K^- beam (128). The same spectrum shows a K*(1420) peak but has no sign of the K*(1320) or L(1800) possibly for the reasons mentioned earlier. Thus this peak may correspond to a natural parity state and to maintain rough agreement with the GMO mass formula the assignment 1^{--} seems more satisfactory than 3^{--}. The only other slight indication of a K* state in the mass region 1500-2000 Mev is that a compilation of data made by French (64) showed a peak at about 1730 Mev from K^+p experiments above 7 Gev/c and a peak at 1700 Mev from K^-p experiments of all momenta. Therefore we could very tentatively enter a K*(1720) in the 3^{--} nonet.

As for the L = 1 nonets the experimental situation is worse for the I = 0 members. There is a $\phi(1650)$ with G = - 1 which probably has I = 0 and a $\phi_A(1830)$, also with G = - 1. The latter could have I = 0 or 1 although there would be no place in the L = 2 nonets for the I = 1 possibility. Both are likely to have unnatural parity, since they are not seen in the $(\pi\pi)$ mass spectrum which has been well studied in this region, and thus they are candidates for the 2^{--} nonet. Because the neutral g-meson peak has a higher mass (1680 Mev) than the charged peak (1640 Mev) it has been suggested (64) that there might be an I = 0 resonance at about 1750 Mev but there has been no confirmation of this. It would have G = C = + 1 and thus could possibly be assigned to the 2^{-+} nonet.

The assignments for the L = 2 nonets are shown in table 8.19. The only reported states in the mass range 1520 - 1900 Mev which have not been accommodated are the $F_1(1540)$, the R_2 and R_3 MMS peaks (although R_2 could correspond to the $\rho(1710)$) and the $K\bar{K}\pi$ peak reported by French et al. (129) which could be the same as R_3.

8.6 Tests of assignments to higher multiplets

8.6.1 Partial decay rates

Having assigned the K*(1320) and L(1800) to nonets in the $(q\bar{q})$ model one can compare their partial decay rates with those of other states in the same nonet. Similar calculations have been carried out before for 1^+ and 2^- nonets (130, 131) but these have been somewhat superceded by subsequent experimental information. The full expression for the partial width of a two-body meson decay may be written (132):

$$\Gamma_i = N \cdot G^2 \cdot \frac{p}{M^2} \left(\frac{p^2 X^2}{p^2 + X^2} \right)^{\ell} \qquad (8.51)$$

where N is the reduced matrix element squared

G is a Clebsch-Gordan coefficient

(p/M^2) is the two-body phase space factor (p being the centre-of-mass momentum and M the mass of the decaying state)

and the last factor represents the angular momentum barrier, X being the inverse interaction radius.

For a set of decays related by SU(3) it is usually assumed that N is constant. A discussion of this and the many other assumptions inherent in the use of (8.51) is given in reference 132. In most applications the value of X is found to be large compared with p and it is customary to set it equal to infinity. The partial widths are then proportional to $G(p^{2\ell + 1}/M^2)$.

The comparison of partial widths is made between the K*(1320) and L(1800) and the I = 1 members of the same octets, as previously assigned. As a check on the assignments of the two K* states to C = -1 octets another comparison is made on the assumption that they belong instead to C = +1 octets. I = 0 states are not considered because of the complications introduced by mixing and also because the experimental evidence concerning them is poorer than that for the I = 1 states. Table 8.20 shows the predictions for decays of the types $1^+ \longrightarrow 1^- + 0^-$, $2^- \longrightarrow 1^- + 0^-$ and $2^- \longrightarrow 2^+ + 0^-$. The Clebsch-Gordan coefficients are taken from reference 133; the choice of symmetric or antisymmetric couplings (denoted by D, F in the table) depends on whether the product of the C-parities of the three octets concerned is even or odd respectively. For the decays involving I = 0 states the G^2 column contains an additional factor of 1/3, corresponding the approximate value of $\sin^2\theta$. A rough measure of the compatibility between the observed and predicted partial widths is obtained by dividing their difference by the sum of their errors. This number is shown in the last column of the table and we can regard the values greater than 2 as being unacceptable while those less than 1.2 seem consistent. There is however one additional factor which has not been considered. For the I = 1 decays which involve D-type (symmetric) coupling there can be contributions to the same decay modes from singlet-octet coupling as well as from octet-octet coupling. This could be taken account of by introducing additional parameters but this is probably not worthwhile here. Such contributions must be particularly important in the decay $B \longrightarrow \omega\pi$ since

TABLE 8.20

COMPARISON OF $I = 1$ AND $I = \frac{1}{2}$ PARTIAL DECAY RATES

C	Decay mode	Type of coupling	G^2	ℓ	$\frac{p^{2\ell+1}}{M^2}$	Partial widths (Mev) Experiment	: Predicted	X
	$1^+ \longrightarrow 1^- + 0^-$							
+	$A_1 \longrightarrow \rho\pi$	F	2/3	0	0.203	95 ± 35	input	-
+	$Q \longrightarrow K^*(890)\pi$	F	1/4	0	0.195	110 ± 24	34 ± 13	2.1
-	$B \longrightarrow \omega^0\pi$	D	1/15	0	0.230	102 ± 20	input	-
-	$Q \longrightarrow K^*(890)\pi$	D	9/20	0	0.195	110 ± 24	390 ± 80	2.7
	$2^- \longrightarrow 1^- + 0^-$							
+	$\pi_A(1640) \longrightarrow \rho\pi$	F	2/3	1	0.093	< 26	input	-
+	$L \longrightarrow K^*(890)\pi$	F	1/4	1	0.090	46 ± 16	< 9	2.3
-	$\rho(1710) \longrightarrow \omega^0\pi$	D	1/15	1	0.102	17 ± 7	input	-
-	$L \longrightarrow K^*(890)\pi$	D	9/20	1	0.090	46 ± 16	98 ± 40	0.9
	$2^- \longrightarrow 2^+ + 0^-$							
+	$\pi_A(1640) \longrightarrow f^0\pi$	D	1/15	0	0.114	23 ± 13	input	-
+	$L \longrightarrow K^*(1420)\pi$	D	9/20	0	0.099	25 ± 19	135 ± 75	1.2
-	$\rho(1710) \longrightarrow A_2\pi$	F	2/3	0	0.117	27 ± 13	input	-
-	$L \longrightarrow K^*(1420)\pi$	F	1/4	0	0.099	25 ± 19	9 ± 4	0.7

the assumption of only octet coupling predicts a partial width of 390 Mev for the corresponding K* state, which is much greater than one would expect. The strongest conclusions come therefore from the F-type couplings and these indicate in all 3 cases definite preferences for the assignment C = -1 to the K*(1320) and the L(1800).

8.6.2. Mass splitting

Following the success of SU(3) as a description of hadron states the group SU(6), which contains as sub-groups SU(3) (for internal symmetry) and SU(2) (for intrinsic spin J), was suggested as a possible symmetry of the hadron spectrum (134). This extension was analogous to Wigner's description of the nucleon-nucleon system in terms of SU(4) at an energy where contributions from strange particles effects were negligible (135).

In the quark model, the low-lying $(q\bar{q})$ states possess SU(6) symmetry (to the extent that the motions of the individual quarks may be treated non-relativistically). The validity of the static approximation may be justified by the large masses that quarks must have (if they exist) for them not to have been easily observed at current accelerator energies. Whether the $(q\bar{q})$ model or SU(6) (or neither) is generally true for the whole meson spectrum is a matter for experimental test.

The L = 0 states correspond in SU(6) to irreducible multiplets with dimensionality 35 and 1, obtained from the product:

$$\underline{6} \otimes \underline{6}^* = \underline{35} \oplus \underline{1} \tag{8.52}$$

The SU(6) singlet is the SU(3) singlet of the $^1S_0$ nonet. Higher clusters in the $(q\bar{q})$ model contain in general 36(2L + 1) states and may be described in terms of the representations of the group $U(6) \otimes U(6) \otimes O(3)$ (136), whereas in SU(6) the higher meson states are usually assigned to the multiplets $\underline{189}$ or $\underline{405}$ (137, 138). One disadvantage of these higher SU(6) multiplets is the presence of exotic states, none of which have been established experimentally.

Mass splitting between $(q\bar{q})$ nonets having the same value of L is caused by the presence of non-central but SU(3) symmetric forces. There are several possibilities for such forces, any or all of which may contribute in a given situation.

a) Spin-orbit force

This is analogous to the Russell-Saunders $(\underline{L}.\underline{S})$ coupling between electrons which is one of the contributions to fine structure in atomic spectra (139); it gives rise to a mass contribution of the form:

$$M^2 = \tfrac{1}{2} a^2 \Big(J(J+1) - L(L+1) - S(S+1) \Big) \tag{8.53}$$

This gives the following contributions (in units of a^2) to the four nonets in a given L-cluster:

$$^3L_{L+1} : {}^3L_L : {}^3L_{L-1} : {}^1L_L = L : -1 : -(L+1) : 0 \tag{8.54}$$

Thus the two L = J nonets have splittings which are independent of L while the states with $J = L \pm 1$ occur on either side of the L = J pair and move farther away as L increases.

b) <u>Spin-spin force</u>

This corresponds to the j-j coupling in atomic spectra (139). It contributes a term

$$b^2 S(S + 1) \tag{8.55}$$

that is, $2b^2$ for triplet states and zero for singlet states.

c) <u>Tensor force</u>

This gives the following contributions to an L-cluster

$$^3L_{L+1} : {}^3L_L : {}^3L_{L-1} : {}^1L_L = \frac{L}{2L+3} : -1 : \frac{L+1}{2L-1} * : 0 \tag{8.56}$$

Thus the two L = J nonets again have L-independent mass contributions whereas those with $J = L \pm 1$ have relative splittings which approach $\frac{1}{2}$ (from below and above respectively) as L increases.

The predictions for the splittings due to these three types of force are shown in table 8.21 for the ten assigned nonets. The relevant nonet mass to use is that of the I = 1 state, which is also shown in the table.

For the L = 0 nonets the spin-spin coupling must be the dominant cause of the large mass splitting since both spin-orbit and tensor forces would predict ^1S_o to lie above $^3S_1$. For the L = 1 cluster, spin-orbit splitting predicts equal mass separations for the states $^3P_2$, $^1P_1$, $^3P_1$, ^3P_o (in order of decreasing mass). The observed separations are 0.165, 0.380 and 0.220 Gev^2 which is quite good agreement compared with the tensor force which would predict ^3P_o to have the highest mass. The <u>S</u>.<u>S</u> forces do not seem important in this case either. (Because of the splitting of the A_2 it is not clear what mass value should be used for the 2^+ state. If a value of 1.32 were used in place of 1.30 the value

TABLE 8.21

MASS SPLITTING WITHIN ASSIGNED $(q\bar{q})$ NONETS

L	Nonet	$M^2(\rho)$	L.S	T	S.S	$(K^*-\rho)$
0	$^3S_1, 1^{--}$	0.585	-1	-1	2	0.211
	$^1S_o, 0^{-+}$	0.019	0	0	0	0.227
1	$^3P_2, 2^{++}$	1.690	1	1/5	2	0.296
	$^3P_1, 1^{++}$	1.145	-1	-1	2	0.400
	$^3P_o, 0^{++}$	0.925	-2	2	2	0.285
	$^1P_1, 1^{+-}$	1.525	0	0	0	0.257
2	$^3D_3, 3^{--}$	2.766	2	2/7	2	0.192
	$^3D_2, 2^{--}$	2.938	-1	-1	2	0.261
	$^3D_1, 1^{--}$	3.349	-3	1	2	0.081
	$^1D_2, 2^{-+}$	2.670	0	0	0	0.086

of the first difference quoted above would be increased to 0.244).

For the L = 2 nonets spin-orbit splitting does not seem to be so dominant. Instead of predicted separations of 2:1:2 the observed values are 0.096 : -o.268 : -0.411. A tensor force gives better agreement for the triplet state where the experimental separations of 0.583, 0.096 are to be compared with the expected ratio of 5:2. The singlet state is too low in mass but this could be explained by the presence of a spin-spin term with the <u>same</u> sign as in the L = 0 case, in contrast to the speculation of Zweig (140). Greenberg (141) has discussed the possibility of obtaining agreement with a suitable mixture of spin-orbit and tensor forces and considers that this can be achieved within errors.

The splitting <u>within</u> a nonet due to SU(3)-<u>breaking</u> interactions can be explained most simply in the quark model by assuming the λ-quark to have a larger mass (by an amount d) than the p and n quarks, which are kept equal in mass to preserve the $SU(2)_I$ symmetry. Each λ-quark which is contained in the quark structure of a state is assumed to contribute an amount d to its mass, weighted by the coefficient of its contribution to the state. Because the I = 0, Y = 0 states can mix, the masses of the physically observed states will be functions of both d and the mixing angle. The best test of the above assumption is therefore to use the I = 1 and I = $\frac{1}{2}$ states, for which the following relation exists between the squares of the masses:

$$d^2 = K^* - \rho \qquad (8.57)$$

The values of d^2 for each of the 10 nonets are shown in table 8.~~20~~ 21 and it can be seen that the above relation is quite well satisfied in most cases, especially when it is considered that the mass values are not known very accurately for the higher multiplets.

One particularly simple form of nonet, often known as an SU(6) nonet, is that proposed by Okubo (87) and which was discussed earlier. (It should be noted that the term "ideal", which is sometimes used for such a nonet, is used by Dalitz (118) to refer to a rather more general type of nonet, namely one satisfying the Schwinger relation). The Okubo ansatz is equivalent in the quark model to having equal masses for the octet and singlet states which make up the nonet. In this case the physical singlet states consist of only non-strange and strange quarks and this implies that states containing only strange or ~~only~~ non-strange quarks respectively cannot couple to the singlet states via a one-quark transition. The resulting mass relations

$$\rho = \omega$$

$$\phi + \omega = 2K^*$$

are well-satisfied for the vector and tensor nonets. This is consistent with the observations that $\phi(1020)$ and f'(1514) decay mainly into strange particles whereas f(1264) does not. Unfortunately it is not easy to test these relations very easily in the case of the higher nonets because the assignment of the I = 0 states is not always possible and, even where it has been done, is probably the most suspect part of the whole scheme. However, as was noticed also by Niizeki (131), the 2^{--} nonet does appear to satisfy the two mass relations fairly well, the values of the two sides being (in mass squared):

$$2.94 = 2.72$$

and $$6.07 = 6.40$$

8.7 Regge trajectory assignments

If the Regge hypothesis (142) is valid for the strong interaction scattering amplitude the spins of the particles and resonant states are expected to be smooth functions of their masses (143). The dependence of J on M may be represented on a Chew-Frautschi plot (144) by smooth curves known as Regge trajectories. Unlike the situation in potential scattering where the Regge hypothesis originated, the strong interaction trajectories appear to be approximately linear. For mesons linearity is better satisfied if mass squared values are used; this can be justified by the same arguments given earlier in the case of mass formulae. The Regge concept is particularly useful in a crossing symmetric situation since the trajectory function which joins the various particles, when extrapolated to the negative mass region, should also describe the particle system which is exchanged in the t-channel (or u-channel in the case of baryon trajectories). The particles which lie on a particular trajectory share the same internal quantum numbers but have spins which differ by units of two. In the case of baryons there are a large number of states with well-established spin-parity and these are found to lie on linear trajectories with slopes of about $1 \mathrm{Gev}^{-2}$. For mesons there have been relatively few conclusive J^P determinations mainly because the technique of phase-shift analysis used for baryons is not applicable (at least not in such a simple way) to meson systems. As a result there have been few Regge recurrences established for mesons. However the description of t-channel processes in terms of Regge trajectory exchange has shown that the hypothesis of linear trajectories is not inconsistent with experiment. States belonging to L = 2 nonets could be the first Regge recurrences of corresponding states in L = 0 nonets. Actually only states in the 3^{--} and 2^{-+} L = 2 nonets can be recurrences since the 2^{--} and 1^{--} correspond to nonsense states for the L = 0 $(q\bar{q})$ system (145). For the first recurrences on trajectories belonging to these last two nonets we would have to go to at least L = 3 $(q\bar{q})$ states and these have not been dealt with here. Instead we can make use of the hypothesis of exchange degeneracy (146) which assumes that the <u>same</u> trajectory function describes pairs of trajectories sharing the same internal quantum numbers except for having opposite values of C, P and signature (the signature of a meson trajectory is ± 1 according to whether it joins states with even or odd spin values). This then implies that states in the unnatural spin-parity nonets ^3L_L, ^1L_L each constitute a single degenerate trajectory. For the natural parity states the situation is not uniquely defined as there are two trajectories for each signature and therefore two ways of combining the four trajectories in order to achieve exchange degeneracy. It seems natural to assume that it is pairs within the same nonets which become degenerate (147). This is supported by the fact that if the other choice is made the combined trajectory would be forced to have a negative slope when passing through some integral spin values, a condition which is not allowed if the trajectory is to give rise to physical resonances at such values.

Exchange degeneracy arises in a natural way for mesons when they assumed to consist of a $(q\bar{q})$ pair (or if they are assumed to be bound states of a baryon-antibaryon system as suggested by Fermi and Yang (148). The difference between a pair of trajectories with opposite signature arises from the presence of a space-exchange potential. In the $(q\bar{q})$ model such a potential corresponds to the exchange of two quarks (or two antiquarks) in the u-channel and this is expected to be weak compared to the direct potential because of the large quark mass.

The assigning of higher meson resonances to Regge trajectories has been discussed before by several authors (147, 149). Many of these discussions have been highly speculative since they have allocated states to trajectories even when there are no indications as to their spin-parities; this is particularly true of the peaks found in the missing mass spectrometer experiments.

A linear Regge trajectory is usually specified by its slope and its intercept at $M^2 = 0$. These parameters have been calculated for the assigned states, assuming exchange degeneracy when necessary due to the lack of two states on a single trajectory. The results are shown in table 8.22 for the $I = \frac{1}{2}$ and $I = 1$ states separately. It can be seen that there is very good agreement between the slopes for corresponding $I = \frac{1}{2}$ and $I = 1$ trajectories. The intercepts for the K* trajectories are lower in every case but this is simply a reflection of the fact that, for a given nonet, the K* states have mass squared values which exceed those of the I = 1 states by about 0.200 Gev^2. For the $^3L_{L+1}$ and ^1L_L cases we have three points which should lie on the same trajectory if the assumption of exchange degeneracy is valid. The lower part of table 8.22 shows the slopes calculated for each pair of particles (the pair 1-3 is the same as that given in the top half of the table). In each case the 1-2 slope is less than the 2-3 slope which means that the trajectory 1-3 is in each case higher than the partner of opposite signatures (to the extent that the linearity of the trajectories is a valid approximation). The small slopes found for the two nonets where exchange degeneracy had to be assumed may be partly due to the same effect but not entirely since their slopes are less even than the calculated 1-2 slopes for the other nonets. The direction of separation is not correlated with the signatures since two nonet sequences ($^3L_{L-1}$ and ^1L_L) have their positive signature trajectories higher while the other two have the negative signature ones higher. Nor is there any connection between natural or unnatural parity and the signature of the higher trajectory.

Although exchange degeneracy is not satisfied exactly the pairs of trajectories from each nonet sequence are fairly cleanly separated from each other. This can be seen from table 8.23 which shows the intercepts for each of the sixteen trajectories. (Where only one state exists on a trajectory the slope used is the mean of the slopes for the better determined cases). In both the $I = \frac{1}{2}$ and $I = 1$ cases the trajectories occur in the order (starting with the highest or leading trajectory) ${}^3L_{L+1}$, ${}^1L_L$, ${}^3L_L$ and ${}^3L_{L-1}$, with some slight overlapping between the middle pair. Thus the hypothesis of exchange degeneracy does seem to be approximately satisfied.

TABLE 8.22

REGGE TRAJECTORY PARAMETERS

	${}^3L_{L+1}$	${}^3L_L$	${}^3L_{L-1}$	${}^1L_L$
$I = \frac{1}{2}$				
slope	0.93	0.61	0.45	0.80
intercept	0.26	0.07	-0.55	-0.20
$I = 1$				
slope	0.92	0.56	0.41	0.75
intercept	0.46	0.36	-0.38	-0.01

Assuming exchange degeneracy

	${}^3L_{L+1}$	${}^3L_L$	${}^3L_{L-1}$	${}^1L_L$
$I = \frac{1}{2}$				
slope 1-2	0.84	0.61	0.45	0.65
" 2-3	1.03	-	-	1.03
" 1-3	0.93	-	-	0.80
$I = 1$				
slope 1-2	0.91	0,56	0.41	0.66
" 2-3	0.93	-	-	0.87
" 1-3	0.92	-	-	0.75

TABLE 8.23

INTERCEPTS OF THE $(q\bar{q})$ MESON TRAJECTORIES

Nonet	Signature	$I = \frac{1}{2}$	$I = 1$
$^3L_{L+1}$	-	0.26	0.46
	+	0.15	0.45
^1L_L	+	-0.20	-0.01
	-	-0.43	-0.14
^3L_L	-	-0.34	0.04
	+	-0.78	0.47
$^3L_{L-1}$	+	-1.05	-0.78
	-	-1.98	-1.81

CHAPTER 9

GENERAL BEHAVIOUR OF REACTIONS AT HIGH ENERGY

Having established the quantum numbers of the K* resonances observed in 10 Gev/c K^-p interactions the second important problem can be tackled, namely that of explaining the dynamics of the production process in each of the four cases.

The following are the quasi two-body reactions which will be discussed:

$K^-p \longrightarrow$	pK^-	a)
	$pK^*(1320)$	b)
	$pL^-(1800)$	c)
	$pK^{*-}(890)$	d)
	$pK^{*-}(1420)$	e)
	$nK^{*0}(890)$	f)
	$nK^{*0}(1420)$	g)
	$N^{*+}(1236)K^-$	h)
	$Y_1^{*+}(1385)\pi^-$	i)

Of these b)-g) are those which are being studied in detail here; the other three reactions will be referred to from time to time by way of comparison.

The experimental information available for a quasi two-body reaction in which a spinless meson hits an unpolarised nucleon target and in which the polarisation of the final state nucleon is undetected, may be divided into 3 categories:

i) total cross section for the reaction;

ii) production angular distribution;

iii) decay angular distribution, when one of the particles decays.

9.1 Total scattering cross sections

Before discussing total cross sections for individual reactions it will be useful to mention briefly the behaviour of the total scattering cross section for a pair of hadrons, that is, the value summed over all possible reactions. In the low energy region (up to about 2 Gev/c incident momentum) this quantity is dominated by a series of peaks due to direct-channel resonances, provided the s-channel quantum numbers are non-exotic. Above this momentum the effect of these resonances dies away and all cross sections fall slowly, some more slowly than others, up to about 30Gev/c. This behaviour seemed to be consistent with the theorem, first proved by Pomeranchuk (150) from dispersion relations and later by other authors from different initial assumptions (151), which requires equal total cross sections for the scattering of a particle and its antiparticle on a given target particle in the limit of infinite energy (this is called the asymptotic limit). The differences between particle and antiparticle cross sections did seem to be monotonically decreasing functions of momentum for the pairs $\pi^{\pm}p$, $K^{\pm}p$ and $\bar{p}p$, pp. (Actually the asymptotic equality of $\pi^{\pm}p$ cross-sections follows from the weaker assumption of I-spin independence (152)). However measurements of $\pi^{-}p$, $K^{-}p$ and $\bar{p}p$ total cross sections up to 65 Gev/c at the Serpukhov proton synchrotron (153) have shown that although the $\bar{p}p$ cross section continues to fall the cross sections for π^{-} and K^{-} flatten off and appear to become constant. As yet no measurements have been made with positive beam particles so the behaviour of the particle-antiparticle cross-section difference is not known. To maintain consistency with the Pomeranchuk theorem it seems as if the $\pi^{+}p$ and $K^{+}p$ cross sections will have to increase from their values at 30 Gev/c.

9.2 Total cross-section for individual reactions

The general behaviours of the total cross section for a particular reaction as a function of increasing energy is that it rises from zero at threshold, reaches a maximum and then falls off monotonically. If the threshold is low enough and if the s-channel quantum numbers are non-exotic there may be dominant resonant peaks superimposed on the otherwise smooth energy dependence in the region below 2 Gev/c incident momentum. Indeed it is just the presence of resonances in the more important reactions at this energy which gives rise to the peaks in the total cross sections.

For some reactions the high-energy cross section falls off very slowly (at a similar rate as do the total cross sections) while for others it falls off very much faster. It is clear that at least some of the partial cross sections must fall off faster than the total scattering cross sections in order to accommodate the new channels which are continually opening up and which are observed to have non-zero cross sections.

In the region above its maximum the total cross section for a reaction is reasonably well described by an expression of the form:

$$\sigma = K(p/po)^{-n} \tag{9.1}$$

where K and n are constants for a particular reaction, p is the incident laboratory momentum and po is a universal scaling factor which may be conveniently taken as 1 Gev/c (154). For quasi two-body reactions it has been found that there is a fairly clean separation into four groups according to the value of the exponent n in (9.1). From the reactions which fall into each group it is clear that there is a correlation between the grouping and the values of B, Y which are exchanged between the initial and final particles:

I) $n = 0.2$: exchange of $B = 0$, $Y = 0$

II) $n = 1.6$: " " $B = 0$, $Y = 0$

III) $n = 2.0$: " " $B = 0$, $Y = 1$

IV) $n = 3$–4 : " " $B = 1$, $Y < 1$

To these one may add a fifth category which corresponds to the exchange of an exotic set of quantum numbers:

V) $n = 10$: exchange of an exotic (B, Y) pair (155)
(These values of n are average values for the reactions in each class).

In the high-energy region all quasi two-body reactions are strongly peripheral. Where $B = 0$ is exchanged it is the momentum transfer t between initial and final mesons (or between initial and final baryons) which takes on only small values. This corresponds to a simple description in terms of t-channel exchanges. (It is assumed here that we are considering a meson-baryon interaction but there is no essential difference involved for reactions with incoming baryons or antibaryons). When the exchanged system has $B = 1$ then the momentum transfer u from initial meson to final baryon (or vice versa) will be dominantly small. Thus each quasi two-body reaction at high energy can be cleanly separated into two reactions, corresponding to the forward and backward peaks. The forward peak reaction will contribute to type I, II, III or V whereas the backward peak will belong to IV or V. The division into just these particular classes is to a certain extent arbitrary. In principle each combination of exchanged quantum numbers should constitute a type whereas the baryon exchange and exotic exchange reactions have each been grouped as a single type. A more detailed study of such reactions might enable subdivisions to be made according to the values of n, for example into strange and non-strange baryon exchange reactions.

The six reactions which are being studied in detail are all of the general form:

$$K^- p \longrightarrow pK^{*-} \text{ or } nK^{*0} \qquad (9.2)$$

In the t-channel these correspond to non-strange meson exchange, that is types I or II; in the u-channel they correspond to type V since a baryon of positive strangeness would need to be exchanged. So far we have not distinguished between categories I and II, both of which involve B = 0, Y = 0 exchange. Reactions in class I are distinguished by having all their exchanged internal quantum numbers zero (or positive for multiplicative ones like G-parity). This set of quantum numbers is often referred to as the set of quantum numbers of the vacuum. The above condition is a necessary but not a sufficient one for a reaction to belong to I because class II also contains reactions with the vacuum quantum numbers exchanged. This class also contains the other reactions with I = 0, Y = 0 exchanged, for example, those where the exchanged I-spin or charge is non-zero or where the exchanged G-parity is negative. Figures 9.1 and 9.2 show the log-log plots of σ against p for reactions f), d), e), g) and h). If (9.1) holds these should be straight lines of slope $-n$. The lines in figure 9.1 are actually drawn for n = 2 whereas in figure 9.2 they are obtained by fitting to the expression (9.1) using data above 3Gev/c.

Table 9.1 shows the values of the exponent n for reactions a) - i). In all cases it is the forward peak (t-channel exchange) which is being considered. The quasi two-body reactions account (as far as is known) for only about 19% of the total cross section at 10 Gev/c so that even if we had a successful description of them we would still not have a complete understanding of the K^-p system.

FIG. 9.1

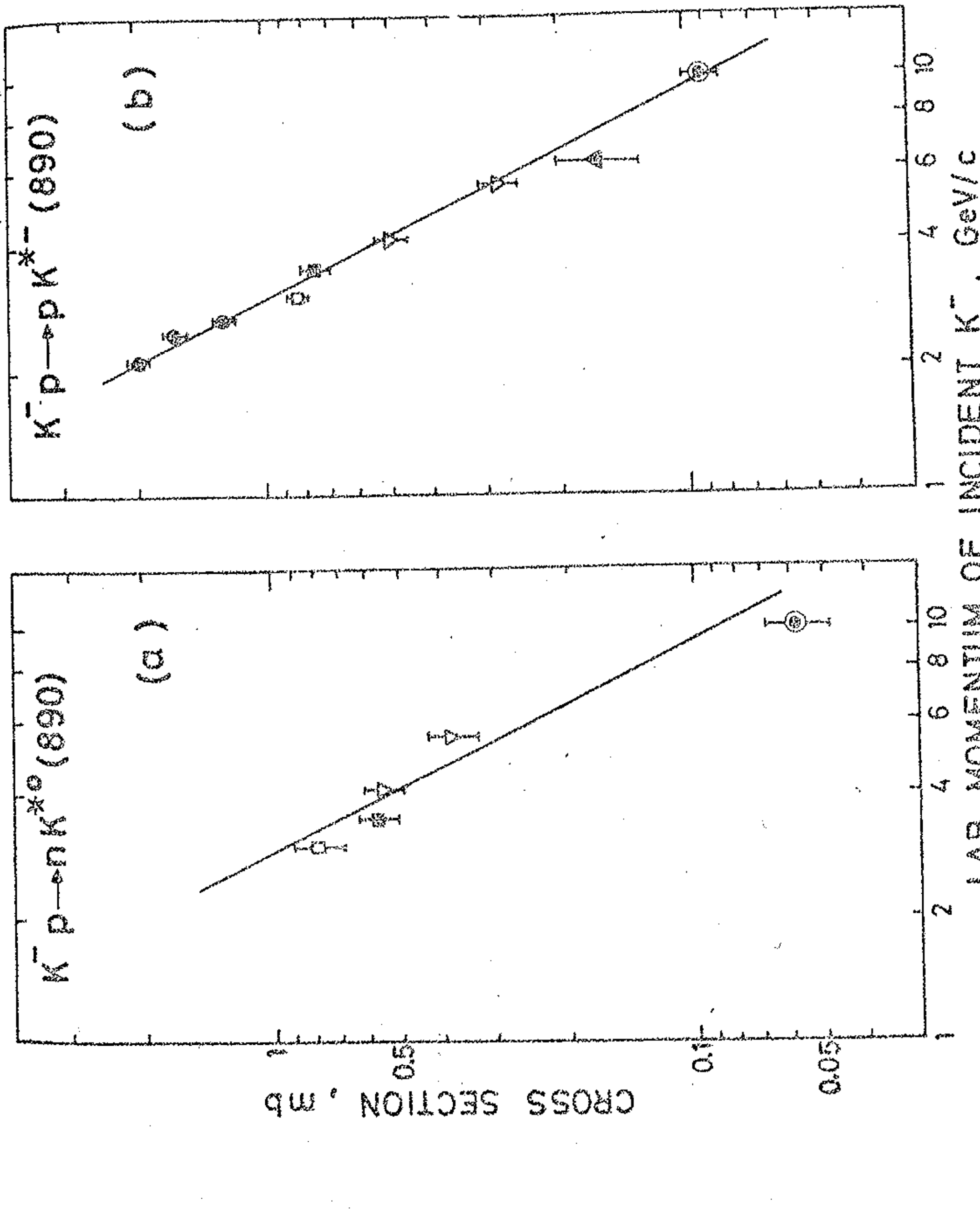
$K^- p \to p K^{*-}(890)$
(b)
$K^- p \to n K^{*0}(890)$
(a)
CROSS SECTION , mb
LAB. MOMENTUM OF INCIDENT K^- , GeV/c
1
0.5
0.1
0.05
1
2
4
6
8
10

Fig.9.

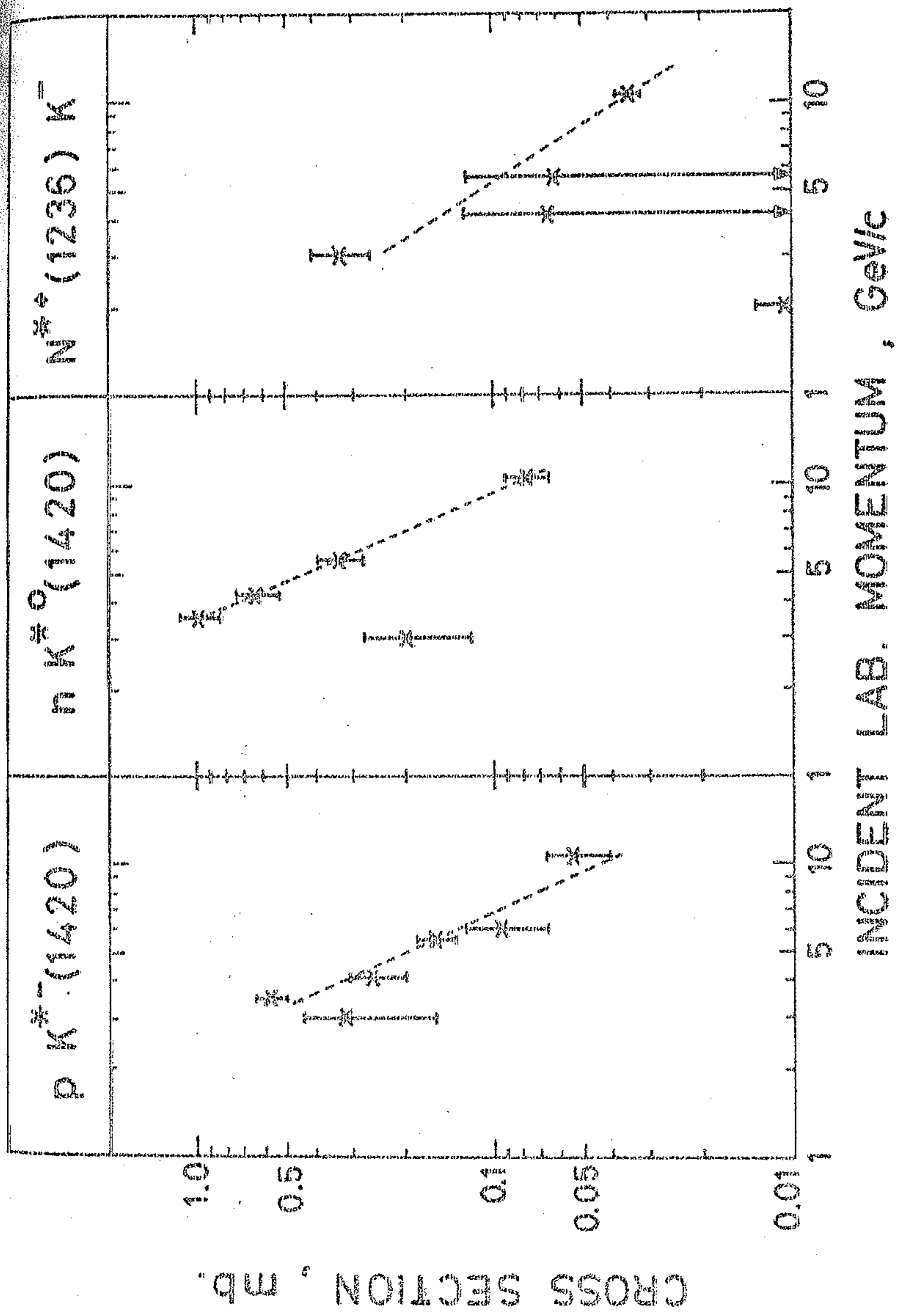
p K^{*-}(1420)
n K^{*0}(1420)
N^{*+}(1236) K^-
1.0
0.5
0.1
0.05
0.01
1
5
10
INCIDENT LAB. MOMENTUM , GeV/c
CROSS SECTION , mb.

TABLE 9.1

TOTAL CROSS SECTIONS FOR TWO-BODY REACTIONS

	Final state	(μb)	exponent n	$(1 - \frac{1}{2}n)$	expected $\alpha(0)$	Type
a)	pK^-	3200 ± 140	0.36 ± 0.01	0.82	1.0	I
b)	$pK^{*-}(1320)$	575 ± 72	~ 0.3	0.85	1.0	I
c)	$pL^-(1790)$	165 ± 39	small	~ 1.0	1.0	I
d)	$pK^{*-}(890)$	92 ± 9	2.01 ± 0.14	0.0	0.46	II
e)	$pK^{*-}(1420)$	58 ± 10	1.98 ± 0.37	0.01	0.46	II
f)	$nK^{*0}(890)$	54 ± 13	2.3 ± 0.4	-0.15	-0.01	II
g)	$nK^{*0}(1420)$	78 ± 14	2.4 ± 0.3	-0.2	-0.01	II
h)	$N^{*+}(1236)K^-$	35 ± 4	1.6 ± 0.4	0.2	0.46	II
i)	$Y^{*+}(1385)\pi^-$	12 ± 4	2.7 ± 0.2	-0.35	0.26	III
	TOTAL	4269				

However the relative simplicity of these reactions compared with the higher multiplicity channels makes them a reasonable starting point.

On the basis of exchanged quantum numbers, reactions f), g) which involve non-zero charge exchange and h) which involves non-zero I-spin exchange would be allocated to type II, which is consistent with the observed exponent of about 2. Reaction i) requires strange meson exchange and has a slightly higher exponent, consistent with that found for type III reactions. Reactions a) - e) could belong to either of the first two categories from exchanged quantum number considerations alone. However the values of n suggest that a) - c) are type I whereas d), e) are type II. This means that the K*(890) and K*(1420) reactions in both charge states are all of the same type which is consistent with the apparent similarity of these four reactions.

Since type I reactions have the smallest values of n they will become the dominant two-body reactions at a sufficiently high energy. That this is already the case at 10 Gev/c can be seen from the cross-sections given in table 9.1. Of the 19.0% two-body contribution to the total cross-section, about 17.5% comes from reactions a) - c). Even if the elastic scattering contribution is excluded the corresponding percentages of 3.3 and 1.5 still show the same effect. It can also be seen that the contributions from type II and type III reactions are progressively less. Upper limits for cross sections of typical type IV and V processes are 0.6 μb for Ξ^-K^+ (11) and 0.3 μb for backward elastic scattering (10).

The above classification can be given a simple-minded interpretation based on the exchange of Regge trajectories. The differential cross-section for a two-body process is given by:

$$\frac{d\sigma}{dt} = \frac{1}{64\pi sK^2} |T|^2 \tag{9.3}$$

where T is the relativistically invariant scattering amplitude and k is the initial centre-of-mass momentum. At high energies the Regge exchange amplitude has the asymptotic form (156):

$$T(s, t) = \sum_i B_i(t) (s/s_o)^{\alpha_i (t)} + O(s^{-\frac{1}{2}}) \tag{9.4}$$

where the sum is over all trajectories which can be exchanged in the process, $B_i(t)$ incorporates the residue and signature functions for the i th trajectory and s_o is an arbitrary scaling constant. The last term represents the contribution from the background integral in the Sommerfeld-Watson transform. At high energies the dominant contribution will come from the trajectory with the largest $\alpha(t)$ (boson trajectories are real functions to a good approximation) provided this trajectory has $\alpha(t) > -\frac{1}{2}$ in the physical region. If a linear trajectory function

$$\alpha(t) = \alpha(o) + \alpha' t \tag{9.5}$$

is assumed then (9.3) becomes

$$\frac{d\sigma}{dt} \doteq \frac{B(t)}{k^2 s} (s/so)^{2\alpha(0)} e^{bt} \tag{9.6}$$

$$\text{where} \quad b = 2\alpha' \ln(s/s_o) \tag{9.7}$$

and some constants have been incorporated in the function B(t).

Since B is only a slowly varying function of t we may, to a reasonable approximation, treat it as constant when integrating over t to obtain the total cross section. Making use of the (exact) relation

$$ks^{\frac{1}{2}} = m_b p \tag{9.8}$$

where m_b is the target mass this then gives:

$$\sigma = B(t)\ (p/po)^{2\alpha(0) - 2}\ (1/b)\ (m_b p/2k^2)^{2\alpha(0)} \tag{9.9}$$

where again B(t) has been modified by the inclusion of any required constant factors. At high energy the last factor in (9.9) can be expanded in inverse powers of p and gives

$$(m_b p/2k^2)^{2\alpha(0)} = 1 + \alpha(0)\ (ma^2 + m_b{}^2/m_b)\ (\tfrac{1}{p}) + O(\tfrac{1}{p}2) \tag{9.10}$$

where m_a is the mass of the beam particle. Since from (9.7) we can see that b is only a slowly varying function of s (compared with $s^{\alpha(0)}$) we obtain the result (9.1) if we make the identification

$$n = 2 - 2\alpha(0) \tag{9.11}$$

Thus the exponent n may be interpreted in terms of the intercept of the leading Regge trajectory. The effect on the value of n due to some of the approximations made in deriving this result are:

i) The contributions of lower trajectories will mean that the observed value of n will be larger than that predicted by (9.11);

ii) Due to the slow s-dependence in the factor b the observed value of n will again tend to be larger than expected;

iii) The effect on n of the kinematic approximation (9.10) depends on the sign of $\alpha(0)$. If this is positive as it will be in general for the leading trajectories in meson exchange reactions, the value of n will again be slightly larger than given by (9.11).

Thus there has been a general tendency to underestimate n so that we might expect the experimental values to be somewhat higher than expected from the leading trajectory intercepts. In principle one could calculate the effect of the above contributions on the value of n but this is probably not justified in such a simple-minded treatment. One would then also have to consider corrections due to non-asymptotic behaviour of a single Regge term.

The values for the intercepts calculated from the experimental values of n are shown in table 9.1. Also shown are the intercepts expected which are taken (except for reactions a - c) from table 8.23. Although the production mechanisms have not yet been discussed it will be shown later that reactions d), e) occur mainly by ω^0-exchange while f), g) are mainly π-exchange. Reactions h), i) cannot occur by pseudoscalar exchange because this would require the coupling of three pseudoscalars at one vertex which as we have seen before is forbidden. They are therefore expected to occur by non-strange and strange vector exchanges respectively. This is consistent with analyses of these reactions at other energies. For reactions d) - i) the values of $\alpha(0)$ predicted from the exponent n are all lower than the known trajectory intercept (as expected) by amounts which range from 0.2 to 0.6. However bearing in mind the approximations involved this may be considered to be reasonable qualitative agreement. Baryon trajectories are known (from Chew-Frautschi plots) to have negative intercepts; this is consistent with type IV reactions where the observed exponents of 3.0 - 3.5 correspond to intercepts of -0.5 to -0.75. As for the type V processes, since no exotic states are known we have no idea of what their trajectory functions would be like. If they have similar slopes to the other trajectories then the first realisations of such particles would have to be at very high masses in order to give rough agreement with an exponent of 10. However it is likely that some mechanism other than single trajectory exchange would be more important, for example simultaneous exchange of two or more particles or, in the Regge picture, the exchange of J-plane cuts.

Again we have left type I reactions to the end of the discussion. This is because we are not so clear about the underlying mechanism for these reactions. If an exchanged trajectory is responsible it seems to have an intercept of approximately 1. This is in fact the maximum intercept allowed for a trajectory because of the bound, first proved by Froissart (157) using unitarity and the Mandelstam representation and later by Martin (158) from quantum field theory axioms that the total cross section cannot grow faster than $(\ln s)^2$ in the asymptotic limit. A trajectory with an intercept greater than 1 would clearly violate this bound. The existence of a trajectory which exactly satisfies the Froissart bound was first suggested by Chew and Frautschi (144) in order to explain the apparent constancy of total cross sections at high energies as shown by the experimental data then available. The trajectory is usually referred to as the Pomeranchuk trajectory (or Pomeron) because of its obvious connection with the Pomeranchuk theorem. To satisfy the latter it must have positive signature; it also has zero for all its additive internal quantum numbers and +1 for all its multiplicative ones so that it is often called the vacuum trajectory since it possesses the vacuum quantum numbers. The first physical particle on this trajectory would be expected to have $J^{PC} = 2^{++}$ and both the f(1264) and f'(1518) mesons have been suggested as possibilities for this state. The latter is more consistent with the slope of about 0.47 obtained from measurements of p-p elastic scattering up to 65 Gev/c (159). However it is probably more likely that the f and f' belong on a more normal type of meson trajectory consistent with their assignments in the 2^{++} nonet. The small slope of the Pomeron, together with the absence of any nearby trajectory with which it could be approximately exchange degenerate may mean that it is not in fact a Regge trajectory at all but the effect of some other type of J-plane singularity. This point will be discussed in more detail later.

9.3 Production angular distribution

This is often called simply the differential cross-section (DCS) although it is strictly the DCS integrated over all relevant kinematic variables except the centre of mass scattering angle θ. It is actually more useful at high energies to use the Mandelstam variable t which is related to θ by:

$$t = (p_a - p_c)^2 = m_a^2 + m_c^2 - 2E_aE_c + 2kk'\cos\theta \qquad (9.12)$$

where E_a, E_c are the energies of particles a, c and k, k' are the centre of mass momenta in the initial and final states. This leads to the expression:

$$2st = 2s(m_a^2 + m_c^2) - (s + m_a^2 - m_b^2)\ (\ s + m_c^2 - m_d^2) + \\ + \cos\theta \quad \lambda^{\frac{1}{2}}(s,\ m_a^2,\ m_b^2)\ \lambda^{\frac{1}{2}}(s,\ m_c^2,\ m_d^2) \qquad (9.13)$$

where the function λ was defined earlier (see relation 8.41). The value of s can be found from the known beam momentum using the relation

$$s \ = \ m_a^2 + m_b^2 + 2m_b\ (m_a^2 + p^2)^{\frac{1}{2}} \qquad (9.14)$$

and its value corresponding to the central value of p in the present experiment is 20.13 Gev^2.

The value of -t is restricted to the range $(-t_{min},\ -t_{max})$ whose extreme values correspond to direct forward and backward scattering ($\cos\ \theta\ = \pm 1$). Values of t_{min} for the reactions studied are shown in table 9.2. They are calculated using central mass values so that for resonances of finite width it is possible to have values which lie outside the above range.

The forward peaks of two-body reactions at high energies can be well represented (within present experimental errors) by the relation

$$\frac{d\sigma}{dt} \ = \ Ae^{bt} \qquad (9.15)$$

where A, b are constants for a particular reaction. The parameter b is usually referred to as the slope of the DCS since it is the gradient of the straight line obtained when (9.15) is displayed with a

TABLE 9.2

SLOPES OF THE DIFFERENTIAL CROSS-SECTION DISTRIBUTIONS AT 10 GEV/C

	Final state	t_{min} (Gev^2)	t'_1 (Gev^2)	Slope values b (Gev^{-2})	
				$t'_2 = 0.4$	$t'_2 = 0.6$
a)	pK^-	0.	0.06	7.7 ± 0.2	7.3 ± 0.1
b)	$pK^{*-}(1320)$	0.01	0.0	7.5 ± 0.6	7.5 ± 0.5
c)	$pL^-(1790)$	0.03	0.0	6.1 ± 0.8	6.1 ± 0.5
d)	$pK^{*-}(890)$	0.004	0.1	5.1 ± 1.4	5.7 ± 0.6
e)	$pK^{*-}(1420)$	0.007	0.05	4.6 ± 1.0	4.9 ± 0.7
f)	$nK^{*o}(890)$	0.004	0.0	4.1 ± 1.0	4.5 ± 0.6
g)	$nK^{*o}(1420)$	0.007	0.0	6.3 ± 1.0	6.4 ± 0.8
h)	$N^{*+}(1236)K^-$	-	0.0	5.9 ± 0.8	5.8 ± 0.5
i)	$Y_1^{*+}(1385)\pi^-$	-	0.1	-	4.2 ± 3.1

Since all values of t given in the table are negative, the sign has been omitted for convenience.

logarithmic scale for the cross-section. Figure 9.3 shows such plots for the nine reactions a) - i). (The significance of the curves drawn on some of these plots is not relevant here.) The independent variable is actually t' which is related to t by

$$t' = t_{min} - t \tag{9.16}$$

Since all possible values of t for the reactions studied are negative we will (as before) often refer to t or t' as being positive quantities in the discussion but in formulae the correct definition will be adhered to. From figure 9.3 one can see that the behaviour (9.15) seems to be satisfied out to values of t' of about 0.8 $(Gev/c)^2$, but that beyond this the DCS bends upwards. Figure 9.4 shows the small t' region for the same reactions d), e) and i) where the cross section appears to decrease strongly near t' = 0. It is here that the usefulness of using t' rather than t as the independent variable can be seen. If t had been used the vanishing of the cross-section at $t = t_{min}$ required on kinematic grounds alone would have masked the fact that three of the reactions show a non-kinematical dip at small t-values.

The values of the slopes are also shown in table 9.2, calculated from an initial t' value t'_1 (chosen to exclude the dips at low t', when present) to each of two final values t'_2, both chosen well below the points at which the cross sections begin to bend upwards. The two sets of values are compatible.

Fig. 9.5

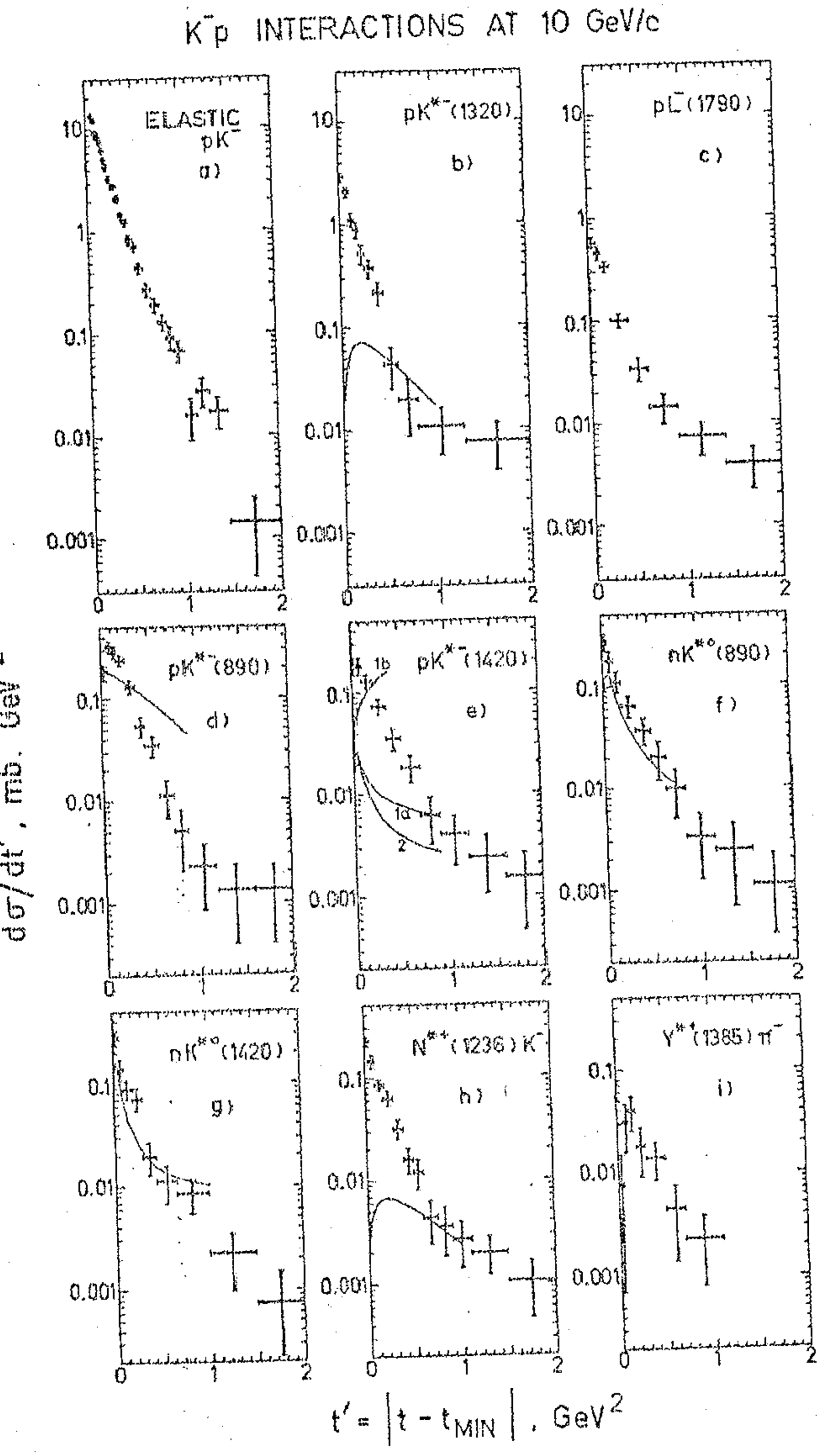
K⁻p INTERACTIONS AT 10 GeV/c
ELASTIC pK⁻
a)
pK*⁻(1320)
b)
pΞ⁻(1790)
c)
pK*⁻(890)
d)
pK*⁻(1420)
e)
1b
1a
2
nK*°(890)
f)
nK*°(1420)
g)
N*⁺(1236) K⁻
h)
Y*⁺(1385) π⁻
i)
dσ/dt′, mb. GeV⁻²
t′ = |t - t_MIN| , GeV²
10
1
0.1
0.01
0.001
0
1
2

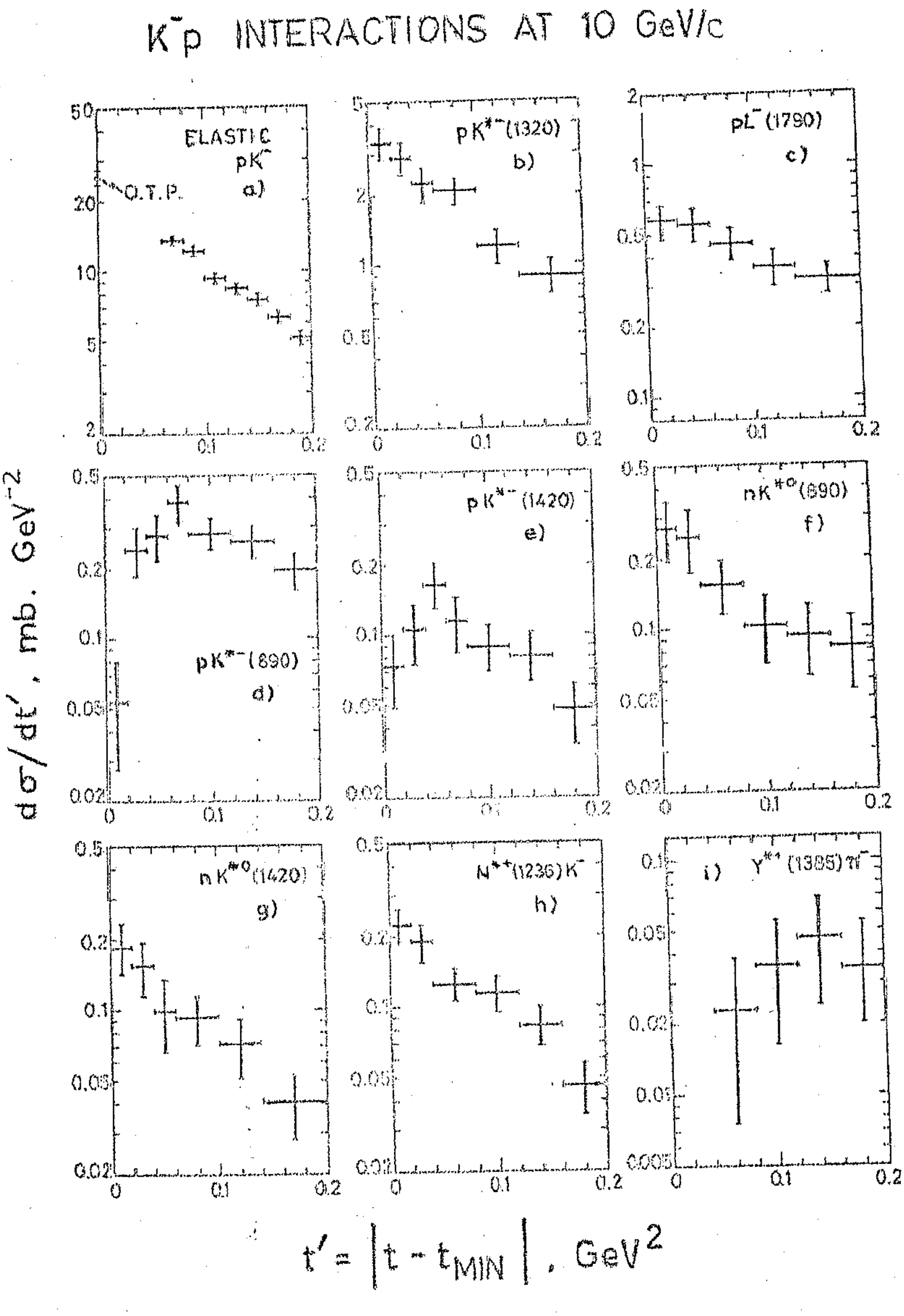
K⁻p INTERACTIONS AT 10 GeV/c
ELASTIC pK⁻
a)
O.T.P.
pK*⁻(1320)
b)
pL⁻(1790)
c)
pK*⁻(890)
d)
pK*⁻(1420)
e)
nK*⁰(890)
f)
nK*⁰(1420)
g)
N*⁺(1236)K⁻
h)
i) Y*⁺(1385)π⁻
dσ/dt', mb. GeV⁻²
t' = |t - t_MIN|, GeV²

As can be seen from (9.6) the simple Regge trajectory exchange amplitude leads to a relation of the form (9.15) if the slow t-dependence in the residue function is neglected. The value of the slope b is predicted to increase with energy like ln s, while the rate of increase depends on the slope of the dominating trajectory (α'). This behaviour is not as universally true as was the total cross-section behaviour. In the case of elastic scattering, for which the available data is most extensive, it is the same trajectory (the Pomeron) which is expected to dominate at high energies. Although the ln s behaviour is fairly well satisfied in all cases, the trajectory slope obtained from different reactions is not the same. For pp scattering the most recent measurements extend to 70 Gev/c (159) and give a value for α' of 0.47; the slopes of the $\pi^{\pm}p$ and K^-p elastic differential cross sections are approximately independent of s which implies $\alpha' = 0$ (160); K^+p elastic scattering leads to a trajectory slope of 0.9; finally, for $\bar{p}p$ scattering the slope b actually decreases with increasing s (161) which corresponds to a negative (unphysical) slope for the trajectory.

For inelastic reactions there is also no universal behaviour. Table 9.3 shows the slopes for the reactions studied as well as those for the corresponding K^+p reactions. The more accurately determined elastic slopes are shown for comparison, while the reactions involving the L(1800) have not been included because of the lack of data from other experiments. There seems to be a tendency for the slope of $pK^{*-}(890)$ to increase with energy whereas that for $pK^{*+}(890)$ is approximately constant. This is the reverse situation to that

TABLE 9.3

SLOPES OF DIFFERENTIAL CROSS SECTIONS AS A FUNCTION OF INCIDENT MOMENTUM FOR $K^{\pm}p$ REACTIONS

K^-p	K^-p	$pK^{*-}(1320)$	$pK^{*-}(890)$	$pK^{*-}(1420)$	$nK^{*0}(890)$	$nK^{*0}(1420)$
4.1 Gev/c	7.62 ± 0.51	-	4.0 ± 0.3	-	3.6 ± 0.3	-
4.6	-	-	4.2 ± 0.5	-	-	-
5.5	7.52 ± 0.50	-	4.6 ± 0.2	-	3.3 ± 0.3	-
6	-	-	4.8 ± 0.5	3.4 ± 0.6	-	-
7.2	7.00 ± 0.65	-	-	-	-	-
7.3	-	~ 8.5	-	-	-	-
9	7.28 ± 0.61	-	-	-	-	-
10	7.11 ± 0.23	7.5 ± 0.5	5.7 ± 0.6	4.9 ± 0.7	4.5 ± 0.6	6.4 ± 0.8
11.9	6.93 ± 0.32	-	-	-	-	-
12.6	-	11 ± 2	-	-	-	-
15.9	6.05 ± 0.40	-	-	-	-	-

K^+p	K^+p	$pK^{*+}(1320)$	$pK^{*+}(890)$	$pK^{*+}(1420)$
3 Gev/c	4.19 ± 0.34	-	3.6 ± 0.4	-
3.5	4.26 ± 0.32	-	3.2 ± 0.3	2.88 ± 0.33
4.3	4.69 ± 0.41	-	-	-
5	5.15 ± 0.54	8.7 ± 1.2	4.2 ± 1.1	4.5 ± 1.6
6.8	5.20 ± 0.50	-	-	-
9	-	-	3.34 ± 0.29	3.0 ± 0.26
9.8	5.88 ± 0.26	-	-	-
10	-	-	3.7 ± 0.5	1.5 ± 0.4
12.7	-	~ 15	4.8 ± 1.0	-
12.8	6.17 ± 0.22	-	-	-
14.8	6.33 ± 0.29	-	-	-

which occurs in the corresponding elastic processes. For the other inelastic reactions there are not enough slope values available to give a significant picture of the energy variation. The slopes for $pK^{*\pm}(1320)$ have been taken from references 101-117; those for $K^*(890)$ and $K^*(1420)$ are reported in references 162-185. There will be some point to point discrepancies in these values arising from the use of different ranges of t in the calculations of different experiments.

9.4 Behaviour of slopes as a function of mass

As mentioned briefly in chapter 7, resonance production at lower energies (2 - 4 Gev/c) is characterised by being much more peripheral than the background processes. Thus, for example, a Chew-Low plot (m^2 against t) gives a very clear indication of resonance production since events in the resonance mass region will be clustered near the low t part of the kinematic boundary. At high energies such behaviour does not occur in most reactions. Instead the type of behaviour illustrated by (9.15) may be a relevant description not only for the quasi-two-body resonance production but also for the background processes. In the latter case t has a generalised definition as the momentum transfer squared from an initial particle to a group of final particles which do not necessarily form a resonance. This behaviour is particularly well illustrated by figure 9.5 in which the slope has been calculated as a function of the mass of the $(K\pi)^-$ and $(K\pi\pi)^-$ systems. The bin sizes have been chosen so that the vertical error bars remain approximately constant.

FIG.9.5

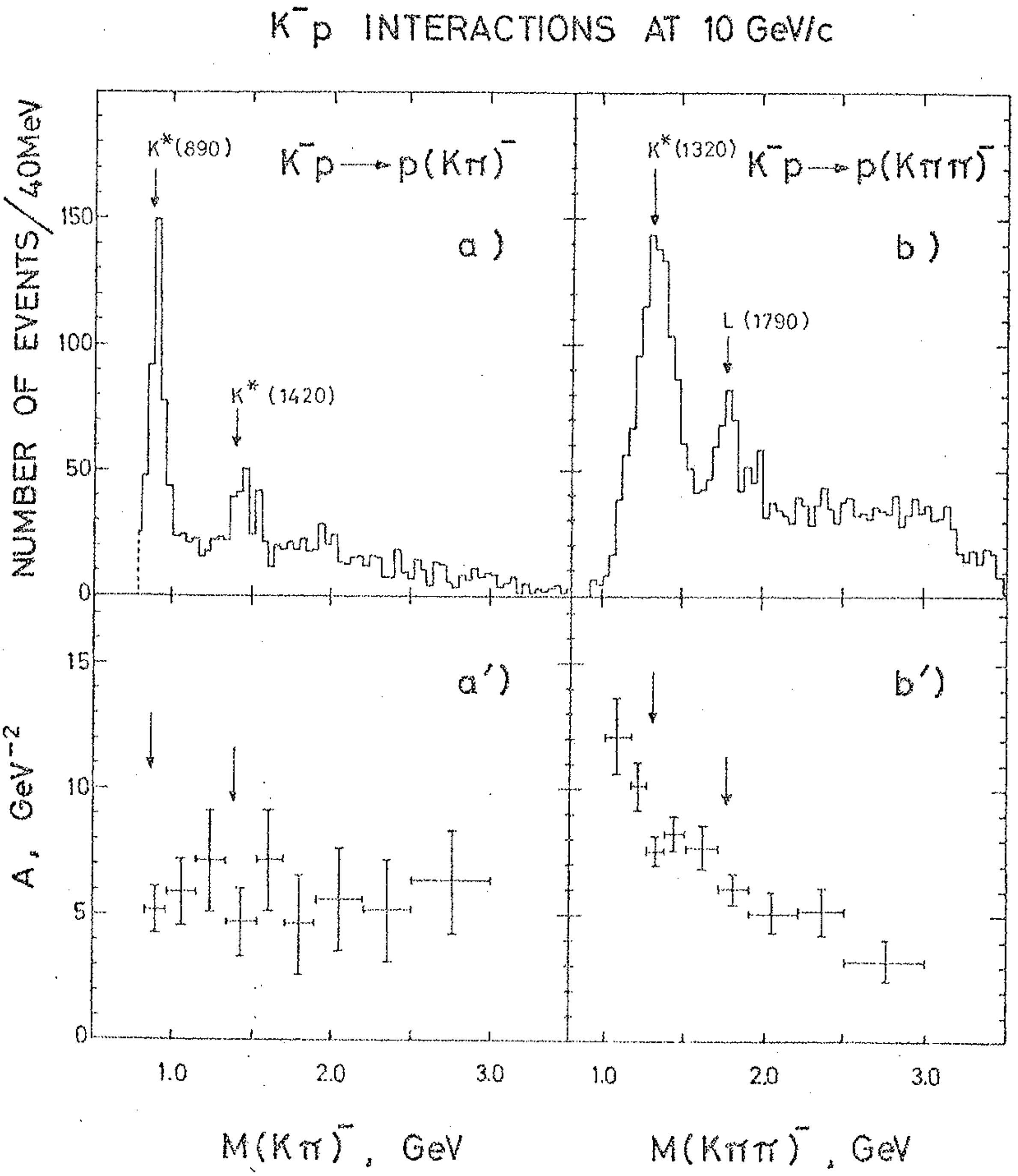
K⁻p INTERACTIONS AT 10 GeV/c
NUMBER OF EVENTS/40MeV
K*(890)
K⁻p → p(Kπ)⁻
a)
K* (1420)
K*(1320)
K⁻p → p(Kππ)⁻
b)
L (1790)
a′)
b′)
A , GeV⁻²
0
50
100
150
5
10
15
1.0
2.0
3.0
M(Kπ)⁻ , GeV
M(Kππ)⁻ , GeV

The lack of structure in the slope when there is clear structure in the mass distributions is a striking feature of the data. In the $(K\pi\pi)$ case the slope slowly decreases with increasing mass whereas for $(K\pi)$ it seems to be fairly constant. Similar behaviour in some π^+p reactions is reported in reference 14.

These features of the data are outside the simple Regge trajectory exchange picture discussed in the earlier sections, since this only applies to quasi two-body reactions. They result in one practical advantage, namely that in calculating the slopes (at least for reactions b-e) it is not necessary to subtract the effect of the background.

9.5 Decay angular distributions

These constitute the third source of experimental information available for the investigation of production mechanisms. If a particle with spin is produced which subsequently decays into two or more particles its decay angular distribution depends on its spin value and on the orientation of its spin in the production process. Thus if its spin is known the production process may be investigated. In the case of a resonance decaying into three particles it can be shown that the information on the angular distribution which is contained in the Dalitz plot is actually independent of the production process. This is why we were able to use the Dalitz plot distribution to determine the spins of the K*(1320) and L(1800) states (see chapter 8).

There are no features connected with decay distributions that can be discussed in a universal way, as was possible for the total and differential cross sections, and further consideration of them will be left to the next chapter.

CHAPTER 10

MODEL INDEPENDENT INVESTIGATION OF PRODUCTION MECHANISMS

The main aim of hadron physics is to develop a theory of strong interactions which will give a good description of the available data and allow predictions to be made which can then be tested experimentally. At the present time the lack of a sound basis for such a theory has resulted in a gulf between theory and experiment. There have been some spectacular advances towards such a theoretical description (such as the success of the unitary symmetry approach) but all too often it is difficult to calculate direct experimental quantities without making additional assumptions. Until a more satisfactory theory is developed (assuming it will be) the recourse has usually been into phenomenology which, at its best, approximates to a kind of theory but, at its weakest, is little more than data assimilation and ordering. (This latter process is an important stage in the classical description of the scientific method but it is only an early one in the sequence observation-assimilation-theory-prediction.)

Certain general properties derivable from fairly rigorous theoretical ideas are expected to hold for the strong interaction scattering amplitude and a proposed phenomenological model should not violate too many of them (if it violates none of them and is successful then we presumably have a tenable theory). The models themselves may be suggested by theories in other branches of physics (for example optical models) or they may sometimes be obtained by non-rigorous extensions of rigorous theoretical ideas in strong interaction physics (for example the derivation of the one particle exchange amplitude from field theory).

The amplitude should satisfy analyticity and unitarity and should be crossing symmetric. These properties can be rigorously derived from quantum field theory for certain simple scattering processes (for example pion-nucleon scattering) but they are assumed to be generally true whether or not such a rigorous derivation exists. There are further restrictions on the structure of scattering amplitudes which come from conservation laws and symmetry arguments: Lorentz invariance implies that they are Poincaré scalars; the conservation of internal quantum numbers suggests that they are SU(2) scalars and, at least in an approximate sense, SU(3) scalars. They may also possess a higher internal symmetry for which several possibilities have been suggested, for example SU(6), O(4,2), U(6,6), $\tilde{U}(12)$. Attempts to combine these higher internal symmetries with Poincaré invariance to provide a complete relativistic description of the amplitude seemed promising at one time (around 1965) but serious difficulties have been subsequently encountered (186).

The rest of this chapter will be devoted to a discussion of those features of the reactions which are independent of the details of particular phenomenological models.

The peripherality of high energy reactions suggests that the underlying mechanism is the exchange of a system with zero baryon number between the two incoming particles. Thus it is likely to be useful to parametrise a reaction $a + b \longrightarrow c + d$ in the t-channel, where it takes the form:

$$a + \bar{c} \longrightarrow e \longrightarrow \bar{b} + d \qquad (10.1)$$

The bars denote antiparticles and e represents the exchanged system. Since the particles may have non-zero spins a description is desired which will include spin in a general way. Such a description, and one which is well suited for high energy reactions, is the helicity amplitude formalism developed by Jacob and Wick (187). The helicity λ_i of a particle i is defined as the projection of its spin along its direction of motion and the scattering amplitude from an initial state with helicities λ_a, λ_c to a final state with helicities λ_b, λ_d is called a t-channel helicity amplitude. (This will be denoted $F_{bd,\ ac}$ where the subscripts will be understood to refer to the helicities of the particles concerned.)

10.1 The Spin Density Matrix

A pure spin state of one of the final particles (c say) is defined as a linear superposition of eigenstates ϕ_m, where m denotes the magnetic quantum number referred to some fixed quantisation axis,

$$\psi_j = \sum_{m=-J}^{J} a_m \phi_m \qquad (10.2)$$

In general such pure states will not be encountered experimentally. For example, in the type of reaction being studied here, the initial state (in the s-channel) contains a mixture of pure states corresponding to the possible spin states of a, b while the final state contains contributions from all possible spin states of the fourth particle d, since the polarisation of d is not detected. Thus the state of c is in general a mixed state in which the pure state ψ_i occurs with probability p_i, that is the expectation value of some operator Q is

$$\langle Q \rangle = \sum_{m,n=-J}^{J} \left(\sum_i p_i \, a_m^* a_n \right) Q_{mn} \tag{10.3}$$

If one writes $$\rho_{nm} = \sum_i p_i a_n a_m^* \tag{10.4}$$

then $$\langle Q \rangle = \sum_{m,n} \rho_{nm} Q_{mn} = \mathrm{Tr}\,(\rho Q) \tag{10.5}$$

The matrix ρ is called the spin density matrix for the particular mixed spin state of the particle c. It is a square matrix of order (2J + 1) whose elements are the relative populations of the various magnetic substates. From (10.4) its diagonal elements are given by

$$\rho_{mm} = \sum_i p_i \, |a_m|^2 \tag{10.6}$$

and are therefore positive. Further,

$$\mathrm{Tr}\,\rho = \sum_i p_i \sum_m |a_m|^2 = 1 \tag{10.7}$$

from which it follows that the diagonal elements must satisfy the inequality

$$0 \leqslant \rho_{mm} \leqslant 1 \tag{10.8}$$

From (10.4) it also follows that the density matrix is Hermitian since

$$\rho_{mn}^* = \rho_{nm} \tag{10.9}$$

A general square matrix of order $(2J + 1)$ with complex elements requires $2(2J + 1)^2$ real parameters to define it. Hermiticity reduces the number of independent parameters by half, to $(2J + 1)^2$, while the trace condition on the (now purely real) diagonal elements further reduces it by 1 to $4J(J + 1)$.

The Hermiticity of ρ implies that it can be diagonalised by a unitary transformation U. If λ_i $(i = 1, 2J + 1)$ are the eigenvalues (nothing to do with the helicity λ mentioned earlier) it follows that

$$\sum_i \lambda_i = 1 \tag{10.10}$$

since the trace is invariant under U. That particular state of c which is a mixture of the $(2J + 1)$ substates ψ_i with probability λ_i has for its density matrix $(\sum_i \lambda_i U_m^i U_n^{i*})$, which is just (ρ_{mn}). Thus the eigenvalues can be interpreted as probabilities which means they must satisfy (10.8) and ρ is therefore a positive semi-definite matrix. This fact, together with the other basic properties of the density matrix, can provide useful relations which should be satisfied by the experimental matrix elements.

The conditions imposed by positivity on a general n x n matrix M are expressible in several equivalent ways.

i) the eigenvalues λ_i must satisfy

$$\lambda_i \geqslant 0 \tag{10.11}$$

ii) since the characteristic equation of M can be written

$$\prod_{i=1}^{n} (\lambda - \lambda_i) = 0 = \lambda^n - c_1 \lambda^{n-1} + c_2 \lambda^{n-2} \mp \ldots + (-)^n c_n \tag{10.12}$$

where $c_1 = \sum_i \lambda_i,$

$$c_2 = \sum_{i \neq j} \lambda_i \lambda_j, \quad \ldots\ldots\ldots \tag{10.13}$$

and finally $c_n = \lambda_1 \lambda_2 \ldots\ldots\ldots \lambda_n$

it is clear that necessary and sufficient conditions for positivity are

$$c_i \geqslant 0 \tag{10.14}$$

iii) another equivalent requirement is that the determinants of the n square sub-matrices of M, each containing the element M_{11} and of order 1, 2, ... n respectively, should be greater than or equal to zero.

Which of these expressions of the positivity condition is the best depends on the particular purpose in hand, for example whether one is interested in deriving general relations for an arbitrary matrix or whether one wants to examine the numerical values of the elements for one particular experimental matrix.

Case ii) provides a neat description of the positivity conditions for a general matrix since the coefficients c_i can be expressed as functions of the traces of M and its higher powers M^2, M^3, ... M^n as follows:

Firstly, $\quad c_1 = \mathrm{TrM}$ (10.15)

Then, using the identity

$$\left(\sum_i \lambda_i\right)^2 = \sum_i \lambda_i^2 + 2 \sum_{i \neq j} \lambda_i \lambda_j \tag{10.16}$$

we get

$$c_2 = \tfrac{1}{2}\left(-\mathrm{TrM}^2 + (\mathrm{TrM})^2\right) \tag{10.17}$$

Using analogous identities obtained by expanding TrM to higher powers one can derive the relations

$$c_3 = (1/6)\ (2\mathrm{TrM}^3 - 3\mathrm{TrM}^2\mathrm{TrM} + (\mathrm{TrM})^3\ ) \tag{10.18}$$

$$c_4 = (1/24)\ (-6\mathrm{TrM}^4 + 8\mathrm{TrM}^3\mathrm{TrM} + 3(\mathrm{TrM}^2)^2 - 6\mathrm{TrM}^2(\mathrm{TrM})^2 + (\mathrm{TrM})^4\ ) \tag{10.19}$$

$$c_5 = (1/120)\ (24\mathrm{TrM}^5 - 30\mathrm{TrM}^4\mathrm{TrM} - 20\mathrm{TrM}^3\mathrm{TrM}^2 + 20\mathrm{TrM}^3(\mathrm{TrM})^2 + 15(\mathrm{TrM}^2)^2\mathrm{TrM} - 10\mathrm{TrM}^2(\mathrm{TrM})^3 + (\mathrm{TrM})^5\ ) \tag{10.20}$$

Higher coefficients are not required for spins of up to 2, which is all that we will be concerned with here. For a matrix with unit trace relations 10.15 - 10.20 simplify considerably and the positivity conditions for a <u>spin</u> density matrix can then be written:

$$-\mathrm{Tr}\,\rho^2 + 1 \geqslant 0 \tag{10.21}$$

$$2\mathrm{Tr}\,\rho^3 - 3\mathrm{Tr}\,\rho^2 + 1 \geqslant 0 \tag{10.22}$$

$$-6\mathrm{Tr}\,\rho^4 + 8\mathrm{Tr}\,\rho^3 + 3(\mathrm{Tr}\,\rho^2)^2 - 6\mathrm{Tr}\,\rho^2 + 1 \geqslant 0 \tag{10.23}$$

$$24\mathrm{Tr}\,\rho^5 - 30\mathrm{Tr}\,\rho^4 + 20\mathrm{Tr}\,\rho^3(-\mathrm{Tr}\,\rho^2 + 1) + 15(\mathrm{Tr}\,\rho^2)^2 - 10\ \mathrm{Tr}\,\rho^2 + 1 \geqslant 0 \tag{10.24}$$

For spin J only the first 2J relations are relevant. Since $c_1 = \mathrm{Tr}\,\rho$ the condition $c_1 \geqslant 0$ is trivially satisfied for a density matrix and has been omitted.

The result (10.21) can also be derived simply from the fact that the eigenvalues lie in (0, 1). $\sum_i \lambda_i(1 - \lambda_i)$ is a sum of non-negative terms, so that

$$\sum_i \lambda_i^2 \leqslant \sum_i \lambda_i \qquad \text{i.e.}\quad \mathrm{Tr}\,\rho^2 \leqslant 1 \tag{10.21}$$

The maximum value of 1 occurs when all of the eigenvalues are zero except for one, that is it corresponds to a pure state. Because of the condition $\mathrm{Tr}\,\rho = 1$ it can be seen that the minimum value of $\mathrm{Tr}\,\rho^2$ occurs when all λ_i are equal to $(2J + 1)^{-1}$. In this case

$$\mathrm{Tr}\,\rho^2 = \sum_i \frac{1}{(2J + 1)^2} = \frac{1}{2J + 1} \tag{10.25}$$

10.21 and 10.25 together lead to the inequality

$$\frac{1}{2J + 1} \leqslant \mathrm{Tr}\,\rho^2 \leqslant 1 \tag{10.26}$$

$(2J + 1)$ is the maximum possible number of independent spin amplitudes required to describe the state of a particle with spin J. If, in a particular situation, the spin state of the particle can be described by at most N independent amplitudes (N is necessarily no bigger than 2J + 1) it can be shown that $\mathrm{Tr}\,\rho^2 \geqslant N^{-1}$ (188). This is an extension of the Eberhard-Good theorem (189). Thus we have finally

$$\mathrm{Max}\left(\frac{1}{N}, \frac{1}{2J + 1}\right) \leqslant \mathrm{Tr}\,\rho^2 \leqslant 1 \tag{10.27}$$

In the case of a particle c produced in the two-body reaction $ab \longrightarrow cd$ the maximum number of independent spin states available for c is no more than $(2J_a + 1)(2J_b + 1)(2J_d + 1)$ which is equal to 4 when a is a spin zero meson and b, d are nucleons. Thus for $J_c \geqslant 2$ not all the spin states can be independent.

For J = 1, we have

$$\frac{1}{3} \leqslant \mathrm{Tr}\,\rho^2 \leqslant 1 \quad \text{or} \quad 0 \leqslant c_2 \leqslant \frac{1}{3} \tag{10.28}$$

while for J = 2, we have

$$\frac{1}{4} \leqslant \mathrm{Tr}\,\rho^2 \leqslant 1 \quad \text{or} \quad 0 \leqslant c_2 \leqslant \frac{3}{8} \tag{10.29}$$

If the production reaction ab $\rightarrow$ cd is parity-conserving there are further restrictions on ρ_{mn}. So far all the derived properties of the density matrix are valid for any quantisation axis but to discuss the implications of parity conservation it is necessary to choose a particular axis for the quantisation of the angular momentum components. One natural choice for a two-body reaction would be to take z perpendicular to the production plane. With such a choice parity conservation implies that alternate elements of ρ are zero (190). However a better choice for high energy reactions dominated by t-channel exchanges is the Jackson frame in which the z-axis for particle c is the direction of particle a as seen in the rest frame of c. This is the same direction (but in the opposite sense) as the momentum carried by the exchanged system e. In this frame it can be shown (191) that the density matrix elements must satisfy the relations:

$$\rho_{mn} = (-)^{m-n} \rho_{\cancel{mn}\,-m,-n} \qquad (10.30)$$

This condition relates one element to the element which it transforms into on reflection through the centre of the matrix. Since Hermiticity relates an element to its reflection in the leading diagonal, the combination of Hermiticity and parity conservation (in a quasi two-body process) divides the elements into 3 classes:

i) <u>the leading diagonal elements</u> are real and there is symmetry about the centre. The number of independent parameters required to fix this set of elements is J (bosons) or J - $\frac{1}{2}$ (fermions), where this also takes account of the trace condition.

ii) the non-leading diagonal elements are related in pairs by both Hermiticity and parity conservation since for these elements the operations of reflection through the centre and reflection in the leading diagonal are equivalent. Thus they are either purely real (bosons) or purely imaginary (fermions), the difference coming from the value of (m - n) in (10.30). The number of independent parameters in this set is J (for bosons, neglecting ρ_{00} which appears also on the leading diagonal) or $J + \frac{1}{2}$ (for fermions).

iii) all other elements are related in groups of 4 by Hermiticity and parity conservation but are in general complex so that each group is specified by 2 real parameters. The number of independent parameters is $2J^2$(bosons) or $2J^2 - \frac{1}{2}$ (fermions).

Thus the total number of independent parameters for a spin J boson is

$$J + J + 2J^2 = 2J(J + 1)$$

of which $J(J + 2)$ appear in real parts of elements and J^2 appear only in imaginary parts. This distinction is relevant since in an experiment with unpolarised initial particles a, b and where the polarisation of the other final particle d is not detected, the decay angular distribution of c depends only on the real parts of ρ_{mn}. (This is true when the quantisation axis lies in the production plane, as is the case for the Jackson frame.) Table 10.1 shows the forms of the density matrix for the cases J = 1, 2 when the requirements of parity conservations and Hermiticity have been imposed. The trace conditions have not been explicitly introduced; it is straight forward to incorporate them when comparisons are

TABLE 10.1

GENERAL FORM OF THE SPIN DENSITY MATRICES AFTER APPLICATION OF HERMITICITY AND PARITY CONSERVATION REQUIREMENTS

Spin 1

$$\rho = \begin{matrix} \rho_{11} & \rho_{10} & \rho_{1-1} \\ \rho_{10}^{*} & \rho_{00} & -\rho_{10}^{*} \\ \rho_{1-1} & -\rho_{10} & \rho_{11} \end{matrix}$$

Spin 2

$$\rho = \begin{matrix} \rho_{22} & \rho_{21} & \rho_{20} & \rho_{2-1} & \rho_{2-2} \\ \rho_{21}^{*} & \rho_{11} & \rho_{10} & \rho_{1-1} & -\rho_{2-1}^{*} \\ \rho_{20}^{*} & \rho_{10}^{*} & \rho_{00} & -\rho_{10}^{*} & \rho_{20}^{*} \\ \rho_{2-1}^{*} & \rho_{1-1} & -\rho_{10} & \rho_{11} & -\rho_{21}^{*} \\ \rho_{2-2} & -\rho_{2-1} & \rho_{20} & -\rho_{21} & \rho_{22} \end{matrix}$$

made with the experimental data.

In the case of bosons (integral J) the requirements of parity conservation make it possible to factorise the characteristic equation (which is of order $2J + 1$ in λ) into a pair of equations of order J, $J + 1$ respectively.(192) The characteristic equation is

$$\det(\rho - \lambda I) = 0 \tag{10.31}$$

where I is the unit matrix of order $2J + 1$. By making suitable linear combinations of rows and columns $\det \overset{=0}{\rho_\lambda}$ can be reduced to the form (192):

$$\begin{vmatrix} A & B \\ C & D \end{vmatrix} = 0 \tag{10.32}$$

where A is $J \times J$, D is $(J + 1)\mathrm{x}(J + 1)$, $C = 0$ and B contains unmodified elements from ρ. The characteristic equation is then reduced to the pair of equations

$$\det(A - \lambda I) = 0, \ \det(D - \lambda I) = 0 \tag{10.33}$$

where the unit matrices have the necessary dimensionality. The particular cases of interest in the present experiment are $J = 1$ for K*(890) and K*(1320) and $J = 2$ for K*(1420) and L(1800). The reduced forms (10.32) for these two cases are shown in table 10.2. The above decomposition is particularly useful in these two cases since it reduces the characteristic equations to fairly manageable forms (no worse than cubics). The positivity conditions can then be expressed as:

$$k_i \geqslant 0 \tag{10.34}$$

where, for $J = 1$,

$$\begin{aligned} \det (A - \lambda I) &= -\lambda + k_1 \\ \det (D - \lambda I) &= -\lambda^2 + k_2\lambda - k_3 \end{aligned} \tag{10.35}$$

TABLE 10.2

REDUCED FORMS OF THE DETERMINANT OF THE SPIN DENSITY MATRIX FOR SPINS 1 AND 2 (SEE TEXT FOR EXPLANATION)

Spin 1

$$\begin{array}{ccc}
\rho_{11} + \rho_{1-1} & \rho_{10} & \rho_{1-1} \\
0 & \rho_{00} & -\rho_{10}^{*} \\
0 & -2\rho_{10} & \rho_{11} - \rho_{1-1}
\end{array}$$

Spin 2

$$\begin{array}{ccccc}
\rho_{22} - \rho_{2-2} & \rho_{21} + \rho_{2-1} & \rho_{20} & \rho_{2-1} & \rho_{2-2} \\
\rho_{21}^{*} + \rho_{2-1}^{*} & \rho_{11} + \rho_{1-1} & \rho_{10} & \rho_{1-1} & -\rho_{2-1}^{*} \\
0 & 0 & \rho_{00} & -\rho_{10}^{*} & \rho_{20}^{*} \\
0 & 0 & -2\rho_{10} & \rho_{11} - \rho_{1-1} & -\rho_{21}^{*} + \rho_{2-1}^{*} \\
0 & 0 & 2\rho_{20} & -\rho_{21} + \rho_{2-1} & \rho_{22} + \rho_{2-2}
\end{array}$$

and, for J = 2,

$$\det(A - \lambda I) = -\lambda^2 + k_1\lambda - k_2$$
$$\det(D - \lambda I) = -\lambda^3 + k_3\lambda^2 - k_4\lambda + k_5 \qquad (10.36)$$

10.1.1 Experimental tests for spin 1

The most extensive data on density matrix elements in the present experiment is for the production of K*(890) in both the negative and neutral charge states. The number of independent elements which are measurable from the decay angular distributions alone is three in this case, the usual choice being ρ_{oo}, ρ_{1-1} and Re ρ_{10}. These are shown as functions of t in figure 10.1. The bin sizes have been chosen to give approximately the same numbers of events in each bin, so that they necessarily become wider at large t-values due to the decrease in the differential cross section. The curves drawn in the figures are not relevant to the present discussion.

From table 10.1 and condition (10.28) it can easily be shown that the condition $c_2 \geqslant 0$, together with the Eberhard-Good theorem, leads to the inequality

$$0 \leqslant 3(\rho_{oo} - \tfrac{1}{3})^2 + 8|\rho_{10}|^2 + 4\rho_{1-1}^2 \leqslant \tfrac{4}{3} \qquad (10.37)$$

This restricts the experimental points to lie on or within an ellipsoid in the three dimensional space (ρ_{oo}, $|\rho_{10}|$, ρ_{1-1}) whose centre is at ($\frac{1}{3}$, 0, 0) and whose semi-axes are 2/3, $1/\sqrt{6}$ and $1/\sqrt{3}$ respectively. The lower limit in (10.37) gives no restrictions since the

FIG.10.1

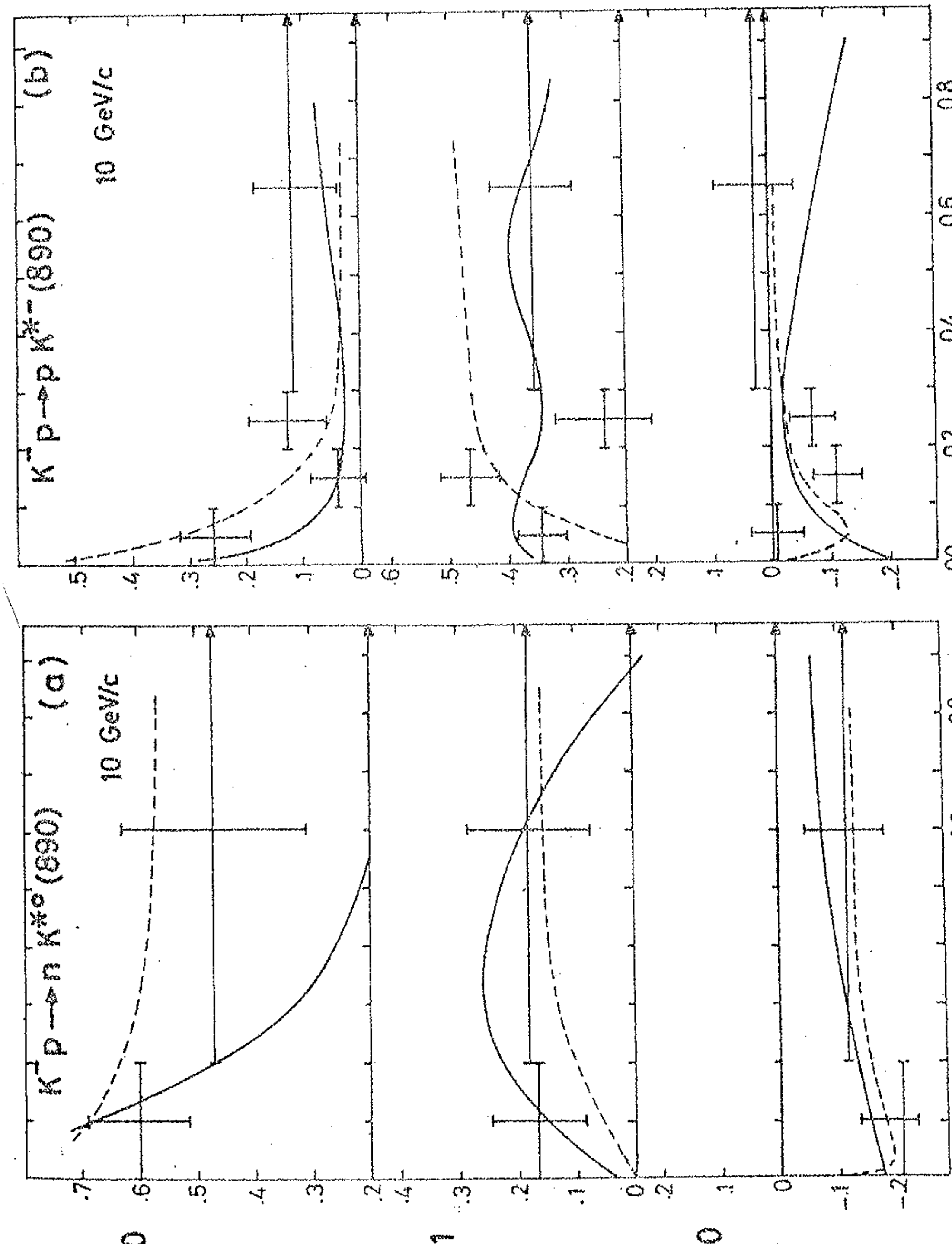

middle expression is positive definite. This is just a consequence of the previously mentioned fact that, for the production of a spin 1 resonance in the type of reaction studied here, the maximum number of independent spin amplitudes (three) can be present.

The condition $c_3 \geqslant 0$ leads to the inequality

$$(\rho_{11} + \rho_{1-1})(\rho_{oo}(\rho_{11} - \rho_{1-1}) - 2|\rho_{10}|^2) \geqslant 0 \qquad (10.38)$$

From table (10.1) it can be seen that the condition $k_1 \geqslant 0$ implies that the first factor in (10.38) is non-negative, which allows one to replace (10.38) by the two conditions

$$\rho_{1-1} \geqslant \tfrac{1}{2}(\rho_{oo} - 1) \qquad (10.39)$$

and

$$\rho_{oo}^2 - \rho_{oo} + 2\rho_{oo}\rho_{1-1} + 4|\rho_{10}|^2 \leqslant 0 \qquad (10.40)$$

where the trace condition has been used to eliminate ρ_{11}. These inequalities restrict the experimental points to lie inside a volume bounded by a plane (10.39) and a cone (10.40). This volume is known as the positivity domain corresponding to the positivity condition (10.38). The intersections of the cone with planes perpendicular to the three axes ρ_{1-1}, $|\rho_{10}|$ and ρ_{oo} are respectively ellipses (all with eccentricity $\frac{1}{2}\sqrt{3}$), hyperbolae (all with asymptotes $\rho_{oo} = 0$, $\rho_{oo} = 1 - 2\rho_{1-1}$) and parabolae (all with directrix $\rho_{1-1} = \frac{1}{2}$). This can be readily seen by keeping the relevant element constant and comparing the form of (10.40) with the conic section

$$ax^2 + by^2 + 2hxy + c = 0 \qquad (10.41)$$

which is an ellipse, parabola or hyperbola according as $ab - h^2$ is greater than, equal to, or less than zero. Typical examples of these sections are shown in figure 10.2 for the particular cases

i) $\rho_{1-1} = 0.2$

ii) $|\rho_{10}| = 0.1$

iii) $\rho_{oo} = 0.5$

It is a general property of the conditions $c_i \geqslant 0$ that the higher the value of i (up to the maximum of 2J + 1) the more restrictive is the condition. Thus, in this case, the contour $c_3 = 0$ lies everywhere within the contour $c_2 = 0$. It is also interesting to note that these two contours meet at the singular points of the c_3 contour, namely where the cone (10.40) and the plane (10.39) intersect. (They do not always intersect, as in example iii) above, in which case the c_2 and c_3 contours do not meet.) More particularly, the requirement that there must be at least one point where the positivity conditions can be satisfied leads to the following restrictions on the elements ρ_{1-1} and $|\rho_{10}|$ (for ρ_{oo}, there are no such restrictions since all values from 0 to 1 allow a solution).

From the C_2 condition,

$$\rho_{1-1} \leqslant 1/\sqrt{3} = 0.577$$

and $$|\rho_{10}| \leqslant 1/\sqrt{6} = 0.408 \qquad (10.42)$$

while, from the C_3 condition, we have the more stringent requirements (as expected)

$$\rho_{1-1} \leqslant \tfrac{1}{2} = 0.500$$

and $$|\rho_{10}| \leqslant 1/\sqrt{8} = 0.354 \qquad (10.43)$$

FIG.10.2

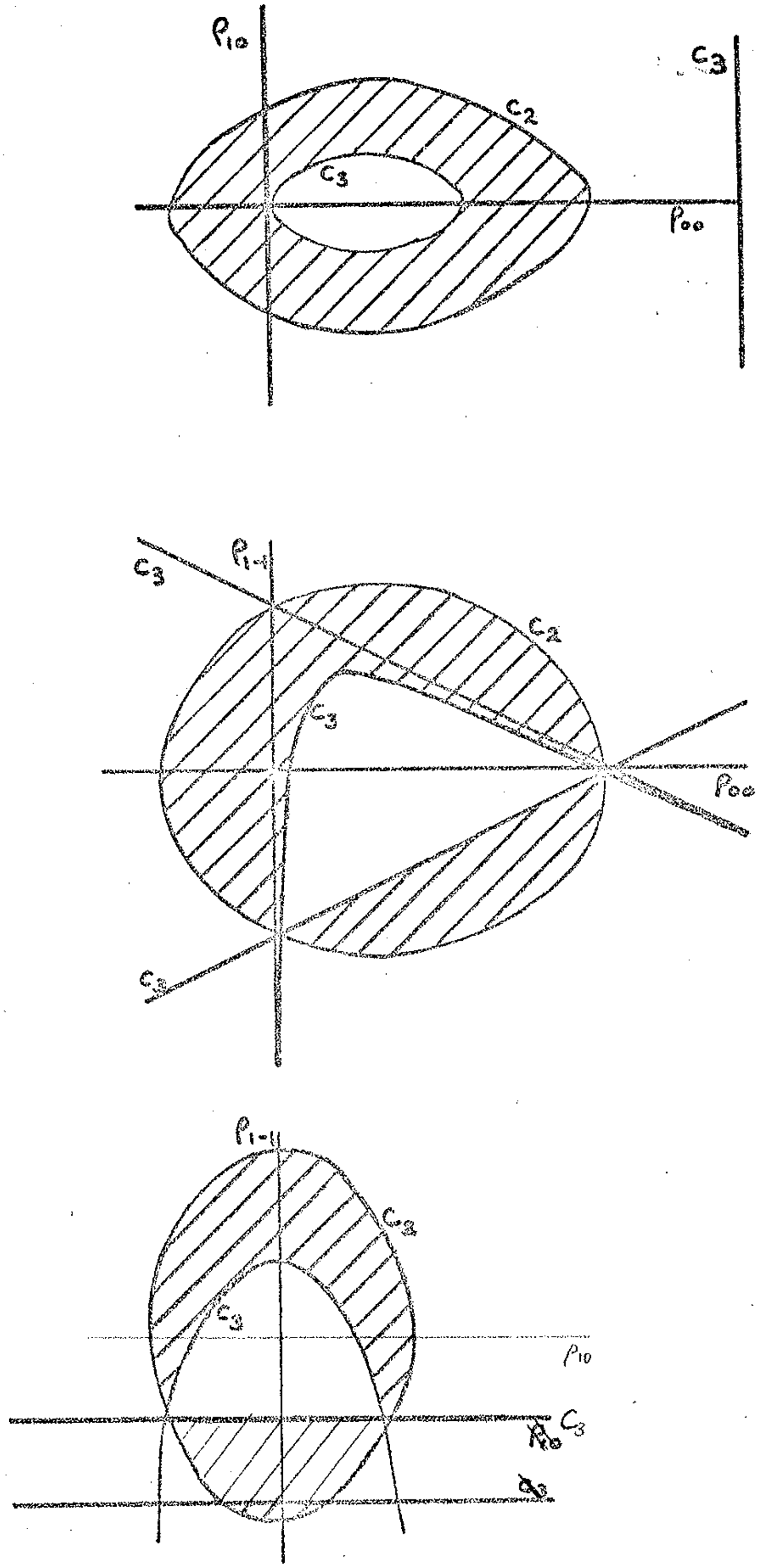

FIG. 10.3

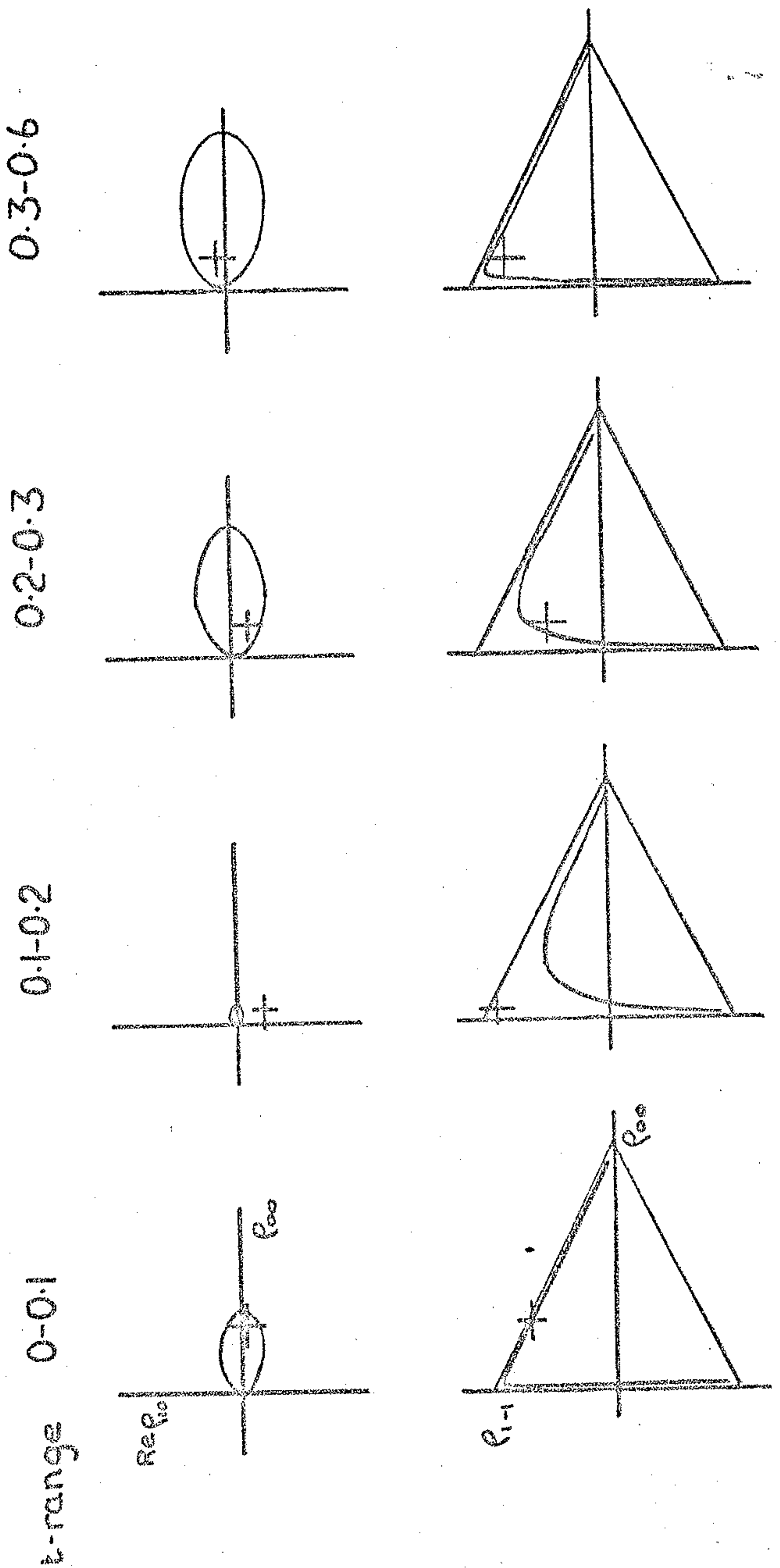

To show that a point lies within the positivity domain it is only necessary to show that it lies within any one of the three sections of the domain corresponding to the fixing of one of the three elements ρ_{1-1}, $|\rho_{10}|$, ρ_{oo}. However because of experimental errors the fixing of the third element will not be precise and the contour obtained will have an associated uncertainty. Instead of showing a contour drawn with errors we show two of the three sections so that the error on each matrix element appears at least once on a plotted point. The sections chosen correspond to cases i) and ii) above. Whereas the elements ρ_{oo}, ρ_{1-1} are directly obtainable from the angular distribution, in the case of $|\rho_{10}|$ we can get only a lower limit since the distribution yields only the real part (see appendix). From (10.37) and 10.40) it can be seen that the replacement of $|\rho_{10}|$ by Re ρ_{10} leads to analogous but weaker positivity conditions which have to be satisfied by the three observed parameters ρ_{oo}, ρ_{1-1} and Re ρ_{10}. Figures 10.3 and 10.4 show the comparisons with the experimental results for the final states $pK^{*-}(890)$ and $nK^{*o}(890)$. In most cases the experimental points lie within the positivity domain. The exceptions are the t-range 0.1 – 0.2 for K^{*-} and the t-range below 0.2 for K^{*o} for which the points are about two standard deviations outside the domain. They do however lie within the less restrictive domain corresponding to the condition $C_2 \geqslant 0$. The reason for the discrepancy is not clear. Apart from the possibility of a statistical fluctuation it could be due to background events in the samples which then may no longer be

FIG. 10.4

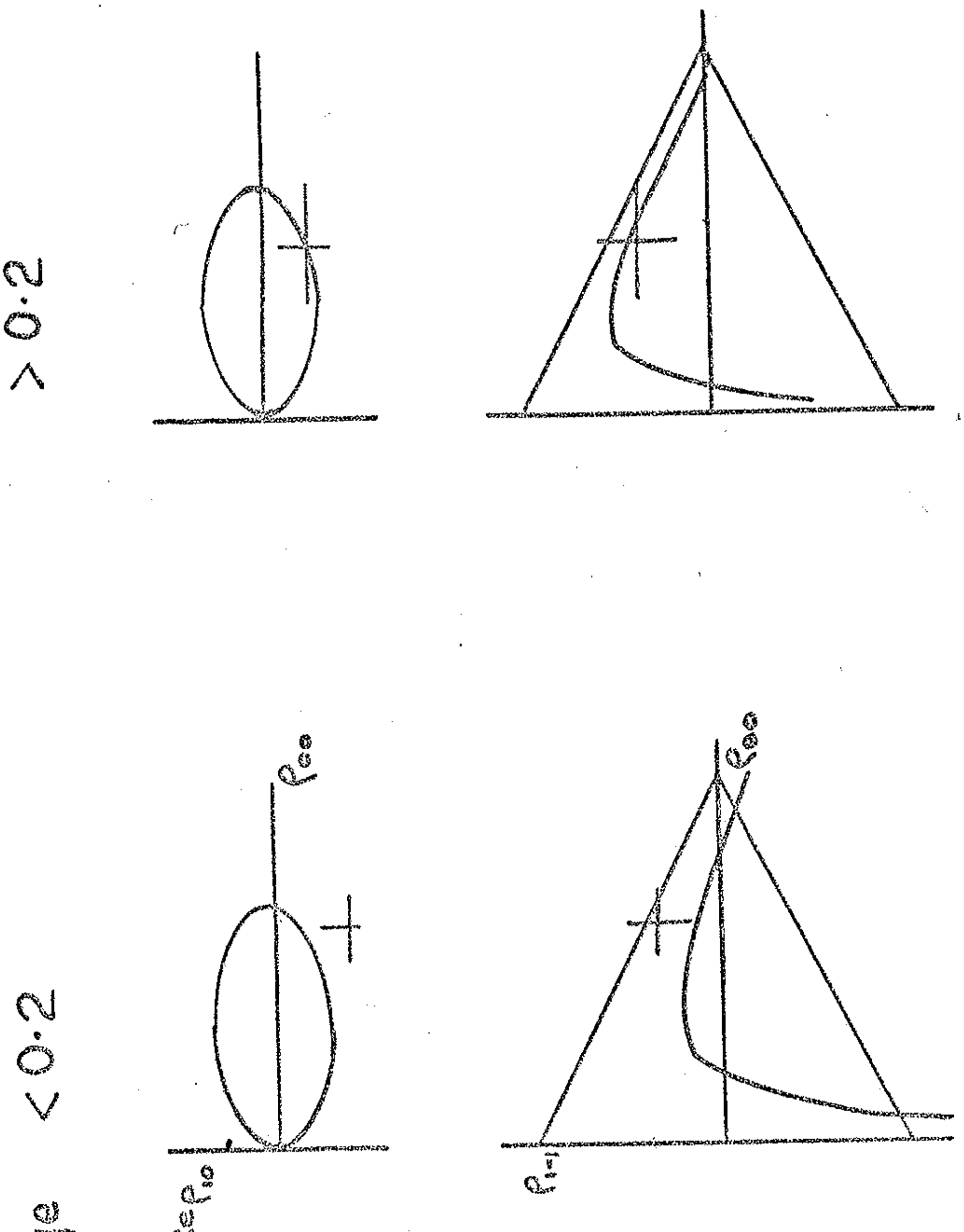

representative of a pure spin 1 state. However such an explanation seems unlikely for K^{*-} since the effect occurs in an isolated bin of t; also the background is smaller here than for K^{*0} (see figure 7.1). Were the spin of the K*(890) not so clearly established these results might have indicated that the spin was different from 1. However this possibility is discounted. For the K*(1320), for which spin 1 is suggested but not well established, it would be useful to repeat the above tests. At the present time the necessary density matrix elements have not been calculated. It should be noted that because the positivity conditions are non-linear functions of the matrix elements it is only valid to test them on samples of events sharing the same values of kinematic quantities. This should hold reasonably well for the bins used here.

Somewhat similar comparisons with positivity conditions have been made before by de Baere et al. (193) for the production of K*(890) and N*(1236) in 5 Gev/c K^+p interactions. However they took for comparison the <u>projections</u> of the positivity domain on planes perpendicular to the three axes rather than the <u>sections</u> of the domain corresponding to the actual experimental values. This means that the positivity requirements are not tested to the fullest possible extent.

10.1.2 Experimental tests for spin 2

Early results from the present experiment for the density matrix elements of K*(1420) gave the following values, averaged over all t values (see appendix).

TABLE 10.3

	$K^{*-}(1420)$	$K^{*0}(1420)$
ρ_{00}	0.31 ± 0.08	0.61 ± 0.11
ρ_{1-1}	0.16 ± 0.07	-0.39 ± 0.08
Re ρ_{10}	0 ± 0.10	0 ± 0.10

Elements ρ_{mn} with m or n greater than 1 were found to be small. In this case the spin 2 positivity conditions obtained from table 10.2 and relation (10.36) reduce to the same form as those for spin 1. Figure 10.5 shows the comparisons with the relevant sections of the positivity domain. For $K^{*0}(1420)$ there seems to be a violation of this condition by about two standard deviations (note that since ρ_{1-1} is negative in this case, the plane 10.39 intersects the elliptic section 10.40). The experimental point does however lie within the domain corresponding to the condition $C_2 \geqslant 0$.

Density matrix elements have yet to be calculated for the L(1800), for which spin 2 is preferred (see chapter 8). Tests of the positivity conditions might help to confirm this value,

FIG. 10.5

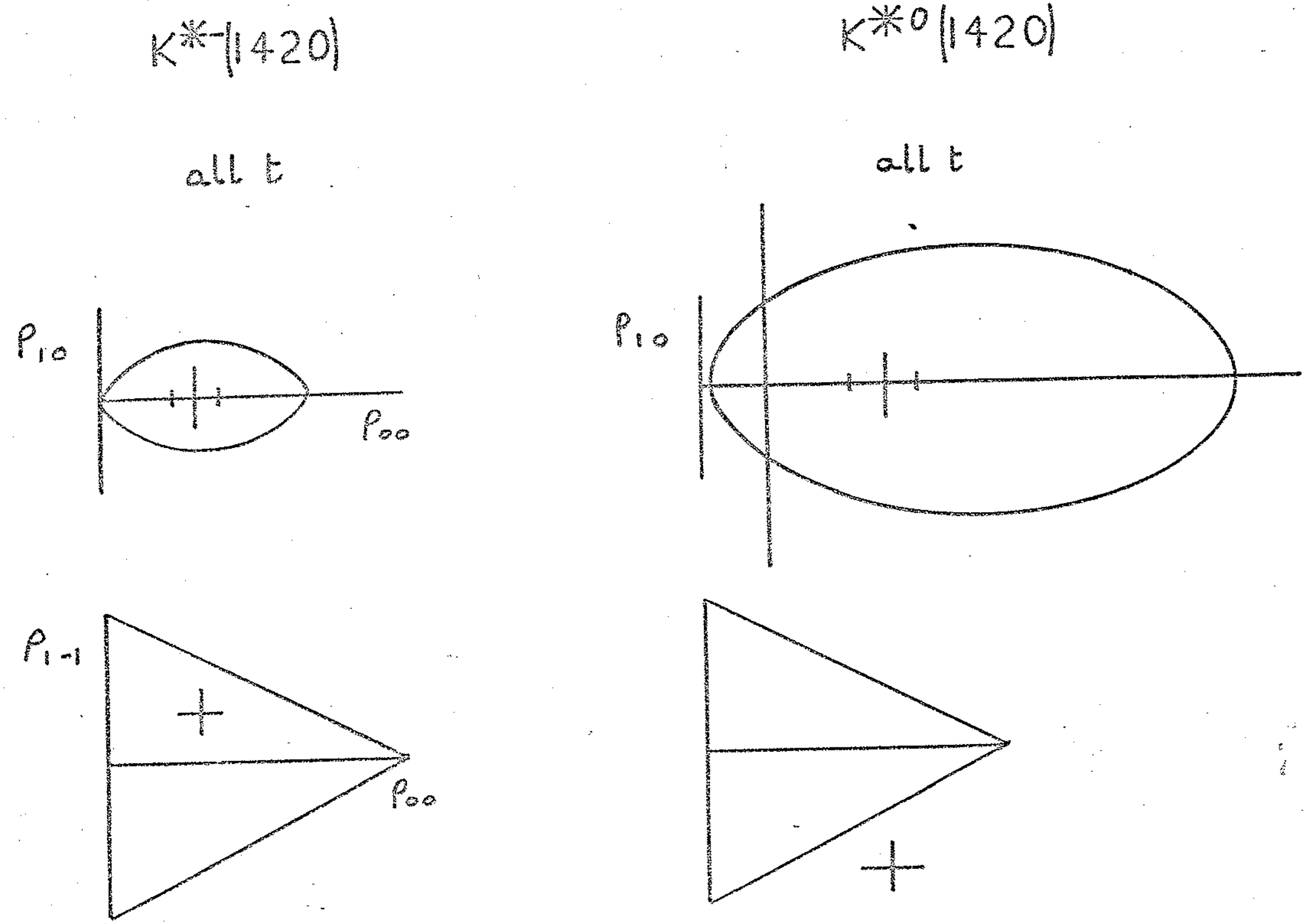

although their usefulness will be lessened by the large background in the L region.

10.2 Minimal requirements for exchanges

The helicity amplitude $F_{bd,ac}$ has the following partial-wave expansion (187):

$$F_{bd,ac}(t, x) = \sum_{J=\lambda_m}^{\infty} f^J_{bd,ac}(t)\, d^J_{\lambda\lambda'}(x) \qquad (10.44)$$

Where f^J denotes the partial-wave helicity amplitudes, x is the cosine of the scattering angle in the t-channel centre of mass system, $\lambda = a - c$, $\lambda' = b - d$ and $\lambda_m = \max(|\lambda|, |\lambda'|)$.
Parity conservation in the production process $a + b \longrightarrow c + d$ can be shown to lead to the requirement (assuming the exchange of definite quantum numbers)

$$f^J_{bd,-a-c} = \sigma_a\, \sigma_c\, \sigma_e\, f^J_{bd,ac} \qquad (10.45)$$

e being the exchanged system, where $\sigma_i = \pm 1$ according as the particle i has natural or unnatural spin-parity, that is, for bosons,

$$\sigma_i = P_i(-)^{J_i} \qquad (10.46)$$

In the present experiment $\sigma_a = -1$ and the helicity of $\underline{a}$ can only be zero because it has zero spin. It therefore follows from (10.45) that all amplitudes with c = 0 vanish when $\sigma_c = \sigma_e = \pm 1$, so that, (194):

$$\rho_{oo} = 0 \tag{10.47}$$

$$\mathrm{Re}\ \rho_{mo} = 0 \tag{10.48}$$

By splitting the helicity amplitudes into contributions from natural and unnatural parity exchanges and using the fact that a single t-channel exchange implies equal phases for all the helicity amplitudes, it can be shown that (195):

for a <u>single</u> exchange with $\sigma_e = \pm\ \sigma_c$,

$$(\mathrm{Re}\,\rho_{mn} \pm (-)^n\ \mathrm{Re}\,\rho_{m-n})^2 = (\rho_{mm} \pm (-)^m \rho_{m-m})(\rho_{nn} \pm (-)^n \rho_{n-n}) \tag{10.49}$$

Furthermore, for the case m = n, one can derive the following inequality, valid (in the high energy limit) for <u>any number</u> of exchanges with the <u>same</u> σ_e :

$$\frac{x^2 - 1}{x^2 + 1} \leqslant \frac{|\rho_{m-m}|}{\rho_{mm}} \leqslant 1 \tag{10.50}$$

where the upper limit is a result of parity conservation. If (10.50) is satisfied the relevant value of σ_e is given by:

$$\mathrm{sign}\ (\rho_{m-m}) = \sigma_e\ \sigma_c (-)^{m+1} \tag{10.51}$$

In the reactions being discussed here the particles b and d are both identical nucleons which means that the t-channel exchanges have to have a definite G-parity. There are four distinct cases to consider, specified by the values of σ and PC for the exchanged system (196) :

TABLE 10.4

σ_e	$(PC)_e$	forbidden amplitudes	
-1	+1	$\lambda_b = \lambda_d$	A_1-type
-1	-1	$\lambda_b \neq \lambda_d$	π-type
+1	+1	none	ρ-type
+1	-1	all	exotic-type*

(* this is an example of an exotic state of the second kind as mentioned in chapter 8, section 5)

With these additional restrictions on the allowed helicity amplitudes, further relations are obtainable:

for either a single π-type or a single A_1-type exchange, (10.49) is now valid with $\sigma_c = \pm 1$ respectively, in addition to its validity with $\sigma_c = \mp 1$ in the situation without G-parity restrictions (both π and A_1 have $\sigma_e = -1$). Furthermore, for any number of π-type exchanges

$$\mathrm{Re}\,\rho_{m-n} = \sigma_c(-)^n\,\mathrm{Re}\,\rho_{mn} \tag{10.52}$$

while, for any number of A_1-type

$$\mathrm{Re}\,\rho_{m-n} = \sigma_c(-)^n\left(\frac{x^2-1}{x^2+1}\right)\mathrm{Re}\,\rho_{mn},\ n \neq 0 \tag{10.53}$$

For the particular case m = n, these last two relations correspond to the extremes of the inequality (10.50). Substitution of either (10.52) or (10.53) in the sum rule (10.49) leads to the simple relation

$$(\mathrm{Re}\,\rho_{mn})^2 = \rho_{mm}\rho_{nn} \tag{10.54}$$

Relations (10.47) - (10.54) can give important information on the exchanges which contribute to the production of the four K* resonances. It should be remembered that they are independent of the assumptions of particular models for the processes. They are of most use when violated since consistency, if it occurs, can in general also be simulated by some more complex combination of exchanges.

10.2.1 Experimental tests for spin 1

In this case, (10.47) - (10.54) give the following relations: for any number of exchanges with $\sigma_e = \sigma_c$:

$$\rho_{oo} = 0 \tag{10.47)'$$

$$\mathrm{Re}\,\rho_{10} = 0 \tag{10.48)'$$

for a single exchange with $\sigma_e = +\sigma_c$:

$$2(\mathrm{Re}\,\rho_{10})^2 = \rho_{oo}(\rho_{11} - \rho_{1-1}) \tag{10.49)'$$

(with $\sigma_e = -\sigma_c$, (10.49) is trivially satisfied since it contains a factor $(1 + \sigma_e\sigma_c)$ on both sides)

for any number of exchanges with the same σ_e:

$$\frac{x^2 - 1}{x^2 + 1} \leqslant \frac{\rho_{1-1}}{\rho_{11}} \leqslant 1 \tag{10.50)'$$

where

$$\text{sign}\,(\rho_{1-1}) = \sigma_e \sigma_c \qquad (10.51)'$$

Then, from the G-parity restrictions:

for any number of π-type exchanges:

$$\rho_{1-1} = -\sigma_c \rho_{11} \qquad (10.52)'$$

$$\rho_{oo} = \sigma_c \rho_{oo} \qquad (10.52)''$$

$$\text{Re}\,\rho_{10} = \sigma_c \text{Re}\,\rho_{10} \qquad (10.52)'''$$

and for any number of A_1-type exchanges:

$$\rho_{1-1} = -\sigma_c \left(\frac{x^2 - 1}{x^2 + 1}\right) \rho_{11} \qquad (10.53)'$$

(this relation does not hold for ρ_{mn} when $n = 0$)

It is interesting to note the close similarity between (10.49)' and the positivity condition (10.40). It can be seen that they can only be mutually satisfied when Im $\rho_{10} = 0$. This result seems to imply that if a single $\sigma_e = +\sigma_c$ exchange is responsible for the production of a spin 1 boson then Im $\rho_{10} = 0$, or alternatively, that such an exchange cannot be the sole contributor to the production mechanism.

10.2.2 Implications for K*(890) production

In this case we have $\sigma_c = +1$ and the following conclusions can be drawn from the relations given in the previous section:

(10.47)': for $K^{*o}(890)$ production at all t' values there must be some $\sigma_e = -1$ exchange present because of the large value of ρ_{oo}. The same is true for $K^{*-}(890)$ production in the low t' region (less then 0.1)

(10.48)': for $K^{*o}(890)$, Re ρ_{10} is non-zero which again indicates the presence of $\sigma_e = -1$ exchange contributions. For $K^{*-}(890)$ this element seems to be significantly less than zero in the t' range 0.1 - 0.2 which leads to a similar conclusion for this range.

(10.49)': from figures 10.3 and 10.4 it can be seen that the experimental points all lie at least one standard deviation away from the contours which suggests that the data ~~is~~ are not consistent with the dominance of a single $\sigma_e = +1$ exchange.

(10.50)', (10.52)', (10.53)': these three relations can all be tested by showing the distribution of $|\rho_{1-1}|/\rho_{11}$ as a function of t' (see figure 10.6). The dotted lines show the limits of the inequality and these also correspond to the equalities (10.52)' and (10.53)' respectively. At high energy the quantity $(x^2 - 1/x^2 + 1)$ increases very quickly from its value of zero at $t = t_{min}$ to a value close to 1 which makes the inequality (10.50)' a very restrictive one. However it also means that, even with a factor of ten reduction in the experimental errors,

FIG. 10.6

$K^{*-}(890)$

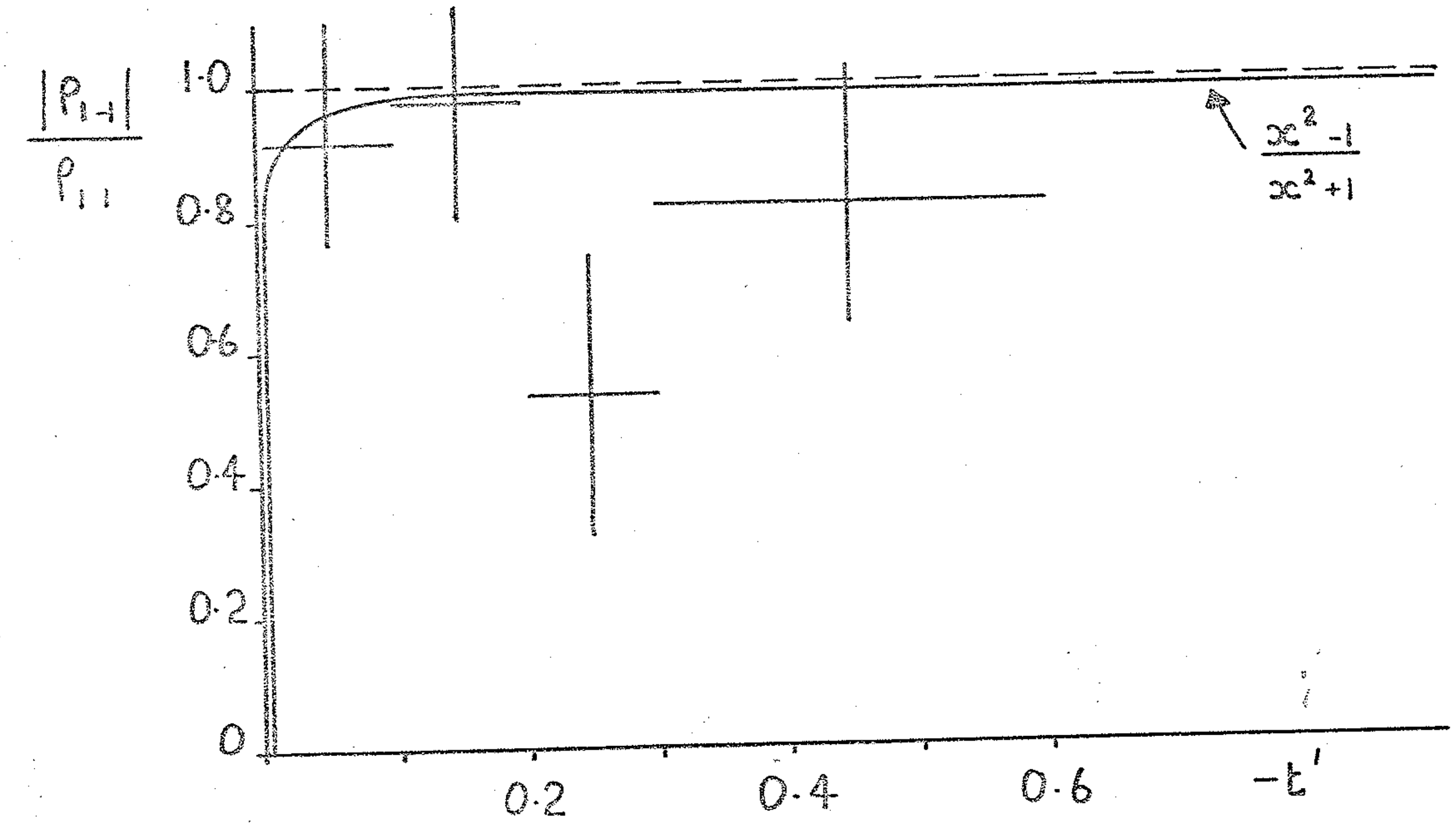

it is not going to be possible to differentiate among the three relations 10.50, 10.52 and 10.53, except possibly at $t' < 0.01$. The data points all lie below the predictions of the three relations but are all within one standard deviation except for the t'-range 0.2 - 0.3 for K^{*-}. This may indicate that there are exchanges with both $\sigma_e = +1$ and -1 contributing in this range.

(10.51)': where (10.50)' is satisfied, the situation is consistent with only $\sigma_e = +1$ exchanges, since ρ_{1-1} is positive.

(10.52)'' and (10.52)''' have no content for $\sigma_c = +1$.

To summarise we have shown that for $K^{*0}(890)$ production there must be some $\sigma_e = -1$ exchange contributions but we have not demonstrated either the presence or the absence of $\sigma_e = +1$ exchanges. For $K^{*-}(890)$ there is evidence from three different relations that some $\sigma_e = -1$ exchange is present in the first three bins of t' and there are also indications of a $\sigma_e = +1$ contribution.

This information may usefully be combined with that obtained for the I-spin of the exchanges in section 8.2.4, namely that $K^{*-}(890)$ had a large contribution from I = 0 exchange. $K^{*0}(890)$ can of course only be produced by I = 1 exchange. Thus $K^{*0}(890)$ production seems to be dominated by an exchange with I = 1, $\sigma_e = -1$, for which the most likely candidate would be the pion, with possibly some contribution from I = 0, $\sigma_e = +1$, which could be ρ or A_2 exchange. For $K^{*-}(890)$ we have not conclusively shown whether the dominant I = 0 contribution has $\sigma_e = +1$ or -1. However the simplest situation (that requiring only a single exchange of each type) would be a dominant I = 0, $\sigma_e = +1$ contribution (e.g. ω or f exchange) and a less important I = 1, $\sigma_e = -1$ exchange which would again presumably be the pion, since I = 1 exchanges must necessarily contribute to both K^{*0} and K^{*-} production if they are present in either.

10.2.3 Implications for K*(1320) production

In this case we have $\sigma_c = -1$ and we obtain mostly the same relations as for K*(890) but with the opposite implications for σ_e if they are satisfied. In addition (10.52)'' and (10.52)''' now have some content but they lead only to the earlier results (10.47)' and (10.48)' so that they contribute no additional information.

The only result available at present on the density matrix of K*(1320) is that ρ_{00} is approximately equal to 1. This implies that there must be a large contribution from $\sigma_e = +1$ exchange. Since it was shown before that this state was produced entirely by I = 0 exchange the best candidates for the exchanged system among the known particles are ω and f. However the Pomeron also has these quantum numbers and it could also be exchanged in K*(1320) production.

10.2.4 Experimental tests for spin 2

In this case (10.47) - (10.54) lead to the following relations, in addition to those obtained for spin 1 which are also valid here:

for any number of exchanges with $\sigma_e = \sigma_c$:

$$\mathrm{Re}\,\rho_{20} = 0 \qquad (10.48)''$$

for a single exchange with $\sigma_e = +\sigma_c$:

$$2(\mathrm{Re}\,\rho_{20})^2 = \rho_{oo}(\rho_{22} + \rho_{2-2}) \qquad (10.49)''$$

for a single exchange with $\sigma_e = \pm\,\sigma_c$:

$$(\mathrm{Re}\,\rho_{21} \mp \mathrm{Re}\,\rho_{2-1})^2 = (\rho_{11} \pm \quad {}_{2-2}) \qquad (10.49)'''$$

for any number of exchanges with the same σ_e:

$$\frac{x^2 - 1}{x^2 + 1} \leqslant \frac{|\rho_{2-2}|}{\rho_{22}} \leqslant 1 \qquad (10.50)''$$

with $\quad \mathrm{sign}\,(\rho_{2-2}) = -\sigma_e\,\sigma_c \qquad (10.51)''$

Then, from G-parity restrictions:

for any number of π-type exchanges

$$\left.\begin{aligned} \rho_{2-2} &= \sigma_c\,\rho_{22} \\ \mathrm{Re}\,\rho_{20} &= \sigma_c\,\mathrm{Re}\,\rho_{20} \\ \mathrm{Re}\,\rho_{21} &= -\sigma_c\,\mathrm{Re}\,\rho_{2-1} \end{aligned}\right\} \quad \text{from (10.52)}$$

and, for any number of A_1-type exchanges,

$$\rho_{2-2} = \sigma_c \left(\frac{x^2 - 1}{x^2 + 1}\right) \rho_{22} \qquad (10.53)''$$

10.2.5 Implications for K*(1420) production

For this case we have $\sigma_c = +1$ and from the limited amount of information available at present on the matrix elements for K*(1420) we can draw the following conclusions:

(10.47)': both charge states require the presence of some $\sigma_e = -1$ exchange.

(10.49)': from figure 10.5 it can be seen that the points are about two standard deviations away from the contours, i.e. the data are incompatible with a single $\sigma_e = +1$ exchange.

(10.51)': the values of $|\rho_{1-1}|/\rho_{11}$ are $+0.46 \pm 0.44$ for K^{*-} and 2.00 ± 0.31 for K^{*o}. The former value suggests the presence of both $\sigma_e = +1$ and -1 exchanges. However, although the value for K^{*o} is inconsistent with a value of about 1, as implied by (10.51)', it is considerably larger than this, which for a pure spin state, would indicate a violation of parity conservation. The effect of background may be partly the reason for this discrepancy.

In the case of the L-meson, for which $\sigma_c = -1$, we obtain the same relations as for K*(1420) but with the opposite implications for σ_e.

All these relations still await a comparison with experiment but, by analogy with K*(1320), it is expected that ρ_{oo} will also be quite large for the L, which would imply a dominant contribution from $I = 0$, $\sigma_e = +1$ exchanges.

(After the work of this chapter was completed it was found that relations (10.17) - (10.24) have in fact been previously obtained by Minnaert (197) and that (10.43) has been quoted by Daboul (198).)

CHAPTER 11

PRODUCTION MECHANISM FOR NATURAL SPIN-PARITY STATES

As shown at the end of the last chapter, the four K* resonances observed in this experiment fall clearly into two pairs as regards their production and decay characteristics. This chapter is concerned with models which attempt to describe the production of the two states with natural spin-parity, K*(890) and K*(1420), in more detail than was possible with the model-independent discussions of the last chapter. In that case we dealt exclusively with the decays of the resonances because these are largely determined by the spin-parity of the exchanged system and do not depend very much on other properties of that system. The differential cross sections, however, are very much more sensitive to these other properties and to obtain predictions for them it is necessary to make assumptions about the exchanged system, that is, to establish a model of some kind.

In terms of a partial-wave description of the reactions, their peripherality implies the dominance of high partial waves; in a classical scattering picture it corresponds to large values of the impact parameter; and in S-matrix theory it is interpreted as the dominance in the interaction of that singularity (in the t-channel in the present case) which is closest to the physical region. All these are equivalent ways of looking at the same experimental result.

As far back as 1935 Yukawa (199) suggested that the short-range strong forces between nucleons could be explained in terms of the exchange of particles of non-zero mass, the then undiscovered mesons. This was analogous to the description of the electromagnetic force in terms of the exchange of photons, the only difference being that the finite range implies mediation by a massive particle. Since the range of such an interaction varies inversely with the mass of the exchanged system, it follows that the dominant exchange in any particular situation will be that of the lightest system compatible with the quantum number requirements. Since the pion is by far the lightest of the hadrons it is reasonable to expect it to be the dominant exchange in strong interaction processes when this is allowable.

In the late fifties these ideas were put on a more quantitative footing by Goebel (200) and Chew and Low (56), who calculated the Feynman diagram involving the exchange of a pion according to the rules of quantum electrodynamics. Their emphasis was on the use of pion-exchange reactions as a possible means of studying the otherwise inaccessible pion-pion interaction, by extrapolating the observed cross-section out of the physical region to the pion pole where it would then describe on-shell pion-pion scattering. However it was realised that, since the pion pole was very close to the physical region at high energies, such a mechanism might be a reasonable approximation for such reactions (201, 202).

All exchange models have a matrix element whose general form is the product of three functions, two of which describe the couplings between the exchanged system and the initial and final pairs of particles in the t-channel and the third the contribution of the virtual exchanged system. For example the one-pion exchange ($O\pi E$) matrix element for the process $a + b \longrightarrow c + d$ has the form:

$$T = V_{a\pi c}(s_c, t)\left(\frac{1}{m_\pi^2 - t}\right) V_{b\pi d}(s_d, t) \tag{11.1}$$

where $(m_\pi^2 - t)^{-1}$ is the pion propagator and the other two factors are the vertex functions. The latter depend on the squares of the effective masses of the groups of final particles c, d respectively and on the square of the momentum transferred between the vertices. If c, d are stable particles $s_c = m_c$, $s_d = m_d$, if c (for example) is a resonance, then s_c will have a Breit-Wigner distribution.

The simplest model one can adopt is the <u>pole approximation</u> of $O\pi E$, in which the vertex functions are set equal to their on-shell values, that is, t is replaced by m_π^2. This assumption is probably too naive for this model to be of any use as it stands, though an adaptation of it is mentioned later.

11.1 <u>Born-term models</u>

This section deals with a class of models which share one underlying feature. The vertex factors are calculated in lowest order perturbation theory according to the Feynman rules using the known spin-parities of the final particles c and d. In the case of one-pion exchange and when particle a is a pseudoscalar, the meson vertex function has the form

$$V_{a\pi c}(t) = \left(\frac{a_c(t)}{a_c(m_\pi^2)}\right)^{J_c} V_{a\pi c}(m_\pi^2) \qquad (11.2)$$

where $a_c(t)$ is the momentum of a in the rest frame of c and $V_{a\pi c}(m_\pi^2)$ is the product of a coupling constant and a spin function. The baryon vertex function can be obtained in a similar way but is a little more complex. In the case of pion exchange the coupling constants are usually known, at the nucleon vertex from NN scattering and at the meson vertex from the width of the decay $c \longrightarrow a + \pi$, assuming c is sufficiently elastic to give an observable decay into this, its formation, channel. This means that the differential cross section for pion-exchange is exactly calculable in this simple Born term model (BTM).

For some reactions pion-exchange is either forbidden or is known from the observed density matrix not to be an important contributor (e.g. the $pK^{*-}(890)$ channel). In such cases the most likely exchanged particles would be the vector mesons and, because of their larger mass, the BTM predicts a less-peaked t-distribution than for pion-exchange reactions.

Comparison of the BTM with experimental data available at the time (mostly in the 1 - 3 Gev/c range) gave poor agreement in several respects:

i) the absolute value of the cross-section in the forward direction was too high, typically by a factor of about two. The peaking of the cross-section at small angles for the pion-exchange reactions was not strong enough, while the vector exchange reactions, for which less peaking is predicted, were found to be at least as peripheral, so that the agreement here was even worse. Furthermore, at a certain value of t the BTM cross-section begins to increase and diverges like $-t$ as $-t \longrightarrow \infty$ because of the factor $a_c(t)$ in (11.2) or corresponding factors for the vector exchange diagram (we are assuming that $J_c \geqslant 1$ as is the case for the reactions being studied);

ii) if a partial wave decomposition is made it is found that the lower amplitudes (s and p waves) violate the unitarity bound:

$$\sigma_j \leqslant \frac{\pi}{k^2} \quad (j + \tfrac{1}{2}) \tag{11.3}$$

iii) the BTM amplitude behaves like s^{J_e} at high energy so that, except for $J_e = 0$, the cross section is asymptotically unbounded. This is bad enough for the reactions where pion exchange is forbidden but, when both pion and vector exchanges can occur, it predicts that it will be the latter which will dominate at a sufficiently high energy, in contradiction with the expected dominance of the lightest possible exchange.

As far as reactions at 10 Gev/c are concerned, whether they be pion- or vector-exchange dominated, the simple BTM will not give a satisfactory description.

11.1.1 Born term model with form factors

As a possible improvement over the BTM it was suggested that the reason for failures i) and ii) above might lie in the neglect of higher order corrections in the derivation of the one particle exchange amplitude (202). There certainly will be some such renormalisation effects associated both with the vertices and the propagator but they are not necessarily the only reasons for the discrepancy with experiment. They may be interpreted (at least in the case of the vertices) as the result of a finite interaction region rather than a point interaction. These higher order corrections cannot be calculated and one can only represent their effects by introducing arbitrary functions of t known as form factors. The introduction of such form factors can of course always be made to give agreement with the data. However the maximum extent to which the vertex form factors can vary with t and still retain physical significance is governed by the electromagnetic form factors of the particle concerned. Quite reasonable agreement was obtained for some pion-exchange reactions in the 1-3 Gev/c region (203) but for vector exchanges it was found that the necessary form factors had a structure corresponding to the exchange of a system with a mass of about $2m_{\pi}$, considerably less than that of the vector mesons and inconsistent with knowledge of the electromagnetic structure of the nucleon. Thus what might be regarded as the essential part of the BTM amplitude, the propagator, has had its t-dependence swamped by the t-dependence of the form factor; in S-matrix terms, the form factor has a pole which is nearer the physical region than the vector meson pole. These features make the BTM model with form factors very implausible for vector exchange reactions, except possibly as a means of parametrising the data. Even for pion exchange reactions the model is not likely to explain data at 10 Gev/c. For example, it was not even possible to obtain simultaneous agreement for both the forward peak and the total cross section of the pion-exchange reaction $K^+p \longrightarrow K^*(890)\ N^*(1236)$ at 1.96 and 3 Gev/c (204) using any one of several suggested form factor functions.

There are further discrepancies of a less drastic kind between the observed density matrix elements and the predictions of the BTM either with or without a form factor modification (the introduction of the form factor does not alter the density matrix predictions). For pion-exchange BTM requires $\rho_{00} = 1$, while for vector exchange it predicts $\rho_{00} = 0$, $\rho_{1-1} \neq 0$ (in general), all other independent elements being zero in each case. Experimentally these relations are approximately but not exactly satisfied, indicating the need for some other exchange contribution.

11.1.2 Born Term model with absorption

The failure of the low partial waves in the BTM to satisfy the unitarity restriction is closely connected with the existence in the momentum region above about 1.5 Gev/c of reactions involving many particles in the final state. Qualitatively one would expect such more complex reactions to occur preferentially at small impact parameters, that is in central rather than peripheral collisions, or in low partial waves. Because of unitarity the two-body amplitude in these partial waves will be suppressed. This effect was first suggested by Dar et al. (205) who, however, used a sharp cut-off in the partial waves which gives rise to minima in the differential cross-section, analogous to optical diffraction from a sharply defined object. Although such behaviour may be seen in some $\overline{N}N$ processes, most reactions can be understood better in terms of a more diffuse diffracting region.

The most common approach for introducing these so-called absorption corrections into the BTM is to use the distorted-wave Born approximation (DWBA) in the form discussed by Sopkovich (206) for the reaction $\bar{p}p \to \bar{\Lambda}^0\Lambda^0$. In the DWBA the wave functions are approximated by those of an optical model potential whose imaginary part simulates the absorptive effect of the competing channels. At high energy the eikonal approximation allows the absorption to be expressed directly in terms of elastic scattering parameters. This leads to the following matrix element for the jth partial wave:

$$M^J_{fi} = (S^J_{ff})^{\frac{1}{2}} B^J_{fi} (S^J_{ii})^{\frac{1}{2}} \qquad (11.4)$$

where B^J is the unmodified BTM expression and i, f denote the initial and final states. The quantities S_{ii}, S_{ff} are the S-matrix elements for the initial and final channels and represent the effects of absorption. They are assumed to be diagonal, that is only elastic rescattering corrections are considered. Helicity indices have been dropped from (11.4) since at high energy the known hadron-hadron elastic scattering amplitudes are helicity preserving and diffractive. This is shown by the fact that the forward elastic scattering amplitude satisfies the optical theorem

$$\sigma_{tot} = \frac{4\pi}{k} \operatorname{Im} T_{el}(s,\ t = 0) \tag{11.5}$$

indicating that its real part is consistent with zero.

In the derivation of (11.4) it is assumed that (207):

a) the absorption is the same in the initial and final states

b) the range of the interaction causing the transition $i \longrightarrow f$ is much less than the ranges of the absorptive interactions $i \longrightarrow i$ and $f \longrightarrow f$. This is certainly not well satisfied for pion exchange reactions.

The matrix elements S_{ii} and S_{ff} are usually parametrised as follows (208):

$$S^J = 1 - C \exp\left(-\gamma(j - \tfrac{1}{2})^2\right) \tag{11.6}$$

where $\quad C = \sigma_{el}/4\pi b \qquad (11.7)$

and $\quad \gamma = (2q^2 b)^{-1} \qquad (11.8)$

b is the slope of the differential cross-section, σ_{el} the total cross-section and q the centre of mass system momentum, for the particular elastic process concerned. The parameters C_i, γ_i for the initial state are obtainable from the elastic scattering data of the experiment. At 10 Gev/c they have the values $C_i = 0.6$, $\gamma_i = 0.016$. For the final state when one or both particles are unstable there is no direct information available on the elastic scattering. From the fact that the stable particles and the resonances occupy an equivalent position in most theoretical frameworks we would not expect the final state parameters to vary wildly from those of accessible elastic scattering reactions, which at high energy have values of C in the range 0.7 - 1.0. On the whole it turns out that the results are not especially sensitive to these absorption parameters. From (11.4) and (11.6) it can be seen that a value of 1.0 for C_i or C_f (or both) leads to complete absorption of the lowest partial wave ($j = \frac{1}{2}$ in the meson-nucleon case). It is customary to choose $C_f = 1.0$ in order to achieve this; such a choice was necessary to obtain agreement in the intermediate energy range where the model was first applied. For γ_f a common choice is $0.75\ \gamma_i$; when the final particles have larger masses than the initial ones, γ_f will be increased because of the smaller value of q in (11.8). Thus the above assumption for γ_f implies a larger slope for the final state elastic scattering. For K*(890) production in the present experiment it corresponds to b = 10.7 while for K*(1420) production the value is about 13.2. The uncertainty present in the knowledge of these parameters is expected to assimilate any errors which may accrue from the invalidity of the assumption b) above in the case of pion-exchange reactions.

Once the absorption parameters have been fixed it is possible to calculate the one pion exchange amplitude with absorption ($O\pi EA$) exactly since the necessary coupling constants are known. These are chosen as follows:

for the $K^*(890)K\pi$ vertex, $\frac{g^2}{4\pi} = 0.75$

for the $K^*(1420)K\pi$ vertex, $\frac{g^2}{4\pi} = 0.65$

for the πNN vertex, $\frac{G^2}{4\pi} = 14.6$

The first two values come from the known decay widths of 50 Mev, 47 Mev respectively, while the last value is obtained from πN scattering data.

The existence of competing channels and the consequent reduction in the lower partial waves has several effects on the predictions of the simple BTM: it reduces the total cross-section, it collimates the angular distribution to a further extent, and it modifies the decay distributions since it effectively involves multiple exchanges. All these features are such as to allow a better description of the data and in the intermediate energy region (2 - 4 Gev/c incident momentum) the model gives satisfactory results for both pseudo-scalar and vector exchanges.

$K^-p \longrightarrow nK^{*0}(890)$

The prediction of $O\pi EA$ for the differential cross-section of this reaction is shown dotted in part (a) of figure 11.1 (this curve was also shown earlier in figure 9.3, page 282). The cross-section predicted by the model is actually too large by a factor of 4 and the curve shown has been normalised to the total cross-section for the reaction. Apart from this important discrepancy the shape is quite well predicted out as far as $t = 1.0$, except possibly near $t = 0.6$ where there seems to be an abrupt fall in the experimental cross-section and for the most forward point which is about twice the predicted size (of course, without the normalisation this point would give the best agreement but in that case all the others would be badly described). The predictions for the spin density matrix elements are shown as the dotted curves in part (a) of figure 10.1 (page 304). It can be seen that the deviations from the simple BTM predictions of 1, 0, 0 respectively for the three elements are well reproduced (including their variation with t) by the absorptive corrections. The observed and predicted values averaged over the t-range (0, 0.3) are shown in the table 11.1. The experimental value of ρ_{00} does not vary much with energy (see table 11.2 which shows values averaged over the t-interval 0 - 0.2). This suggests that there is not much change in the underlying mechanism for this reaction over the range 2 - 10 Gev/c. In particular it means that there is no sign of a contribution from ρ-exchange at the higher energies. This justifies the consideration of only pion exchange as a contributor to this reaction.

FIG. II.1

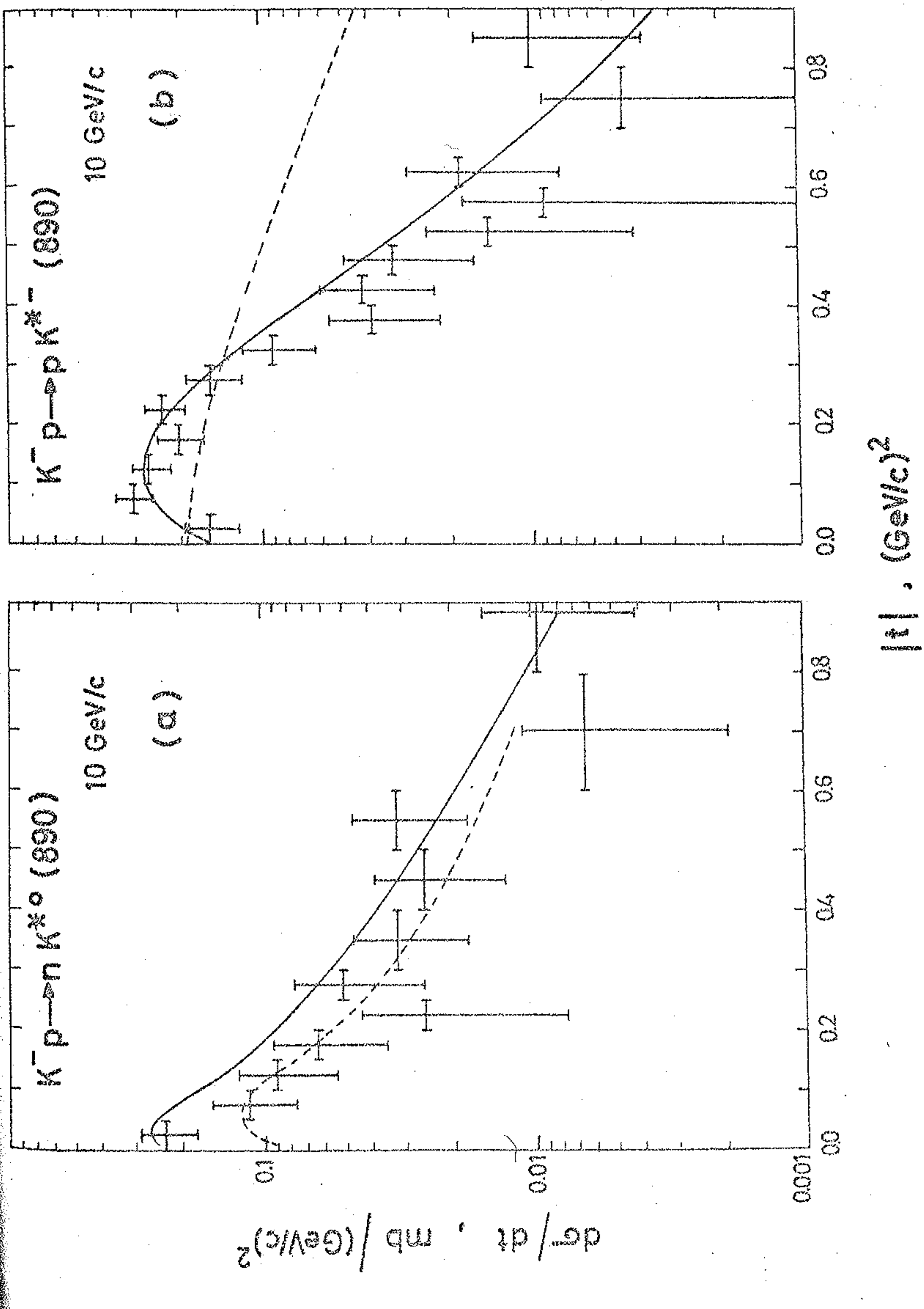

$K^- p \to n K^{*o}$ (890)
10 GeV/c
(a)
$K^- p \to p K^{*-}$ (890)
10 GeV/c
(b)
0.1
0.01
0.001
0.0
0.2
0.4
0.6
0.8
$d\sigma/dt$, mb / $(GeV/c)^2$
$|t|$, $(GeV/c)^2$

TABLE 11.1

SPIN DENSITY MATRIX ELEMENTS FOR $K^{*0}(890)$

	Experiment	$O\pi EA$ prediction
ρ_{00}	0.60 ± 0.09	0.68
ρ_{1-1}	0.16 ± 0.04	0.08
Re ρ_{10}	-0.21 ± 0.06	-0.17

TABLE 11.2

ρ_{00} FOR $K^{*0}(890)$ AND $K^{*-}(890)$ AT DIFFERENT INCIDENT MOMENTA

Momentum	ρ_{00} for $K^{*0}(890)$	ρ_{00} for $K^{*-}(890)$	Reference
1.33	0.62 ± 0.05	-	62a
2.64	0.68 ± 0.07	0.54 ± 0.03	164
3.0	-	0.34 ± 0.08	166
4.1	0.57 ± 0.08	0.27 ± 0.08	169
4.6	0.63 ± 0.10	-	171
5.5	0.63 ± 0.12	-	169
6	-	0.22 ± 0.08	172
10.1	0.60 ± 0.09	0.17 ± 0.07	13
11.2	0.58 ± 0.05	-	173

$K^-p \longrightarrow nK^{*0}(1420)$

The predictions of OπEA for the differential cross-section of this reaction is shown in figure 9.3 (page 282). In this case the curve shown has not been normalised and gives a fairly good description of the data out to $t = 1.0$.

For the reactions $K^-p \longrightarrow pK^{*-}(890)$, $pK^{*-}(1420)$ we have already seen that there is evidence for a contribution from $I = 0$, natural parity exchange. Assuming this is vector exchange we have ω and ϕ as the two candidates but, since ϕ has a much weaker coupling to nucleons than does ω, its contribution will be neglected. Any $I = 1$ exchange which contributes to K^{*0} production must, because of I-spin conservation, also contribute to K^{*-} production with an amplitude one-half of that in the charge exchange reaction. Thus there is an exactly known contribution from pion exchange in the K^{*-} reactions. However, it is not possible to determine the coupling constants of ω at the $K^*(890)$ vertex since this vertex cannot appear in an observable decay because the $K^*(890)$ is below the $K\omega$ threshold. For $K^*(1420)$ it is possible to determine the required coupling constant from its decay into $K\omega$ but the partial width for this decay is not accurately known. At the nucleon vertex the ω coupling constant is also not well-known since there is no possibility of carrying out ωN scattering. In order to calculate the vector-exchange amplitude in the OPEA model only the product of the vector coupling constants is required but since there are two possible couplings of the vector meson at the nucleon vertex, the tensor (Pauli) coupling G_T and the vector (Dirac) coupling G_V there are two unknown parameters involved. There are two possible procedures to follow:

i) best values of the two parameters may be determined by a fit to the data

ii) the vector coupling constants may be expressed in terms of the known pseudoscalar ones by using the predictions of a higher symmetry in which both vector and pseudoscalar mesons are contained within the same multiplet.

The first of these two methods is adopted here. The two parameters are chosen to be the following dimensionless functions of the coupling constants (207):

$$\xi = \frac{f(G^V + G^T)}{2gG} \qquad (11.9)$$

$$\eta = \frac{fG^T}{gG} \qquad (11.10)$$

where g, G were defined above for pseudoscalar exchange and f is the coupling of ω to K*K.

$\underline{K^- p \longrightarrow pK^{*-}(890)}$

For this reaction three maximum likelihood fits were carried out to determine the pair of parameters (ξ, η). The best values found were approximately:

a) using differential cross section data only: (0.2, 0.2)

b) " density matrix elements " : (0.4, 0.0)

c) " both sets of data together : (0.4, 0.2)

Fits were also carried out with the absorption parameter γ_f, the most arbitrarily chosen of the four, set equal to 0.005 (half of its previous value). There was no appreciable difference in the results obtained.

Figure 11.2 shows the differential cross section (DCS) predicted by each of these sets of values. It can be seen that fit a), which uses only the data in this distribution, is very poor and, from inspection alone, seems hardly better than the other two fits. The results for the density matrix elements from the three fits are shown in table 11.3. In part b) of figure 10.1 (page 304) the dotted curves are those obtained using the combined data, that is fit c). (For the record, the dotted curve in part b) of figure 11.1 and the curve in figure 9.3, page 282, also correspond to this fit). The agreement is better than that obtained for the DCS, consistent with the comment made at the start of this chapter that at least the main features of the density matrix elements are determined by the exchange causing the transition $i \longrightarrow f$. Certain features present in the data for ρ_{oo} and Reρ_{10} seem to be reproduced but ρ_{1-1} is not well explained.

The value of ρ_{oo} for $K^{*-}(890)$ production shows a considerable variation with energy, in contrast to the situation for K^{*o} (see table 11.2). There is a steady fall-off with increasing energy which may be interpreted as an increase in the vector exchange contribution.

In the Born term model, either with or without form factors there is no interference between the contributions from pseudoscalar and vector

FIG. II.2

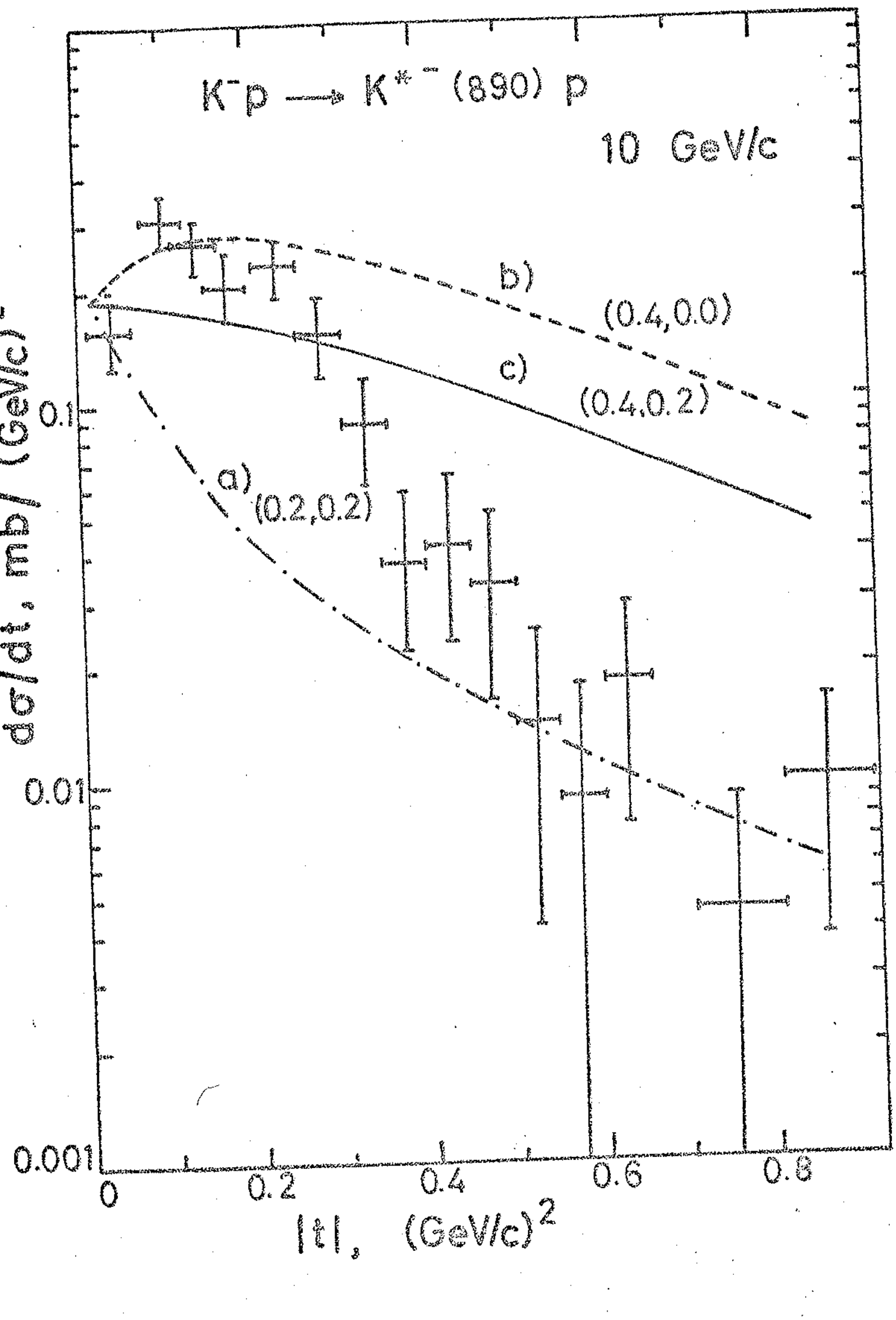

K⁻p ⟶ K*⁻(890) p
10 GeV/c
b)
(0.4,0.0)
c)
(0.4,0.2)
a)
(0.2,0.2)
dσ/dt, mb/ (GeV/c)²
0.1
0.01
0.001
0
0.2
0.4
0.6
0.8
|t|, (GeV/c)²

Table 11.3

Comparison of density matrix elements for reaction (2) with absorption calculations for different values of (ξ, η)

$\|t\|$ $(GeV/c)^2$	0.0 – 0.10		0.10 – 0.20		0.20 – 0.30		0.30 – 0.60	
ρ_{mn}	EXP	THEOR	EXP	THEOR	EXP	THEOR	EXP	THEOR
ρ_{00}	0.27 ± 0.08	$0.54^{a)}$ $0.34^{b)}$ $0.36^{c)}$	0.05 ± 0.07	$0.33^{a)}$ $0.12^{b)}$ $0.11^{c)}$	0.13 ± 0.07	$0.22^{a)}$ $0.07^{b)}$ $0.06^{c)}$	0.12 ± 0.07	$0.13^{a)}$ $0.05^{b)}$ $0.03^{c)}$
$\rho_{1,-1}$	0.34 ± 0.05	$0.07^{a)}$ $0.29^{b)}$ $0.22^{c)}$	0.46 ± 0.06	$0.21^{a)}$ $0.43^{b)}$ $0.41^{c)}$	0.23 ±0.09	$0.30^{a)}$ $0.46^{b)}$ $0.45^{c)}$	0.36 ± 0.08	$0.39^{a)}$ $0.47^{b)}$ $0.42^{c)}$
Re $\rho_{1,0}$	- 0.015 ± 0.05	$-0.21^{a)}$ $-0.08^{b)}$ $-0.13^{c)}$	- 0.11 ± 0.05	$-0.14^{a)}$ $-0.02^{b)}$ $-0.04^{c)}$	- 0.07 ± 0.04	$-0.10^{a)}$ $-0.01^{b)}$ $-0.02^{c)}$	0.025 ± 0.07	$-0.05^{a)}$ $-0.01^{b)}$ $-0.01^{c)}$

a) $(\xi, \eta) = (0.2, 0.2)$ from fit to $d\sigma/dt$

b) $(\xi, \eta) = (0.4, 0.0)$ from fit to $\rho_{mn}(t)$

c) $(\xi, \eta) = (0.4, 0.2)$ from fit to $d\sigma/dt$ and $\rho_{mn}(t)$

exchanges (204). This is no longer true when absorption is introduced and the interference between π and ω exchanges in K*(890) production leads to somewhat different predictions for the DCS and for ρ_{00} in the low t region where the two amplitudes have comparable magnitudes. Both these quantities will have larger values if there is constructive interference than if the interference is destructive. For K^{*-} production, these two cases correspond to $\xi > 0, \xi < 0$ respectively. For $K^{*+}(890)$ production in K^+p reactions the reverse is true since the vector exchange amplitude in this charge conjugate reaction changes sign under the C-parity operation whereas the pion exchange amplitude does not. In the intermediate energy range the difference in the absorption parameters for the K^+ and K^- reactions results in a larger cross-section for $K^{*+}(890)$ production in the small t region. Thus if there is constructive interference for $K^{*+}(890)$ the effects of interference and absorption enhance one another, while in the opposite case they tend to cancel out. This allows the sign of the interference to be easily determined and experiments with K^- at 2.64 Gev/c (210) and 3.0 Gev/c (166a, 208) and with K^+ at 3.0 Gev/c (177a, 208) all agreed with the choice $\xi > 0$, that is, constructive interference for K^{*-} and destructive for K^{*+}. (It should be noted that in references 208 and 210 the relative sign change between K^{*+} and K^{*-} has been omitted and the conclusions of these papers should therefore be reversed for the K^{*-} case.)

At high energies, because of the increasing contribution from vector exchange (as shown by the steady decrease in ρ_{00}) the region where interference is appreciable shifts to smaller t values. Even when there is constructive interference the DCS turns over near $t = 0$ because the w-exchange contribution, necessitating as it does spin-flip at the baryon vertex, must vanish at $t = 0$ due to angular momentum conservation. Also there is no longer any difference between K^{*+} and K^{*-} caused by the difference in absorption parameters and within the present experimental errors it is therefore difficult to distinguish between the two possible signs for ξ. The most sensitive place to look for such a distinction is in the value of ρ_{00} at small t, where there is a substantial difference remaining even at 10 Gev/c (211). In this experiment the value of ρ_{00} for the t-range 0 - 0.1 is 0.27 ± 0.08. At 10 Gev/c K^+ there is a reported value of 0.01 ± 0.07 (184). This is averaged over the whole t-range but because the cross-section is highest at small t values much of the contribution must come from this region (and ρ_{00} should never be negative). This therefore seems more consistent with $\xi > 0$, in agreement with the lower energy results.

If the absorption model is to have any physical meaning for vector exchange, the vector coupling constants determined by fitting data at different energies must really <u>be</u> constant. Figure 11.3 shows the values of (ξ, η) determined for $K^{*-}(890)$ production as a function of the incident momentum. It can be seen that, far from being constant, they both show a strong variation with energy which can be approximated by $(p_{lab})^{-1}$. Thus the OPEA model for vector exchange does not seem at all satisfactory over this energy range. It is at high energy that it is worse since in the intermediate energy range it did at least give reasonable fits to the DCS with the relevant values of the coupling parameters. It is clear that

FIG. 11.3

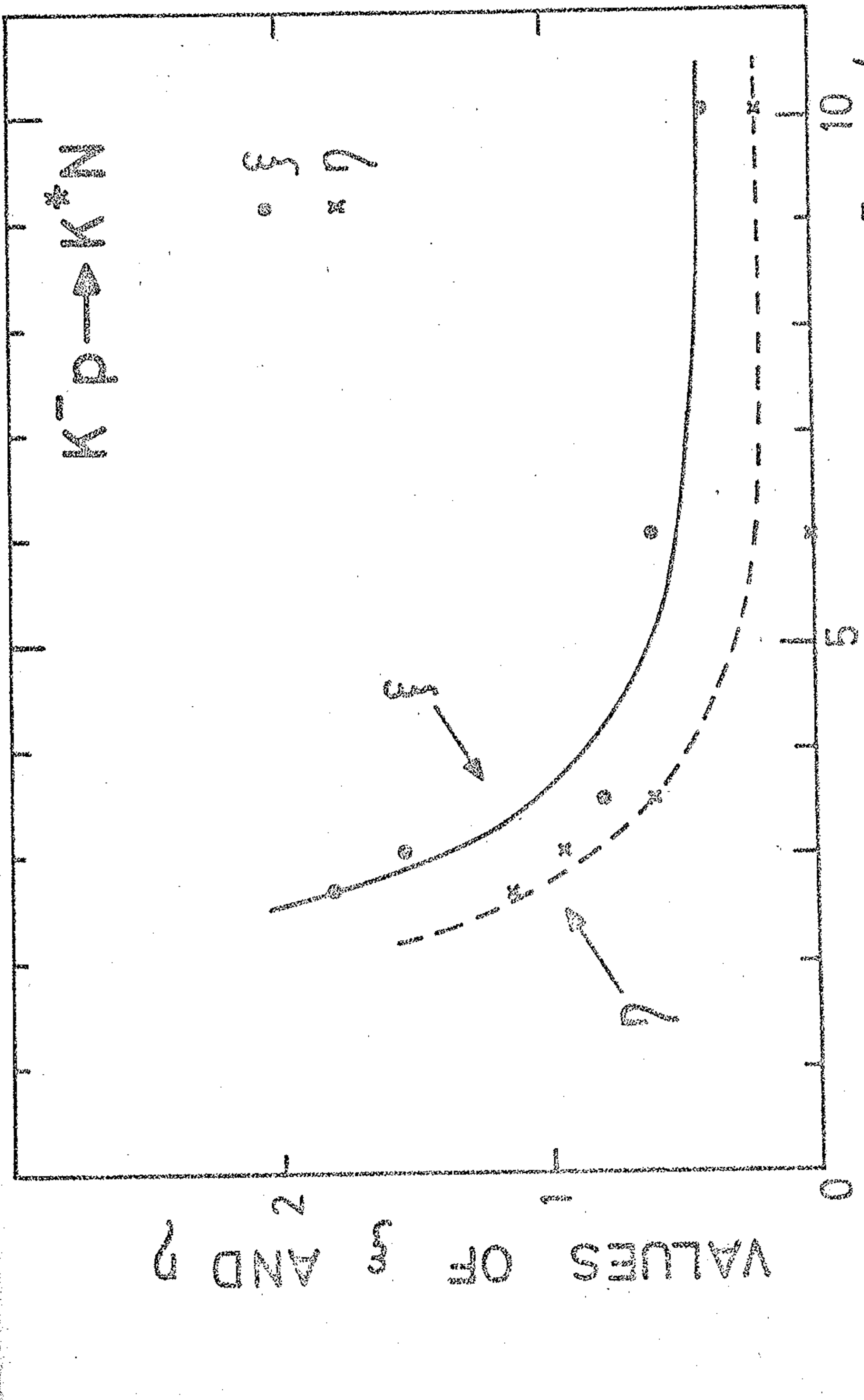

$K^- p \rightarrow K^* N$
• ξ
× η
ξ
η
0
5
10
LAB. MOMENTUM OF INCIDENT K^-, GeV/c
1
2
VALUES OF ξ AND η

the main inadequacy of the model, namely the divergent behaviour of the vector exchange cross-section at high energy, is simply being incorporated by an artificial reduction in the coupling "constants" ξ, η. This can achieve some compatibility with the total cross section (though not one with any physical significance) but the t-dependence cannot be explained in this way and at high energies the prescription used does not even serve as a useful means of parametrising the data. The fit a), which was the best (!) fit to the DCS data alone, is equivalent to assuming a very small vector exchange contribution as can be seen from the unacceptable predictions it gives for the density matrix elements (table 11.3). This is clearly just the best way in which the parameters can be varied so as to reduce the large vector exchange cross-section and the fit itself is physically meaningless.

It is interesting to compare the values of ξ, η obtained experimentally with the predictions for these quantities which are given by a higher symmetry scheme such as SU(6). Since we have not made any quantitative determination of the ρ-exchange contribution we can only compare quantities which depend only on ω-exchange. (However the fact that the ρ-exchange contribution is small is consistent with SU(6).) In the low t limit the predictions of relativistic SU(6) for the ω-couplings are (212):

$$\xi/2\xi - \eta = 0.15 \tag{11.11}$$

$$2\xi - \eta = -1 \tag{11.12}$$

From the results of fit c) above, we have the values 0.33 and 0.6 for these quantities. The first of these is in reasonable agreement with the prediction but the second, although agreeing in magnitude, differs in sign. This sign is determined by the interference between pion and vector exchange and a negative value is not favoured experimentally, as we saw earlier. In this connection, the analysis of $K^{*-}(890)$ production at 4.1 and 5.5 Gev/c (169) is interesting. The SU(6) couplings are introduced from the start and the agreement with experiment is claimed as evidence for their validity. However it seems probable that the predictions with the opposite sign for would give at least as good agreement. Unfortunately these predictions are not shown.

$\underline{K^-p \longrightarrow pK^{*-}(1420)}$

The DCS for this reaction has been calculated for three combinations of pion and vector exchange and the results are shown in figure 9.3 (page 282). The curve marked 1b corresponds to the same values of (ξ , η) that were used in the combined fit c) for $K^{*-}(890)$ production and gives very bad agreement with the data. Curve 1a) has an increased amount of vector exchange while curve 2 is for vector exchange only. These two appear to give better agreement for the shape of the DCS but the normalisation is badly predicted.

11.1.3 Absorption and form factors

The main trouble with the Born term model with empirical form factors discussed in section 11.1.1 was that in the vector exchange situation the form factors required had to vary more strongly with t than was reasonable. Since absorptive effects provide a natural way to sharpen the production angular distribution, it is possible that less drastic form factors, which must be present at some level, could usefully be introduced. They would reduce the amount of absorption required to fit the DCS and thus the density matrix elements would have values somewhat closer to the simple BTM predictions.

The inclusion of form factors and absorption to describe reactions in the intermediate energy range was found to give reasonable agreement (213) although in no case could it be said that the data actually required the presence of the form factor. This is of course in the energy region where the absorption model works quite well, even for vector exchange.

At 10 Gev/c the introduction of a t-dependent form factor will not improve the description of either the π-exchange reactions, where the t-dependence is already quite well described, or the vector exchange reactions, where the discrepancy is too large to be saved by a form factor of no more than the allowable strength.

11.1.4 Criticism of Born term models

The inclusion of absorption in the BTM amplitude according to the Sopkovich formula (11.4) does seem to go part of the way towards achieving better agreement with experiment and probably contains some physical truth. With this in mind several authors have attempted to derive it in a more rigorous way. Approaches via S-matrix theory have been made by Ball and Frazer (214) and Omnes (215). The former retained a more general result with the aid of assumptions which are plausible for pion exchange but not at all so for vector exchange. They did not require to make the assumption that the absorptive interactions were of shorter range than the primary interaction described by the Born term, an assumption which is certainly not true for pion-exchange reactions. The failure to derive (11.4) for vector exchanges seems consistent with the failure of the model at high energy for such reactions. Although such derivations are based on principles which are believed to be more relevant for strong interactions than potential scattering, they do involve assumptions of their own and it is difficult to see exactly what status the Sopkovich formula has. It is probably only strictly valid for high partial waves. In spite of its usefulness in reducing the contributions of the lower partial waves below the unitarity bound it does not itself satisfy unitarity exactly since, for example, only elastic interactions are considered for the absorbing processes. Two ways in which it could be unitarised are provided by the K-matrix (216) or N/D (217) methods. The latter is more suited to the treatment of bound state problems and becomes very complex at high energy when there are many open channels, but it has been discussed for the absorption situation (218). The K-matrix method has been applied to K^+p reactions at 3 Gev/c (219). Using only the four final states K^+p, K*N, KN* and K*N* the DCS cannot be sharpened sufficiently to give agreement with experiment and the elastic channel has a much too large imaginary amplitude. Inclusion of other channels can improve the collimation but only at the expense of making the elastic amplitude still bigger.

In conclusion, the modifications of the simple Born term model have mostly only attempted to improve the deficiencies i) and ii) mentioned earlier, namely the strong unitarity violation in the low partial waves and the inconsistent behaviour of the DCS at large enough t values when particles with spin are produced (not exchanged). But none have attempted to deal with the violent behaviour which is predicted when the model is applied to the exchange of particles with spin at high energy. No finite sum of such exchanges is likely to give any better agreement.

11.2 Reggeised models

Soon after it was shown that form factors were not able to improve much on the results of the Born term model for vector exchange reactions, it was suggested (220) that if the exchanged system were a Regge trajectory instead of a single elementary particle, the high energy S^J catastrophe present in all Born term amplitudes ($J \geqslant 1$) could be removed. In the single Regge trajectory exchange model the DCS behaves like $S^{2\alpha(t)-2}$ at high energy (see equations 9.3 and 9.4), compared with the S^{2J-2} behaviour of the BTM. Although $\alpha(t)$ is equal to J at $t = m^2$ this point is not in the physical region. Unlike the case of an elementary particle which corresponds to a fixed pole in the angular momentum plane, the Regge trajectory moves with t and, since it has a positive slope and an intercept at $t = 0$ of no more than one (157), it follows that in the scattering region (which always corresponds to negative t in the reactions being studied here), the largest power of s that can be present is s^0, that is a constant.

This $s^{\alpha(t)}$ behaviour of the single Regge exchange amplitude at high energy implies that the trajectory with the largest $\alpha(t)$ will be the dominant one in the scattering at that value of t. This is only strictly true when the two external particles at each vertex have equal masses, that is for elastic scattering (or to a good approximation) charge exchange scattering. For the reaction $a + b \longrightarrow c + d$ with arbitrary masses, the t-channel centre of mass system scattering angle is given by:

$$\cos\theta_t = \frac{-2t(s - m_a^2 - m_b^2) + (t + m_a^2 - m_c^2)(t + m_b^2 - m_d^2)}{\lambda^{\frac{1}{2}}(t, m_a^2, m_c^2)\ \lambda^{\frac{1}{2}}(t, m_b^2, m_d^2)} \tag{11.13}$$

where the function λ has been defined earlier.

In the pairwise equal mass situation $m_a = m_c$, $m_b = m_d$,

$\lambda^{\frac{1}{2}}(t, m_a^2, m_c^2) = t(t - 4m_a^2)$ etc., so that

$$\cos\theta_t = \frac{2(s - m_a^2 - m_b^2) + t^2}{(t - 4m_a^2)^{\frac{1}{2}}(t - 4m_b^2)^{\frac{1}{2}}} \tag{11.14}$$

In the limit $t \longrightarrow 0$ these expressions for $\cos\theta_t$ reduce to 1 and $s/2m_a m_b$ respectively and only in the latter case is the asymptotic approximation for $P_\alpha(\cos\theta_t)$ valid in the limit $s \longrightarrow \infty$. It is this approximation which leads to the $s^{\alpha(t)}$ behaviour of the Regge exchange amplitude. In the unequal mass case for finite s there is a region around the forward direction where the necessary approximation is invalid. In the case of spinless particles analyticity at $t = 0$ requires the existence of a family of daughter trajectories with intercepts which are successively one unit below that of the original parent trajectory (221). For the case of particles with spin it is convenient to define reduced helicity amplitudes $\bar{f}$ given by:

$$\bar{f}_{bd,\, ac} = f_{bd,\, ac} \,/\, (\sin\tfrac{1}{2}\theta t)^{|\lambda-\mu|}(\cos\tfrac{1}{2}\theta t)^{|\lambda+\mu|} \tag{11.15}$$

where $\lambda = a - c$, $\mu = b - d$ are the helicity changes at the two vertices. Then one may write

$$f_{bd,\, ac} \pm f_{-b-d,\, ac} = K_\pm(t)\, C_\pm(s, t) \tag{11.16}$$

where $K_\pm(t)$ are functions involving the kinematical singularities and have been given explicitly by Wang (222), and $C_\pm(s, t)$ are analytic functions except for possible dynamical singularities. One may carry out the usual Reggeisation process for C to obtain

$$C_{\pm}(s, t) = \gamma_{\pm}(t)\ s^{\alpha - M}\ \xi(t) \qquad (11.17)$$

where $M = \max(|\lambda|, |\mu|)$ and $\xi(t)$ is the signature factor. Thus for small t the power of the asymptotic s-dependence has been reduced by M but for large t the additional S^M dependence needed to regain the $S^{\alpha(t)}$ behaviour is provided by the half-angle factors in (11.15). The functions $\gamma_{\pm}(t)$ are smooth functions of t but may contain functions of $\alpha(t)$ (223). When these functions are zero they give rise to zeros in the helicity amplitudes.

11.2.1 Regge pole exchange

An analysis of the production of K*(890) in both its charged and neutral states in terms of the exchange of Regge trajectories has been carried out. Full details are given in reference 224. Contributions from other J-plane singularities (e.g. cuts or fixed poles) have been neglected. Unfortunately the number of trajectories which can be exchanged in these reactions is quite large, due to the lack of quantum number restrictions. Exchanges of both G-parity are allowed as are those of both natural and unnatural spin-parity. Furthermore, for $K^{*-}(890)$ both I = 0 and I = 1 exchanges are possible. Six trajectories are considered, three with I = 0 (P, P', ω) which can contribute only to K^{*-} production, and three with I = 1 (π, ρ, A_2) which can contribute to both reactions. Of these six only the pion has unnatural spin-parity. The trajectory functions for ρ and A_2 are well-known from analyses of the reactions $\pi^- p \longrightarrow \pi^0 n$, $\eta^0 n$ respectively where they are the only known trajectories which can contribute. (Since no well-established Regge recurrences exist the meson trajectory functions cannot be determined from the Chew-Frautschi plot.) The P and P' trajectories are also well-known from Regge pole fits to elastic scattering reactions. Indeed these were specifically introduced in order to understand the behaviour of elastic scattering. No particles are known which lie on either of these trajectories and it is possible that they represent the effect of something other than a Regge trajectory. However for the time being they will be retained since no better parametrisation is available. The Pomeron trajectory P is not expected to contribute strongly to K^{*-} production since the cross-section for this reaction decreases quite rapidly with increasing energy. Also in the SU_3 symmetric limit it cannot couple to a KK^* system. This is borne out by the small contribution obtained in the fit. The contribution of P' is also negligible.

The remaining two trajectories (π and ω) are assumed to be linear but since they are less well-known their slopes and intercepts are left to be determined in the fit. In addition to these parameters the contribution of each trajectory contains a scaling factor S_0 and the function $\gamma(t)$ which is assumed to be constant. However, allowing S_0 to vary from trajectory to trajectory effectively allows the residues to have a strong t-dependence.

An analysis of the type described here would be meaningless if applied only to data at a single energy. For this reason data for K^{*-} and K^{*0} production at 4.1 and 5.5 Gev/c (169) have been used as well as data from $K^{*+}(890)$ production in K^+p reactions at 3, 3.5 and 5 Gev/c (177b, 180). The K^{*+} amplitude involves the same trajectory contributions as K^{*-} but with a relative change of sign between those having $C = +1$ and those with $C = -1$.

The results from the fit for the differential cross-sections at 10 Gev/c are shown as the solid curves in figure 11.1. The curves have been normalised to the total reaction cross-sections and it can be seen that the shapes are well reproduced by the model. In particular the agreement is much better for K^{*-} than the OPEA prediction (dotted curve). For $K^{*0}(890)$ the two models give practically identical results, remembering that the OPEA prediction was not normalised but divided instead by a somewhat arbitrary figure of 4.

The predictions for the density matrix elements are shown as the solid curves in figure 10.1 (page 304). Again the agreement is reasonable except perhaps for Re ρ_{10} in the case of K^{*-}. It is difficult to say whether the extent of the observed agreement is to be expected simply as a result of the flexibility allowed in the fit by the large number of undetermined parameters (twenty-two in all). However the minimum value of chi-squared obtained (232) is not at all small which suggests that one is doing more than just arbitrary curve fitting. Hopefully then, the approximate consistency between the fit and the 10 Gev/c data is physically significant, at least in its main features.

The amplitudes which contribute to the two reactions are as follows. For K^{*-} production the ω non-spin-flip amplitude is the dominant one out to $t = 0.7$ except in the very forward direction where the pion non-flip amplitude dominates. The importance of pion exchange in this region compared with the higher lying ω trajectory can be understood from (11.17). Because of the symmetry properties of helicity states under the parity transformation, natural parity exchanges couple to the K^* helicity states ± 1 only, whereas unnatural parity exchanges allow $\lambda = 0$ as well (225). Thus the pion trajectory can asymptotically dominate in the very forward region if it is the leading trajectory of unnatural parity.

In K^{*0} production the pion non-flip amplitude gives the dominant contribution at all t values. The ρ contribution is small while A_2 exchange only contributes substantially beyond $t = 0.4$. The dominance of the pion trajectory even away from the forward direction in this reaction is not so easily understood. The unimportance of ρ-exchange (in both reactions) is consistent with the small coupling constants predicted by SU(6).

11.3 Other models

There have been many other models proposed from time to time to explain various features of high energy reactions.

A form factor approach somewhat different from the one discussed earlier has been proposed by Durr and Pilkuhn (226). The divergence of the BTM matrix element (11.2) at high $-t$ values when particles with spin are produced is not present if the naive pole approximation mentioned at the very beginning of the chapter is used. The latter is a bad description at low t values so they suggest the addition of a form factor. Wolf (227) has analysed several pion-exchange reactions with this model over a wide range of energy and finds good agreement. This model has not yet been applied to the $K^{*0}(890)$ or $K^{*0}(1420)$ production reactions.

Several approaches have been made to combine the Regge and absorption approaches since they tend to describe quite well the s and t dependences respectively of the scattering amplitude. It is not very clear if any absorption effects are included automatically in the Reggeised exchange amplitude. Van Hove has shown that the Regge amplitude is obtained in the limit of an infinite sum of single particle exchanges spaced along a linear rising trajectory at intervals of two in spin.(228) The inclusion of absorptive effects is equivalent to the inclusion of contributions from the exchanges of branch cuts in the angular momentum plane.

The amplitude first written down by Veneziano for the $\pi\pi \longrightarrow \pi w$ reaction (229) has led to many intersting developments and has provided for the first time a method for describing the behaviour of multi-body reactions. Its relevance to the two-body reactions discussed here is that in limit when the $(K\pi)$ combination forms a $K^*(890)$ or $K^*(1420)$ the Veneziano amplitude reduces to single Regge exchange. At the present time the formulation of the Veneziano model is such that only a single trajectory can be included to describe this single Regge limit so that no improvement in the description of the K* production reactions will be obtained by using it.

CHAPTER 12

PRODUCTION MECHANISM FOR UNNATURAL SPIN-PARITY STATES

This chapter presents a very brief discussion of the present state of knowledge concerning the production mechanisms of the two states of unnatural spin-parity observed in this experiment, K*(1320) and L(1800).

The earliest meson resonances to be discovered were those which were eventually assigned to the 1^- and 2^+ nonets, that is they had natural spin-parity. As the previous chapter showed there has been considerable progress in the understanding of the production of such states. In contrast it is only fairly recently that the mechanisms involved in the production of the less well-established unnatural parity meson states have been studied and most of the results so far are only qualitative.

For a long time there was controversy as to whether the peaks observed in, for example, the $(K\pi\pi)$ mass spectra were really resonant states or whether they were merely "kinematic" effects. Deck (61) proposed a non-resonant explanation of the peaks involving the exchange of a pion at the top vertex of a peripheral graph, followed by diffraction scattering of this virtual pion at the baryon vertex. In the intermediate momentum range this mechanism was able to give a fairly satisfactory description of the $(K\pi\pi)$ mass distribution but at high energy this is no longer a tenable explanation since it is not able to reproduce the sharpness of the observed

FIG. 12

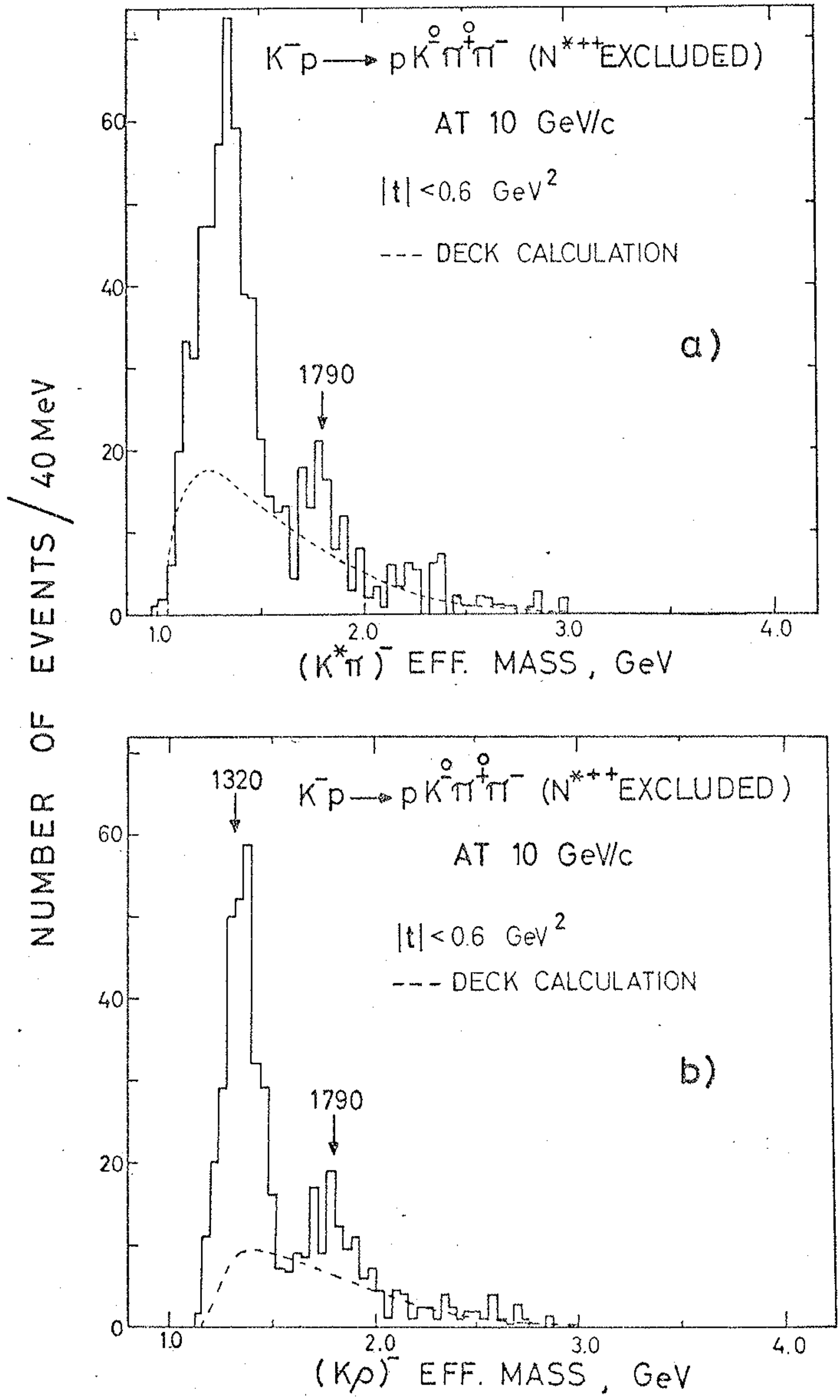

$K^- p \rightarrow p K^o \pi^+ \pi^-$ (N^{*++} EXCLUDED)
AT 10 GeV/c
$|t| < 0.6$ GeV^2
--- DECK CALCULATION
a)
1790
0
20
40
60
1.0
2.0
3.0
4.0
$(K^*\pi)^-$ EFF. MASS , GeV
NUMBER OF EVENTS / 40 MeV
1320
$K^- p \rightarrow p K^o \pi^+ \pi^-$ (N^{*++} EXCLUDED)
AT 10 GeV/c
$|t| < 0.6$ GeV^2
--- DECK CALCULATION
b)
1790
$(K\rho)^-$ EFF. MASS , GeV

peaks. This is shown in figure 12.1 which shows the mass distribution predicted by the Deck process (dotted curves). In a Reggeised model the Deck graph is a double Regge graph where the exchanges are a pion and a Pomeron. The realisation that there is at least a partial duality involved in the description of such systems as either resonances or background effects has to a large extent made such questions less vital (230).

As discussed in chapter 10 the production of the K*(1320) and L(1800) states seems to occur exclusively by the exchange of a system with natural spin-parity and zero I-spin. Since these reactions also have cross-sections which are approximately constant in energy it is very likely that they are produced by the exchange of the Pomeron trajectory. By analogy with high energy elastic scattering which has a purely imaginary amplitude characteristic of optical diffraction, reactions like those involving K*(1320) and L(1800) are often referred to as inelastic diffraction processes. Because the Pomeron trajectory seems to be rather different from other meson trajectories (it has a much smaller slope and no physical states are known to lie on it) its exact nature is unknown and it may represent the effect of some more complex J-plane singularity.

Morrison (231) has shown that for all reactions which seem to be of the Pomeron exchange type the following selection rule is satisfied

$$\Delta P = (-)^{\Delta J} \tag{12.1}$$

where the delta-symbols represent the changes in parity and spin that occur at one vertex. For pseudoscalar-meson-baryon scattering this means that states of unnatural spin-parity appear to be diffractively produced but states of natural spin-parity do not. This is consistent with the absence of Pomeron exchange in K*(890) and K*(1420) production. The above empirical rule should appear naturally in a theory for the production mechanism of these reactions, at least for the cases in which its validity has been demonstrated even if the simple form (12.1) does not hold in general. Some progress towards such a description has been made by Carlitz et al. (232)

As discussed in chapter 8 the possibility of there being more than one K* state in the Q region has been suggested. One might well expect that the K* states which belong to the 1^{++} and 1^{+-} nonets in the quark model classification would lie in this mass region. These two K* states have identical quantum numbers since they are not eigenstates of C, the quantum number which distinguishes the two nonets. This gives rise to the possibility of mixing but reasons were given earlier why this might only be small, due to the fact that it is zero in the limit of SU(3) symmetry. Quite independently of the mixing the proximity of two states with the same spin and parity allows interference to occur. As shown first by Goldhaber (233) and later by Fogli et al. (234) the assumption of various values for the relative phase angle between the two production amplitudes gives very different predictions for the positions of the peaks in the mass distribution. If this phase angle varies with energy this might provide an explanation of the variation in the number and position of the peaks in the $(K\pi\pi)$ spectrum reported by different experiments. If such a description is valid a comparison of the observed mass spectra with those predicted by the simple phase-difference model might enable the variation of the phase angle with energy to be determined. At present this is difficult as there are not enough experiments with the necessary low mass resolution and high statistics.

The obvious explanation of the two production mechanisms involved here is that the K* state with $C = +1$ would be produced by Pomeron exchange and would therefore have a constant asymptotic cross-section, while the state with $C = -1$ would be produced by the exchange of a meson with $C = -1$ and $I = 0$ (for example ω^0). This explanation assumes that the couplings at the meson vertex are (at least approximately) SU(3) invariant so that one may apply the conservation of C-parity. This explanation is in contradiction with the preference of $C = -1$ for the nonet to which the K*(1320) belongs obtained in chapter 8 from a consideration of relative decay rates. The even more favoured assignment of $C = -1$ for the L-meson obtained in an analogous way (though using other decay modes) is also hard to reconcile with its constant cross-section.

There is certainly a long way to go before such processes are understood as well as those which involve the exchanges of reputable meson trajectories. No mention has been made here of the many attempts that have been made to understand these inelastic diffractive processes in terms of models of the optical type, in particular the coherent droplet model (235).

CHAPTER 13

CONCLUSIONS AND FUTURE PROSPECTS

The four reactions whose analysis has formed the main part of the work in this thesis are typical examples of the hadron scattering processes which have been extensively studied at available accelerator energies during the last ten years, that is, ever since the discovery of the existence of excited states of meson systems.

The production of the two natural spin-parity states, K*(890) and K*(1420), is described by the exchange of a mesonic system in the t-channel, once the energy is sufficiently high for the effect of s-channel resonances to have become negligible. The exact details of the production mechanism for such reactions are still under discussion but, in a phenomenologic way, we believe we understand them. This cannot be claimed for the other two processes studied (those involving the production of the K*(1320) and L(1800) states) which are diffractive in character. We really understand very little about such reactions and it is therefore fortunate that they appear to represent an increasing proportion of the total two-body reactions as the energy is raised, due to their approximately constant cross-sections. One must not however forget that the quasi two-body processes themselves only form a relatively small part of the total scattering cross-section and that the study of multi-body final states is also vital for the understanding of hadronic systems. Such studies are at present only in their early stages.

The current complexity of strongly interacting systems is very suggestive of some simpler underlying sub-structure and if this turns out to be correct, the extension of present experiments into the new "high energy" region up to 500 Gev/c may well provide evidence for this structure. These energies should become available in the not too distant future.

It would be satisfying to suppose that this new increase in available energy will lead to an understanding of the various interactions of the present "elementary" particles. But we have only our past experience as a guide and this hope may well prove unfounded. Certainly the diffractive type of process seems to have an essentially smooth behaviour in most physical variables (for example the absence of spin dependence and the constant cross-section) which does not seem likely to lead to the discovery of deeper structure.

It is now nearly forty years since the strong nuclear force began to be a prime object of study in physics. Involving as it does the interactions of matter at the most basic level yet investigated it underlies (at least in a conceptual if not in a direct practical way) all other processes which take place in the physical world and must therefore be regarded as one of the most basic fields of research. Yet during this time nothing of the most fundamental significance has emerged by way of a theoretical understanding of these phenomena, compared for example with the advances made in the period 1900 - 1930 (quantum theory, special relativity and quantum mechanics) which revolutionised almost all previous physical concepts. This is in spite of the fact that probably more experimental and theoretical effort has been expended in this time in the field of particle physics than the total of all previous work in the whole of physics.

Hopefully future experiments will uncover new and unexpected features of the particle interactions and will lead in turn to a more complete understanding of them. If not we shall have all been wasting our time.

APPENDIX

Determination of spin density matrix elements

The spin density matrix elements in this experiment have been calculated (where accessible) from the decay angular distributions of the resonant states concerned, using the method of maximum likelihood. The polar and azimuthal decay angles θ, ϕ are defined in the Gottfried-Jackson frame of reference (see chapter 10 for a definition of this frame). For a two-body decay the direction of either of the two (oppositely directed) decay products serves as an analyser, whereas for a three-body decay the relevant vector is the normal to the decay plane.

For the decay of a $J^P = 1^-$ state into two or three pseudoscalar (0^-) particles, the angular distribution is given by (191):

$$W_1(\cos\theta, \phi) = \frac{3}{4\pi}\left(\rho_{oo}\cos^2\theta + \rho_{11}\sin^2\theta - \rho_{1-1}\sin^2\theta\cos 2\phi - \right.$$
$$\left. - \sqrt{2}\,\mathrm{Re}\,\rho_{10}\sin 2\theta\cos\phi\right) \quad (A.1)$$

with the trace condition $\rho_{oo} + 2\rho_{11} = 1.$

When this is integrated over ϕ or θ it leads to the following single angle distributions, each of which depends on only one independent matrix element:

$$W_1(\cos\theta) = \frac{3}{2}\left(\rho_{oo}\cos^2\theta + \rho_{11}\sin^2\theta\right) \quad (A.2)$$

$$W_1(\phi) = \frac{1}{2\pi}\left(1 - 2\rho_{1-1}\cos 2\phi\right) \quad (A.3)$$

A distribution involving only the third independent element $\mathrm{Re}\,\rho_{10}$ can be obtained by integrating over $\sin 2\theta \cos\phi$.

For the decay of a $J^P = 2^+$ state into two pseudoscalars:

$$W_2(\cos\theta, \phi) = \frac{15}{16\pi}\Big\{3\rho_{oo}(\cos^2\theta - \tfrac{1}{3})^2 + 4\rho_{11}\sin^2\theta\cos^2\theta + \rho_{22}\sin^4\theta$$
$$-2\cos\phi\sin 2\theta\left[\mathrm{Re}\,\rho_{21}\sin^2\theta + \sqrt{6}\ \mathrm{Re}\,\rho_{10}(\cos^2\theta - \tfrac{1}{3})\right]$$
$$-2\cos 2\phi\sin^2\theta\left[2\rho_{1-1}\cos^2\theta - \sqrt{6}\ \mathrm{Re}\,\rho_{20}(\cos^2\theta - \tfrac{1}{3})\right]$$
$$+2\mathrm{Re}\,\rho_{2-1}\cos 3\phi\sin 2\theta\sin^2\theta + \rho_{2-2}\cos 4\phi\sin^4\theta\Big\} \qquad (A.4)$$

with the trace condition $\rho_{oo} + 2\rho_{11} + 2\rho_{22} = 1.$

The corresponding single angle distributions are:

$$W_2(\cos\theta) = \frac{15}{8}\left\{3\rho_{oo}(\cos^2\theta - \tfrac{1}{3})^2 + 4\rho_{11}\sin^2\theta\cos^2\theta + \rho_{22}\sin^4\theta\right\} \qquad (A.5)$$

$$W_2(\phi) = \frac{1}{2\pi}\left\{1 + \rho_{2-2}\cos 4\phi\right\} \qquad (A.6)$$

If the production of the 2^+ state is assumed to occur by the exchange of spins no higher than one, only the matrix elements ρ_{oo}, ρ_{11} and ρ_{1-1} in (A.4) are non-zero. This results in a considerable simplification of the expression.

REFERENCES AND FOOTNOTES

NC = Nuovo Cimento
NCL = Lettere e Nuovo Cimento
NP = Nuclear Physics
PL = Physics Letters
PR = Physical Review
PRL = Physical Review Letters
RMP = Reviews of Modern Physics

(1) H.L. Anderson et al., PR 85, 936 (52).
(2) A. Barbaro-Galtieri et al., RMP 42, 87 (70).
(3) M. Gell-Mann, PL 8, 214 (64).
(4) C.B.A. Mc.Cusker & I. Cairns, PRL 23, 658 (69).
I. Cairns et al., PR 186, 1394 (69).
W.T. Chu et al., PRL 24, 917 (70).
(5) R.K. Adair & H. Kasha, PRL 23, 1355 (69).
H. Frauenfelder et al., PRL 24, 33 (70).
D.C. Rahm & R.I. Louttit, PRL 24, 279 (70).
(6) G.F. Chew & S.C. Frautschi, PRL 7, 394 (61).
(7) D.A. Glaser, PR 87, 665 (52).
(8) The names of the participating institutions are:
A) Physikalisches Institut der Technischen Hochschule, Aachen.
B) Forschungsstelle für Physik Hoher Energien der Deutschen Akademie der Wissenschaften zu Berlin, Zeuthen.
C) CERN, European Organisation for Nuclear Research, Geneva.
L) Physics Department, Imperial College, London.
V) Institut für Hochenergiephysik der Universität, Wien.

(9) Observation of a ($K\pi\pi$) resonance near 1800 Mev.
J. Bartsch et al., PL 22, 357 (66).

(10) K^-p elastic scattering at 10 Gev/c.
M. Aderholz et al., PL 24B, 434 (67).

(11) Ξ, Ω^- and Antibaryon production in 10 Gev/c K^-p interactions.
J. Bartsch et al., NP B4, 326 (68).

(12) Lambda production in 10 Gev/c K^-p interactions.
M. Aderholz et al., NP B5, 606 (68).

(13) K*(890) Production in 10 Gev/c K^-p interactions and comparison with Absorption and Regge Pole models.
M. Aderholz et al., NP B5, 567 (68).

(14) Mass dependence of the small angle differential cross-section for high energy interactions.
J. Bartsch et al., PL 27B, 336 (68).

(15) Total and Differential Cross Sections in 10 Gev/c K^-p interactions
M. Aderholz et al., NP B7, 111 (68).

(16) Analysis of the K*(1320) and L-meson produced in 10 Gev/c K^-p interactions. J. Bartsch et al., NP B8, 9 (68).

(17) Evidence for a new Ξ resonance at 2500 Mev in 10 Gev/c K^-p interactions. J. Bartsch et al., PL 28B, 439 (69).

(18) Ω^- production in 10 Gev/c K^-p interactions.
R. Speth et al., PL 29B, 252 (69).

(19) Production of Strange Particles in 10 Gev/c K^-p interactions and comparison with the predictions of the multiperipheral model.
J. Bartsch et al., NP B11, 373 (69).

(20) Production of proton-antiproton and kaon-antikaon pairs in four-body reactions of 8 Gev/c π^+ and 10 Gev/c K^- on protons.
M. Aderholz et al., NP B14, 255 (69).

(21) A study of the reaction $K^-p \longrightarrow p\bar{K}^0\pi^-$ with the Veneziano model.
J. Bartsch et al., NP B20, 45 (70). (D.Ph.II 70-03)

(22) Comparison of $\pi^{\pm}p$ and K^-p reactions with a multiperipheral model using the Van Hove Hexagon and Cuboctahedron plots.
J. Bartsch et al., NP B19, 381 (70).

(23) J. Alitti et al., PRL 22, 79 (69).

(24) E. Regenstreif, CERN Reports 59-29 (59), 60-26 (60), 62-03 (62) (English translations).

(25) E. Keil & W.W. Neale, Int. Conf. on High Energy Accelerators, Dubna (63), P.782.
M. Bell et al., ibid., P.798.

(26) P. Lazeyras, CERN/TC/Beam 66-7 (66).
P. Bernard et al., CERN Report 68-29 (68).

(27) W.K.H. Panofsky, Stanford Report HEPL-82 (56).
W. Schnell, CERN Report 61-5 (61).
E. Keil, CERN Report 66-21 (66), P.43.

(28) Pl Bramham et al., PL 15, 290 (65).

(29) F. Seitz, Physics of Fluids, 1, 2 (58).

(30) L. Riddiford et al., Proc. Int. Conf. on High Energy Accelerators and Instrumentation, CERN (1959), P.445.

(31) C. Peyron & H.S. Bridge ibid., P.454.

(32) W.T. Welford, Applied Optics 2, 981 (63).

(33) F. Früngel et al., Applied Optics 2, 1017 (63).

(34) Experimental determinations of the exponent n in the relation $b = c/\beta^n$ for bubble densities in hydrogen have given the following results:

1.935 ± 0.077	V.P. Kenney, PR 119, 432 (60).
consistent with 2	R.M. Lea & C. Vittitoe, Rev.Sci.Instr. 33, 243 (62).
" "	2 C. Peyrou, Conf. on Instrumentation for High Energy Physics (1960), P.157.
1.86 ± 0.37	A. Ahmadzadeh & N.N. Biswas, NC 19, 958 (61).
1.91 ± 0.05	B. Sechi-Zorn & G.T. Zorn, NC. Supp. 26, 197 (62).
2.02 ± 0.14	B.N. Fabian et al., Rev.Sci.Instr. 34, 484 (63).

(35) This device is usually known as an HPD following the original suggestion by P.V.C. Hough & B.W. Powell, NC 18, 1184 (60).

(36) M. Ibbotson, Ph.D Thesis, Imperial College (63), P.46.

(37) CERN Track Chamber (T.C.) Program Library.

(38) W.G. Moorhead, CERN Report 60-33 (60).

(39) B. Ronne, 1964 Cern School Vol. 1, P.87 (Cern report 64-13).

(40) R. Böck, Cern Report 60-30 (60).

(41) M.E. Mermikides, Ph.D Thesis, Imperial College (69).

(42) N.C. Mukherjee, Ph.D. Thesis, Imperial College (68).

(43) A.H. Rosenfeld & W.E. Humphrey, Ann.Rev.Nuc. Sci. 13, 103 (63).

(44) W. Galbraith et al., PR 138B, 913 (65).

(45) F. Schweingruber et al., PR 166, 1317 (68).
(46) S.E. Derenzo & R.H. Hildebrand, Nuc. Instr. Meth. 69, 287 (69).
(47) G. Kellner, private communication.
(48) P. Peeters et al., Nuc. Instr. Meth. 76, 125 (69).
(49) H.J. Martin, Nuc. Instr. Meth. 64, 185 (68).
(50) G. Breit & E.P. Wigner, PR 49, 519 (36).
(51) J.D. Jackson, NC 34, 1644 (64).
(52) E. Fermi, Prog. Theor. Phy. 5, 570 (50).
(53) M.H. Alston et al., PRL 6, 300 (61).
(54) N. Hague et al., PL 14, 338 (65).
(55) H. Cramér, Mathematical Methods of Statistics (Princeton University Press, 1946).
F.T. Solmitz, Ann. Rev. Nuc. Sci. 14, 375 (64).
(56) G.F. Chew & F.E. Low, PR 113, 1640 (59).
(57) S.P. Almeida et al., PL 14, 240 (65)
(58) P.J. Dornan et al., PRL 19, 271 (67)
(59) L. Leprince-Ringuet, Ann. Rev. Nuc. Sci. 3, 39 (53).
W.H. Barkas et al., PR 101, 778 (56).
(60) A. Barbaro-Galtieri et al., PRL 22, 1207 (69).
(61) R.T. Deck, PRL 13, 169 (64).
(62) J.R. Ficenec et al., PR 169, 1034 (68); PR 175, 1725 (68).
(63) D.J. Crennell et al., PRL 22, 487 (69).
(64) B. French, Proc. XIVth Int. Conf. on High Energy Physics, Vienna (68), P.91 (estimate made by A.H. Rosenfeld).
(65) B. Levrat et al., PL 22, 714 (66).
M.N. Focacci et al., PRL 17, 890 (66).
G. Chikovani et al., PL 25B, 44 (67).
(66) H. Benz et al., PL 28B, 233 (68).
D.J. Crennell et al., PRL 20, 1318 (68).
W. Kienzle, Meson Spectroscopy (based on Philadelphia conference 1968), P.265.
(67) M.L. Goldberger & K.M. Watson, PR 136B, 1472 (64).
A.S. Goldhaber, Meson Spectroscopy (Benjamim, 1968), P.297.
K.E. Lassila & P.V. Ruuskanen, PRL 17, 490 (66); PRL 19, 762 (67).
H. Rosdolsky, PR 180, 1403 (69).
(68) P.J. Davis et al., PRL 23, 1071 (69).

(69) W. Heisenberg, ZFP 77, 1 (32).

B. Cassen & E.U. Condon, PR 50, 846 (36).

E.P. Wigner, PR 51, 106 (37).

(70) T. Nakato & K. Nishijima, Prog. Theor. Phy. 10, 581 (53).

K. Nishijima, Prog. Theor. Phy. 12, 107 (54); 13, 285 (55).

M. Gell-Mann, PR 92, 833 (53).

(71) S. Mandelstam, PR 112, 1344 (58).

T.W.B. Kibble, PR 117, 1159 (60).

(72) G. Alexander et al., NP B13, 503 (69).

(73) M.G. Bowler, PL 31B, 318 (70).

(74) G. Veneziano, NC 57A, 190 (68).

(75) G. Otter, private communication.

(76) F. Selleri, NC 57A, 678 (68); NC 60A, 291 (69).

A. Peres, NCL 1, 245 (69).

F. Selleri, 3rd Int. Conf. on High Energy Physics and Nuclear Structure, Columbia University, Sept. 1969.

(77) M. Gell-Mann,(Caltech. Report) Cal. Inst. of Tech. Syn. Lab. rep. CTSL - 20 (61) (unpublished).

(78) W. Chinowsky et al., PRL 9, 330 (62).

(79) G. Bassompierre et al., NP B13, 189 (69).

(80) R.H. Dalitz, Phil. Mag. 44, 1068 (53).

E. Fabri, NC 11, 479 (54).

(81) C. Zemach, NC 32, 1605 (64); PR 133B, 1201 (64); 140B, 97, 109, (65).

(82) W. Majerotto et al., NP B2, 449 (67).

(83) S.G. Wojcicki et al., PR 135B, 495 (64).

(84) M.A.B. Bég et al., PR 124, 622 (61).
A. Fujii, PR 124, 1240 (61).
M.J. Sweig, PR 131, 860 (63).
(85) F. Cerulus, NC. Supp. 15, 402 (60).
K. Zalewski & J.A. Danysz, NP B2, 249 (67).
(86) V.E. Barnes et al., PRL 12, 204 (64).
(87) S. Okubo, Prog. Theor. Phy. 27, 949 (62).
(88) J.J. Sakurai, PRL 9, 472 (62).
S.L. Glashow, PRL 11, 48 (63).
(89) G. Zweig, Cern Reports TH 401, TH412 (64) (unpublished).
(90)a S. Ishida, Prog. Theor. Phy. 32, 922 (64); 34, 64 (65).
b J. Iizuka, Prog. Theor. Phy. 35, 117, 309 (66).
c R.H. Dalitz, Proc. 13th Int. Conf. on High Energy Physics, Berkeley (66), P.215.
(91) L. Michel, NC 10, 319 (53).
(92) S. Meshkov et al., PRL 10, 361 (63).
(93) G.L. Kane, PR 156, 1738 (67).
(94) P. McNamee & F. Chilton, RMP 36, 1005 (64).
(95) The motivation for using $(mass)^2$ values for bosons is usually attributed to a private remark of R.P. Feynman. However there is not universal agreement on this point (see for example ref. 90b)
(96) E.E. Salpeter & H.A. Bethe, PR 84, 1232 (51).
(97) A.J. Macfarlane & R.H. Socolow, PR 144, 1194 (66).
(98) S.L. Glashow & R.H. Socolow, PRL 10, 329 (65).
(99) J. Schwinger, PR 135B, 816 (64).
(100) S. Okubo, PL 5, 165 (63).

$(K\pi\pi)$ systems have been studied in several $K^{\pm}P$ experiments, mostly above 3 Gev/c. The following list contains only the most recent reports from each of the experiments:

K^-p experiments:

(101) 2.1 - 2.7 Gev/c: J.H. Friedman & R.R. Ross, Bull. Amer. Phy. Soc. 12, 539 (67).
(102) 4.6 & 5.0 Gev/c: P.J. Dornan et al., PRL 19, 271 (67).

(103) 5.5 Gev/c: J.C. Park et al., PRL 20, 171 (68).
J.C. Park & S. Kim, PR 174, 2165 (68).
(104) 6 Gev/c: D.C. Colley et al., NC 59A, 519 (69).
(105) 7.3 Gev/c: S.U. Chung et al., BNL-13115 (69) (unpublished).
(106) 8 Gev/c: G. Otter, private communication.
(107) 12.6 Gev/c: J. Andrews et al., PRL 22, 731 (69).

K^+p experiments

(108) 3 & 3.5 Gev/c: W. de Baere et al., NC 49A, 373 (67).
(109) 3.54 Gev/c: A.R. Erwin et al., NP B9, 364 (69).
J.M. Bishop et al., NP B9, 403 (69).
(110) 4.6 Gev/c: B.C. Shen et al., PRL 17, 726 (66).
(111) 5 Gev/c: G. Bassompierre et al., PL 26B, 30 (67).
M. Jobes et al., PL 26B, 49 (67).
(112) 5.5 Gev/c: F. Bomse et al., PRL 20, 1519 (68).
P. Antich et al., NP B _, (70).
(113) 7.3 Gev/c: C.Y. Chien et al., PL 28B, 143 (68).
(114) 9 Gev/c: G. Alexander et al., NP B13, 501 (69).
(115) 10 Gev/c: Birmingham-Glasgow-Oxford collaboration, Topical Conf. on Hadrons, Cern (68), Report 68-7, 2, 121. See also: Proc. Int. Conf. on Elementary particles, Lund (69), P.316 (submitted paper 82).
(116) 12 Gev/c: A. Barbaro-Galtieri et al., PRL 22, 1207 (69); Proc. Int. Conf. on Elementary Particles, Lund (69) P.316 (submitted 88).
(117) 12.7 Gev/c: J. Berlinghieri et al., PRL 18, 1087 (67); Topical Conf. on Hadrons, Cern (68), Report 68-7, 2, 172.
(118) R.H. Dalitz, Topical Conf. on Meson Spectroscopy, Philadelphia (68) published in Meson Spectroscopy, Benjamin (1968)).
(119) A. Astier et al., NP B10, 65 (69).
(120) W. de Baere et al., NC 51A, 401 (67).
(121) T.G. Trippe et al., PL 28B, 203 (68).
(122) G. Goldhaber et al., Proc. Int. Conf. on Elementary Particles, Lund (69), paper 429 and UCRL - 19229.
(123) A. Bettini et al., NC 42A, 695 (66).
R.A. Donald et al., NP B11, 551 (69).
(124) W. Beusch et al., PL 25B, 357 (67).

(125) A.H. Rosenfeld, Topical Conf. on Meson Spectroscopy, Philadelphia (68) (published in Meson Spectroscopy), UCRL - 18266.

(126) D.J. Crennell et al., PL 28B, 136 (68).

(127) C. Caso et al., NC 54A, 983 (68).

(128) L. Dubal et al., Proc. 13th Int. Conf. on High Energy Physics, Berkeley (66), P.143 (submitted paper 7.10).

(129) B. French et al., NC 52A, 438 (67).

(130) G. Goldhaber, Proc. 13th Int. Conf. On High Energy Physics, Berkeley (66), P.101.

(131) K. Niizeki, Prog. Theor. Phy. 40, 906 (68).

(132) H. Goldberg et al., NC 45A, 169 (66).

(133) J.J. de Swart, Rev. Mod. Phy. 35, 916 (63).

(134) F. Gürsey & L.A. Radicati, PRL 13, 173 (64).
B. Sakita, PR 136B, 1756 (64).

(135) E.P. Wigner, PR 51, 106 (37).

(136) M. Gell-Mann, PRL 14, 77 (65).
E. Borchi & R. Gatto, PL 14, 352 (6).
R. Gatto et al., NC 39, 1192 (6).
see also D.K. Choudhury & A.N. Mitra, PR D1, 351 (70), for a recent extension of this idea.

(137) Chia-Hwa Chan & Nguyen-Huu Xuong, PR 142, 1132 (66).
D. Horn et al., PR 147, 980 (66).

(138) M. Resnikoff & R.R. Silbar, PR 149, 1245 (66).

(139) E.U. Condon & G.H. Shortley, Theory of Atomic Spectra.

(140) G. Zweig, Meson Spectroscopy, Benjamin (68), P.485.

(141) O.W. Greenberg, Proc. Lund Conf. on Elem. Particles (69), P.387.

(142) T. Regge, NC 14, 951 (59).

(143) S.C. Frautschi et al., PR 126, 2204 (62).

(144) G.F. Chew & S.C. Frautschi, PRL 8, 41 (62).

(145) M. Gell-Mann, CERN Report TH 533 (64), unpublished.
R.G. Newton, The Complex J-Plane, Benjamin (1964), P.463.

(146) R.C. Arnold, PRL 14, 657 (65).

(147) S. Minami, NC 46A, 544 (66).

(148) E. Fermi & C.I. Yang, PR 76, 1739 (49).

(149) O. Sinanoglu, PR 145, 1205 (66); PRL 16, 207 (66).
D. Cline, NC 45A, 750 (66).
A. Ahmadzadeh, NC 46A, 415 (66).
D.G. Sutherland, NP B2, 157 (67).
A. Ahmadzadeh & R.J. Jacob, PR 176, 1719 (68)

(150) I. Ia. Pomeranchuk, Zhur, Eksp. i Teoret. Fiz. 34, 725 (58); English translation - Soviet Phys. JETP 7, 499 (58).

(151) D. Amati et al, PRL 4, 89 (60).
S. Weinberg, PR 124, 2049 (61).
A. Martin, NC 39, 704 (65).

(152) L.B. Okun & I.Ia. Pomeranchuk, Zhur. Eksp. i Teoret. Fiz. 30, 424 (56); English translation - Soviet Phys. JETP 3, 307 (56).

(153) J.V. Allaby et al., PL 30B, 500 (69).

(154) D.R.O. Morrison, PL 22, 528 (66); see also Proc. of Stony Brook Conference on High-Energy Two-Body reactions, (1966), unpublished.
T. Hofmokl & A. Wroblewski, PL 31B 391 (70).

(155) D.R.O. Morrison, Proc. Lund Conf. on Elementary Particles, 1969, P.237. Also appears as CERN report D.Ph. II/69-28.

(156) See, for example, the lectures given at the 1967 CERN School by B.E.Y. Svensson, CERN Report 67-24, volume II.

(157) M. Froissart, PR 123, 1053 (61).

(158) A. Martin, NC 42A, 930 (66).

(159) G.G. Beznogikh et al., Proc. Lund Conf. on Elementary Particles (69), submitted paper 426.

(160) T. Lasinski et al., PR 179, 1426 (69).

(161) K.J. Foley et al., PRL 11, 503 (63).

The following references report the production of K*(890) and K*(1420) in kaqn-nucleon interactions above 2 Gev/c. The target is a proton unless stated otherwise and the reactions concerned are two-body ones with $K^* \rightarrow K\pi$

K^- experiments

(162) 2.0 & 2.24 Gev/c: M. Dickenson et al., PL 23, 505 (66).

(163) 2.24 Gev/c : G.W. London et al., PR 143, 1034 (66).

(164) 2.1 — 2.7 Gev/c : J.H. Friedman, Ph.D. Thesis, Berkeley, UCRL - 18860 (69), unpublished.

(165) 2.63 & 2.70 Gev/c : J.R. Ficenec et al., PR 175, 1725 (68).

(166) 3 Gev/c : R. Barloutaud et al., PL 12, 352 (64).
A. Verglas et al., NC 41A, 629 (66).
S. Focardi et al., PL 16, 351 (65).

(167) 3.5 Gev/c : N. Haque et al., PL 14, 338 (65).
BGLOR collaboration, Rutherford Lab. report RPP/H 29 (unpublished).

(168) 3.9 Gev/c K^-d : D.J. Crennell et al., PRL 22, 487 (69).

(169) 4.1 & 5.5 Gev/c : F. Schweingruber et al., PR 166, 1317 (68).

(170) 4.5 Gev/c K^-d : R.L. Eisner et al., PL 28B, 356 (68).
D.D. Carmony et al., Purdue report COO-1428-166 (70).

(171) 4.6 & 5.0 Gev/c : M. Goldberg et al., PRL 18, 680 (67).
4.6 Gev/c : Y.W. Kang, PR 176, 1587 (68).

(172) 6 Gev/c : D.C. Colley et al., NC 53A, 522 (68).

(173) 11.2 Gev/c : B.D. Hyams et al., NP B7, 1 (68).

K^+ experiments

(174) 2.26 Gev/c : F. Bomse et al., PR 158, 1298 (67).

(175) 2.3 K^+d : S. Goldhaber et al., PRL 15, 737 (65).

(176) 2.1 - 2.7 Gev/c : J. Brunet et al., Proc. Lund Conf. on Elementary Particles (69).

(177) 3 Gev/c : G.R. Lynch et al., PL 9, 359 (64).
M. Ferro-Luzzi et al., NC 36, 1101 (65).
P. Sallstrom et al., NC 49A, 348 (67).
P. Sallstrom & G. Blomqvist, Arkiv for Fysik 37, 463 (68).

(178) 3 Gev/c : W.P. Dodd et al., PR 177, 1991 (69).

(179) 3 Gev/c K^+d : G. Bassompierre et al., Cern report D.Ph.II 69-29 (to be published in Nuclear Physics B).

(180) 3.5 Gev/c : Y. Goldschmidt-Clermont et al., NC 46A, 539 (66).
W. de Baere et al., NC 51A, 401 (67).

(181) 4.6 Gev/c : C. Fu, UCRL-18417 (68), unpublished.

(182) 5 Gev/c : G. Bassompierre et al., NP B13, 189 (69).

(183) 9 Gev/c : V.G. Lind et al., NP B14, 1 (69).

(184) 10 Gev/c : BGO collaboration, Topical Conf. on Hadrons, CERN (68), Report 68-7, 2, 121.

(185) 12.7 Gev/c : J.C. Berlinghieri et al., NP B8, 333 (68).

(186) L. O'Raifeartaigh, PR 139B, 1052 (65).
L. Michel, PR 137B, 405 (65).

(187) M. Jacob & G.C. Wick, Ann. Phy. 7, 404 (59).

(188) M. Peshkin, PR 123, 637 (61).
M. Ademollo et al., PR 140B, 192 (65).

(189) P. Eberhard & M.L. Good, PR 120, 1442 (60).

(190) R.H. Capps, PR 122, 929 (61).

(191) J.D. Jackson, NC 34, 1644 (64).

(192) G. Bassompierre et al., NP B13, 189 (69).

(193) W. de Baere et al., NC 61A, 397 (69).

(194) J.P. Ader et al., NC 56A, 952 (68).

(195) G.A. Ringland & R.L. Thews, PR 170, 1569 (68).

(196) R.L. Thews, PR 155, 1624 (67).

(197) P. Minnaert, PR 151, 1306 (66).

(198) J. Daboul, NP B4, 180 (68).

(199) H. Yukawa, Proc. Phys.-Math. Soc. Japan 17, 48 (35).

(200) C.J. Goebel, PRL 1, 337 (58).

(201) S.D. Drell, PRL 5, 342 (60); Rev. Mod. Phy. 33, 458 (61).
F. Salzmann & G. Salzmann, PRL 5, 377 (60); PR 120, 599 (60); PR 121, 1541 (62).
F. Bonsignori & F. Selleri, NC 15, 456 (60).

(202) E. Ferrari & F. Selleri, NC 21, 1028 (61); Supp. NC 24, 453 (62); NC 27, 1450 (63).

F. Selleri, PL 3, 76 (62).
(203) U. Amaldi & F. Selleri, NC 31, 360 (64).
(204) J.D. Jackson & H. Pilkuhn, NC 33, 906 (64); erratum NC 34, 1841 (64).
(205) A. Dar et al., PRL 12, 82 (64).
A. Dar & W. Tobocman, PRL 12, 511 (64).
A. Dar, PRL 13, 91 (64).
(206) N. Sopkovich, NC 26, 186 (62).
(207) K. Gottfried & J.D. Jackson, NC 34, 735 (64).
(208) J.D. Jackson et al., PR 139B, 428 (65).
(209) J.D. Jackson, Rev. Mod. Phy. 37, 484 (65).
(210) J.H. Friedman & R.R. Ross, PRL 16, 485 (66); erratum 16, 832 (66).
(211) J.T. Donohue, PR 163, 1549 (67).
(212) B. Sakita & K.C. Wali, PR 139B, 1355 (65).
(213) M. Bander & G.L. Shaw, PR 139B, 956 (65).
P.C.M. Yock & D. Gordon, PR 157, 1362 (67).
(214) J.S. Ball & W.R. Frazer, PRL 14, 746 (65).
(215) R. Omnes, PR 137B, 649 (65).
(216) R.H. Dalitz & S. Tuan, Ann. Phy. 10, 307 (60).
R.H. Dalitz, Rev. Mod. Phy. 33, 471 (61).
R. Arnold, PR 136B, 1388 (64).
J.S. Trefil, PR 147, 1452 (66).
(217) G.F. Chew & S. Mandelstam, PR 119, 467 (60).
(218) E.J. Squires, NC 34, 1328 (64).
(219) K. Dietz & H. Pilkuhn, NC 37, 1561 (65); 39, 928 (65).
(220) K. Gottfried & J.D. Jackson, PL 8, 144 (64).
K. Gottfried & J.D. Jackson, NC 33, 309 (64).
(221) D.Z. Freedman & J.M. Wang, PR 153, 1596 (67).
(222) L.L. Wang, PR 142, 1187 (66).
(223) M. Gell-Mann et al., PR 133B, 145 (64).
(224) M. Markytan, NP B10, 193 (69).
(225) L. Jones, PR 163, 1523 (67).
(226) H.P. Dürr & H. Pilkuhn, NC 40A, 899 (65).
J. Benecke & H.P. Dürr, NC 56A, 299 (68).
(227) G. Wolf, PR 182, 1538 (69).

(228) L. Van Hove, PL 24B, 183 (67).

(229) G. Veneziano, NC 57A, 190 (68).

(230) R. Dolen et al., PRL 19, 402 (67); PR 166, 1768 (68).
G.F. Chew & A. Pignotti, PRL 20, 1078 (68).

(231) D.R.O. Morrison, PR 165, 1699 (68),

(232) R. Carlitz et al., PRL 23, 1134 (69).

(233) G. Goldhaber, PRL 19, 976 (67).

(234) G. Fogli et al., NCL 1, 352 (69).

(235) N. Byers & C.N. Yang, PR 142, 976 (66).
T.T. Chou & C.N. Yang, PR 175, 1832 (68).

ACKNOWLEDGEMENTS

I would like to thank Professor C.C. Butler for the opportunity of working in the High Energy Nuclear Physics Group at Imperial College and Dr. S.J. Goldsack for his supervision of the work in this thesis.

An experiment of this kind could not succeed without the cooperation of all the members of the collaborating groups and of the scanning, measuring, computing and technical staffs in each of the laboratories. In particular I would like to thank my colleagues M.J. Losty, M.E. Mermikides and N.C. Mukherjee for their hard work in the routine analysis of the experiment and Miss Margaret Urquhart for her very efficient organisation of the scanning, measuring and data processing stages.

Finally I am grateful to the Science Research Council for the award of a postgraduate studentship between 1964 and 1967 and to the college for a subsequent post as Research Assistant.

To

G.H.B.S.

"Those who have handled sciences have been either men of experiment or men of dogmas. The men of experiment are like the ant; they only collect and use; the reasoners resemble spiders, who make cobwebs out of their own substance. But the bee takes a middle course; it gathers its material from the flowers of the garden and of the field, but transforms and digests it by a power of its own. Therefore from a closer and purer league between these two faculties, the experimental and the rational (such as has never yet been made), much may be hoped".

FRANCIS BACON, Novum Organum (1620).